



Università degli Studi di Napoli Federico II
Ph.D. Program in
Information **T**echnology and **E**lectrical **E**ngineering
XXXV Cycle

Thesis for the Degree of Doctor of Philosophy

Integration and Control of the NPC Multi-Source Inverter in Multimode Rail Vehicles

by
Emanuele Fedele

Supervisor: Prof. Diego Iannuzzi

Co-supervisor: Prof. Andrea Del Pizzo



Scuola Politecnica e delle Scienze di Base
Dipartimento di **I**ngegneria **E**lettrica e delle **T**ecnologie dell'**I**nformazione

*A Lello e Maria,
angeli custodi.*

Integration and Control of the NPC Multi-Source Inverter in Multimode Rail Vehicles

Ph.D. Thesis presented
for the fulfillment of the Degree of Doctor of Philosophy
in Information Technology and Electrical Engineering
by

Emanuele Fedele

October 2022



Approved as to style and content by

Diego Iannuzzi

Prof. Diego Iannuzzi, Supervisor

Andrea Del Pizzo

Prof. Andrea Del Pizzo, Co-supervisor

Università degli Studi di Napoli Federico II

Ph.D. Program in Information Technology and Electrical Engineering
XXXV cycle - Chairman: Prof. Stefano Russo



<http://itee.dieti.unina.it>

Candidate's declaration

I hereby declare that this thesis submitted to obtain the academic degree of Philosophiæ Doctor (Ph.D.) in Information Technology and Electrical Engineering is my own unaided work, that I have not used other than the sources indicated, and that all direct and indirect sources are acknowledged as references.

Parts of this dissertation have been published in international journals and/or conference articles (see list of the author's publications at the end of the thesis).

Napoli, December 27, 2022



Emanuele Fedele

Abstract

Rolling stock manufacturers are developing a new generation of multimode rail vehicles equipped with a combination of hydrogen fuel cells and energy storage devices. Multimode trains benefit from high energy efficiency, lower current absorption and voltage fluctuations on the main supply, and low or null local emissions when running without electrification. Laying at the core of multimode traction architectures, power electronic converters interconnect and control the energy flows among power sources, storage devices, and traction loads. To cope with the low specific energy and power of the onboard sources and storage devices, compact and lightweight power electronics are required.

This Ph.D. thesis aims at exploring the integration and control of the NPC Multi-Source Inverter (MSI) as main traction converter of multimode rail vehicles to reduce the size and weight of the onboard traction equipment. By providing a direct connection between two dc sources and one ac load in a single conversion stage, the MSI can reduce the power rating and size of the onboard dc/dc converters.

A broad review of the traction architecture and energy control of recent multimode vehicles is first presented. The concept and fundamentals of the MSI are then revised, and an original PWM strategy for the converter is presented, which overcomes all the limits of the established literature approach and increases the feasible operating modes of the MSI. The integration and coordinated control of the MSI and dc/dc converter in a semi-active traction architecture are then discussed and validated experimentally. Finally, numerical investigations are carried out to quantify the effective reductions in size and weight achieved by an MSI-based traction architecture for two case studies based on real multimode vehicles.

Keywords: power electronics, traction systems, multimode trains, rail transportation.

Sintesi in lingua italiana

I costruttori di veicoli ferroviari stanno sviluppando una nuova generazione di veicoli multimodali facenti uso di celle a combustibile e dispositivi di accumulo energetico. I treni multimodali esibiscono un maggior rendimento energetico, minori assorbimenti di corrente dalla linea esterna, ed emissioni locali ridotte o assenti nel funzionamento in assenza di linea elettrificata. Alla base del sistema di propulsione multimodale, i convertitori elettronici interconnettono le sorgenti ai motori di trazione e ne controllano i flussi di potenza. Per far fronte alle basse densità di energia e potenza delle sorgenti e dei sistemi di accumulo di bordo, si rende necessario l'impiego di convertitori elettronici leggeri e compatti.

La presente tesi di Dottorato esplora l'integrazione ed il controllo dell'inverter NPC multi-sorgente (MSI) come convertitore di trazione in veicoli ferroviari multimodali, allo scopo di ridurre la taglia del sistema propulsivo. Grazie alla possibilità di connettere direttamente due sorgenti dc indipendenti allo stesso carico ac, l'MSI può ridurre la potenza di dimensionamento e la taglia dei convertitori dc/dc di bordo.

Un'ampia panoramica delle architetture di trazione e degli algoritmi di controllo energetico di veicoli multimodali in attuale o recente funzionamento è inizialmente presentata. Successivamente ad un richiamo sul principio di funzionamento dell'MSI, è presentata una nuova tecnica di modulazione in grado di migliorare ed ampliare le modalità operative del convertitore. Una proposta di integrazione e controllo coordinato dell'MSI e del convertitore dc/dc in una architettura di trazione multimodale è discussa e validata sperimentalmente. Infine, un'estesa analisi numerica è condotta per quantificare i benefici apportati da un'architettura di propulsione basata su MSI in due casi studio basati su veicoli multimodali reali.

Parole chiave: elettronica di potenza, sistemi di trazione, treni multimodali, trasporto ferroviario.

Contents

Abstract	i
Sintesi in lingua italiana	ii
Acknowledgements	vii
List of Acronyms	xi
List of Figures	xix
List of Tables	xxii
List of Symbols	xxiii
1 Introduction	1
1.1 Background and motivation	1
1.2 Contribution	5
1.3 Thesis layout	6
2 Multimode rail vehicles	9
2.1 Energy sources and storage devices	9
2.1.1 Batteries	10
2.1.2 Supercapacitors	12
2.1.3 Fuel cells and hydrogen storage	12
2.1.4 Comparison	13
2.2 Review of real applications	14
2.2.1 Vehicles with onboard batteries	14

2.2.2	Vehicles with onboard supercapacitors	20
2.2.3	Vehicles with onboard hybrid storage systems	24
2.2.4	Vehicles with onboard fuel cells	26
2.2.5	System-level comparison	30
2.3	Advantages and challenges	33
2.3.1	Onboard energy storage in electrified railways	33
2.3.2	Potential for diesel replacement in non-electrified railways	35
3	Traction architectures and control strategies	41
3.1	State of the art	41
3.1.1	Multimode vehicles with external supply or diesel generators	41
3.1.2	Multimode fuel cell vehicles	48
3.2	Alternative energy management strategies	50
3.3	Non-conventional traction converters	52
4	Multi-source inverter: topology and modulation	57
4.1	Introduction	57
4.2	Topology and switching configurations	59
4.3	Interleaved two-level modulation	62
4.3.1	Analytical study	63
4.3.2	Operating domain	69
4.3.3	Experimental results	71
4.4	The multi-objective vector modulation	77
4.4.1	MSI space-vector model	78
4.4.2	Computation of the duty cycle signals	79
4.4.3	Operating domain	83
4.4.4	Experimental results	89

5	Multi-source inverter: integration and control	97
5.1	Integration in semi-active architectures	97
5.2	Coordinated control of the power converters	100
5.3	Experimental results	102
5.3.1	Non-receptive source on the high-voltage bus	103
5.3.2	Non-receptive source on the low-voltage bus	112
5.3.3	Discussion	118
6	Comparative numerical analysis	121
6.1	Case study: battery tram	122
6.1.1	System architecture and control	122
6.1.2	Sizing of power converters	126
6.1.3	VA rating, weight, and volume comparison	133
6.1.4	Dynamic performance and power losses	135
6.2	Case study: fuel cell train	144
6.2.1	System architecture and control	144
6.2.2	Sizing of power converters	148
6.2.3	VA rating, weight, and volume comparison	153
6.2.4	Dynamic performance and power losses	155
6.3	Discussion	161
7	Conclusions	163
A	Small-scale rail traction drive simulator	167
B	Traction circuit simulation models	171
B.1	Complete model	171
B.1.1	Vehicle dynamics	172
B.1.2	Traction motors	172
B.1.3	Traction inverters	174
B.1.4	Interleaved dc/dc converters	176

B.1.5	Passive filters	176
B.1.6	Power sources and energy storage devices	176
B.1.7	Auxiliaries	178
B.2	Simplified model	179
C	Filters and heatsink design in power converters	181
	Bibliography	191
	Author's Publications	207

Acknowledgements

The research presented in this dissertation has been supported by the Italian Ministry of University and Research (MUR) under the program PON 2014-2020 (CCI 2014IT16M2OP005), Fondo Sociale Europeo, Azione I.1: "Dottorati Innovativi con Caratterizzazione Industriale", project ID: DOT1318930, CUP: E65F19001220007.

List of Acronyms

The following acronyms are used throughout the thesis.

2S	Two-Stage
APS	Auxiliary Power Supply
BEMU	Battery Electric Multiple Unit
BMS	Battery Management System
DEMU	Diesel Electric Multiple Unit
DMU	Diesel Multiple Unit
EMS	Energy Management Strategy
EMU	Electrical Multiple Unit
ESS	Energy Storage System
FC	Fuel Cell
FEA	Finite Element Analysis
FOC	Field-Oriented Control
GA	Genetic Algorithm

GHG	Green-House Gas
HEMU	Hydrogen Electrical Multiple Unit
HESS	Hybrid Energy Storage System
HPHS	High-Pressure Hydrogen Storage
HV	High Voltage
HVO	High-Voltage-Only
IGBT	Insulated Gate Bipolar Transistor
LCO	Lithium Cobalt Oxide
LFP	Lithium Iron Phosphate
LiB	Lithium-ion Battery
LMO	Lithium Manganese Oxide
LRV	Light Rail Vehicle
LTO	Lithium Titanate Oxide
LV	Low Voltage
LVO	Low-Voltage-Only
MMC	Modular Multilevel Converter
MOVVM	Multi-Objective Vector Modulation
MPC	Model Predictive Control
MSI	Multi-Source Inverter
NCA	Nickel Cobalt Aluminum

NiMHB	Nickel-Metal Hydride Battery
NMC	Nickel Manganese Cobalt
NPC	Neutral-Point-Clamped
PEM	Proton-Exchange Membrane
OCV	Open-Circuit Voltage
PI	Proportional-Integral
PWM	Pulse Width Modulation
RB	Rule-Based
RMS	Root Mean Square
RTRI	Railway Technical Research Institute
S2S	Semi-Two-Stage
SiC	Silicon Carbide
SC	Supercapacitors
SOC	State of Charge
SVM	Space Vector Modulation
THD	Total Harmonic Distortion
UC	Ultracapacitors
VSI	Voltage Source Inverter

List of Figures

- 1.1 Global energy consumption and well-to-wheel CO₂ equivalent emissions per passenger-kilometer, for different means of passenger transport. 2
- 1.2 Global evolution of diesel and electricity usage in passenger (a) and freight (b) rail services, and share of electrified lines (c) from 2000 to 2016. 3

- 2.1 Spider plots of the six major lithium-ion chemistries. 11
- 2.2 Main features of Nickel-Metal Hydride Batterys (NiMHBs), Lithium-ion Batterys (LiBs), Supercapacitorss (SCs), Fuel Cells (FCs), and High-Pressure Hydrogen Storage (HPHS) technologies for rail applications. 13
- 2.3 Onboard stored energy vs. off-wire autonomy of reported rail vehicles with onboard batteries. 22
- 2.4 Energy and power ratings of batteries and SCs alone or in conjunction with external supply (a-b), FC systems with Energy Storage Systems (ESSs) (c-d), and system-level Ragone plot of all technologies (e). 32

2.5	Comparison of rolling stock and infrastructure costs of Diesel Multiple Units (DMUs), Electrical Multiple Units (EMUs), Battery Electric Multiple Units (BEMUs), and Hydrogen Electrical Multiple Units (HEMUs) on five European regional lines.	40
3.1	Vehicle layout and traction system architecture of JR East’s EV-E301 catenary/battery train.	42
3.2	Layout and traction system architecture of Bombardier’s Flexity 2 catenary/battery tram.	44
3.3	Layout and traction system architecture of Hitachi’s BEC-819 catenary/battery train.	45
3.4	Traction system architecture of Hitachi’s KiHa E200 hybrid Diesel Electric Multiple Unit (DEMU).	46
3.5	Layout and traction system architecture of Siemens’ Combino Plus tri-mode tram.	47
3.6	Layout and traction system architecture of CRRC Tangshan’s FC/LiB/SC tri-mode tram.	48
3.7	Layout and traction system architecture of Alstom’s iLint FC/LiB bimode train.	49
3.8	Examples of integrated Modular Multilevel Converter (MMC) topologies for: (a) catenary/ ESS rail vehicle; (b) hydrogen rail vehicle.	53
3.9	Variants of the NPC multi-source inverter concept: (a) the sources share the common ground terminal; (b) the sources are connected in series.	54
4.1	Conceptual diagrams of: (a) standard semi-active architecture employing a Voltage Source Inverter (VSI); (b) alternative semi-active architecture employing an Multi-Source Inverter (MSI).	58

4.2	MSI converter: a) ideal circuit; b) Neutral-Point-Clamped (NPC) implementation; c) T-NPC implementation.	60
4.3	Switching configurations for the (a) NPC and (b) T-NPC circuits.	61
4.4	Switching waveforms for the interleaving modulation strategy.	64
4.5	(a) One sector of the space-vector voltage plane of the interleaved Space Vector Modulation (SVM) modulation. (b) Generation of the interleaving square-wave signal.	65
4.6	Quantization of the current-sharing control action.	70
4.7	Operating area of the interleaved modulation technique. . .	70
4.8	Setup for the experimental tests on the interleaved SVM modulation: (a) power circuit, (b) control diagram.	72
4.9	Results of the speed-ramp test at a constant duty cycle. . .	73
4.10	Motor current waveforms and frequency spectra for different MSI operating conditions.	75
4.11	Results of the driving cycle test with the interleaved SVM.	76
4.12	Currents supplied by the dc sources during the driving cycle test.	77
4.13	MOVM space vector diagram.	81
4.14	Block diagram of the multi-objective vector modulation. . .	83
4.15	Modulation limits and operating domain of the Multi-Objective Vector Modulation (MOVM) technique.	85
4.16	Switching waveforms of the MOVM in modulation region A.	86
4.17	Switching waveforms of the MOVM in modulation region B.	87
4.18	Switching waveforms of the MOVM in modulation region C.	88
4.19	Control scheme for the experimental tests on the MOVM. .	90
4.20	Steady-state ac and dc currents obtained with the MOVM.	92
4.21	Steady-state dc currents drawn by the MSI.	93

4.22	Results of the driving cycle test for the MOV M modulation technique: (a) motor speed, (b) dq-axis current control, (c) system power flows.	94
5.1	Conceptual system power flows in: (a) a conventional two-stage architecture based on the VSI , (b) semi-two-stage architecture based on the MSI	99
5.2	Coordination of the MSI and dc/dc converter reference currents when (a) the traction system is supplied by both sources and (b) by the Low Voltage (LV) source only. . . .	101
5.3	Power circuit configuration (a) and control scheme (b) for the tests on the Semi-Two-Stage (S2S) architecture with a non-receptive source on the High Voltage (HV)-bus.	104
5.4	Experimental results for the S2S architecture with a non-receptive source on the HV -bus: (a) motor speed, (b) dq axis current control, (c) system power flows.	106
5.5	Experimental results, battery at 250 V: (a) HV -bus currents, (b) LV -bus currents, (c) motor and dc sources voltages, (d) MSI first-leg duty cycles.	108
5.6	Experimental results, battery at 140 V: (a) system power flows, (b) LV -bus currents, (c) HV -bus currents, (d) motor and dc voltages, (e) duty cycles of the MSI first leg.	111
5.7	Power circuit configuration (a) and control scheme (b) for the tests on the S2S architecture with a non-receptive source on the LV -bus.	113
5.8	Experimental results for the S2S architecture with a non-receptive source on the LV -bus: (a) motor speed, (b) dq axis current control, (c) system power flows.	115

5.9	Experimental results for the S2S architecture with a non-receptive source on the LV -bus: (a) HV -bus currents, (b) LV -bus currents, (c) motor and dc sources voltages, (d) MSI first-leg duty cycles.	117
6.1	Battery tram: (a) vehicle layout, (b) traction effort/power curves, (c) Open-Circuit Voltage (OCV)-State of Charge (SOC) curve of the batteries.	122
6.2	Traction circuits: (a) baseline semi-active architecture, (b) S2S semi-active architecture.	124
6.3	Control diagrams of the Two-Stage (2S) and S2S traction circuits in catenary and catenary-free modes.	125
6.4	Driving cycle of the tram.	126
6.5	One leg inductor in the S2S architecture: (a) geometry, (b) flux-density distribution at peak current, (c) temperature distribution at peak Root Mean Square (RMS) current.	127
6.6	Temperatures in the dc/dc converter for (a) S2S topology, (b) 2S topology.	129
6.7	VSI line inductor: (a) geometry, (b) flux-density distribution at peak current, (c) temperature distribution at peak current.	132
6.8	Temperatures in the traction converters: (a) MSI , (b) VSI	133
6.9	VA ratings of the power converters in the 2S and S2S topologies.	134
6.10	Breakdown of volume and weight of power converters in the S2S and 2S architectures.	134
6.11	Simulation results with high and low SOC s: (a) traction effort and motor RMS current, (b-c) dc power levels and battery SOC	136

6.12	Waveforms of the main dc and ac variables at different time stamps of the driving cycle at high SOC.	138
6.13	Motor power losses (a) and efficiency (b) over the driving cycle in the 2S and S2S topologies.	139
6.14	Battery internal losses in the S2S and 2S topologies.	140
6.15	Breakdown of power losses (a) and cycle energy losses (b), and efficiency (c) of the MSI and VSI traction converters.	141
6.16	Breakdown of power losses (a) and cycle energy losses (b), and efficiency (c) of the dc/dc converter in the S2S and 2S topologies.	143
6.17	Fuel cell train: (a) vehicle layout, (b) traction effort/power curves, (c) OCV-SOC curve of the battery, (d) polarization curve and (e) efficiency curve of one FC stack.	145
6.18	Traction circuits: (a) baseline semi-active architecture, (b) S2S semi-active architecture.	146
6.19	Driving cycle of the fuel cell train.	148
6.20	Temperatures in the dc/dc converter in: (a) S2S topology, (b) 2S topology	151
6.21	Temperatures in the traction converters: (a) MSI, (b) VSI.	154
6.22	Breakdown of volume and weight of power converters in the S2S and 2S architectures.	155
6.23	Simulation results with medium and low SOC: (a) traction effort and motor RMS current of one traction drive, (b-c) dc power levels and battery SOC.	156
6.24	Waveforms of the main dc and ac variables at different time stamps of the driving cycle at medium SOC.	158
6.25	Breakdown of power losses (a) and cycle energy losses (b), and efficiency (c) of the VSI and MSI traction converters.	160
6.26	Breakdown of energy losses (a) and efficiency (b) of the dc/dc converter in the S2S and 2S topologies.	161

A.1	Mechanical subsystem of the rail traction drive simulator: traction motor, gearbox, wheel sets, and driven flywheels. . .	168
A.2	(a) MSI converter, (b) dc/dc converter, (c) battery pack. . .	169
B.1	Modeling of the asynchronous traction motors.	173
B.2	Modeling of the traction converters: (a) VSI, (b) MSI. . . .	175
B.3	Interleaved dc/dc converter modeling.	177
B.4	Modeling of inductors and capacitors.	177
B.5	Modeling of power sources and ESSs: (a) external line, (b) battery, (c), fuel cell.	179
C.1	Geometries of the iron-core (a) and air-core (b) inductors. . .	183
C.2	Flowchart of the heatsink sizing procedure.	189

List of Tables

- 2.1 Available data of reported vehicles with onboard batteries . 21
- 2.2 Available data of reported vehicles with onboard supercapacitors 25
- 2.3 Available data of reported vehicles with onboard hybrid energy storage systems 27
- 2.4 Main data of reported vehicles with onboard fuel cells . . . 31
- 2.5 Comparison of different energy-saving solutions in electrified railways 35
- 2.6 Operating and maintenance costs of rolling stock and infrastructure for conventional and alternative rail systems. . 38

- 4.1 Switching states of an **MSI** leg 59
- 4.2 Test bench parameters 71
- 4.3 **MSI** operating modes enabled by the **MOV**M 89

- 5.1 Test bench parameters 103
- 5.2 Test bench parameters 112
- 5.3 Overview of the experimental results 118

- 6.1 Leg inductors of the dc/dc converter: design specifications . 126
- 6.2 Leg inductors of the dc/dc converter: design results 127

6.3	Dc/dc converter Insulated Gate Bipolar Transistors (IGBTs) VA rating	128
6.4	LC filter of the dc/dc converter: design specifications	128
6.5	LC filter of the dc/dc converter: design results	129
6.6	Heatsink of the dc/dc converter: design results	129
6.7	Inverter IGBTs VA rating	130
6.8	LC filter of the traction inverter: design specifications	131
6.9	LC filter of the traction inverter: design results	131
6.10	Heatsink of the traction inverter: design results	132
6.11	Leg inductors of the dc/dc converter: design specifications	149
6.12	Leg inductors of the dc/dc converter: design results	149
6.13	Dc/dc converter IGBTs VA rating	149
6.14	LC filter of the dc/dc converter: design specifications	150
6.15	LC filter of the dc/dc converter: design results	150
6.16	Heatsink of the dc/dc converter: design results	151
6.17	Inverter IGBTs VA rating	151
6.18	LC filter of the traction inverter: design specifications	152
6.19	LC filter of the traction inverter: design results	153
6.20	Heatsink of the traction inverter: design results	153
A.1	Main parameters of traction motor and driveline	168

List of Symbols

The following symbols are used within the thesis

\check{i}	Complex conjugate of space vector of the ac currents
i	Space vector of the ac currents
v	Space vector of the ac voltages
ΔV	Difference between the MSI high and low voltage input levels
\hat{V}_{LL}	Peak value of the fundamental line-to-line ac output voltage
i	Imaginary unit
ω_r	Motor rotational speed in rad/s
ϕ_r	Rotor flux-linkage magnitude
ψ_r	Rotor flux-linkage angle
C_{HV}	Filter capacitor at the MSI high-voltage terminal
C_{LV}	Filter capacitor at the MSI low-voltage terminal
d_{cs}	Duty cycle of the interleaved SVM modulation
$d_{\Delta k}$	Differential duty cycle of the MSI k -th leg

d_{Bk}	Duty cycle of the bottom switch in the MSI k -th leg
d_{Tk}	Duty cycle of the top switch in the MSI k -th leg
$i_{\text{dcdc,in}}$	dc/dc converter input current
$i_{\text{dcdc,out}}$	dc/dc converter output current
i_d	d-axis motor current
i_d^*	d-axis motor current reference
i_{HV}	High-voltage source output current
$i_{\text{HV}}^{(lim)}$	Limit HV-bus current
i_k	Output current of the MSI k -th leg
i_{LV}	Low-voltage source output current
$i_{\text{msi,C}}$	Switched current drawn by the MSI at the low-voltage terminal
$i_{\text{msi,HV}}$	MSi input current at the high-voltage terminal
$i_{\text{msi,LV}}$	MSi input current at the low-voltage terminal
$i_{\text{msi,T}}$	Switched current drawn by the MSI at the low-voltage terminal
I_{ph}	Steady-state ac load RMS current
i_q	q-axis motor current
i_q^*	q-axis motor current reference
i_{vsi}	VSI input current
k	Running index of the inverter output variables
m_{HV}	Modulation index of the MSI high voltage level

m_{LV}	Modulation index of the MSI low voltage level
p_{ac}	ac power
p_{HV}	High-voltage source output power
p_{LV}	Low-voltage source output power
$s_{\Delta k}$	Differential switching signals of the MSI k -th leg
s_{Bk}	Gate signal of the bottom switch in the MSI k -th leg
s_{Tk}	Gate signal of the top switch in the MSI k -th leg
T_{cs}	Control frequency of the interleaved SVM modulation
T_{cs}	Control period of the interleaved SVM modulation
T_{sw}	Switching period
u_{cs}	Interleaved SVM modulation control signal
$V_{HV,br}^*$	HV-bus voltage reference during braking
V_{HV}	Voltage level of the high-voltage source
V_{HV}^*	HV-bus voltage reference
v_k	Output voltage of the MSI k -th leg
V_{LV}	Voltage level of the low-voltage source
V_{ph}	Steady-state ac load RMS voltage
V_{ph}	Steady-state ac load power factor
v_α	Real part of the ac voltages space vector
v_β	Imaginary part of the ac voltage space vector

Introduction

1.1 Background and motivation

The reduction of carbon emissions is a key factor to tackle climate change and improve air quality, with important effects on public health, environment, and economy. Transport currently accounts for almost 23% of global energy-related Green-House Gas (GHG) emissions [1]. To chase a reduction in GHG emissions towards climate-neutrality targets [2], the transport sector economy is experiencing an increasing shift towards decarbonization and electrification.

Rail is already among the least-emitting and most efficient means of transport for both passenger and freight services, as shown in Figure 1.1. Indeed, despite an 8% share of total passenger travel and 9% of total freight transport activity, railways account for less than 2% of direct and well-to-wheel GHG emissions and about 3% of the final overall energy use [3]. The low energy demand per passenger-km is due to lower losses caused by friction and drag, the higher efficiency of electrical drives compared to combustion engines, the possibility to recover braking energy, and higher load capacities. On the other hand, electrification plays a key role in the low GHG emissions of rail transport. The carbon impact of electrification depends on the generation mix among fuel and renewable sources, and many railway operators already use a significant share of renewable energies. Worldwide, several rail operators are increasingly operating their own power plants to provide the demanded traction energy

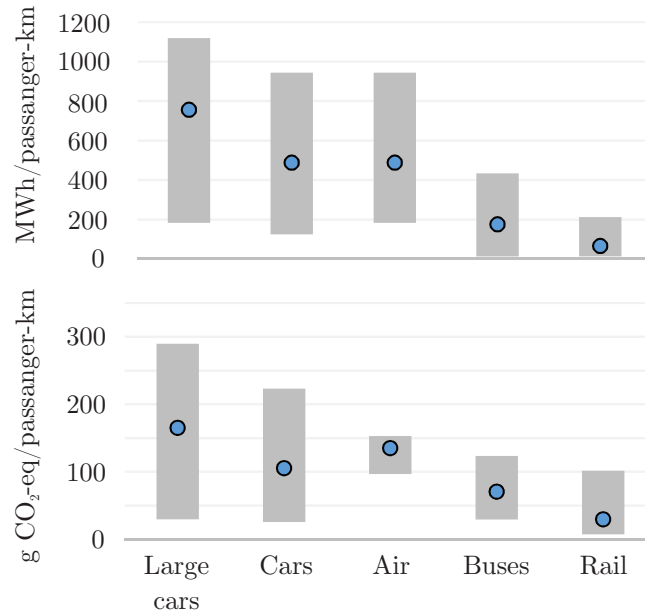


Figure 1.1. Global energy consumption and well-to-wheel CO₂ equivalent emissions per passenger-kilometer, for different means of passenger transport.

with a lower carbon imprint. In Europe, almost 40% of the electricity mix is low-carbon, with an average 20% produced directly from renewables [3].

Figure 1.2 summarizes the global evolution of fuel utilization and railway tracks electrification from 2000 to 2016 [4]. Electric trains run 75% of passenger-km and about 48% of freight tonne-km worldwide. Passenger transport is significantly more electrified than freight transport, and areas with the highest share of electricity use (i.e. Europe, Japan, and Russia) tend to be those with the highest passenger rail activity. In fact, electrified rail routes have higher utilization rates than non-electric ones: on average, five times more passenger-km per track-km and twice as many tonne-km run on electrified tracks. Indeed, high throughput of passengers or freight is necessary to shorten the payback period of the needed investments. Virtually all urban networks use electric trains, while suburban and intercity networks rely on electricity by 60% [5]. However, large differences exist among countries and between freight and passenger activity: Japan, Russia, and Europe lead the chart while North and South America still rely

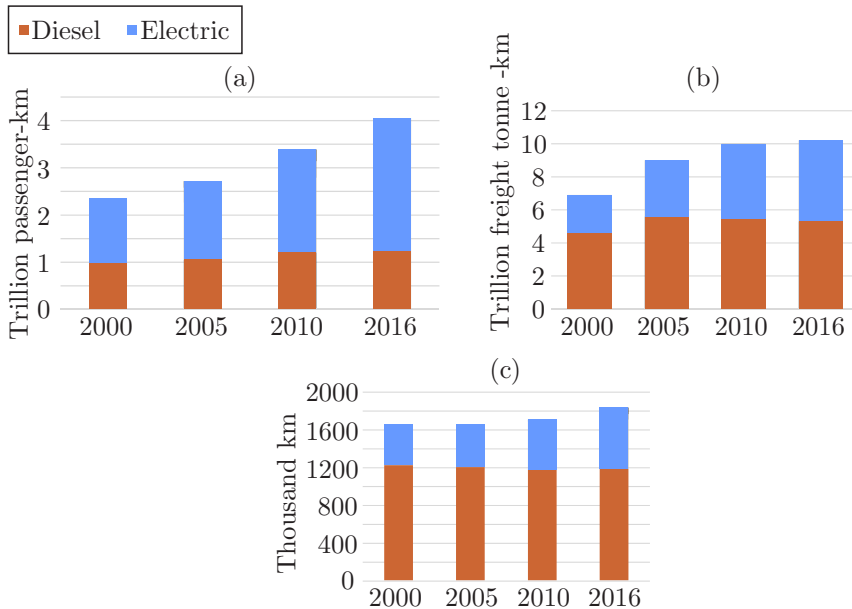


Figure 1.2. Global evolution of diesel and electricity usage in passenger (a) and freight (b) rail services, and share of electrified lines (c) from 2000 to 2016.

heavily on diesel. Despite a high share of electric trains in passenger transport and a general trend toward electrification, only one-third of the rail tracks worldwide are electrified. Again, deep differences among countries exist: from more than 75% tracks in Korea to 50-60% in Europe, Japan, Russia, and India, to a modest few percent in North and South America [5]. In fact, railway electrification requires considerable investments in infrastructure and an expensive connection to the power grid. Therefore, priority is given to the electrification of rail networks with high activity, where payback periods for the investment costs are shorter. On the other hand, many medium-traffic branches are still partially or totally lacking electrical infrastructure and are operated by diesel trains. At the same time, electrification may result unfeasible also in the case of urban tracks crossing historical sites, due to the aesthetic impact of overhead wires.

In the effort to reduce fuel consumption, improve energy efficiency, and limit overhead infrastructures, rolling-stock manufacturers have been increasingly developing new *multimode* propulsion systems. These systems

feature alternative energy sources (hydrogen fuel cells) and energy storage devices (batteries, supercapacitors) in combination with or replacement of traditional supplies (overhead or ground-level power lines, onboard diesel generators). Multimode rail vehicles can benefit from high energy savings due to braking energy recuperation, lower current absorption and voltage swings on the external supply, and null local emissions when operating in absence of electrified infrastructure [6].

Laying at the heart of multimode traction architectures, power electronic converters interconnect and control the energy flows among power sources, traction motors, and auxiliary loads. Conventionally, all power converters are connected to a common dc-bus, whose rated voltage level depends on the type of network on which the vehicle is operated. The traction and auxiliary loads are supplied through dc/ac VSIs, while the sources and storage devices are interfaced by means of unidirectional and bidirectional dc/dc converters. Employing several dc/dc converters enables the highest versatility in the design and management of the onboard power sources. However, they result in increased cost and complexity of the multimode powertrain, and their size is usually constrained by the volume occupied by fuel cells and storage elements. To cope with the low energy densities of the primary sources and storage devices, compact power electronics have to be developed. On one hand, higher power densities can be obtained by exploiting the technological potential of wide band-gap semiconductors. On the other hand, alternative powertrain architectures that make use of non-conventional converter topologies and configurations can be investigated.

This thesis aims at exploring the adoption of the NPC MSIs¹ as traction converter in multimode rail traction systems. MSIs allow a single-stage interconnection of two independent dc sources to the same ac load through a conventional NPC circuit. By means of a proper Pulse Width Modulation (PWM) technique, the converter can independently control the power flowing in the dc sources and the fundamental voltage supplying the ac load. Therefore, when properly integrated in a multimode traction

¹The term *multi-source inverter* can be generically used to address many types of power converters. However, for sake of brevity, the acronym MSI will be used throughout this thesis for multi-source inverters based on the three-level NPC topologies (NPC and T-NPC).

system, the **MSI** enables the reduction of power processed by the dc/dc converters with potential benefits in terms of power losses, weights, and volumes of the traction equipment.

As the concept of **MSI** has been proposed and developed recently, very little research work has addressed the topic so far. The ultimate objective of this thesis is twofold:

- Develop an original **PWM** modulation strategy that improves the **MSI** performance with respect to the state-of-literature modulation in terms of feasible operating modes, control flexibility, and harmonic distortion of the dc currents.
- Discuss the integration and control of the **MSI** in a non-conventional *semi-two-stage* architecture and quantify its potential of reducing the power rating and size of the onboard traction equipment.

These objectives are pursued with the aid of extensive experimental tests on a small-scale traction drive and numerical simulations for two case studies based on real multimode vehicles.

1.2 Contribution

The contributions brought by the present thesis to the research on multimode rail transport can be summarized as follows:

- Extensive review of recent multimode rail vehicles in passenger operation, with a focus on the technology of onboard sources and storage systems, the traction circuit architectures, and the energy management concepts.
 - Development of a novel modulation strategy of the **MSI** for improved performance of the converter in a multimode propulsion system.
 - Proposal of the integration and coordinated control **MSIs** and dc/dc converters in a non-conventional semi-two-stage traction architecture for multimode rail vehicles.
 - Assessment of the semi-two-stage **MSI**-based topology compared to the conventional **VSI**-based architecture for two case studies based on the data of real multimode vehicles.
-

1.3 Thesis layout

The thesis is organized into seven chapters. Chapter 1 has introduced the motivation for research on **MSIs** in the field of multimode rail vehicles, together with the thesis's main contributions.

Chapter 2 presents a comprehensive review of the energy sources and storage systems employed for multimode rail transport. In particular, the design and operating data of real multimode trains in prototype or commercial operation are collected. A discussion is presented on the techno-economic advantages and challenges of energy storage and fuel cell systems for energy saving in electrified networks and as alternatives to diesel power in non-electrified networks.

In Chapter 3, the traction system architectures and energy management strategies of many real multimode vehicles in prototype or commercial operation are detailed according to the available information retrieved from manufacturers and from the literature. Some non-conventional converter topologies are also revised to highlight recent research trends and proposals in the field of rail traction drives.

Chapter 4 resumes the fundamentals of the **MSI**, including the converter topology and the **PWM** established in the literature so far. The operation of the **MSI** under the state-of-literature modulation is studied analytically and assessed experimentally to understand the conditions that enable full control of the dc sources and ac motors through the **MSI**. Moreover, a novel modulation strategy named **MOVm** is derived from the **MSI** mathematical model to overcome many limitations of the literature approach. The feasible operating modes and modulation limits of the **MOVm** are discussed extensively and verified with simulations and experiments.

Chapter 5 discusses the integration of the **MSI** in the propulsion system of bimode rail vehicles, which results in a **S2S** traction architecture. Thanks to the direct connection path provided by the **MSI** and the versatility of the **MOVm** technique, the **S2S** topology can lead to a relevant reduction in the power processed by the onboard dc/dc converters. A strategy for the coordination of the power converters is presented to achieve the maximum reduction in the power rating of the dc/dc converter. Its feasibility is validated with extensive experiments for different

configurations and voltage levels of the dc sources.

In chapter 6, the effective potential of the proposed S2S architecture in reducing power losses, weight, and volume of the onboard power electronics is evaluated by means of comprehensive circuit, magnetic, and thermal simulations for two case studies based on real vehicle designs: a tram with onboard batteries, and a hydrogen fuel cell train. The design and operation of the power converters are discussed, and the two topologies are compared based on a detailed breakdown of their VA rating, size, poundage, power losses, and efficiencies.

Finally, Chapter 7 draws the conclusions and outlines possible future research work in the field of multi-source inverters for hybrid propulsion systems.

Multimode rail vehicles

Rail transport has experienced significant improvements in energy efficiency and [GHG](#) emissions reductions, equating to more than a 20% change in each over the past 20 years [4]. To accomplish further reductions in energy use and fuel consumption, rolling-stock manufacturers have been proposing a wide range of *multimode* vehicles. A multimode rail vehicle is equipped with a combination of alternative energy sources and storage systems to complement or replace the traditional supply from the external line (for electrified networks) or onboard diesel generators (for non-electrified networks).

2.1 Energy sources and storage devices

The most relevant storage systems and alternative energy sources for rail applications are represented by batteries, supercapacitors, and fuel cells. For all these systems, some major performance metrics can be identified: specific energy (energy per unit mass), specific power (power per unit mass), cyclability and lifetime (cycling and calendar durability), and efficiency. Specific energy and power relate to the intrinsic ability to store a high amount of energy and deliver it to the load in a short amount of time. Cyclability and lifetime refer to the number of cycles and length of inactive time before degradation occurs in component performance. Other important parameters are cost, safety and tolerance to stresses, and ease of maintenance. Most of these metrics show opposite trends, and each tech-

nology features its own advantages and weaknesses. A non-exhaustive overview of the operating principle, composition, and performance of batteries, supercapacitors, and fuel cells for rail is given in the next sections.

2.1.1 Batteries

Electrochemical storage systems, also called electrochemical batteries or simply batteries, represent one of the most used energy storage devices. In batteries, energy is stored and delivered to the outer electrical circuit thanks to reversible reactions. These reactions occur between two metallic electrodes that are immersed in an aqueous or non-aqueous ionic conductor, known as electrolyte. The elementary unit where electrochemical reactions take place is known as cell. Many cells can be connected to form series and parallel strings, depending on the power and energy rating required from the overall battery pack.

Among different chemistries, NiMHs and LiBs represent nowadays a popular solution for rail traction applications. Ni-MH batteries are the most common nickel-based batteries on the market. They employ nickel hydroxide as the positive electrode, an alkaline solution as the electrolyte, and a metal alloy capable of absorbing and releasing hydrogen as the negative electrode. This technology guarantees robust reliability and low maintenance but generally exhibits poor efficiency and a high self-discharge rate [7]. Li-ion batteries represent the leading technology for portable electronics and have gained momentum in electric traction applications due to considerable incentives and cost reductions. These batteries exhibit higher energy and power densities, with high efficiencies and low self-discharge rates. However, they suffer from limited durability and high capital costs [8]. Although Li-ion batteries are sometimes treated as a homogeneous group, different materials yield different types of cells with peculiar performances. In cells with a graphite anode, the cathode is made of Lithium Cobalt Oxide (LCO), Lithium Manganese Oxide (LMO), Nickel Manganese Cobalt (NMC), Lithium Iron Phosphate (LFP), or Nickel Cobalt Aluminum (NCA). In case of an LMO or NMC cathode, the anode can be alternatively made of Lithium Titanate Oxide (LTO).

Figure 2.1 (adapted from [9]) shows the spider plot of these six major chemistries. The diagrams suggest that NMC cells have excellent values

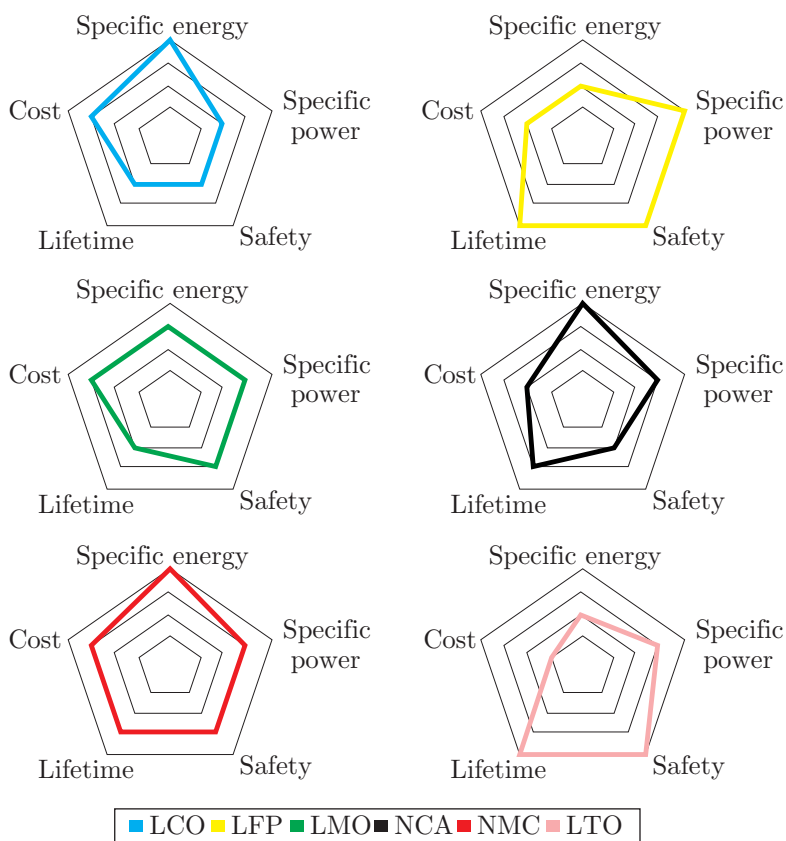


Figure 2.1. Spider plots of the six major lithium-ion chemistries.

in most of the key metrics, thus representing a leading chemistry for light-duty electric traction applications. **NCA** also demonstrates high specific energy and reasonable specific power but at higher costs compared to **NMC**, due to a higher concentration of cobalt. **LFP** and **LTO** demonstrate relatively low specific energy and higher cost, but benefit from very long life span, excellent cold weather performance, and very high safety, which makes them attractive for heavy-duty applications.

2.1.2 Supercapacitors

SCs, also called Ultracapacitorss (UCs), store energy via an electrostatic field. They are constituted of two activated carbon electrodes, an aqueous or organic electrolyte, and an organic or inorganic separating membrane. Thanks to the porous electrodes and the internal structure, SCs exhibit an extremely large surface area and an extremely thin double-layer distance, which results in very high values of capacitance.

As no chemical reactions occur in supercapacitors, they exhibit high power density, cyclability, lifetime, and efficiency [10]. Conversely, the main disadvantages are low energy density, significant self-discharge, and spark hazards when shorted.

2.1.3 Fuel cells and hydrogen storage

FCs allow the direct conversion of the chemical energy stored in the hydrogen into heat and electric power by means of reduction-oxidation (redox) reactions between hydrogen and oxygen. Each cell is composed of activated carbon electrodes, ionic-conductor electrolyte, diffusion backings, and bipolar plates. As redox reactions at relatively low temperatures are slow, catalysts (often platinum) are distributed on the electrodes. The backings are thin layers of porous and conductive material and allow the diffusion of hydrogen and air toward the electrodes. Bipolar plates are generally made of graphite and fulfill several functions: direct the gases towards the backings, manage water flows, and collect current to the outer circuit.

For the proper operation of the plant, the fuel cell must be combined with several components such as hydrogen storage components, valves, humidifiers, water separators, compressors, and pumps. The presence of such components affects the overall plant efficiency, which can be as low as 25% in the case of hydrogen production through electrolysis [10].

Fuel cells differ in the type of electrolyte, operating temperature, and fuel. For transportation applications, Proton-Exchange Membrane (PEM) fuel cells are mostly adopted. The electrolyte is in Nafion, a synthetic solid polymer that conducts protons. Due to their high power density, low operating temperatures of 60-80 °C, and fast start-up, PEMFCs are mostly adopted for transportation applications [11]. However, they require

hydrogen with a high degree of purity and careful management of heat and water flows.

Hydrogen can be stored in liquid or gaseous form. Liquefaction is obtained in cryogenic reservoirs at temperatures of approximately 20 K and at ambient pressure. Due to the energy consumed by the liquefaction process and the complexity of the cryogenic reservoirs, hydrogen liquefaction is not economical. On the other hand, hydrogen storage by compression is easier to accomplish but results in lower energy densities, unless very high-pressure levels are reached. Today, compression at 350 – 700 bar is mostly adopted for hydrogen storage in transportation applications.

2.1.4 Comparison

An overall comparison of specific energy and power, energy density, efficiency, cyclability, and lifetime at component level is shown in Figure 2.2 based on data reported in [7, 8, 11–18]. From the comparative plot, it

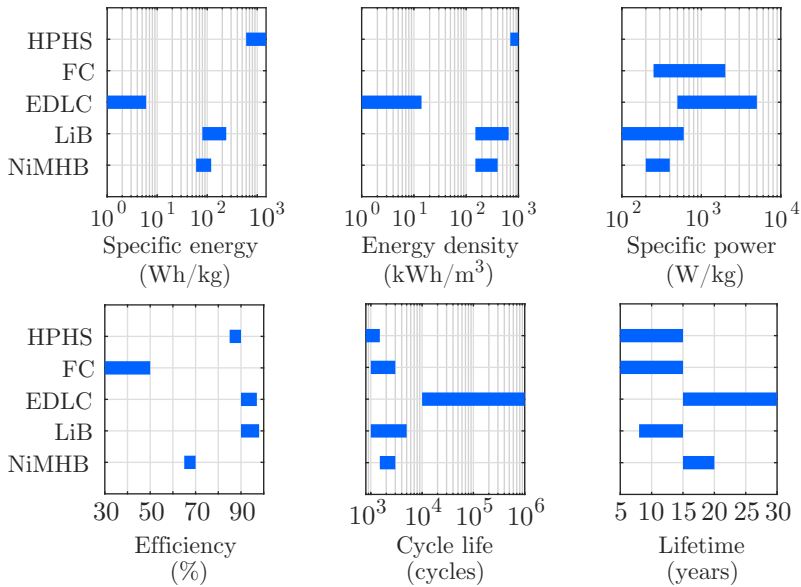


Figure 2.2. Main features of NiMHBs, LiBs, SCs, FCs, and HPHS technologies for rail applications.

can be stated that battery cells exhibit much higher energy densities compared to supercapacitors, but lower power density, cyclability, and lifetime. Hydrogen storage offers the highest energy density and is thus attractive when high energy amounts are required. However, hydrogen power plants still suffer from low overall efficiency, cyclability, and lifetime compared to batteries and supercapacitors, due to a less mature technological status of the active materials and the presence of many auxiliary subcomponents.

2.2 Review of real applications

The interest in multimode rail vehicles for energy-saving enhancement and catenary-less operation has grown significantly in the last twenty years. In the following sections, a thorough review of many prototype and commercial vehicles for passenger service with onboard storage systems and fuel cells is presented, with a focus on the employed storage technologies and achieved performances.

Classifying passenger rail in subsets is a non-trivial task, and many categorizations are found in the technical literature. Following [5] and [12], passenger rail services can be broadly categorized as:

- Urban and suburban rails: networks providing rail services within metropolitan areas and surroundings with up to 50 km extension. They comprise metro, tramway, and light rail/commuter systems.
- Regional rails: networks providing rail services between cities in a regional extension of up to 150 km.
- Intercity and high-speed rails: networks providing rail services among major population hubs on medium to long distances. Maximum speeds can be above 250 km/h.

2.2.1 Vehicles with onboard batteries

Thanks to their relatively high energy density and reasonable power density, onboard batteries have been installed in vehicles operating on both electrified and non-electrified networks with the main goal of braking energy recuperation, peak shaving of line power during high-load traction phases, and short to medium wireless operation.

In April 2003, a catenary/battery hybrid tramcar with LMO batteries was put on a test run by the Railway Technical Research Institute (RTRI) in Japan [19]. The distance achieved in wireless operation was 17.4 km, with stops every 250 m and speeds up to 40 km/h. The battery's maximum power, energy, and weight were 300 kW, 33.0 kWh, and 1160 kg, respectively. The energy density of the whole device was 28 Wh/kg, approximately one-half the energy density of single LMO cells [20]. In January 2005, this vehicle was equipped with a new contact-wire/battery hybrid current reversible step-down chopper corresponding to a 750 VDC or 1500 VDC electrified line.

A prototype LMO LiB pack for battery tramcar testing was developed at Fukui University in Japan in 2007 [21]. The battery pack consisted of eighteen submodules, each comprising nine parallel-connected strings of twelve cells. The energy and weight of the battery pack were 45 kWh and 540 kWh, respectively, with an overall energy density of 83 Wh/kg, around 30% less than the energy density of the single cells and three times higher than what was achieved by RTRI in 2003. The prototype car was tested on the Fukubu business line of Fukui railway and ran up to 25 km on one charge with a maximum speed of 65 km/h.

In collaboration with East Japan Railway Company, Hitachi developed the prototype NE Train equipped with a series-hybrid powertrain. A diesel generation unit and a Li-ion storage system powered two electric motors for a total traction power of around 400 kW. The experience gathered through the NE Train project eventually led to the realization of the KiHa E200 series hybrid DEMUs [22]. In these single-car vehicles, each of the two roof-mounted battery packs comprises eight submodules for a total installed energy and power of 15 kWh and 270 kW [23]. Together with a 230 kW diesel generating unit, the batteries supply two induction motors for a traction power of around 200 kW. Since 2007, these hybrid units are in regular service together with standard DMUs on the Koumi line in Japan. In 2010, the HB-E300 and HB-E210 series railcars with the same hybrid system as the KiHa E200 began operational service on Japan's Ou, Gono, and Senseki Tohoku lines.

JR Hokkaido and Hitachi Nico Transmission Ltd performed tests on a prototype diesel/battery hybrid railcar with a parallel-hybrid powertrain in 2007. In this vehicle, a 240 kW diesel engine was assisted by a 120 kW

traction motor connected to it through a proper transmission system. The motor was powered by a Li-ion battery with rated energy and power of 7.5 kWh and 190 kW [24]. The running tests aimed to evaluate the reduction in fuel consumption for a baseline diesel configuration. The differences between the considered parallel-hybrid architecture and the more common series hybrid one were also addressed.

Since November 2007, a fleet of Alstom Citadis catenary/battery hybrid tram vehicles has been in regular passenger service on the T1 tramway line in Nice. The tramcars are equipped with NiMHBs and have estimated energy and weight of 27.7 kWh and 1450 kg, respectively [25]. Catenary-free operation is carried out on a four-stop 900 m segment between Massena and Garibaldi, as the installation of overhead wires would severely impact the aesthetics of the historical center.

In Japan's electrified line of Sapporo Municipal Transport, a prototype catenary/battery hybrid LRV by Kawasaki Heavy Industries named SWIMO was put in operation from December 2007 to March 2008. The vehicle, equipped with proprietary Ni-MH battery technology, could run up to 37.5 km with a maximum speed of 40 km/h on a single charge [19]. The onboard storage system consisted of a series of sixteen modules of 7.5 kWh and 200 kg each, for a total energy density of around 37.5 Wh/kg [26]. SWIMO is currently available in the portfolio of low-floor Light Rail Vehicles (LRVs) by Kawasaki.

In November 2007, a 240 kW prototype catenary/battery hybrid tram called Hi-tram with onboard LMO LiBs was developed and tested by RTRI. The rated value of maximum power, rated energy, and weight was 600 kW, 72 kWh, and 2000 kg, for an overall installed energy density of 36 Wh/kg [25]. Several tests were conducted on the Hi-tram from November 2007 to November 2009. The maximum catenary-free distance achieved during tests on Sapporo tramway in 2007–2008 was 25.8 km at a maximum speed of 40 km/h, while 4 km or more could be run with a 60 s partial recharge (around 14% of rated capacity) from the catenary at a current of 1000 A. The recorded regenerative ratio, the amount of regenerated energy divided by the energy consumed in operation, was 41%. In November 2009, further testing was carried out at higher speeds on the Yosai railway, resulting in 60 min, 49.1 km catenary-free operation with a regenerative ratio of 23.9 % [27].

RTRI completed in 2013 the conversion of a series 817-100 ac EMUs into an ac catenary/hybrid BEMU test train [28]. The project's primary purpose was to analyze the capabilities of battery-powered vehicles running on routes with partial ac electrification. The onboard air-cooled battery was based on LMO Li-ion cells and featured rated energy and weight of 83 kWh and 1536 kg, respectively, for an overall energy density of around 54 Wh/kg. Running tests were performed on the electrified Chikuho main line and the non-electrified Hitahikosan line. The longest distances achieved in wireless operation at a maximum speed of 80 km/h ranged from 30.4 km in the summertime to 20 km in wintertime, depending on the amount of energy absorbed by air-conditioning. Quick-charging tests were also conducted—the battery SOC increased by 20% to 95% for a charging time of eight to twelve minutes, depending on the battery temperature. According to the authors, the experimental results demonstrated sufficient performance of the dual-source EMU on electrified and non-electrified routes.

After the commissioning of the hybrid diesel KiHa E200 railcar in 2007, JR East has continued to work to reduce the environmental impact of railway vehicles. In 2008, development was started on a hybrid powertrain that could operate on non-electrified segments [29]. As a result, in March 2014, the catenary/battery hybrid series EV-E301 trains began commercial service on the electrified Tohoku line and the non-electrified Karasuyama line. The trains are equipped with two Li-ion battery packs of 95 kWh each and four induction motors with a total traction power of 380 kW. On the Karasuyama line, the trains run without catenary for 22.4 km at a maximum speed of 100 km/h and are recharged at the terminal station of Karasuyama through stationary fast-charge facilities [30].

A prototype catenary/battery hybrid EMU was put into passenger service in January 2015 in the United Kingdom. As part of a project founded by Network Rail, Bombardier modified an existing Class 379 Electrostar train by installing a LiB on board [31]. The target was to operate the train on battery power up to 120 km/h for a distance up to 50 km, requiring a battery capacity of around 500 kWh [32]. The vehicle could also be powered and recharged by the 25 kVAC overhead line. Bombardier has since received orders for battery electric units—for example, a contract was signed with Austrian Federal Railway (ÖBB) in July 2018 for the

delivery of 25 battery EMUs to be operated in regional transit [33].

In 2015, Kagoshima Transportation Bureau and Toshiba started running tests on a new catenary/battery hybrid tram [34]. Drawing power only from a 23.4 kWh LiB LTO battery pack manufactured by Toshiba, the vehicle ran approximately 10 km in catenary-free mode on the Toso line from Kagoshima eki-mae to Korimoto.

Japanese railway operator JR Kyushu put several BEC819 series catenary/battery hybrid trains manufactured by Hitachi into service between 2016 and 2019. These units can run under both catenary and onboard battery power. The rated energy of the onboard battery is about 360 kWh at 1600 V [28]. Battery power is mainly employed on two non-electrified routes: an 11 km section on the Wakamatsu main line and the entire Chikuhō regional line. On the latter route, one halfway recharge is needed for the trains to cover the entire distance of 25.4 km.

Since 2014, a fleet of Flexity 2 catenary/battery hybrid tramcars manufactured by Bombardier and CSR Puzhen is in service in the Chinese city of Nanjing [35]. The vehicles are equipped with proprietary PRIMOVE battery technology based on NMC Li-ion chemistry, which provides 98 kWh of nominal energy for each tram. The vehicles are operated on the 8 km long Hilin line and 9 km long Hexi line and run catenary-free for around 90% of their route, as overhead wires are installed mainly in stations or steep-gradient sections [36]. The battery packs are charged at stops in around 45 s.

Several city authorities around Europe and America have ordered and put into commercial service battery tramcars from 2014 on [35]. In the United States, the manufacturer Brookville Equipment Co. has provided its Liberty Modern catenary/battery hybrid streetcar to the cities of Dallas (TX), Detroit (MI), and Oklahoma City (OK). The streetcar has an installed traction power of around 280 kW and can run without catenary on non-electrified segments due to an NMC Li-ion battery installed on board. In these cities, the average catenary-free operation is carried out on half of the total length of the tramway lines. In Dallas, battery power is used along the 1.6 km Houston Street viaduct between Union Station and Trinity River, which lacks overhead wires. In Seattle, the First Hill Streetcar line is operated since 2016 with six catenary/battery hybrid Trio 121 streetcars by railway manufacturer Inekon. Each car is equipped with

two Li-ion battery packs featuring 30.4 kWh of rated energy and 1500 kg of the total weight for an overall energy density of around 20 Wh/kg. The streetcars operate without overhead wire for the entire 3.8 km inbound journey, which is predominantly downhill. In Brazil, a fleet of catenary/-battery hybrid Tramlink V4 tramcars is in service in the metropolitan area of Santos. The onboard storage enables catenary-free operation on a short section of the route in the city center [37].

In Europe, a few other LRVs with only batteries as an additional energy source have been put into service since 2007. In Konya, Turkey, twelve Forcity Classic 28T catenary/battery tramcars started operation in 2015. The vehicles are equipped with batteries based on LTO Li-ion cells and can run without overhead wire for a distance of approximately 2 km [31]. In 2018, railcar manufacturer CAF proposed a retrofitting of the operating fleet of Urbos 100 tramcars on the West Midlands Metro line connecting Wolverhampton with Birmingham [38]. The catenary/-battery hybrid vehicles are equipped with 80 kWh LFP Li-ion batteries to operate without overhead wire on a non-electrified extension in Birmingham city center between Grand Central and Library stops, which has been completed in December 2019 [39]. Catenary-free operation is also considered on the Edgbaston and Wolverhampton extensions currently under construction. In July 2019, the city of Timisoara in Romania signed a contract with Bozonkaya A.S. to deliver sixteen battery-powered trams to enter operation in 2021 [40].

In 2018, Bombardier's Talent 3 catenary/battery train was unveiled to the public. The vehicle is a 3-car BEMU meant for regional transport. It can run under 15 kV ac catenary and battery power with a maximum speed of 140 km/h. The onboard battery packs of a first demonstrator feature NMC technology with overall rated energy of 300 kWh and a catenary-free range of around 40 km [41]. The project is now in the testing and homologation phase. Delivery orders for fleets of Talent 3 trains have been signed recently by Bombardier with transportation authorities in Austria, Germany, and Italy [41].

Stadler Rail and Welsch railway operator Keolis Amey Operations Ltd. signed a contract to deliver twenty-four multimode multiple units in February 2019 [42]. These units can travel under overhead lines at 25 kVAC and on non-electrified routes owing to onboard battery energy. The accumu-

lators are based on **LiB LTO** technology and have a rated energy of 180 kWh, enabling the vehicle to range up to 80 km in catenary-free mode. Diesel generation units are also provided for battery charging and improved dependability in case of battery failure. The vehicles are expected to begin operation on the partially electrified South Wales railway network by 2023. In the same year, Vivarail launched a two-car Class 230 demonstrator equipped with two **LiB** packs. The batteries have rated energy of around 420 kWh and enable wireless operation up to 64 km [43]. The prototype vehicle ran successfully in trial passenger service on the Bo'ness & Kinneil Railway with the support of Transport Scotland and Scotrail in October 2018. Moreover, trials on a three-car diesel-battery hybrid Class 230 train have been carried out since the autumn of 2019. This vehicle is based on the two-car battery prototype but includes a third car equipped with four diesel generators. A fleet of five such units was scheduled to start passenger service by Transport of Wales rail services in 2020 [33,44].

Since September 2019, a prototype catenary/battery **BEMU** manufactured by Siemens for ÖBB has entered passenger operation on non-electrified routes in low Austria as part of the Update Fleet Strategy 2035 program undertaken by the local operator [45]. The train has a maximum traction power of 2.6 MW and is powered from a 15/25 kVAC overhead line and a 528 kWh LTO Li-ion battery with an expected catenary-free range of around 80 km [46]. The test program will determine the availability of such trains on the ÖBB network. Potential sites for charging stations will be identified to offer an alternative to diesel traction for regional rail service.

The collected data are summarized in Table 2.1, while Figure 2.3 provides a scatter plot of the stored energy versus off-wire autonomy for the reported battery vehicles in urban/suburban and regional/long-distance service.

2.2.2 Vehicles with onboard supercapacitors

Due to their high power density and cyclability, **SCs** are considered a valid storage technology for vehicles in fully-electrified urban networks. They guarantee braking energy recovery with high efficiency and significant power assist to the external line. On the other hand, off-wire operation is enabled only on very short segments.

Table 2.1. Available data of reported vehicles with onboard batteries

#	Place and year	Vehicle info (rated power and voltage)	Battery type	Energy (kWh)	Power (kW)	Off-wire length (km)
1	Japan 2003	Mo3301 car (120 kW, 750-1500 VDC)	LMO	33	300	17.4
2	Fukui (JP) 2007	Nagoya Railroad 602-type (600 VDC)	LMO	45	45	25
3	Japan 2007	KiHa E200 DEMU (400 kW)	LMO	15.2	270	78.9
4	Japan 2007	LRV (360 kW)	Li-ion	7.5	192	-
5	Nice (FR) 2007	Citadis 302 tram (750 VDC)	Ni-MH	7.7	200	0.91
6	Sapporo (JP) 2007	LRV (100 kW, 600 VDC)	Ni-MH	120	250	37.5
7	Sapporo (JP) 2007	LRV (240 kW, 600 VDC)	LMO	72	600	up to 49
8	Japan 2007	Series 817-1000 EMU (600 kW)	LMO	83	560	up to 30
9	Japan 2014	EV-E301 EMU (380 kW, 1.5 kVDC)	LMO	190	630	22.4
10	Nanjing (CN) 2014	Flexity 2 tram (480 kW, 750 VDC)	NMC	98	244	16
11	Essex (UK) 2015	Class 379 Electrostar EMU (25 kVAC)	LFP	500	-	up to 50
12	Dallas (US) 2015	Liberty Modern streetcar (390 kW, 750 VDC)	NMC	84.1	340	1.6
13	Konya (TR) 2015	Forcity Classic 28T tram (400 kW, 750 VDC)	LTO	-	-	1.8
14	Santos (BR) 2015	Tramlink V4 tram (420 kW, 750 VDC)	LTO	-	-	0.4
15	Kagoshima (JP) 2015	Little Dancer tram (600 VDC)	LTO	24.3	-	up to 10
16	Japan 2016	BEC-819 EMU (380 kW, 20 kVAC)	Li-ion	360	1080	10.8
17	Seattle (US) 2016	121 Trio streetcar (260 kW, 750 VDC)	Li-ion	60.7	-	4
18	Detroit (US) 2017	Liberty Modern streetcar (260-300 kW, 750 VDC)	NMC	-	-	5
19	Okla. City (US) 2018	Liberty Modern streetcar (260-300 kW, 750 VDC)	Li-ion	-	-	3
20	Japan 2018	BEC-819 EMU (380 kW)	Li-ion	360	1080	25.4

#	Place and year	Vehicle info (rated power and voltage)	Battery type	Energy (kWh)	Power (kW)	Off-wire length (km)
21	Birmingham (UK) 2018	Urbos 100 tram (750 VDC)	LFP	80	400	2.3
22	Wales (UK) 2018	Class 230 EMU	Li-ion	420	-	64
23	Germany 2018	Talent 3 EMU (1500 kW, 15 kVAC)	NMC	300	-	40
24	Wales (UK) 2023	Flirt Hybrid DMU (2.6 MW, 25 kVAC)	LTO	180	-	80
25	Austria 2019	Cityjet Eco EMU (2.6 MW, 15/25 kVAC)	LTO	528	1300	80
26	Germany 2023	Mireo Plus B (1.7 MW)	-	700	-	120

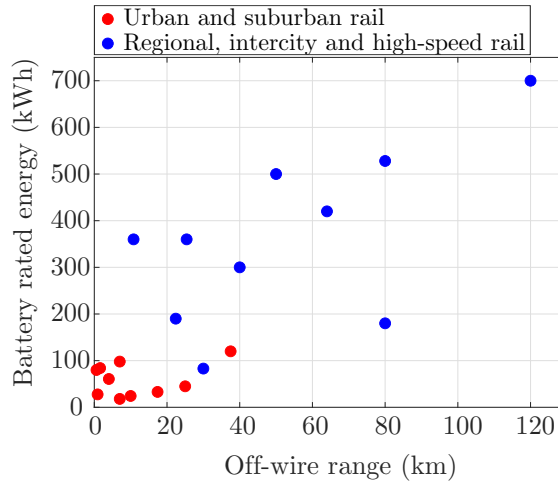


Figure 2.3. Onboard stored energy vs. off-wire autonomy of reported rail vehicles with onboard batteries.

The first representative example of supercapacitors for onboard installation is the MITRAC module, first developed by Bombardier in 2003 [47]. The storage system was installed and demonstrated on a prototype LRV with a catenary/SC hybrid powertrain and a total traction power of around 380 kW. Each SC module featured a rated energy and capacitance of 850 Wh and 45 F, respectively, while providing a maximum power of

300 kW with a weight of 477 kg. This resulted in specific energy and power of 1.78 Wh/kg and 629 W/kg for each air-cooled module. The tests carried out showed a considerable reduction in the power and energy demand from the overhead line, with a 50% reduction in the current drawn from the pantograph and consequent stabilization of the line voltage [48]. Furthermore, the vehicle was operated in catenary-free operation for 500 m with a speed of up to 26 km/h. After the initial testing, the system has become commercially available on Bombardier's Flexity 2 trams. Since 2012, Variobahn rolling stock equipped with MITRAC module is in passenger service on the Mannheim to Heidelberg line in the Rhine-Neckar Land, Germany [35].

In January 2005, the Central Japan Railway Company (JR Central) and Toshiba Co. installed an onboard experimental storage system based on SCs on the Series 313 trains operating on the electrified Chuo line in Japan [49]. The storage devices featured 600 Wh and 180 kW of rated energy and power, with a total weight of 430 kg and consequent specific energy and power of 1.4 Wh/kg and 418 W/kg, respectively. Experimental tests on the catenary/SC hybrid units showed a modest 1.6% reduction in the peak power demand from the overhead wire during accelerations due to the amount of energy stored in previous braking phases. Moreover, the systematic use of regenerative braking led to a relevant reduction in the pressure and temperature distribution at the brake cylinders and wheel treads, resulting in reduced mechanical wear and improved lifetime.

Several catenary/SC hybrid Citadis 402 tram vehicles started passenger service on the T3 line Paris in 2009, under the STEEM project undertaken by Alstom, public transport operator RATP, and public research institute INRETS [50]. The main aims of the project were energy-saving and wireless operation capability. Each vehicle was equipped with 48 submodules for an overall energy and power rating of 1.6 kWh and 500 kW. The entire system weight was 1340 kg, resulting in specific energy and power of 1.2 Wh/kg and 373 W/kg. Measures performed in spring-time showed an average daily energy reduction of 13% compared with a baseline vehicle, a good result considering the high receptivity of the chosen tramway line. Moreover, the catenary-free operation was successfully achieved on a 300 m-long segment between Porte d'Italie and Porte de Choisy.

Spanish manufacturer CAF has been developing onboard storage solutions for railway vehicles since around 2010. One of these, the Greentech Evodrive system, is based only on SC and has been specially designed for trams to recover kinetic energy during frequent braking phases [51]. Catenary/SC hybrid trams equipped with Evodrive systems have been in commercial service in Cuiabà, Brazil, and Tallinn, Estonia since 2015 [52].

During the same period, Siemens entered the market of onboard SC with the Sitras MES module, which is claimed to be versatile enough to be installed on new vehicles or integrated into existing vehicles for retrofitting. Application of Sitras MES can be found on tramways of Innsbruck, Austria, and Guangzhou, China. According to the first case, a 0.85 kWh, 288 kW, and 820 kg system has been employed by the manufacturer [12]. This translates into overall specific energy and power values of approximately 1 Wh/kg and 351 W/kg. The vehicles run without catenary on the entire non-electrified 7.7 km long route on the Guangzhou tramway, with the SC being the only available energy source [35].

Other tram vehicles equipped with SCs in passenger service can be found in Shenyang (China), Kaohsiung (Taiwan), Portland (USA), Rostock (Germany), and Wrocław (Poland) [35]. In Shenyang, supercapacitors are employed together with an overhead line and a wireless operation only on short sections. On the other hand, the vehicles in Kaohsiung are powered only by SCs for operation on the non-electrified 8.2 km long route in present service and on the future 13.4 km long extension currently under completion [12].

Table 2.2 summarizes the available data of reported vehicles with onboard supercapacitors.

2.2.3 Vehicles with onboard hybrid storage systems

Hybrid Energy Storage Systems (HESSs) comprising batteries and SC can offer unique characteristics due to the combination of the advantages of the two technologies. For this reason, HESSs have found applications also to multimode rail traction systems.

In 2008, light metro trains operated on the Metro Ligeiro da Margem Sul do Tejo (MTS) railway in Almada, Portugal, were fitted with a HESS developed by Siemens. This system, named Sitras HES, was installed to reduce the power demand from the overhead wire and enable partial

Table 2.2. Available data of reported vehicles with onboard supercapacitors

#	Place and year	Vehicle info	Energy rating (kWh)	Power rating (kW)	Off-wire length (km)
1	Mannheim (DE) 2003	LRV (380 kW, 750 VDC)	0.85	300	0.5
2	Japan 2005	313 Series EMU (1.5 kVDC)	0.6	180	-
3	Paris (FR) 2009	Citadis 402 tram (750 VDC)	1.6	500	0.35
4	Innsbruck (AT) 2011	LRV (600 VDC)	0.85	288	n.a.
5	Portland (US) 2012	SD660 tram (700 kW, 750 VDC)	0.7	-	none
6	Cuiabà (BR) 2012	Urbos tram (750 VDC)	0.8	400	n.a.
7	Shenyang (CN) 2013	LRV (750 VDC)	-	-	2.5
8	Tallinn (EE) 2013	Urbos tram (750 VDC)	0.8	400	-
9	Rostock (DE) 2014	Tramlink 6N2 tram (400 kW, 750 VDC)	-	-	none
10	Guangzhou (CN) 2014	LRV (750 VDC)	0.85	288	all route
11	Wrocław (PL) 2015	Twist tram (750 VDC)	-	-	none
12	Kaohsiung (TW) 2019	Citadis 305 tram (750 VDC)	-	-	all route

catenary-free operation [31]. Since then, the vehicles have been in standard revenue service. Sitras HES is a flexible modular solution whose rated energy and power can be made application specific. In MTS trams, the NiMHB features rated energy and power of 18 kWh and 85 kW, respectively, while the SCs rated power output is 288 kW. The total weight of the hybrid storage system is 1646 kg, resulting in specific energy and power of 11.45 Wh/kg and 226 W/kg, respectively. The storage solution demonstrates effective energy savings and wireless operation capability up to 2.5 km. Since 2016, tram vehicles running on the tramway line in Doha, Qatar, have been equipped with Sitras HES devices for catenary-free op-

eration on the entire 11.5 km long route, with the storage system being recharged at each of the twenty-five stops [8].

Spanish rolling stock manufacturer CAF is an established player in the market of onboard HESSs. Its Freedrive modules comprise air-cooled supercapacitor and air-cooled battery branches. As of 2014, each SC branch featured rated energy and power of 435 Wh and 50 kW (100 kW peak power), while each battery branch is made up of Ni-MH cells for total energy and power of 12 kWh and 10 kW (48 kW of peak power), respectively [25]. Since 2011, CAF has delivered fleets equipped with Freedrive modules to the cities of Seville, Zaragoza, and Granada in Spain, Kaohsiung in Taiwan, Luxembourg in Luxembourg, Newcastle in Australia [8, 32]. Some of these tramways are completely catenary-free with charging at stops, while others are typically electrified and require onboard energy only along a segment of the route.

Although usually associated with ground power supply technology, Alstom has also developed its own proprietary modular HES solution, named Ecopack. Reported applications of such systems can be found in the Citadis trams operating in Rio de Janeiro, Brazil, and Nice, France, since 2015 and 2018, respectively [25]. In the Brazilian city, onboard storage is used in conjunction with ground power supply since 2015 to avoid catenary installation on the entire line. In Nice, the vehicles equipped with Ecopack modules have NiMHB with rated energy of 13.5 kWh that can be recharged at stops and ensure catenary-free operation on the entire 11.3 km long T2 tram line [7].

Table 2.3 overviews the reported applications of HESS onboard rail vehicles.

2.2.4 Vehicles with onboard fuel cells

Hydrogen technology has been long suggested as a promising alternative for many road and railway transport applications, due to the very high energy content of compressed hydrogen compared to other storage technologies. Indeed, fuel cells for heavy-duty transportation have made significant steps beyond the proof-of-concept phase in the last decades, with ongoing applications from trams and buses to regional trains in Asia, Europe, and America [53]. Due to their intrinsic characteristics, FC plants are often employed with secondary storage devices such as batteries or SC.

Table 2.3. Available data of reported vehicles with onboard hybrid energy storage systems

#	Place and year	Vehicle info	Energy rating (kWh)	Power rating (kW)	Off-wire length (km)
1	Almada (PT) 2008	Combino plus tram (730 kW, 750 VDC)	0.85 (SC) 18 (LiB)	288 (SC) 85 (LiB)	2.5
2	Seville (SP) 2011	Urbos 3 tram (750 VDC)	0.8 (SC) 15 (LiB)	400	0.6
3	Zaragoza (SP) 2013	Urbos 3 tram (750 VDC)	0.8 (SC) 15 (LiB)	400	2.2
4	Rio de Janeiro (BR) 2015	Citadis tram (750 VDC)	-	-	22.8 (with GLPS)
5	Kaohsiung (TW) 2015	Urbos 100 tram (750 VDC)	0.8 (SC) 15 (LiB)	400	8.2
6	Doha (QA) 2016	Avenio tram (750 VDC)	-	-	11.5
7	Granada (SP) 2017	Urbos 3 tram (750 VDC)	0.8 (SC) 15 (LiB)	4.9	8.2
8	Nice (FR) 2018	Citadis 405 (750 VDC)	13.5 (NiMHb)	-	8.8
9	Luxembourg (LU) 2018	Urbos 100 (750 VDC)	0.8 (SC) 15 (LiB)	400	3.6
10	Newcastle (UK) 2019	Urbos 100 (750 VDC)	0.8 (SC) 15 (LiB)	400	2.7

In Japan, the first trials involving prototype vehicles equipped with FC systems were started in 2006. Two main projects were carried out by JR East and RTRI [53]. Both prototypes were LRVs intended for regional service, with a traction power of around 190 kW per motored car. Their powertrains were essentially derived from a standard battery/diesel series hybrid configuration, with the FC stack replacing the diesel generator unit. The trial car proposed by JR East was a modification of the NE train and featured 270 l of hydrogen stored at 350 bar and two PEMFC stacks with a total power of 130 kW. A 19.5 kWh, 340 kW Li-ion battery was connected directly to the dc bus for power assist and braking energy recovery [54]. The prototype vehicle developed by RTRI featured a single 120 kW PEMFC stack and LiB with 36 kWh of rated energy, 360 kW of rated power, and a total weight of 1200 kg, for an energy and power density of around 30 Wh/kg and 300 W/kg, respectively. The battery

was connected to the dc bus through an additional bidirectional dc/dc converter. Hydrogen was stored in four cylinders at a pressure of 350 bar for a total capacity of 720 l [55]. Both projects were mainly aimed at unveiling hydrogen potential and all the technical shortcomings related to its integration onboard a passenger train. In Europe, one of the first reported applications of light rail transport with onboard hydrogen storage dates back to 2011. In that year, a prototype series 3400 railcar was remodeled and tested on the Santander-Oviedo regional line in Spain [35, 56]. The vehicle had a total traction power of around 120 kW and featured a complex hybrid storage system with a FC stack, LiBs, and SCs. A total of 600 L of hydrogen were stored at a pressure of 200 bar, while the battery featured a rated energy of around 50 kWh.

In Oranjestad, Aruba, the first hydrogen trams began passenger operation in February 2013 [56]. The vehicles operate on the non-electrified 2.7 km line connecting the cruise port to the city. The storage system is based on a 14 kW FC stack and LiBs with rated energy of 160 kWh, powering four traction motors for a total of around 190 kW. Each vehicle can store up to 4 kg of hydrogen, which is enough for a one-day operation. Hydrogen is produced by electrolysis of water, and refueling/recharging of the fleet is carried out at night-time. It is claimed that the fuel cells generate more than half of the daily required energy, while the braking energy recovery enabled by batteries is around 12%.

In recent years, many FC-based tram systems have been put into service in China thanks to a partnership between Chinese rolling stock manufacturer CRRC and fuel cell supplier Ballard. In Qingdao, a fleet of catenary/FC hybrid Skoda Forcity 15T trams equipped with PEMFCs is in service since 2016 [56]. Part of the route has a 750 VDC overhead electrification, while in other segments, the vehicles rely entirely on hydrogen power [57]. In Tangshan, a FC light-rail commercial trial with a traction power of around 370 kW was launched in October 2017 [58]. The tram has a hybrid storage system comprising two 150 kW FC stacks, two battery packs of 20 kWh each, and two SC modules with a rated capacitance of 45 F each. A total amount of around 12 kg of hydrogen at 350 bar is stored onboard each vehicle, yielding an average range of approx. 40 km with speeds up to 70 km/h [53]. In December 2019, running tests on a fleet of Forcity 15T hydrogen trams began in Foshan [59]. The vehicles are

equipped with Ballard's fuel cell stacks and are claimed to have a range of about 100 km with a maximum speed of 70 km/h. The fleet is expected to operate on the 17.4 km Gaoming line by the end of 2020 [60]. Testing of trial hydrogen trams has started recently in the cities of Saint Petersburg, Russia, and San Bernardino, California [61].

An important application of hydrogen power in railway traction is represented by Alstom's Coradia iLint, a **HEMU** regularly operated on the RB33 regional line in Lower Saxony, Germany, together with standard **DMUs**, since September 2018 [53]. The trains are equipped with a hybridized powertrain that combines a hydrogen fuel cell as the primary energy source with batteries mainly used for acceleration and energy recovery during braking phases. Hydrogen storage capacity and pressure for each train are 260 kg and 350 bar, respectively, allowing a maximum range of 1000 km, which is enough for a full day of operation without refueling [62]. The fuel cell stack can output a total power of 400 kW, with extra power being provided by two 110 kWh Li-ion NMC battery units for a total rated traction power of around 570 kW [63]. The local government has increased the fleet with fourteen additional units in service since August 2022 [64]. A similar order has been signed between Alstom and Frankfurt-am-main transport authority to deliver twenty-seven iLint trains by 2022 [35]. In May 2018, the Austrian operator of Zillertalbahn regional railway awarded Stadler a contract to supply five hydrogen trains to replace diesel units for regular passenger service by the end of 2022 [65]. In March 2020, Alstom performed further testing of the iLint on the 65 km line between Groningen and Leeuwarden in the north of the Netherlands for a pilot project agreement among Alstom and other public and private Dutch parties. The Dutch railway network has around 1000 km of non-electrified lines currently covered by diesel trains. The Netherlands thus became the second country in Europe to test hydrogen-powered railway solutions [66].

In 2017, Siemens and Ballard Power Systems announced an agreement to develop an **FC/LiB** hybrid version of Mireo **EMU**, with initial deployment planned for 2021. The power system comprises two 200 kW fuel cells and a 350-kWh **LTO** battery [67]. The vehicle is designed for a range of up to 1000 km in the three-car configuration, allowing one refueling per day. For this project, the manufacturers claim impressive improvements

in fuel cell performance: 50% higher power density and three times longer service life than market standards. Other trial projects are currently being developed in Europe. In 2019, a collaboration among Porterbrook, Ballard, the University of Birmingham, and several other collaborators led to the realization and testing of the United Kingdom's first hydrogen train HydroFLEX. The train is a single-car prototype derived from a Class 319 EMU and equipped with a PEMFC stack of 100 kW working as a range extender, a 200 kW LiB pack, and 20 kg of hydrogen stored in HPHS tanks. The train can also run under 25 kVAC overhead catenary, thus making it a tri-mode vehicle. The prototype was successfully demonstrated in 2019 and will be further tested on the mainline railway for passenger service [68]. Vivarail and Siemens also have ongoing projects to integrate hydrogen power plants on board electrical multiple units [33].

In 2020, JR East, Hitachi Ltd., and Toyota entered an agreement to develop an FV-E991 FC/LiB hybrid train as an evolution of the former FC NE train [69]. The two-car train is to be equipped with a PEMFC stack of 240 kW and two battery modules of 120 kWh each, powering four induction motors for a total traction power of 380 kW. Hydrogen will be stored in 20 vessels at a pressure of 700 bar to achieve a longer autonomy (estimated at about 140 km), compared to the 350 bar storage [70]. The vehicle will be used for trial purposes on the Tsurumi and Nambu lines in Japan aimed at commercialization by 2030.

The main data of the reported multimode vehicles with onboard fuel cell systems is summarized in Table 2.4.

2.2.5 System-level comparison

The ranges of energy and power levels of batteries, supercapacitors, and hydrogen plants (high-pressure H₂ storage and fuel cells) and the corresponding Ragone plot are presented in Figure 2.4, using the system-level data reported in the previous sections. Batteries and supercapacitors find wide application in combination with the external line supply for vehicles operating on electrified urban and suburban networks. The reported battery installations have an average system-level density of around 35 Wh/kg, with the highest value of 83 Wh/kg. The shortest full charge/discharge times are in the range of a few minutes and belong to metro and light rail applications. Supercapacitors exhibit the highest power densities

Table 2.4. Main data of reported vehicles with onboard fuel cells

#	Place and year	Vehicle info	Energy sources	H ₂ storage	Aux. storage energy (kWh)	Power ratings (kW)
1	Japan 2007	R291 series (190 kW)	FC/LiB	720 l @350 bar	36	120 (FC) 360 (LiB)
2	Japan 2009	LRV (190 kW)	FC/LiB	270 l @350 bar	19.5	130 (FC) 340 (LiB)
3	Valencia (SP) 2011	LRV (120 kW)	FC/LiB/SC	600 l @200 bar	50 (LiB) 0.43 (SC)	24 (FC), 89 (SC) 120 (LiB)
4	Oranjestad (NL) 2013	Streetcar (194 kW)	FC/LiB	4 kg	160	14 (FC) 180 (LiB)
5	Qingdao (CN) 2016	Forcity 15 tram (745 kW, 750 VDC)	catenary/PEMFC	-	-	-
6	Tangshan (CN) 2017	LRV (370 kW VDC)	FC/LiB/SC	460 l @350 bar	40 (LiB) 3.5 (SC)	300 (FC) 600 (SC)
7	China 2017	LRV (200 kW)	FC/SC	1.75	150 (FC) 370 (SC)	
8	Lower Saxony (DE) 2018	Coradia iLint (540 kW)	FC/LiB	6820 l @350 bar	220	400 (FC) 450 (LiB)
9	Foshan (CN) 2019	Forcity 15T tram	PEMFC	-	-	200
10	UK 2019	Class 319 EMU	PEMFC/LiB	20 kg	-	100 (FC) 200 (LiB)
11	Japan 2020	FV-E991 EMU (380 kW)	PEMFC/LiB	1020 l @700 bar	240	240 (FC)
12	Germany 2021	Mireo Plus H (1.7 MW)	PEMFC/LiB	250 kg	350	400 (FC)

at the system level, too; however, power density is considerably reduced (up to ten times) compared to single-cell levels and approaches an upper limit of around 650 Wh/kg. SC full-discharge time is in the range of seconds and comparable to the typical braking times of rapid transit systems, representing a good solution for energy recovery. For regional and intercity rails, SCs become no more attractive, and medium- to high-size batteries with longer discharge times of up to one hour are employed to cope with increased power requirements and longer wireless capability. Hydrogen systems can store very high amounts of energy and deliver it at intermediate power levels. The system-level power density is below 100 W/kg but a high density of usable energy in the range of 200–600 Wh/kg can be achieved. These values yield usage times ranging from tens of minutes to several hours, compatible with medium- to long-distance service. Batteries and supercapacitors of smaller sizes are employed in conjunction

with hydrogen systems to overcome their lower power density and manage bidirectional power flows.

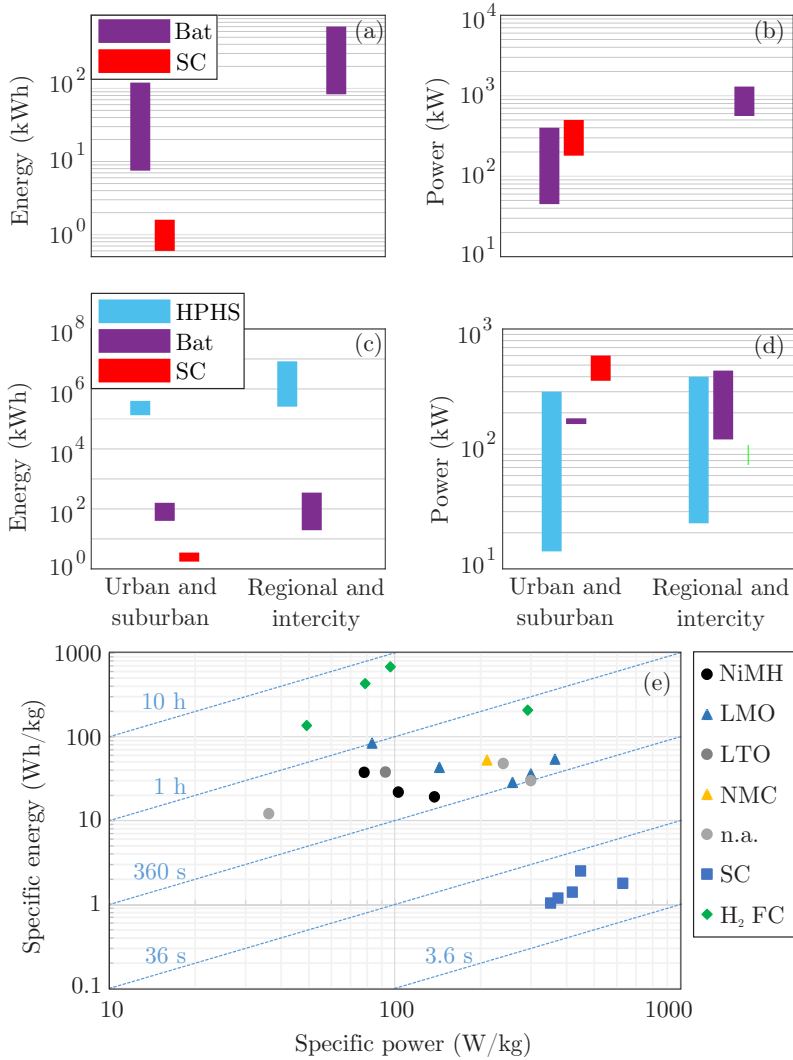


Figure 2.4. Energy and power ratings of batteries and SCs alone or in conjunction with external supply (a-b), FC systems with ESSs (c-d), and system-level Ragone plot of all technologies (e).

2.3 Advantages and challenges

2.3.1 Onboard energy storage in electrified railways

The experience gained through tests and commercial operation indicates that multimode vehicles with onboard **ESSs** can indeed provide several technical advantages to electrified rail systems [71, 72]:

- power peaks shaving during accelerations, leading to higher efficiency and reduced energy demand per driving cycle.
- voltage stabilization of the external line due to reduced current demand, possibly leading to higher traffic densities without modifications in the infrastructure.
- partial catenary-free operation, with reduced load on infrastructures and tolerance towards possible failures of the main power supply.

When used in combination with the electrified line, batteries and **SCs** allow for a considerable improvement in braking energy recovery. Indeed, braking energy is not wasted on rheostats or sent back to the line if feasible, but rather stored onboard the vehicle and reused for subsequent acceleration. Energy savings are more effective for urban transit vehicles, characterized by low commercial speed and frequent accelerations and braking. For this particular goal, **SCs** usually represent the best choice thanks to high power density, cyclability, and lifetime. Available data from some of the installations reported in the previous sections have shown reductions in energy drawn by the catenary from 10% to more than 30%. Line-current shaving and voltage stabilization are important secondary effects of onboard storage and improve the efficiency and service quality of the electrified infrastructure. Moreover, **ESSs** can be used for partial catenary-free operation on urban and regional lines, from a few hundred meters to several kilometers. For such applications, batteries can entail lower investments than electrification and are compliant with aesthetics, noise, and pollution requirements typical of urban environments. For instance, Siemens asserts that their Sitras MES results in up to 80 tons/year of CO₂ reduction per vehicle [73].

These advantages generally come at the expense of increased weight of the system and high modification costs [74]. More stringent safety

requirements have to be applied due to the presence of passengers on board. On the other hand, maintenance of the storage units necessarily entails vehicle downtime. Moreover, the sizing of the storage devices for vehicles operating on electrified networks represents a non-trivial problem. An optimal combination between electrified infrastructure and onboard energy should minimize the total operational costs while meeting system lifetime and reliability constraints [75]. Multiobjective optimization is often employed in literature case studies to allocate sufficient onboard energy capacity, define electrified and catenary-less sections, and locate charging points [76,77]. The optimal solutions bring a significant reduction in the total costs of the system. However, the overall procedure has a relevant computational burden and relies on many assumptions and cost indexes that need to be finely tuned.

Operators can implement other strategies to enhance the energy efficiency of electrified rail systems. The main alternatives to multimode rolling stocks are represented by reversible substations and wayside storage units [8]. Reversible substations allow bidirectional energy flows between the ac and dc grids. Therefore, they can improve the receptivity of the dc overhead line since the excess braking energy can be fed back to the ac distribution network. The substations must be designed to fulfill several requirements: prioritize the exchange of energy among vehicles, ensure power quality on the ac side, and control the dc-side voltage during all operation modes. If a complete upgrade of the unidirectional substations is not feasible, IGBT inverters can be added in parallel to manage the reverse energy flow that occurs during braking [78]. The installation of reversible substations requires no modification of the rolling stock but entails significant infrastructure costs. Moreover, the effectiveness of energy recuperation can be negatively affected by the excessive distance between the braking vehicle and substation and the conversion chain's overall efficiency.

Wayside energy storage installation can be a more efficient and cost-effective solution for off-board braking energy recuperation. They can reduce the energy provided by the ac grid and stabilize the dc grid voltage through proper peak-shaving action. Moreover, their design is not affected by space and weight restrictions. Their installation and maintenance do not directly affect rail system operation if a certain overall degree of system

Table 2.5. Comparison of different energy-saving solutions in electrified railways

Solution	Advantages	Disadvantages
Onboard ESS	<ul style="list-style-type: none"> • High efficiency • Catenary-free operation • Line voltage stabilization and load leveling • No infrastructure costs 	<ul style="list-style-type: none"> • Space and weight constraints • Increased vehicle costs • Downtime for maintenance • Safety constraints
Reversible substations	<ul style="list-style-type: none"> • Realisation and maintenance during operation • Less safety constraints compared to onboard storage • No vehicle modification costs 	<ul style="list-style-type: none"> • Very high infrastructure costs • No off-wire operation • Lower efficiency compared to onboard storage • No voltage stabilization or line load reduction
Wayside ESS	<ul style="list-style-type: none"> • Medium efficiency • Line voltage stabilization • No weight or space constraints • Implementation and maintenance do not interrupt operation • Less safety constraints compared to onboard storage • No vehicle modification costs 	<ul style="list-style-type: none"> • Fine-tuned analysis for sizing and location • Medium infrastructure costs • No pantograph load reduction • No off-wire operation

redundancy is assured. However, attention must be paid to the displacement of the storage units along the route to minimize transmission losses while containing capital costs. The variability of traffic conditions must be carefully considered to avoid oversizing. Moreover, wayside storage systems cannot reduce the burden of the overhead supply line nor enable catenary-free operation [8]. A comparison of the different energy-saving solutions in electrified rail systems is given in Table 2.5.

2.3.2 Potential for diesel replacement in non-electrified railways

On short to medium ranges, charging times are not an issue and can be effectively accomplished under catenary on electrified sections and at stops through dedicated fast-charging facilities. For instance, Bombardier reports a full charge time of seven to ten minutes for their Talent 3 to run 40 km without overhead line [41]. Other manufacturers claim similar

charging-time-to-range ratios. For longer distances and higher amounts of stored energy, hydrogen represents a competitor of batteries as a clean alternative to diesel. Alstom claims CO₂ savings of 700 tons/year per vehicle for their hydrogen train [79]. This translates to a 45% reduction compared with the emissions of a standard Lint unit when hydrogen is produced from natural gas. Indeed, several academic research activities on the decarbonization potential of hydrogen endorse the claims of Alstom. In [80], the performances of a 600 kW, 72-ton diesel train were compared with those of fuel cell and FC/battery hybrid trains derived from the same baseline design. Performances were evaluated on an 80 km regional route in proximity to Birmingham. Under the requirements of equal journey time and passenger capacity and one-day operation without refueling, a reduction of 34% in fuel consumption for the FC vehicle and 55% for the FC/battery vehicle was observed for the baseline diesel unit. The global CO₂ emissions, assuming steam reforming to produce hydrogen, were found to be lower for both hydrogen-powered trains: 55% for the hydrogen-powered and 72% for the hydrogen-hybrid, assuming that hydrogen is produced from natural gas. In 2016, a collaboration among the University of Birmingham, Hitachi Ltd., and Fuel Cell System Ltd. resulted in a preliminary study on the potential of converting existing DMUs and new regional multiple units to hydrogen power using a FC/battery hybrid traction system [81]. Given the same timetable requirements of the baseline diesel units, a 50% reduction in fuel energy demand was evaluated for the hydrogen-powered fleet.

Despite a common set of advantages, battery and FC trains pose technical and non-technical challenges to their adoption as widespread alternatives to diesel power units. Large-size batteries require much longer charging times with respect to standard refueling of diesel trains. For a 200 km range, a battery pack currently could require approximately 50 minutes for a full charge [79]. On the contrary, the relationship between operating range and refueling time is much more attractive for hydrogen trains and comparable to standard diesel units: 15 minutes of refueling enable up to 1000 km of range. Furthermore, hydrogen trains allow for a high operational and network flexibility like diesel units, while battery vehicles must strictly follow the mission profile to which their accumulators have been tailored. Hydrogen fuel tanks are separated from the

power conversion elements, the fuel cells, leading to a higher versatility in the system design. Battery power and energy are correlated and limited by the electrochemical characteristics of the device. A fine-tuning of the battery size must be carried out in the design phase according to the specific mission profile to avoid oversizing. Battery charging can be done at stations or depots using pre-existing electrified infrastructures. However, when a long-range operation is required, dedicated fast-charging islands along the route become necessary to avoid battery oversizing.

Dedicated facilities are even more necessary for FC trains, since large quantities of hydrogen should be produced, distributed, and stocked every day. For instance, a fleet of twenty iLint would require approximately 3750 kg of hydrogen to cover a daily range of 750 km, considering an average hydrogen consumption of 250 g/km [82]. On the Lower Saxony line, hydrogen by-products of certain industries such as the chemical sector will be used in the beginning [64]. Compressed hydrogen is a highly efficient methodology for storage but entails high costs for the vessels and is intensively energy-consuming [17]. Due to less on-field experience, challenges in mechanical and thermal stresses are common to both technologies and must be addressed carefully to ensure the rated operation and adequate lifetime. The health management of batteries and FC should be addressed carefully given the long mission requirements of trains, as low reliability would result in high operational costs for the rolling stock. Indeed, an incorrect evaluation of lifetime and health state during train operation can lead to wrong sizing and energy management strategies, and increased overall costs [83]. Reliability-oriented energy management strategies can be implemented to tackle these issues and adequately account for FC degradation. This is, for instance, presented in [84], where degradation metrics are included in the energy control of a hydrogen-powered hybrid traction system. However, a significant computational effort is required to solve the stochastic optimization problem and derive the control look-up table.

On the other hand, legal barriers represent a major disincentive to hydrogen adoption. Indeed, the existing regulatory framework for hydrogen, fuel cells, and related infrastructure is not specific to rail applications, entailing a time-consuming permitting and approval process for manufacturers and railway operators [53]. This is particularly true for hydrogen distribution and storage facilities. Large amounts of pressurized gas in

Table 2.6. Operating and maintenance costs of rolling stock and infrastructure for conventional and alternative rail systems.

	DMU	EMU	BEMU	HEMU
Energy consumption	15÷20 (kWh/km-train)	6÷8 (kWh/km-train)	5÷6 (kWh/km-train)	7.5÷9 (kWh/km-train)
Fuel consumption	1.5÷2 l/km	-	-	230÷360 g/km
Energy/fuel price	1.2 €/l	12÷15 c€/kWh	12÷15 c€/kWh	4.5÷5.8 €/kg-H ₂
Vehicle maintenance costs	0.9÷1.2 €/km-train	0.65÷0.8 €/km-train	0.85 €/km-train + 600÷1300 €/kWh/8y (accu.)	0.7÷1.0 €/km-train + 1000÷2000 €/kW-5y (fuel cells)
Infrastructure costs	350 k€/station	0.9÷1.1 M€/km-line	5 M€/E-station	1 M€/H ₂ -station

the tanks can lead to hazards and require dedicated safety procedures, which have not been standardized yet. Similar arguments can be made for defueling and maintenance procedures of hydrogen refueling stations.

To assess the economic attractiveness of conventional and multimode train technologies, different cost items have to be considered and quantified. In general, technology-dependent and technology-independent costs can be identified. Within the first group, it is possible to list:

- capital costs of rolling stock;
- capital costs of infrastructure for electrification, charging, or refueling;
- energy and fuel consumption per km
- cost of energy per kWh, cost of fuels per liter or kilogram;

Possible ranges of technology-dependent costs are given in Table 2.6 for diesel, electric, and multimode units for regional service [5,53,62]. In broad terms, DMUs and EMUs exhibit lower provisioning costs for rolling stock, regardless of the characteristics of the route. This is due to the high capital costs per unit energy/power of batteries and fuel cells. Infrastructure costs are almost null for DMUs and usually the highest for EMUs, for whom the extension of the network and its traffic volume are key factors. Costs of operation are comparable for the four different technologies, while regular

maintenance is regarded as more expensive for DMUs because of the higher operating temperatures and vibrations experienced by diesel power units. However, power components must be replaced more frequently for HEMUs and BEMUs, given the shorter expected lifetime of batteries and fuel cells compared with diesel engines. Standard EMUs and BEMUs exhibit the lowest costs for traction energy due to the poor efficiency of diesel engines and the high price of hydrogen either when purchased or produced on-site via electrolysis. In [53, 62], an accurate calculation is made for the total cost of ownership of electric, battery, and hydrogen trains as alternatives to diesel propulsion. The study considers five European regional networks that are currently operated with DMUs. The resulting technology-related costs are reported in Figure 2.5, together with the main characteristics of each route in terms of electrification rate, length of off-wire sections, and traffic volume. For each route, the costs of the competitor technologies are normalized to the total cost of the diesel units. Non-technological cost items, like track and station fees, are excluded for better comparison.

On high-traffic networks with short lines (route b), electrification stands as the most competitive solution. Energy and operating costs are the lowest, while the short extension of the infrastructure and the high traffic volume justifies the corresponding investments. Battery trains represent a feasible alternative to diesel for off-wire operation on short non-electrified routes (route a) or in networks characterized by a high electrification rate (route c), where batteries can be recharged under catenary and do not require dedicated infrastructure. In these short-range applications, the benefits of hydrogen energy do not outweigh the cost penalties of fuel and infrastructure. On the other hand, HEMUs gain competitiveness and outperform BEMUs on low-traffic lines of over 100 km (routes d and e). On these lines, electrification makes no economic sense, and diesel is currently the dominant technology. Battery trains would require bulky and expensive accumulators, with extra costs in fast recharging facilities along the route. In contrast, HEMUs can fully benefit from the high energy density and flexibility of hydrogen. These vehicles allow for long off-wire operation with a reduced amount of refueling and corresponding infrastructures. In most cases, DMUs still represent the most cost-attractive solution today. However, the economic disadvantage of battery and hydrogen trains may already be low depending on some key route characteristics.

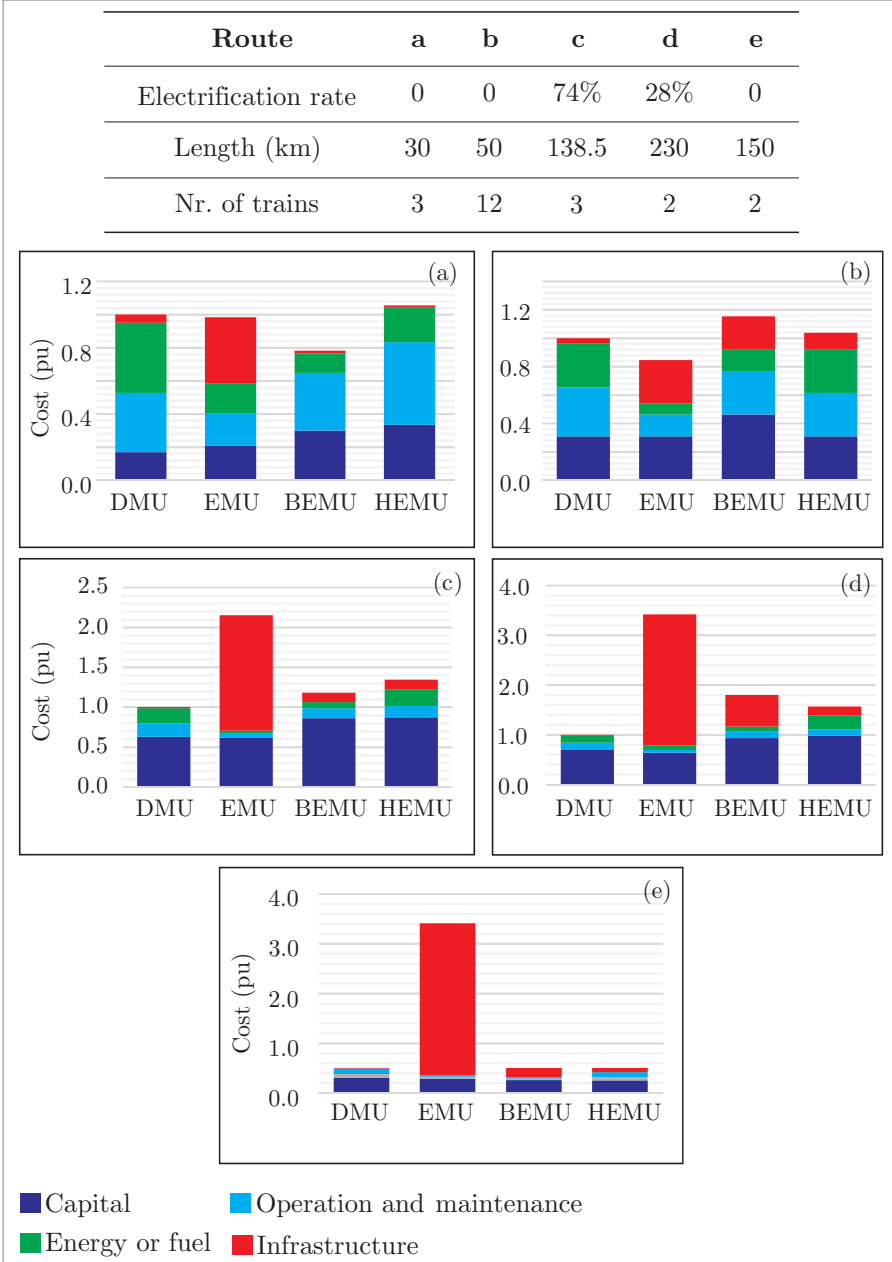


Figure 2.5. Comparison of rolling stock and infrastructure costs of DMUs, EMUs, BEMUs, and HEMUs on five European regional lines.

Traction architectures and control strategies

The energy sources and storage devices in a multimode propulsion system can be arranged into many different configurations. Moreover, many possibilities arise for the Energy Management Strategy (**EMS**) controlling the system power flows. The **EMS** is of great importance for the safe, reliable, and energy-efficient operation of a multimode traction system. The following sections present some architectures and energy management strategies of the real vehicles reviewed in the previous chapter, together with alternative **EMS** approaches and non-conventional power converter topologies proposed in the literature.

3.1 State of the art

3.1.1 Multimode vehicles with external supply or diesel generators

In battery hybrid vehicles, the battery modules can be connected to the dc bus either directly or through a dedicated dc/dc power converter. A direct connection is employed in the hybrid EV-E301 rail vehicle operated by JR East on routes with partial electrification. Its car configuration and traction circuit architecture are shown in Figure 3.1 [29]. Each car comprises a trailer bogie and a motored bogie, which is powered by two

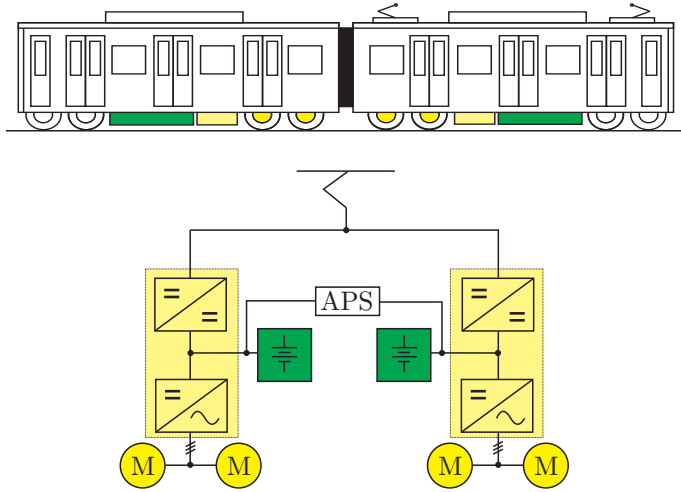


Figure 3.1. Vehicle layout and traction system architecture of JR East's EV-E301 catenary/battery train.

induction motors. All power components for traction and auxiliaries are accommodated in the underfloor space. The battery modules have a rated voltage of 630 V and are connected directly to dc side of the traction inverters. Two separate dc/dc converters interface each bus with the 1500 VDC overhead line, whose voltage needs to be stepped down at the accumulator voltage level. The configuration of the power electronic converters on each car, where only one dc/dc converter is employed to manage the two sources, is known as *semi-active* [85].

The EMS for this vehicle is deployed over four different modes of operations: powering control and standard charging; powering control in non-electrified section; regenerative brake charging control; high-power charging control. The transition between different modes depends on the availability of the catenary and the SOC of the battery system. In powering control and standard charging, the catenary is available. The front-end dc/dc converter controls the energy flow required for traction, Auxiliary Power Supply (APS), and battery charging. When the SOC reaches its upper threshold, charging is stopped, and only traction and auxiliary power are fed to the system. In non-electrified sections, the battery must provide full traction and auxiliary power. During braking, energy is sent back to

the dc bus and is used for APS and to partially recharge the battery. In rare cases when the battery SOC is at its maximum and the vehicle is braking, the dc/dc converter returns regenerative power to the catenary if the sum of the braking power (negative) and auxiliary power (positive) is negative. When the vehicle is stopping at stations, high power charging mode is entered. The dc/dc converters draw a high current from the catenary to fasten the battery charging process. The thermal limits of the pantograph act as the main constraint to the charging current set point.

A higher redundancy characterizes the traction circuit of Bombardier's Flexity 2 hybrid trams operating in Nanjing, China. As shown in Figure 3.2, the dc bus is derived directly between the 750 VDC overhead wire and the ground. Four of the six axles are powered by induction motors, each fed by a dedicated inverter on a parallel branch of the dc bus. The total amount of energy stored onboard is divided into two units comprising two submodules each. They are connected to the dc bus through a bidirectional dc/dc converter which steps up their rated voltage of around 530 V to the rated system voltage. This can be again classified as semi-active architecture, since the overhead supply is connected directly to the traction inverters, and dc/dc converters are employed only for the battery interface.

For this vehicle, catenary power is available only in the proximity of each station and is used to charge the batteries and provide the required traction effort for accelerations [86]. In this context, traction has priority on battery charging. The catenary is implemented as overhead bus bars integrated into the station roof to enable higher charging currents. When the vehicle exits the station area, the pantograph is lowered, and cruising is accomplished only by battery power. In contrast, when the tram enters a station, the pantograph is raised to connect the dc bus to the overhead system. The transitions between catenary and catenary-free modes are done dynamically. Thus, particular care is taken to avoid current arcs when lowering the pantograph or feedback currents from the battery when raising it. This is accomplished by adequate control of the dc bus voltage and the conduction states of the static contactors.

The catenary/battery trams manufactured by CAF for the Birmingham tramway share the same semi-active configuration, with traction inverters connected directly to the external line and battery units interfaced

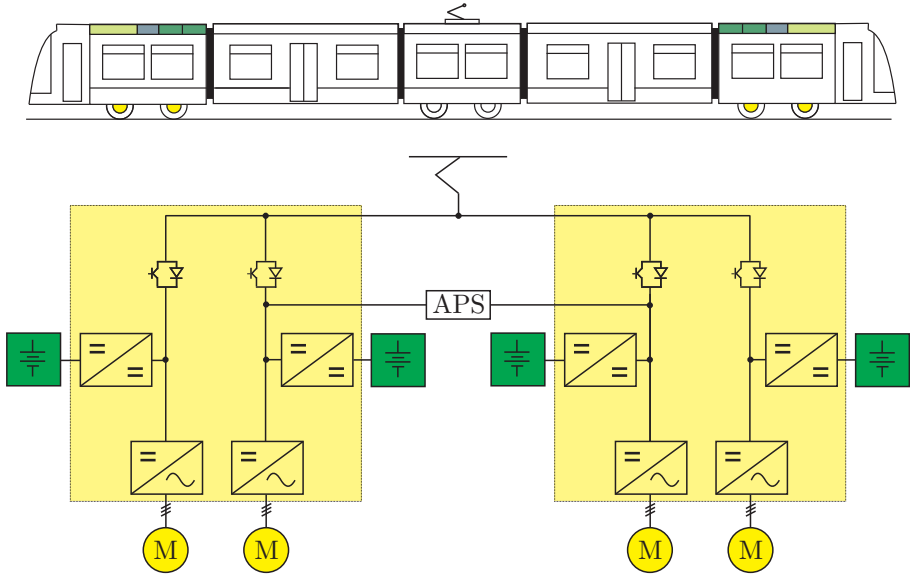


Figure 3.2. Layout and traction system architecture of Bombardier's Flexity 2 catenary/battery tram.

via dedicated dc/dc converters [38]. The same generally applies to LRVs equipped with supercapacitors, as dc/dc converters enable exploitation of the entire SC voltage range and add a degree of freedom for their sizing.

The BEC-819 train is an ac catenary/battery hybrid train manufactured by Hitachi. Its layout and traction architecture are shown in Figure 3.3. This vehicle can be supplied both by the ac catenary and by onboard batteries. The 20 kV, 60 Hz catenary voltage is reduced by a low-frequency transformer and rectified to a value of around 1600 VDC by two front-end active rectifiers. The converters supply power to the dc buses and control the charge and discharge of three battery units. The adoption of high-voltage batteries was found necessary to avoid additional power converters in favor of a semi-active topology. All four axles of the powered bogie are motored by four induction motors split into groups of two and fed by two traction inverters. The integrated traction converter and transformer are in the motor car, while the battery modules are accommodated in the trail car. All power components are placed in the underfloor space. The EMS is similar to the maximum-SOC control previously described for

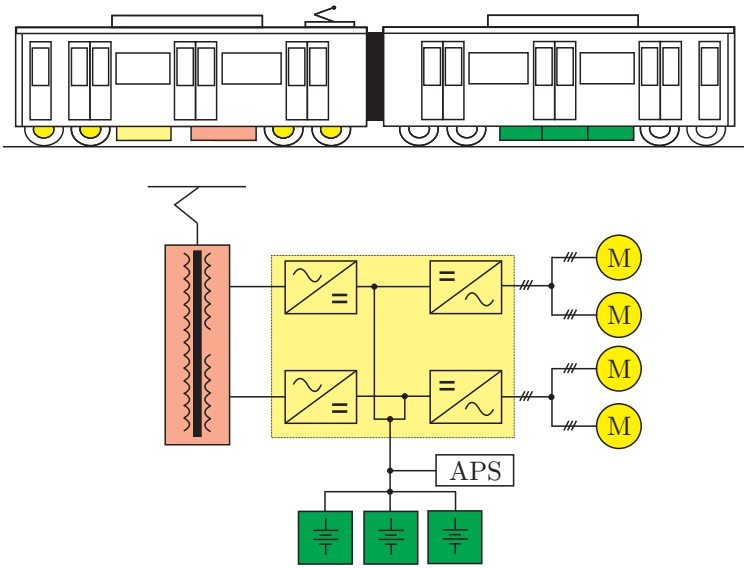


Figure 3.3. Layout and traction system architecture of Hitachi’s BEC-819 catenary/battery train.

other battery vehicles. When the catenary is available, the active front-end rectifier controls the amount of power to be drawn from the line. During traction mode, line power is sent to the motors and APS while the batteries are not used, meaning no line voltage or current control is implemented. During coasting, the traction inverters require no power, and batteries are recharged. With the pantograph lowered, traction and auxiliary power demand are met by batteries alone. Regenerative braking is managed irrespective of the presence of an overhead wire: braking power is entirely utilized to charge the battery, and none of it is sent back to the catenary through the active rectifier. In this context, onboard storage is employed as an alternative to diesel when electrification is missing.

When the battery is added onboard a DEMU, the resulting configuration is usually a series hybrid type. The onboard storage system supplies additional power to the electric traction motors and enables fuel-free operation when required. This is the case of Hitachi’s KiHa E200 hybrid DEMUs in operation in Japan. The powertrain configuration of the motored car of these units is depicted in Figure 3.4 [22]. In this application,

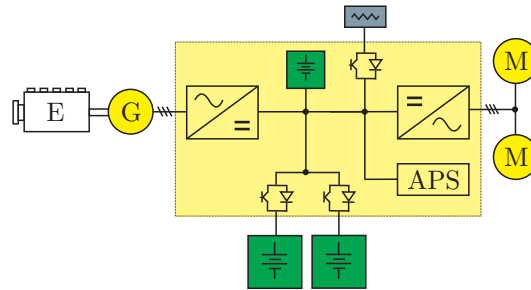


Figure 3.4. Traction system architecture of Hitachi's KiHa E200 hybrid DEMU.

the dc system voltage of around 700 VDC is derived directly from the battery modules and no dc/dc converter is employed. An emergency battery module is also present for extra redundancy, and its primary function is to crank the diesel engine if the main batteries fail. In such a case, the diesel unit alone has to provide sufficient power for traction and APS loads and to charge the emergency battery. The EMS implemented for this powertrain is as follows. The batteries operate as only energy sources at stops and during early acceleration up to a speed of 30 km/h. The diesel genset is then activated for further acceleration and supports batteries during cruising/coasting to avoid excessive discharge and keep their SOC at a medium level. During regenerative braking, the generator output is shut down, and as much braking energy as allowed by the SOC level is sent to the batteries.

Siemens' Combino Plus operated in Almada, Portugal is a tri-mode tram vehicle with the power system architecture shown in Figure 3.5 [87]. Three traction inverters supply six induction motors fed by a common dc bus powered directly by the 750 VDC overhead supply. The roof-mounted LiB and SC units are installed as single units and are interfaced to the dc bus through two independent dc/dc converters. This configuration can be regarded as the tri-mode extension of a semi-active topology because the external power supply lacks a dedicated dc/dc converter.

Thanks to the presence of a **HESS** combined to the external power supply, the **EMS** is more complex and depends on the availability of catenary power [88]. On electrified sections, the storage devices contribute to accelerations and high load conditions so that pantograph current is reduced, and line voltage fluctuations are minimized. During braking, the hybrid storage system can be employed for more efficient regeneration of kinetic energy. On non-electrified routes, batteries and **SCs** can still manage acceleration, cruising, and braking phases. Specifically, **SCs** are more involved during early acceleration and braking, i.e. when high power transients occur. In fact, their power and energy rating are designed to meet the requirements of the acceleration phase. Cruising requires more energy but less power and is thus accomplished at the expense of the energy stored in the battery. When the vehicle is at standstill, both storage devices are recharged by the stationary charging infrastructure according to their respective states of charge and thermal constraints.

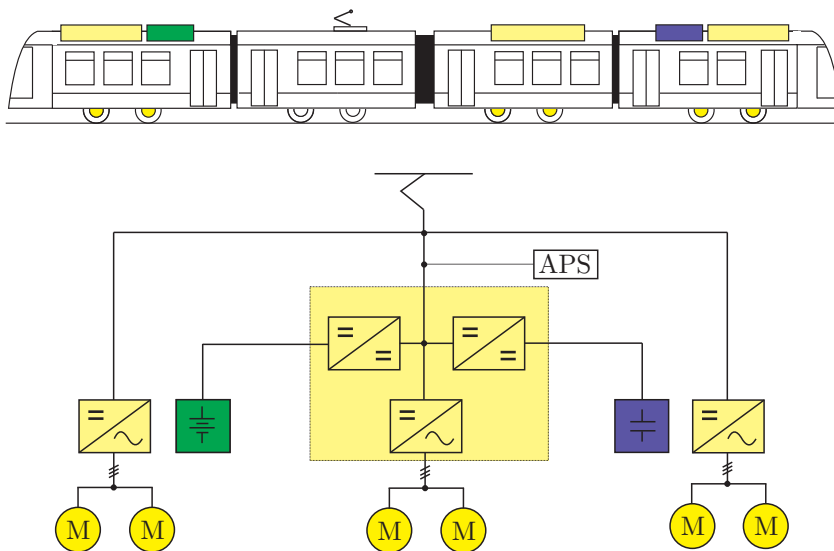


Figure 3.5. Layout and traction system architecture of Siemens' Combino Plus tri-mode tram.

3.1.2 Multimode fuel cell vehicles

In [89, 90], a detailed explanation of the power system architecture of the FC/battery/SC tramcars manufactured by CRRC Tangshan is reported. The vehicle layout and traction system are depicted in Figure 3.6. The tram is composed of two motored cars and one central trailer car. Eight permanent-magnet synchronous motors power four of the six axles. On the roof of the trailer car, the whole hydrogen plant is accommodated. The plant comprises the HPHS tanks, two PEMFCs with their dedicated unidirectional dc/dc converters, and the FC auxiliary subsystems. The storage devices, traction inverters, bidirectional dc/dc converters, and brake resistors are mounted on the roof of each motored car. Each storage unit has a dedicated dc/dc converter for the interface to the common dc bus, which is operated at the rated voltage of 750 VDC. The adoption of a dedicated dc/dc converter for each energy source and storage system results in a *fully-active* topology. The fuel cells are used as the primary energy source to meet the average traction power demand and are controlled in a small power range of around 250 kW. The SC modules

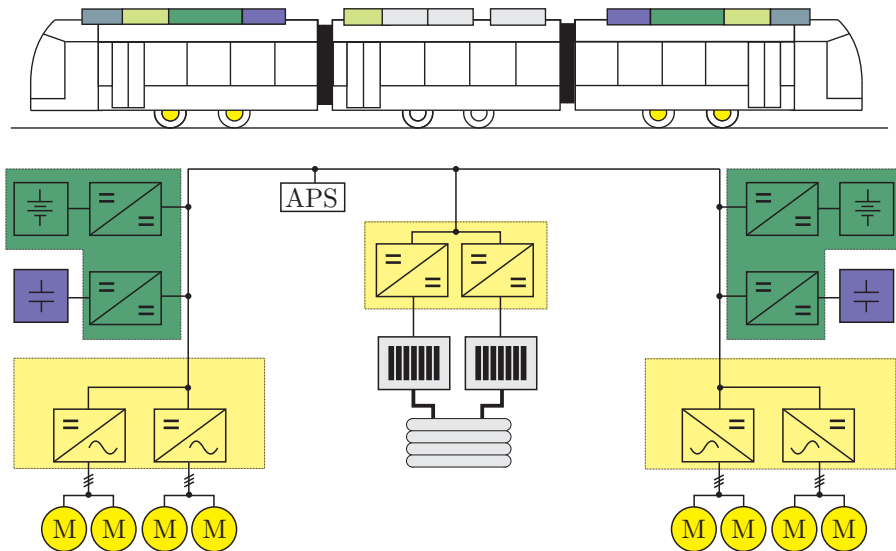


Figure 3.6. Layout and traction system architecture of CRRC Tangshan's FC/LiB/SC tri-mode tram.

are employed to supply the additional power needed during accelerations when the total power demand can be higher than 900 kW. They are also the prime utilizers of the energy recovered by the motors during braking. The contribution of batteries to traction is lower with respect to the other sources. They are mainly employed as backup energy sources in the failure or unavailability of the fuel cells, allowing the vehicle to complete its route and return to the depot [90]. At stops, FCs are kept in operation to recharge the batteries and SCs. By doing so, the standby operation of cells is minimized to extend their lifetime.

Alstom's Coradia iLint FC/LiB bimode train features a simpler semi-active traction architecture, shown in Figure 3.7. The battery storage system consists of two submodules of 800 V and 110 kWh of rated voltage and energy, each one mounted in the underfloor space next to the APS converter on the trailer bogies [63]. The batteries are directly connected to the dc bus, without additional power electronics. The hydrogen generation plant is divided into two units installed on the roof of the two cars. Each unit comprises a hydrogen storage tank and a 200 kW FC stack connected to the vehicle dc bus through a unidirectional boost converter. The dc/dc

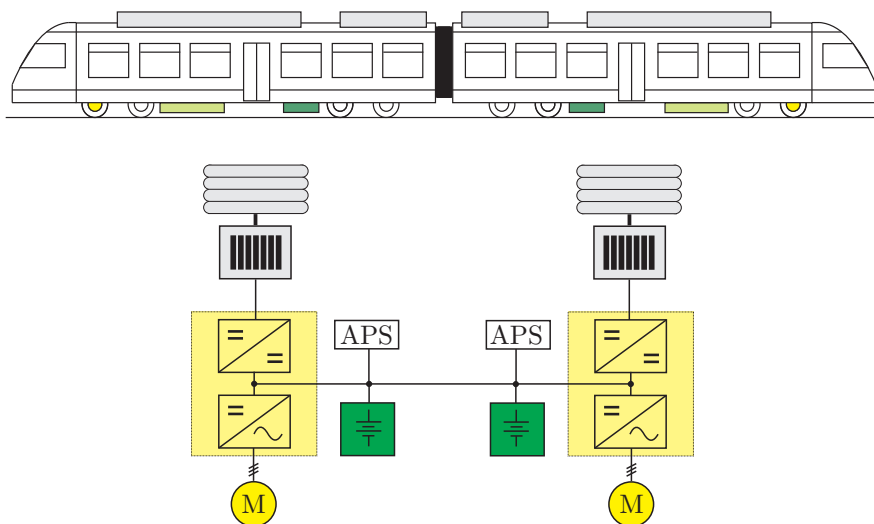


Figure 3.7. Layout and traction system architecture of Alstom's iLint FC/LiB bimode train.

and dc/ac converters are integrated into a single converter box accommodated underfloor with the 127 kW traction motors. The EMS controls the bimode architecture so that hydrogen represents the primary energy supply to the train and is the only one that remains active when the train is coasting. The batteries are mainly employed during accelerations to compensate for fuel cell power limitations as well as during braking to recover kinetic energy. During cruising, the batteries are controlled to perform load balancing so that, irrespective of the instantaneous traction effort, fuel cells can be operated in a small power range for maximum operating efficiency, reduced stress, and extended lifetime.

The very same semi-active architecture has been chosen by JR East for the FV-E991 FC/battery prototype train [70].

3.2 Alternative energy management strategies

The energy management strategies reported in the previous sections can be classified as Rule-Based (RB) strategies. They use a predefined set of rules to split the load power demand among onboard sources. These rules generally consider the train power demand and the SOC of storage units as main decision boundaries. In [91], two simple RB EMSs are proposed and tested on a battery/SC bimode powertrain. The first simple strategy consists of switching between batteries and SCs based on a hysteresis control. The controller operates the SCs alone as long as their SOC is above the minimum threshold. In case of excessive discharge, the battery is turned on to provide traction power and recharge the supercapacitors. The second rule-based technique decomposes the traction current in low and high-frequency components. The low-frequency component is supplied by the battery, while the high-frequency one is delivered by the SCs. In [92], the authors propose a hybrid approach to the energy management of a battery/SC hybrid system. The control strategies integrate a set of rules with a meta-heuristic optimization routine. In particular, a rule-based control layer restricts the search space based on SOC threshold and traction power demand. Within the restricted search space, a heuristic optimization routine calculates the reference values of battery and SC power. A set of equality and inequality constraints is included to account for the dynamics of the energy sources and their operating limits

(i.e. SOC and power limits). Despite their simplicity, these strategies can already exploit the potential of HESSs and improve system performance. RB EMSs are easy to define and implement and guarantee stable operation of the powertrain and proper control of the dc bus voltage [93]. However, rules are set according to qualitative reasoning; that is, no mathematical formulation is employed for their derivation. Therefore, the resulting energy management is likely to be non-optimal for system losses and overall energy consumption [94].

To overcome such limitations, a different class of energy control has been primarily proposed in the literature. These controls address the power-split problem through optimal control theory [95]. In [96], a comparison between rule-based and optimal control strategies is presented. In detail, RB EMSs are evaluated against a more sophisticated Model Predictive Control (MPC). The MPC algorithm aims at calculating the power targets of batteries and SCs by minimizing a loss function over a future time window of short length. The objective function is expressed as a weighted sum of multiple objects that include battery losses, battery current transients, and SC voltage. MPC is shown to provide low battery degradation and reduced lifecycle costs. Nevertheless, RB EMSs work comparably well in the considered scenario, with the advantage of lower computational requirements. A slightly modified MPC is proposed in [94] to optimize battery/SC hybrid LRVs. The idea is that, differently from road electric vehicles, the power demand profile of a rail vehicle is known in advance with a good degree of precision. Therefore, the authors propose a predictive control in which, at each instant, the cost function spans over the whole remaining part of the LRV traction cycle. Since the loss function is expressed in terms of ESS power losses and SOC deviations from targets, the control is shown to achieve lower power losses during the driving cycle and thus a higher energy efficiency. A similar control, but with a more complex cost function comprising also a limitation on the battery, is developed in [97] and achieves comparable reductions in system losses. A different approach is proposed in [98], where the authors suggest the adoption of Genetic Algorithm (GA) to derive the optimal EMS for a catenary/battery/SC tri-mode tram. In particular, GA optimization is used to derive the ESS power targets that minimize a multiobjective cost function. This function accounts for the capital, maintenance, and

replacement costs of batteries and SCs and the cost of energy drawn by the overhead line expressed in EUR/day. The resulting control strategies achieve a simulated average reduction of 17% in the system's total costs. Again, an off-line optimization procedure can be justified by the fact that the load profile of an LRV is largely known in advance and well predictable.

Literature studies show that optimal controls can effectively improve the energy efficiency or reliability of a multimode system, but at the expense of increased complexity and computational burden. Therefore, a trade-off between these conflicting factors must be considered to choose the alternative that best fits practical real-time applications. The implementation of optimal EMSs for multimode vehicles in commercial operation is unknown due to confidentiality reasons.

3.3 Non-conventional traction converters

As shown above, the vast majority of rail traction architectures feature two-level VSIs traction drives and unidirectional or bidirectional dc/dc converters (mostly based on the non-isolated half-bridge topology). Novel power converter topologies have been proposed and analyzed in recent years, with the primary goal of obtaining size and weight reductions.

One popular emerging solution is represented by the MMC. MMCs offer many attractive features such as modularity, scalability to high power and voltage levels, and fault tolerance [99]. Its basic architecture was first proposed in [100] as a single-stage interface between the low-frequency ac line voltage and the medium-frequency transformer. It has been developed and tested by Siemens at power ratings of 2 and 5 MW [101]. The MMC was then introduced in many other fields, including medium voltage traction drives [102]. More recently, the converter has been investigated as a highly integrated solution for electric traction systems using a combination of energy sources and storage devices. Figure 3.8(a) shows the concept of embedding distributed battery or SC submodules in the MMC circuit. The performance of an MMC with distributed SC cells for catenary/SC bimode rail vehicles was analyzed in [103, 104]. The results showed that this configuration can effectively control the power flowing among the motors, external line, and onboard SC. However, complex multilayer control

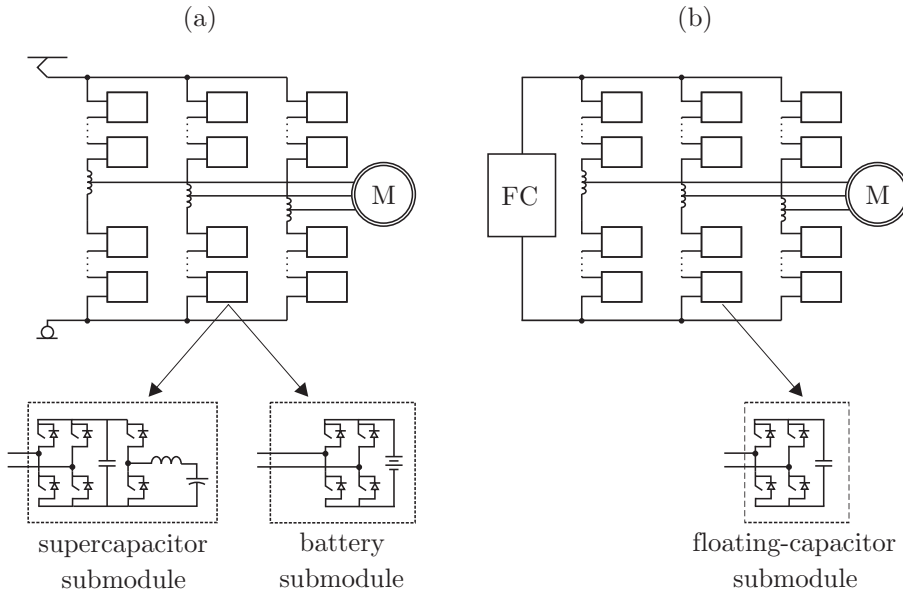


Figure 3.8. Examples of integrated MMC topologies for: (a) catenary/ESS rail vehicle; (b) hydrogen rail vehicle.

schemes are needed to control the SOC levels of the SC cells and attenuate the low-frequency component of the circulating current. Moreover, the SOC unbalance among SC cells directly affects the distortion of the output voltage. Similar studies have addressed the battery-based architecture but with application to the automotive field [105]. The MMC topology for hydrogen LRVs depicted in Figure 3.8(b) was investigated in [106]. The converter provides a single-stage dc/ac conversion with boost capability to compensate for the variations in FC terminal voltage under load conditions. A reference case-study comparative design showed that the volume and weight of passive components can be significantly reduced by the proposed converter compared to a standard configuration (i.e., the series connection of a boost converter to a VSI). However, a complex control scheme must be employed to properly control the arm and submodule voltages within their limits in the full speed range of the motors. Efficiency is also reduced in the motor full-load area compared to a standard architecture.

The cascaded two-level inverter topology has been investigated to supply traction power from two different dc sources without additional dc/dc converters [107, 108]. The circuit can supply the motor with multilevel phase voltages and control the power-sharing between the two sources, also in the case of different dc voltage levels. Further analysis of this configuration is found in [109] for an FC/SC hybrid traction drive, with a focus on the recharging of the SC during motor operation and at stops. These studies show that the cascaded-inverter topology can effectively manage energy flows between sources while supplying the traction motor to track the reference torque and speed. It has several advantages over a standard configuration with a common dc link, such as redundancy, multilevel output voltage, and reduced voltage on the switches. Nevertheless, the modulation technique needs non-trivial adjustments for the converter to achieve all operating modes. More importantly, the motor windings have to be accessible at both ends, which is not a standard configuration for traction motors.

A different power converter architecture, shown in Figure 3.9(a), was originally proposed in [110] to avoid the use of the ESS dc/dc converter in a catenary/ESS bimode LRV. The converter shares the same topology of a three-level T-NPC multilevel converter. However, the circuit is arranged so that the dc supply is connected across the full dc link, while the ESS is connected to the central point of the converter. By proper switching, the circuit can be used to supply the motor from either source or to interleave the sources according to a defined power-sharing rule. More recently,

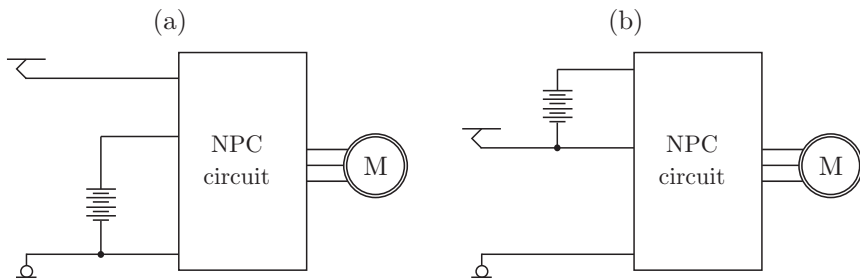


Figure 3.9. Variants of the NPC multi-source inverter concept: (a) the sources share the common ground terminal; (b) the sources are connected in series.

the concept of controlling NPC converters as *multi-source inverters* was resumed, broadened, and specialized to automotive powertrains in [111–113].

A distinct configuration of the NPC multi-source traction converter for a catenary/battery bimode train was explored recently in [114]. The power circuit is shown in Figure 3.9(b) and is arranged so that the dc overhead line is connected to the central point of the converter, while the battery is inserted between its central and top terminals. To control the battery charge/discharge and maintain the SOC within the nominal range, the multi-source converter is controlled through an original level-shifted multi-carrier PWM. The modulation exploits the injection of a constant zero-sequence phase voltage so that the battery is inserted or disconnected from the traction circuit according to its SOC and to the vehicle operating condition. By adding up the battery voltage to the catenary voltage, this layout benefits from a voltage-boost capability that extends the constant-torque region of the traction motors and cannot be obtained from the original MSI converter connection. However, the envisioned converter and its modulation show some inherent limits. First and most important, the proposed modulation only achieves a rough hysteresis-type regulation of the SOC, while no precise control of the battery power level is achievable, as opposed to what is accomplished with a standard dc/dc converter used to interface the ESS to the dc link. Indeed, as discussed in the previous sections, precise control of the battery power is required in a vast number of common EMSs for multimode rail vehicles. Furthermore, the discharge/recharge of the battery should be feasible also when the train stops, but this is not achievable through the series-connection arrangement of the two dc sources. In the scheme of Figure 3.9(b), in the case of a non-receptive catenary, a negative current will flow through the battery into the dc link capacitor, and rheostatic braking has to be activated. In other words, although a ESS is integrated board the train, the proposed circuit cannot achieve complete regenerative braking. This is a major drawback, as the adoption of an onboard ESS is primarily intended to maximize the recovery of braking energy and minimize the traction cycle energy demand. Furthermore, the effect of the modulation pattern on the harmonic content of the battery current is not clear. An input filter connected between the battery and the converter is likely needed to smooth

the battery current and prevent early degradation. Lastly, a higher total dc-link voltage requires semiconductors with a higher blocking voltage rating, which leads to a severe increase in the VA rating and cost of the converter.

In light of the mentioned limits of the series-connection arrangement, the thesis will focus on the circuit configuration in Figure 3.9(a) which, as will be shown, can cope with all the requirements of a multimode rail traction circuit with a proper integration and control of the converter. The next chapters of this thesis are dedicated to presenting original research results on the control and integration of multi-source inverters with application to bimode rail vehicles.

Multi-source inverter: topology and modulation

4.1 Introduction

As reported in Chapters 2 and 3, many multimode rail vehicles belong to the category of bimode vehicles, i.e., they feature one ESS (batteries or supercapacitors) and one main energy source (external line, diesel generator, or fuel cell system). As already pointed out, bimode traction architectures are often arranged into a *semi-active* layout, in which only one dc/dc converter is employed. In fact, semi-active architectures exhibit a good tradeoff between performance and system costs, volumes, and overall complexity [96].

In the standard semi-active configuration shown in Figure 4.1(a), the dc/dc converter controls the power exchange between the LV source¹ connected to its input terminals and the HV dc bus. In terms of power flow, the LV source and its dc/dc converter are connected in series, i.e., all the power drawn from the source has to flow through the converter to the dc bus. Hence, the dc/dc converter has to be sized for the peak power rating of the LV source. High-power choppers require bulky and heavy passive elements, and inductors usually determine the main share of their weight and volume [115]. To downsize the passive filters, a higher switching fre-

¹For sake of readability, the term *source* will be referred both to actual energy sources and to energy storage devices.

quency must be adopted. However, switching losses in silicon IGBTs and also high-voltage hybrid Silicon Carbide (SiC) modules restrict the switching frequency of high-power choppers between a few hundred Hz and some kHz [116–118]. On the other hand, reducing the peak power processed by the chopper power would unquestionably decrease the volume, weight, and power losses of the converter.

This chapter presents the topology and modulation of the NPC MSI. MSIs can connect two independent dc sources to the ac output in a single stage through a conventional NPC circuit. The MSI can be integrated into a semi-active traction architecture to replace the VSI, as schematically depicted in Figure 4.1(b). In such a configuration, the power processed by the dc/dc converter can be reduced thanks to the direct connection provided between the LV source and the traction loads. The reduction in the peak-power rating of the dc/dc converter is expected to yield savings in the weight and volume of the converter. For a proper integration of the MSI in a bimode traction system, a versatile PWM technique must be

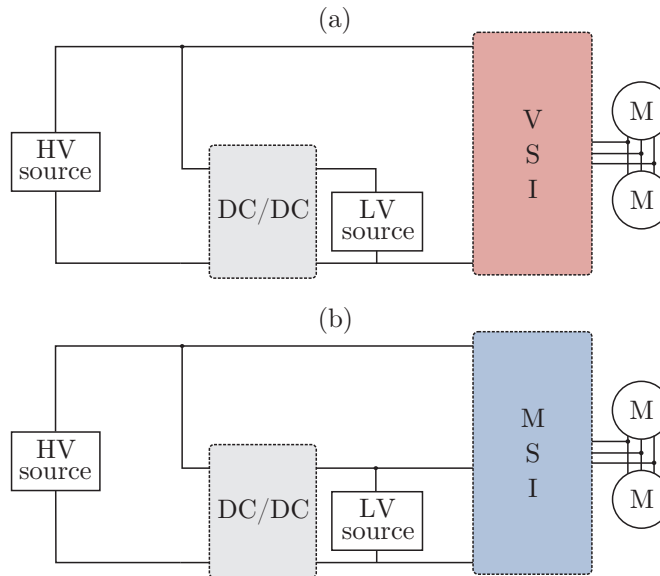


Figure 4.1. Conceptual diagrams of: (a) standard semi-active architecture employing a VSI; (b) alternative semi-active architecture employing an MSI.

envisioned to obtain the highest possible control on the dc input currents and ac output voltages on the entire operating range of the traction motors.

In the following sections, the fundamentals of the **MSI** are reviewed, and the state-of-literature modulation technique is analyzed. Finally, a novel **PWM** modulation is proposed that overcomes the limitations of the literature technique and significantly improves the performance of the converter.

4.2 Topology and switching configurations

The ideal converter topology together with the nomenclature adopted hereinafter for the circuit variables is shown in Figure 4.2(a). The **NPC** and **T-NPC** circuit implementations of the **MSI** are shown in Figure 4.2(b-c). In the **NPC** topology, every conduction path consists of two semiconductors in series (either two active switches or one switch and one clamping diode). In the **T-NPC** topology, the leg current can either flow through only one outer switch or through both inner switches. Naming the switching signals as shown in Figure 4.2 (where $k = 1, 2, 3$ refers to the generic converter phase and the four semiconductors are divided into two couples that are controlled in a complementary way, i.e., s_{T_k}/\bar{s}_{T_k} and s_{B_k}/\bar{s}_{B_k}) has the advantage that the same switching pattern can be used for both topologies. Each ac output node can be connected to one input dc terminal according to the general switching states of one **MSI** leg listed in Table 4.1. The state $\{1, 0\}$ is unfeasible in practice since it makes the output voltage dependent on the direction of the output current (for **NPC** implementations) or leads to a short circuit across the high-voltage source

Table 4.1. Switching states of an **MSI** leg

Output voltage v_k	Switching state	
	s_{T_k}	s_{B_k}
V_{HV}	1	1
undefined	1	0
V_{LV}	0	1
0	0	0

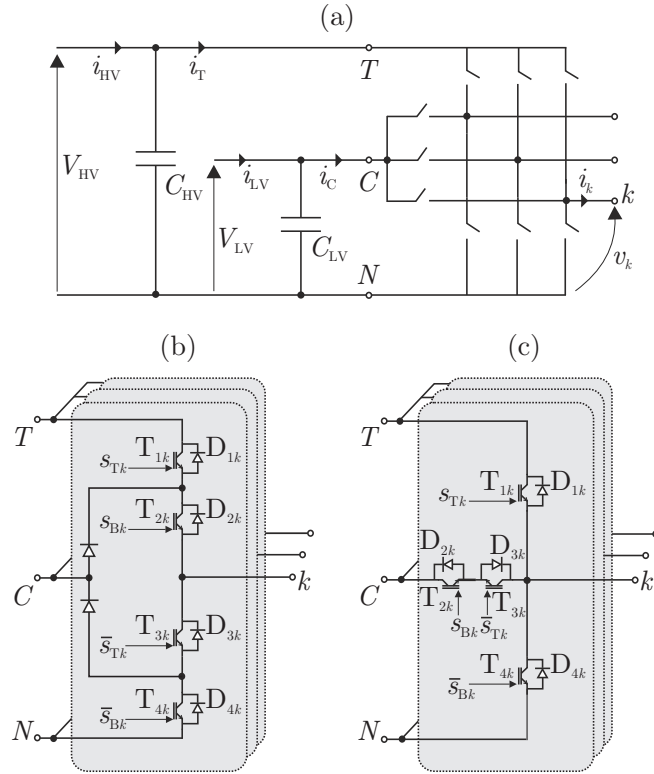


Figure 4.2. MSI converter: a) ideal circuit; b) NPC implementation; c) T-NPC implementation.

(for T-NPC implementations). Any other switching configuration (apart from all switches off) is either non-functional, potentially destructive, or destructive. The array of possible switching configurations is presented in Figure 4.3 for a positive or negative output current i_k in both circuit configurations.

For the NPC circuit, commutation paths can be either short or long. Long paths occur when two couples of switches are involved by the commutations (i.e., $D_5T_2 \rightarrow D_3D_4$). On the other hand, short paths affect only one active switch (i.e., $T_1T_2 \rightarrow D_5T_2$). The distinction also applies to the geometric length of the commutation loop because short commutation paths occur within one half of the leg, while in long commutation

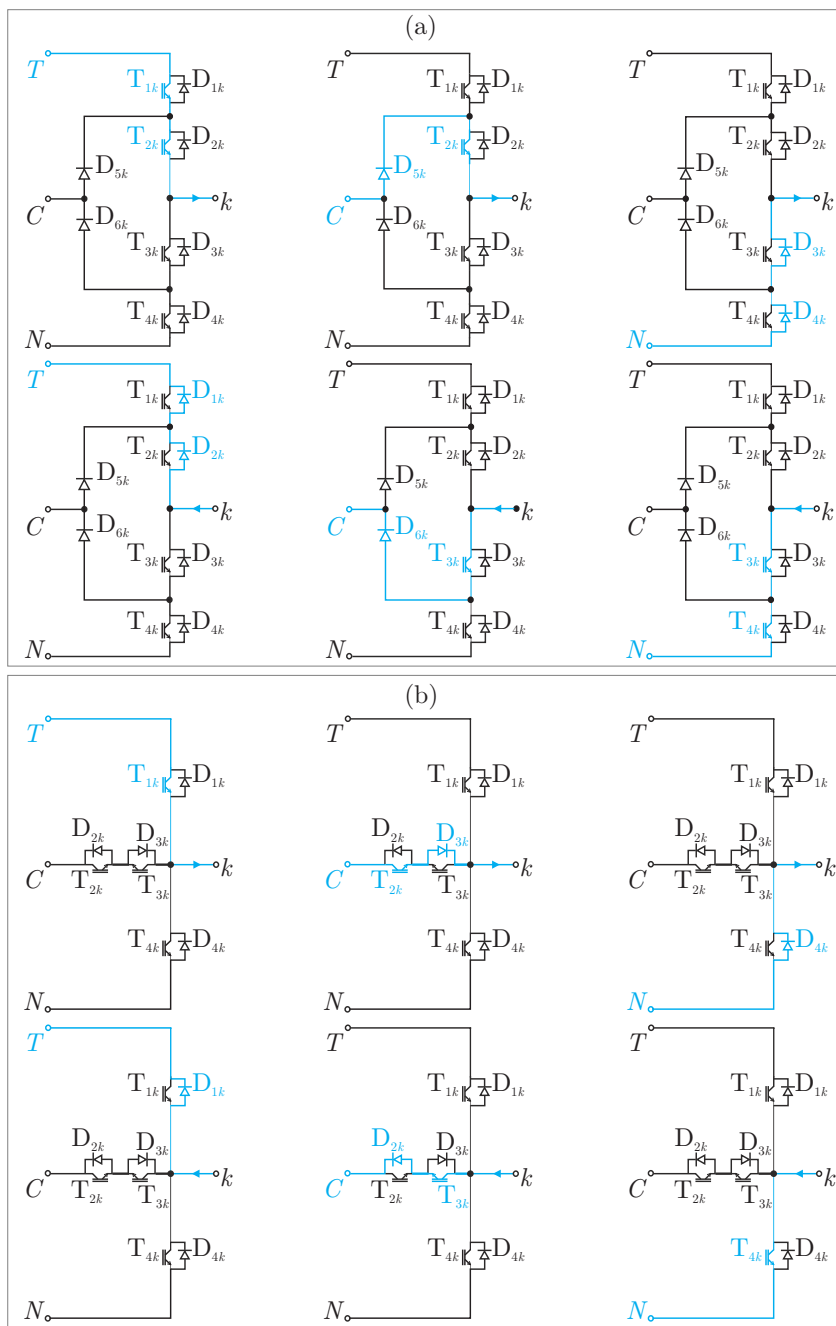


Figure 4.3. Switching configurations for the (a) NPC and (b) T-NPC circuits.

paths the current shifts from one half to the other. In the T-NPC circuit, all commutations share the same geometric length and involve one outer switch and both inner switches (i.e., $T_1 \rightarrow T_2D_3$).

Despite their circuit analogy, the MSI conceptually differs from standard NPC multilevel converters in that it is supplied by two independent dc sources. The HV and LV sources are connected across terminals $T - N$ and $C - N$, respectively, with the terminal N being the common ground. They are electrically independent and operate at different and unrelated voltage levels V_{HV} and V_{LV} (with $V_{HV} > V_{LV}$ to avoid short-circuiting of the dc inputs through the freewheeling or clamping diodes). Therefore, the MSI does not have a neutral point. Two distinct input capacitors C_{HV} and C_{LV} are connected in parallel to each source and close to the semiconductor devices, in order to provide some filtering of the input currents i_T and i_C and guarantee low-inductance switching loops.

Due to this fundamental functional difference, the control of MSIs differs from that of conventional 3L converters. In fact, the main concern about three-level NPC converters is to keep the neutral point at half of the dc-link voltage. This requires controlling the neutral-point current to an average value of zero, while at the same time avoiding possible low-frequency voltage oscillations [119]. On the other hand, the voltage across the input capacitors in the MSI topology is fixed by the input sources. The central current i_C must be controlled to inject or draw the desired amount of power in the LV source. In other words, the goal of any MSI modulation strategy is twofold: produce an ac voltage of variable frequency and magnitude, and control the currents of the input sources.

4.3 Interleaved two-level modulation

The state-of-literature modulation strategy operates the MSI as two interleaved two-level VSIs in parallel. A first equivalent VSI is obtained if the upper switches T_{1k} are off and switches T_{2k} , T_{3k} , and T_{4k} are properly fired. Based on Figures 4.2(b-c) and Table 4.1, T_{3k} is left always on (i.e., $s_{T_k} = 0$), and switching between T_{2k} and T_{4k} occurs by generating proper PWM signals s_{B_k} . It is clear that in this circuit configuration, here named Low-Voltage-Only (LVO) mode, the terminal T is always disconnected and the load is entirely supplied by the LV source. Similarly, a second

equivalent **VSI** is obtained by switching T_{1k} and T_{2k} simultaneously and opposed to T_{3k} and T_{4k} . In other terms, the two switching signals are equal (i.e., $s_{T_k} = s_{B_k}$), and the clamping diodes never conduct. In this configuration, here named High-Voltage-Only (**HVO**) mode, the terminal C is disconnected and the load is entirely supplied by the **HV** source. In either conduction mode, only one distinct switching signal per leg must be computed, like for standard two-level **VSIs**. This can be done by means of standard carrier-based **PWM** [110] or **SVM PWM** [113] techniques. In the following analysis, the **SVM** will be considered with no loss of generality, since it is equivalent to a carrier-based modulation with *min-max* third harmonic injection [120]. By alternating between the two circuit configurations, the **MSI** can interleave the two dc sources. The relative conduction time of either source determines its share of the total power drawn by the load. Therefore, a desired *power distribution* between the sources can be achieved with properly-timed interleaving. Figure 4.4 shows the switching waveforms of the interleaved **SVM**.

4.3.1 Analytical study

For the proper control of the interleaved operation, a fixed time window of length T_{cs} and a corresponding duty cycle d_{cs} are introduced. The interleaving duty cycle d_{cs} is defined as the relative conduction time of the **LV** source. In other words, the **MSI** operates in **LVO** and **HVO** mode for a duration equal to $d_{cs}T_{cs}$ and $(1 - d_{cs})T_{cs}$, respectively. The interleaved **SVM** results in a $\alpha\beta$ voltage plane where two hexagons (one for each mode and corresponding dc voltage level), 12 active vectors, and one zero vector can be identified. Figure 4.5(a) represents one sector of the plane. In each conduction mode, **SVM** is applied to the corresponding modulation area of the space vector diagram to generate the desired ac voltages. Let u_{cs} (subscript *cs* stands for *current-sharing*) be a square-wave control signal that codes the interleaving action:

$$u_{cs} = \begin{cases} 1 & \text{in LVO mode} \\ 0 & \text{in HVO mode} \end{cases} \quad (4.1)$$

Such signal can be easily obtained by comparing a carrier waveform of period T_{cs} with the duty cycle signal d_{cs} , as shown in Figure 4.5(b). Since

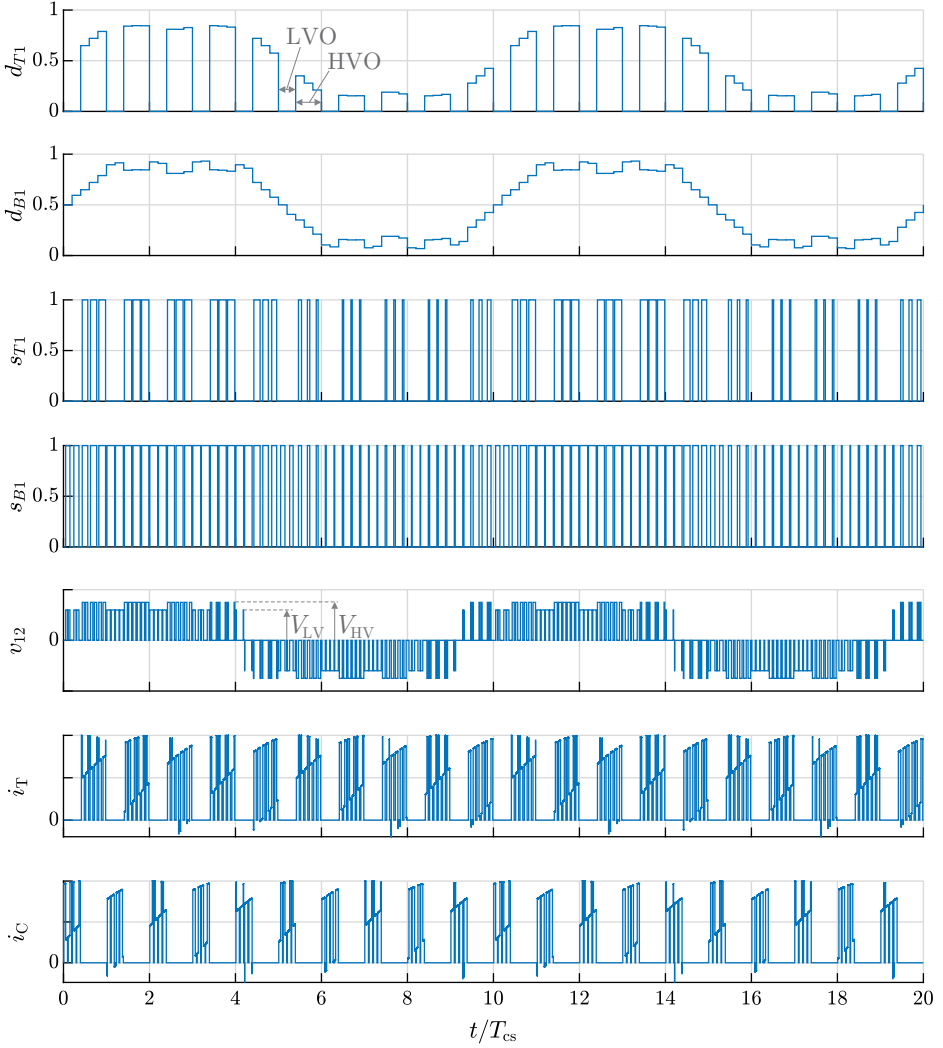


Figure 4.4. Switching waveforms for the interleaving modulation strategy.

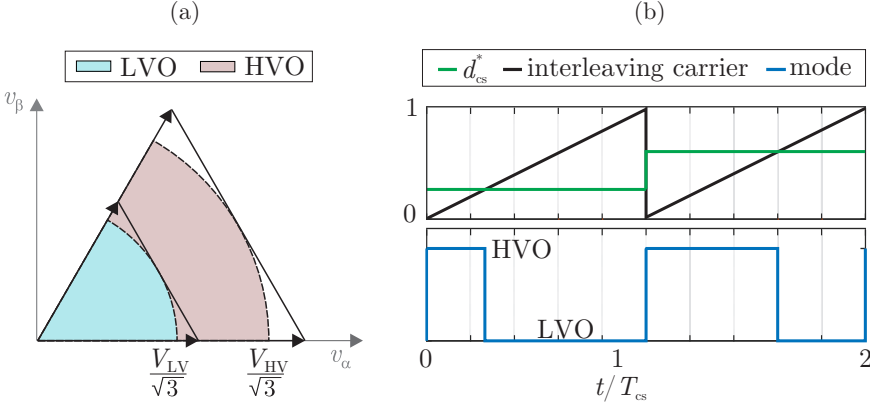


Figure 4.5. (a) One sector of the space-vector voltage plane of the interleaved SVM modulation. (b) Generation of the interleaving square-wave signal.

u_{cs} activates and deactivates the two MSI inputs on an instantaneous basis, the following power balance equations can be written:

$$V_{HV}i_T = (1 - u_{cs})p_{ac} \quad (4.2a)$$

$$V_{LV}i_C = u_{cs}p_{ac} \quad (4.2b)$$

where p_{ac} is the ac output power. Supposing that sinusoidal currents are drawn from the ac terminals of the converter, the output power can be expressed as:

$$p_{ac} = 3 V_{ph} I_{ph} \cos \varphi \quad (4.3)$$

where $\cos \varphi$ is the load power factor, V_{ph} is the RMS value of the fundamental motor phase voltages, and I_{ph} is the RMS value to the sinusoidal output currents. The phase voltage V_{ph} can be related to the dc voltages through two indexes m_{HV} and m_{LV} defined as:

$$\sqrt{2}V_{ph} = \begin{cases} m_{HV} \frac{V_{HV}}{2} & \text{in HVO mode} \\ m_{LV} \frac{V_{LV}}{2} & \text{in LVO mode} \end{cases} \quad (4.4)$$

Rearranging (4.2a)-(4.4) to make the modulation indexes explicit yields:

$$i_T = \frac{3}{2\sqrt{2}} (1 - u_{cs}) m_{HV} I_{ph} \cos \varphi \quad (4.5a)$$

$$i_C = \frac{3}{2\sqrt{2}} u_{cs} m_{LV} I_{ph} \cos \varphi \quad (4.5b)$$

By averaging (4.5a)-(4.5b) over one interleaving period and assuming that all the ripple components of i_T and i_C flow in the dc capacitors, the source currents can be calculated as

$$i_{HV} = \frac{3}{2\sqrt{2}} (1 - d_{cs}) m_{HV} I_{ph} \cos \varphi \quad (4.6a)$$

$$i_{LV} = \frac{3}{2\sqrt{2}} d_{cs} m_{LV} I_{ph} \cos \varphi \quad (4.6b)$$

Equations (4.6a)-(4.6b) explicitly relate the currents supplied by the dc sources to the interleaving duty cycle and modulation indexes. The relation governing their ratio can be then derived:

$$\frac{i_{LV}}{i_{HV}} = \frac{m_{LV}}{m_{HV}} \frac{d_{cs}}{(1 - d_{cs})} \quad (4.7)$$

The current split between dc sources depends not only on d_{cs} , but also on the modulation indexes. The quantity d_{cs} represents a degree of freedom while the modulation indexes depend on the ac output voltage, which, in a traction drive, is roughly proportional to the motor speed in its constant-torque operating area. The average MSI output voltage over one interleaving period can be obtained from (4.1) and (4.4) as:

$$V_{ph} = m_{HV} \frac{V_{HV}}{2\sqrt{2}} (1 - d_{cs}) + m_{LV} \frac{V_{LV}}{2\sqrt{2}} d_{cs} \quad (4.8)$$

Ultimately, by multiplying both sides of (4.6a)-(4.6b) with V_{HV} and V_{LV} , respectively, and using (4.4), the average power balance between dc sources and ac load is derived

$$V_{HV} i_{HV} = (1 - d_{cs}) 3V_{ph} I_{ph} \cos \varphi \quad (4.9a)$$

$$V_{LV} i_{LV} = d_{cs} 3V_{ph} I_{ph} \cos \varphi \quad (4.9b)$$

Equation (4.9b) can be used to determine the instantaneous value of d_{cs} based on the load power and on the LV source target power.

The limit of linear modulation may be reached during LVO and HVO modes depending on the magnitude of ac voltage reference and on the dc voltage levels. By denoting with \mathbf{v}_s^* the space vector of the reference ac voltage and considering the $\alpha\beta$ voltage plane of the interleaved SVM, three conditions can occur:

- A) \mathbf{v}_s^* lays inside the inner circle of the hexagon associated to V_{LV} : the MSI is operated in linear modulation during both HVO and LVO, that is $m_{HV} < m_{LV} < 2/\sqrt{3}$;
- B) \mathbf{v}_s^* lays outside the inner circle associated to V_{LV} but within the larger circle associated to V_{HV} : the MSI is at the limit of linear modulation during LVO mode and in linear modulation during HVO mode, that is $m_{HV} < m_{LV} = 2/\sqrt{3}$;
- C) \mathbf{v}_s^* lays outside the larger circle associated to V_{HV} : the MSI always works at the limit of linear modulation, that is $m_{HV} = m_{LV} = 2/\sqrt{3}$.

Condition A allows a stable operation of the MSI drive and full control of the current split between dc sources. In fact, as both modulation indexes are below unity, their ratio can be related to the ratio of the dc input voltages through (4.4):

$$\left. \frac{m_{LV}}{m_{HV}} \right|_A = \frac{V_{HV}}{V_{LV}} \quad (4.10)$$

By substituting the above relation into (4.7), the following relation for the dc currents split is valid

$$\left. \frac{i_{LV}}{i_{HV}} \right|_A = \frac{V_{HV}}{V_{LV}} \frac{d_{cs}}{(1 - d_{cs})} \quad (4.11)$$

In condition B, the modulation index m_{LV} saturates to unity. During LVO mode, the MSI operates at the limit of linear modulation and the actual voltage output has a lower magnitude than its reference, which results in the ac currents starting to drift from their reference. Nevertheless, as the HVO conduction mode is entered, the full dc voltage enables the MSI to regain control of the currents. This means that the overall average

phase voltage:

$$V_{\text{ph}}|_{\text{B}} = m_{\text{HV}} \frac{V_{\text{HV}}}{2\sqrt{2}} (1 - d_{\text{cs}}) + \frac{V_{\text{LV}}}{\sqrt{6}} d_{\text{cs}} \quad (4.12)$$

is still sufficient for the traction loads to work properly and develop full torque. However, due to this dynamic, a high ripple at interleaving frequency f_{cs} is expected to appear in the ac currents. Furthermore, the load current split between sources is no more controllable by acting on the interleaving duty cycle. In fact, by specializing (4.7) to the case $m_{\text{LV}} = 1$, one derives:

$$\frac{i_{\text{LV}}}{i_{\text{HV}}}|_{\text{B}} = \frac{1}{m_{\text{HV}}} \frac{d_{\text{cs}}}{(1 - d_{\text{cs}})} \propto \frac{1}{\omega_{\text{r}}} \frac{d_{\text{cs}}}{(1 - d_{\text{cs}})} \quad (4.13)$$

where the last relation holds true since the magnitude of the motor phase voltage increases with the rotational speed ω_{r} , and so does the modulation index associated with the HV source. Therefore, for a fixed interleaving duty cycle, the current split between dc sources is no longer constant but is expected to decrease as the drive speed increases. By imposing $m_{\text{LV}} = 1$ in (4.6b), a relation for i_{LV} can be derived:

$$i_{\text{LV}}|_{\text{B}} = \sqrt{3/2} I_{\text{ph}} \cos \varphi d_{\text{cs}} \quad (4.14)$$

The above quantity is almost constant for a fixed duty cycle and a constant magnitude of the phase currents (e.g., in the constant-torque region of the traction motor). Hence, the current and power delivered by the LV source will saturate when the MSI operates in condition B.

Ultimately, condition C represents the most undesirable working condition for the converter. SVM is at the linear modulation limit during the whole interleaving time window, and the average phase voltage supplied to the load has an RMS value equal to

$$V_{\text{ph}}|_{\text{C}} = \frac{V_{\text{HV}}}{\sqrt{6}} (1 - d_{\text{cs}}) + \frac{V_{\text{LV}}}{\sqrt{6}} d_{\text{cs}} \quad (4.15)$$

This value may be insufficient to keep full the ac currents to their reference. In such cases, the output power decreases, and the system loses control.

4.3.2 Operating domain

Three main limitations affect the interleaved modulation technique. Firstly, interleaving the two sources determines that the power contribution of each source cannot be greater than the load demand or of the opposite sign. In other words, both sources can only supply or recover from zero to full load power when the motors are motoring or braking, respectively. In fact, as per its definition, $d_{cs} \in (0, 1)$ and, from (4.9a)-(4.9b) it is clear that $p_{HV} \in (0, p_{ac})$ and $p_{LV} \in (0, p_{ac})$. Any other operating mode that is feasible with a standard semi-active topology (e.g, one source draws power from the other source during motoring or at standstill) cannot be achieved.

Secondly, to keep full control of the power sharing through the interleaving duty cycle d_{cs} , both dc input voltages must be compatible with the maximum voltage required by the load, irrespective of their actual power output. However, as seen in Chapters 2 and 3, onboard storage devices and fuel cells are usually characterized by a rated voltage below the system dc-bus voltage, with the two sub-systems being interfaced by the dc/dc converter. For instance, supercapacitors exhibit a 50% voltage variation when discharged from 100% to 25% SOC and thus cannot guarantee this constraint over their whole charge/discharge cycle.

Thirdly, to avoid the generation of subharmonics in the dc currents, the ratio between the interleaving period T_{cs} and the SVM switching period T_{sw} must be an integer number N , i.e., $T_{cs} = NT_{sw}$. This determines an inherent quantization of the interleaving duty cycle equal to $T_{sw}/T_{cs} = 1/N$. As an example, Fig. 4.6 depicts the case in which $N = 5$ and the desired d_{cs} is set to 0.25 (which would correspond to the LV source supplying the 25% of load power). Due to the quantization of $1/N = 0.2$, the SVM actually operates in LVO mode for two-fifths of the interleaving time window, and a wrong duty 40% share of load power is actually drawn by the LV source. A smaller quantization and better control resolution are achieved with higher values of N , i.e., by enlarging T_{cs} . However, this results in a higher distortion of the input currents since the length of their null intervals increases (see Figure 4.4). Therefore, a too-long T_{cs} would result in excessive sizing of dc filter capacitors to obtain smooth source currents, and a trade-off exists.

The operating area of a generic MSI modulation technique can be

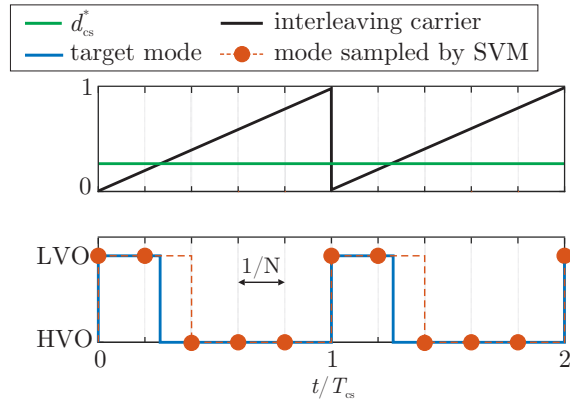


Figure 4.6. Quantization of the current-sharing control action.

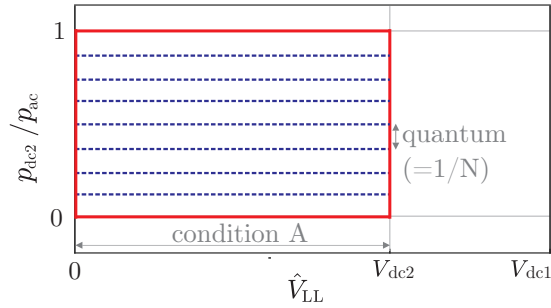


Figure 4.7. Operating area of the interleaved modulation technique.

defined as the locus of feasible operating conditions on a power-voltage plane. Each condition is identified by defined values of the power delivered by the LV source (normalized with respect to the ac output power) and of the ac output voltage. In light of its operating limits, the operating area of the interleaved modulation can be represented by Figure 4.7. In fact, the MSI can draw from the LV source only quantized power levels (represented by the horizontal dotted lines) that cannot exceed the load power (i.e., $p_{LV}/p_{ac} > 1$) or be of opposite sign (i.e., $p_{LV}/p_{ac} < 1$). Moreover, the peak magnitude of the fundamental line-to-line ac voltage \hat{V}_{LL} is bounded by V_{LV} for the MSI to be in operating condition A and preserve full control on the dc input currents through the interleaving duty cycle.

4.3.3 Experimental results

The analytical study of the interleaved SVM is validated with a series of experimental tests run on a small-scale rail traction drive simulator, detailed in Appendix A. The main system and control parameters used in this series of tests are reported in Table 4.2, while the power circuit and control schemes are depicted in Figure 4.8 (variables highlighted by gray circles are either measurements or reference signals). The MSI control algorithm comprises two sections: a standard Field-Oriented Control (FOC) scheme with orientation on the rotor flux and Proportional-Integral (PI) regulators, defining the $\alpha\beta$ reference voltages based on the motor speed reference; and the interleaved SVM algorithm which defines the duty cycle according to the motor power and the LV source reference power.

Speed ramp at constant duty cycle

A constant-torque acceleration is requested from the MSI drive. In order to observe all the MSI operating conditions, the maximum motor reference voltage is set higher than both dc input voltages. Indeed, a $285V_{\text{rms}}$ line-to-line voltage can be obtained from a dc supply of 400 V or more, while the rectifier output voltage is set to 350 V by acting on the input auto-transformer (not shown). During this test, the interleaving duty cycle is kept constant. Figure 4.9 shows the experimental waveforms

Table 4.2. Test bench parameters

Component	Item	Value
Diode bridge rectifier	Output voltage	350 V
Battery pack	Rated voltage	250 V
MSI	Switching period	200 μs
	Interleaving period	2 ms
Motor	Connection	Wye
	Maximum power	4.2 kW
	Base speed	1090 rpm
	Limit voltage	285 V_{rms}
	Maximum current	11.4 A_{rms}

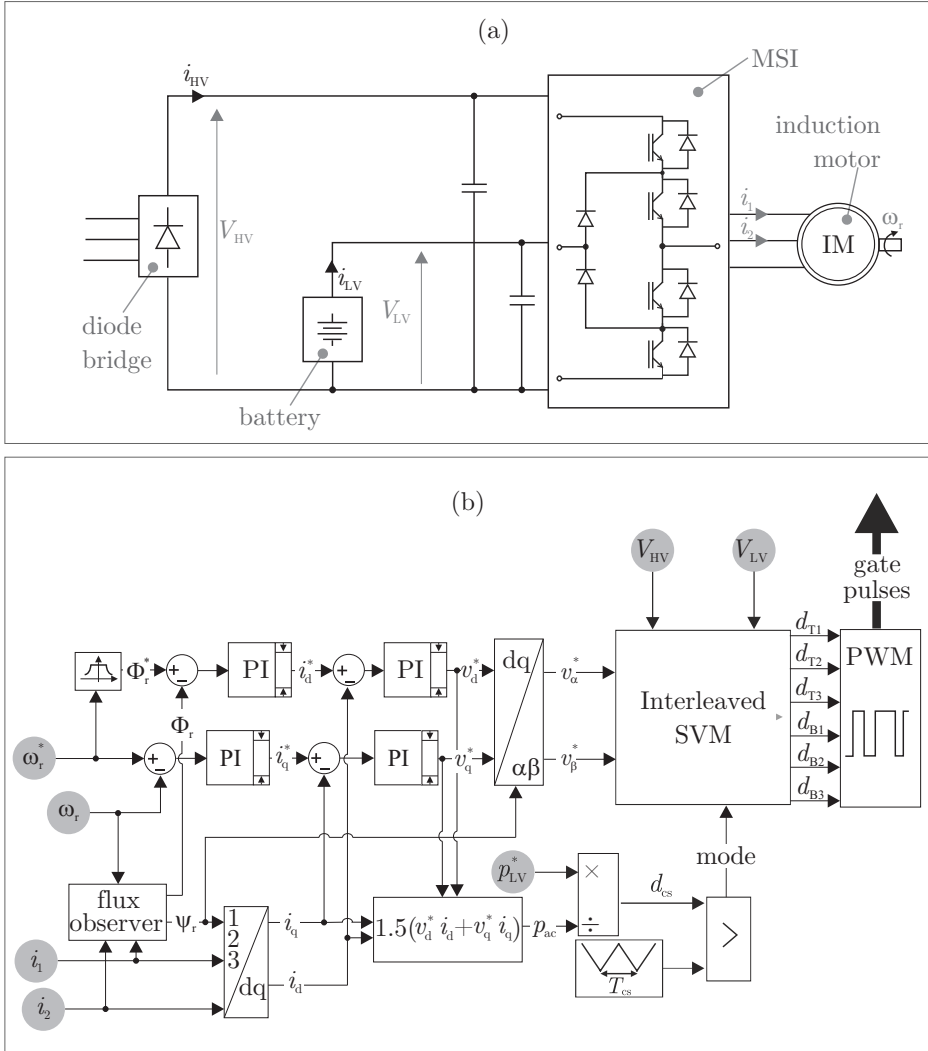


Figure 4.8. Setup for the experimental tests on the interleaved SVM modulation: (a) power circuit, (b) control diagram.

of motor speed and q-axis current, rectifier and battery power, and the ratio of dc currents.

In the early stages of the acceleration, the MSI is in condition A.

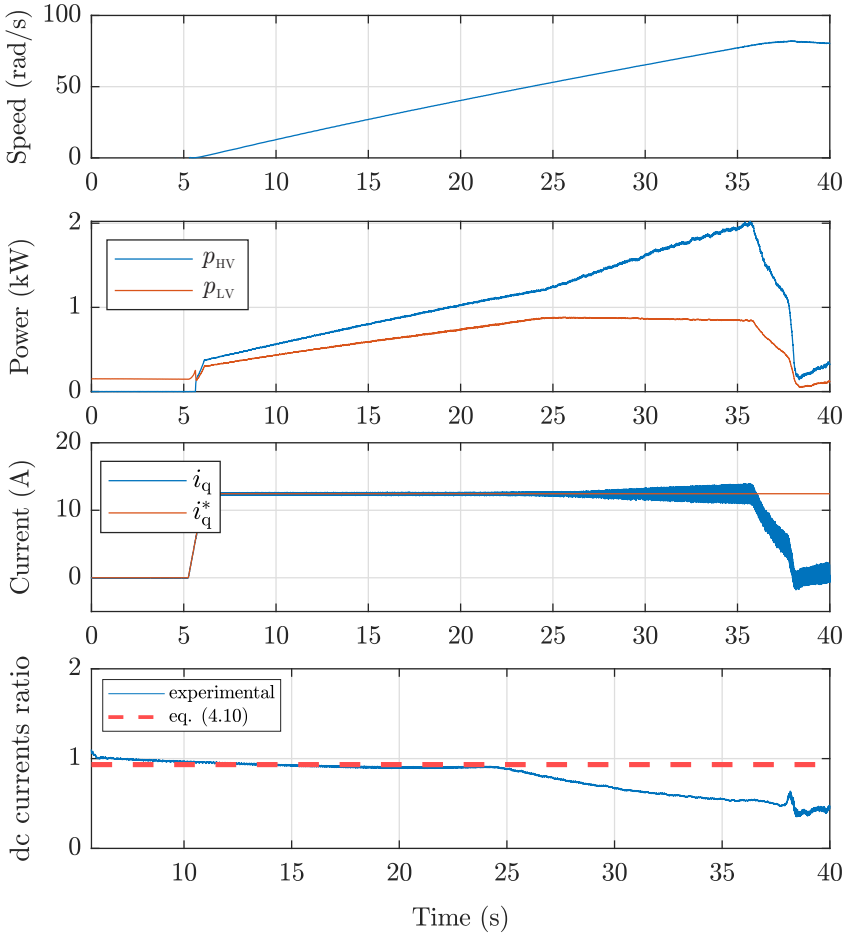


Figure 4.9. Results of the speed-ramp test at a constant duty cycle.

The q-axis current is stable at its reference, the power output of the two sources increases linearly, and the dc currents follow the ratio dictated by (4.11) with good approximation. When the MSI enters condition B, the q-axis current is still at its reference, but with a sensibly higher ripple at interleaving frequency f_{cs} . The battery power p_{LV} saturates to an almost constant value, and the slope of the rectifier power p_{HV} increases subsequently. Hence, no active control of the power split between sources

can be further achieved, and the dc currents ratio decreases with the motor speed, as prescribed by (4.13). In the last part of the acceleration, the motor reference voltage is too high and working condition C occurs. The converter loses control over the q-axis current, and the torque decreases to almost zero. The motor finds a working point of equilibrium at an unpredictable speed, and the corresponding power is supplied by the two sources with a non-controllable ratio.

The effect of the working condition on the motor currents can be better appreciated from the scope acquisition shown in Figure 4.10. In condition A, the current is almost sinusoidal with a small ripple at switching frequency and low-order harmonics due to inherent motor non-idealities. In condition B, a ripple at interleaving frequency appears in the current due to the voltage saturation occurring in every LVO conduction mode. In the low-frequency spectrum, sidebands centered around the interleaving frequency and its multiples become apparent.

Full driving cycle

As the interleaving control works best when the LV source is at a voltage level compatible with the motor, a driving cycle test is carried out in this condition to assess the performance of the MSI in what would be a real-case operating scenario. In order to keep the MSI always in condition A without replacing the battery with one of higher voltage, the winding connection of the motor is changed from wye to delta. The following EMS defines the battery power target during the cycle:

- Peak shaving during acceleration: the battery assists the rectifier and limits its power output to a value of 2 kW.
- Idle during cruising: when the total traction power falls below 2 kW, the battery is disconnected, and the rectifier alone supplies the motor.
- Full regeneration during braking: the battery recovers the entire amount of braking energy, and the rectifier is disconnected.

The control scheme for this test is similar to the one in Figure 4.8(b), with the duty cycle d_{cs} now computed online through (4.9b) according to the power reference of the battery set by the EMS controller.

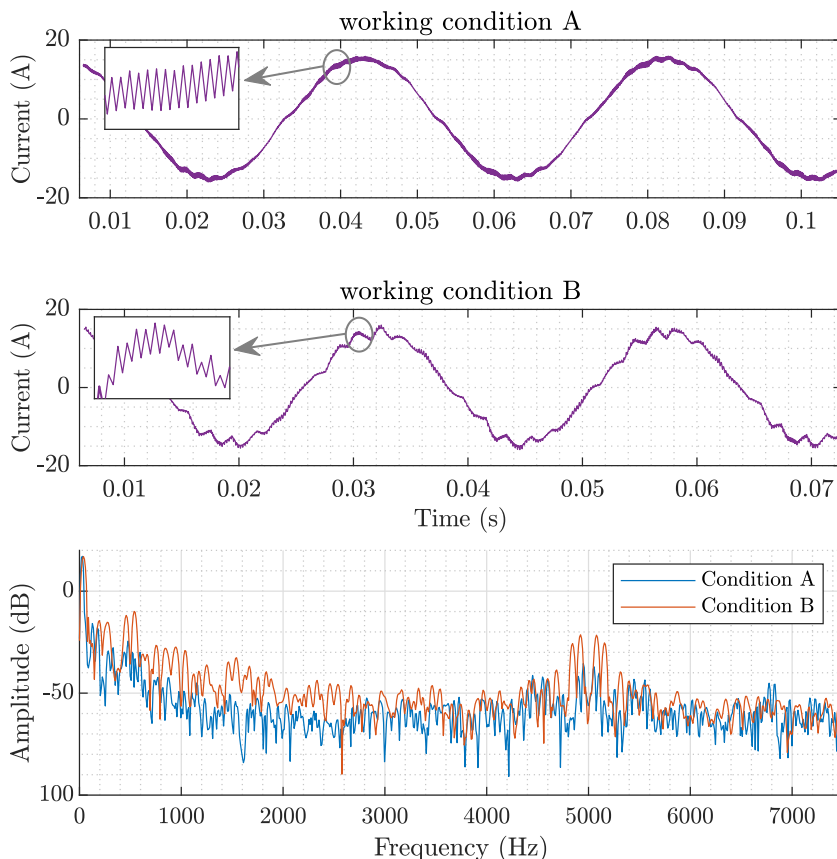


Figure 4.10. Motor current waveforms and frequency spectra for different MSI operating conditions.

The results of the test are presented in Fig. 4.11, where all the variables are sampled at interleaved SVM control frequency f_{cs} . As the motor power increases beyond 2 kW during the acceleration, the EMS controller increases the interleaving duty cycle to draw power from the battery. The peak-shaving action is properly carried out by the MSI during both the constant-torque and flux-weakening operation of the motor. It can be noticed that p_{LV} increases at steps rather than continuously, due to the quantization of the interleaving duty cycle. This determines the sawtooth-like shape of p_{HV} . When cruising begins, the battery power rapidly falls

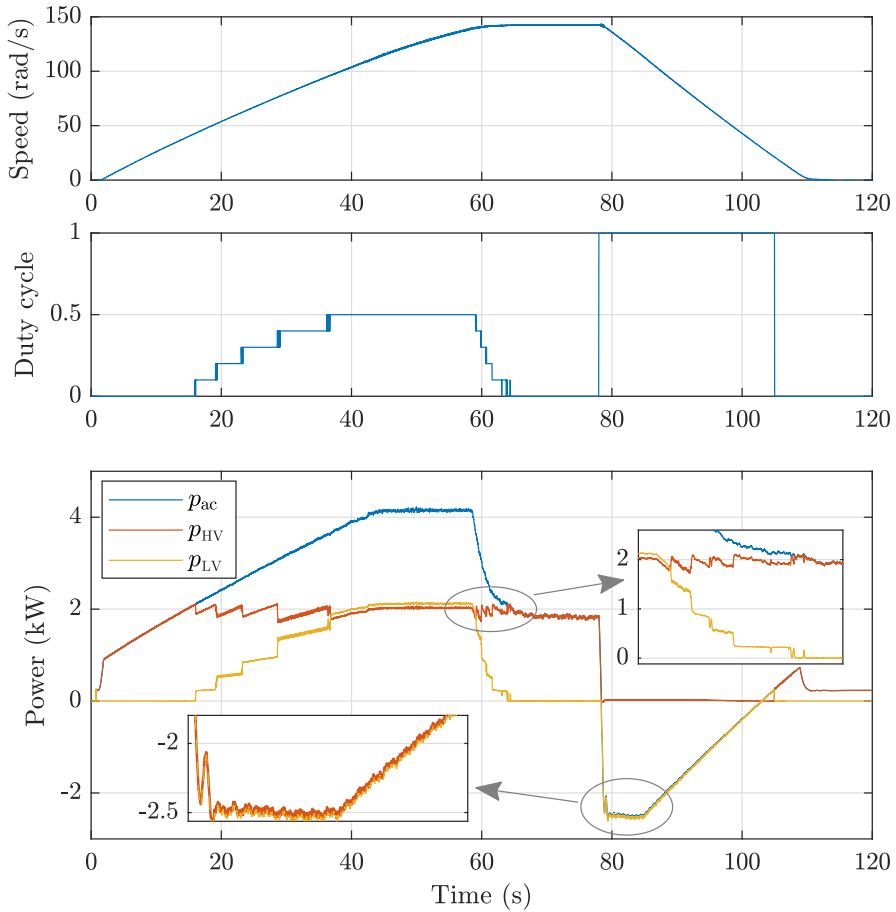


Figure 4.11. Results of the driving cycle test with the interleaved SVM.

toward zero with a similar step-by-step profile and the rectifier acts as the only source. It is worth noticing that, at this stage, battery recharging from the rectifier cannot be accomplished through the interleaved SVM. Ultimately, braking starts and the duty cycle increases to unity so that the rectifier is disconnected and the battery recovers all the braking power.

A scope acquisition of the currents drawn from the dc sources in a short time window of the peak-shaving phase is reported in Figure 4.12. As visible, the currents are almost triangular due to the low-pass filter-

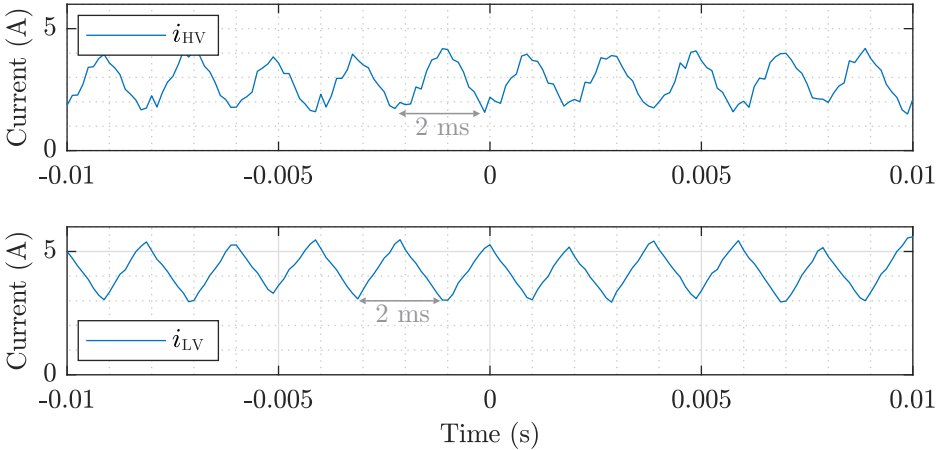


Figure 4.12. Currents supplied by the dc sources during the driving cycle test.

ing performed by the input capacitors on the highly discontinuous current drawn from the MSI (see also Figure 4.4). A visible ripple at interleaving frequency affects the dc currents and could be reduced either by choosing larger input capacitors or by increasing the interleaving frequency. However, this latter choice would result in a coarser resolution on the interleaving duty cycle.

4.4 The multi-objective vector modulation

The limits of the interleaved SVM are due to the fact the MSI is operated as two two-level inverters, irrespective of the actual NPC topology of the converter. The multi-objective vector modulation (MOV_M) overcomes all the drawbacks of the state-of-literature technique by integrating the twofold task of ac voltages and dc currents control in the pulse width modulation algorithm. This can be effectively achieved by exploiting the analytical model of the MSI converter written in a space-vector formalism.

In the following sections, the space-vector model of the MSI converter is derived and the fundamental steps of the MOV_M are explained. Then, a discussion on the resulting operating plane of the converter controlled through this novel technique is given, and further experimental results are

presented to assess the algorithm and compare it to the interleaved SVM.

4.4.1 MSI space-vector model

By considering the semiconductor devices as ideal switches, the following equations can be derived through direct inspection of Figures 4.1(b)-(c):

$$v_k = s_{Bk}V_{LV} + s_{Tk}(V_{HV} - V_{LV}) \quad (4.16a)$$

$$i_T = \sum_{k=1}^3 s_{Tk}i_k \quad (4.16b)$$

$$i_C = \sum_{k=1}^3 (s_{Bk} - s_{Tk})i_k \quad (4.16c)$$

A way to avoid the potentially destructive switching state $\{1, 0\}$ is to constraint the gate signals s_{Bk} and s_{Tk} according to

$$0 \leq s_{Tk} \leq s_{Bk} \leq 1, \quad k = 1, 2, 3 \quad (4.17)$$

By introducing the differential switching signal

$$s_{\Delta k} = s_{Bk} - s_{Tk} \quad (4.18)$$

and averaging (4.16a)-(4.16c) over a modulation period, the converter averaged model writes as

$$\langle v_k \rangle = d_{Bk}V_{HV} - d_{\Delta k}(V_{HV} - V_{LV}) \quad (4.19a)$$

$$i_{HV} = \sum_{k=1}^3 d_{Tk}\langle i_k \rangle \quad (4.19b)$$

$$i_{LV} = \sum_{k=1}^3 d_{\Delta k}\langle i_k \rangle \quad (4.19c)$$

where d_{Bk} and $d_{\Delta k}$ are the duty cycles corresponding to the switching signals s_{Bk} and $s_{\Delta k}$, and all the other variables inside angle brackets in (4.19a)-(4.19c) represent the average values of the corresponding variables in (4.16a)-(4.16c) over a modulation period. In (4.19a)-(4.19c), the hy-

pothesis is made that all the switching ripple in the input currents flows into the capacitors, as can be achieved by proper sizing of the input filters. By replacing (4.18) into (4.17) and averaging, the following constraint for the bottom and differential duty cycles is obtained:

$$0 \leq d_{\Delta k} \leq d_{Bk} \leq 1, \quad k = 1, 2, 3 \quad (4.20)$$

When the duty cycles are compared to a common triangular carrier, (4.20) automatically ensures (4.17).

It is useful to rewrite the averaged model of the converter by means of the space vector formalism. For ease of reading, the brackets will be dropped in the following, and all variables will refer to averaged quantities. By applying the stationary $\alpha\beta$ transform [121] to (4.19a), the ac output voltage vector \mathbf{v} can be expressed as

$$\mathbf{v} = v_\alpha + i v_\beta = \mathbf{d}_B V_{HV} - \mathbf{d}_\Delta \Delta V \quad (4.21)$$

where $\mathbf{d}_\Delta = d_{\Delta\alpha} + i d_{\Delta\beta}$ and $\mathbf{d}_B = d_{B\alpha} + i d_{B\beta}$ are the space vectors of the differential and bottom duty cycles, and $\Delta V = V_{HV} - V_{LV}$. Similarly, the top and central-point currents can be expressed as

$$i_{HV} = \frac{3}{2} \Re \left\{ \mathbf{d}_B \cdot \check{\mathbf{i}} \right\} \quad (4.22a)$$

$$i_{LV} = \frac{3}{2} \Re \left\{ \mathbf{d}_\Delta \cdot \check{\mathbf{i}} \right\} \quad (4.22b)$$

with $\check{\mathbf{i}}$ being the complex conjugate of the ac currents space vector. Equations (4.21)-(4.22b) represent the space-vector averaged model of the MSI converter.

4.4.2 Computation of the duty cycle signals

The differential duty cycles $d_{\Delta k}$ represent the fraction of the switching period during which the k -th leg is connected to the central point. Hence, as per (4.22b), they directly affect the magnitude of the average central-point current. On the other hand, based on (4.21), the averaged output voltages can be obtained from several combinations of \mathbf{d}_B and \mathbf{d}_Δ . Therefore, in a framework of multi-step modulation of the NPC converter (i.e.,

with two modulating signals per leg and a common carrier [122, 123]), the quantity \mathbf{d}_Δ can be exploited as a degree of freedom to control the current drawn from the LV source. Indeed, the aim of MOVIM is to derive the two modulating signals per phase d_{Bk} and d_{Tk} based on the ac voltage vector reference \mathbf{v}^* and central point current reference i_{LV}^* . The duty cycles are then compared to a common carrier waveform at switching frequency to generate the proper PWM gate pulses. To this aim, (4.21)-(4.22b) can be arranged into the equation system

$$\begin{cases} d_{B\alpha}V_{HV} - d_{\Delta\alpha}\Delta V = v_\alpha^* \\ d_{B\beta}V_{HV} - d_{\Delta\beta}\Delta V = v_\beta^* \\ \frac{3}{2}(d_{\Delta\alpha}i_\alpha + d_{\Delta\beta}i_\beta) = i_{LV}^* \end{cases} \quad (4.23)$$

where the $\alpha\beta$ components of the ac voltage and dc current references are the inputs, and the $\alpha\beta$ components of \mathbf{d}_B and \mathbf{d}_Δ are the unknowns. System (4.23) has three linear equations in four scalar unknowns and is thus under-determined. Therefore a degree of freedom exists, and an additional constraint must be formulated. A convenient constraint that simplifies the solution of the equation system is the following:

$$\frac{\mathbf{d}_\Delta}{|\mathbf{d}_\Delta|} = \frac{\mathbf{v}^*}{|\mathbf{v}^*|} \quad (4.24)$$

This constraint allows to express the reference current i_{LV}^* as directly proportional to the ac power p_{ac} through the vector of differential duty cycles \mathbf{d}_Δ :

$$i_{LV}^* = \frac{3}{2} \frac{|\mathbf{d}_\Delta|}{|\mathbf{v}^*|} (v_\alpha^* i_\alpha + v_\beta^* i_\beta) = \frac{\mathbf{d}_\Delta}{\mathbf{v}^*} p_{ac} \quad (4.25)$$

By arranging together (4.23) and (4.25), a simple and well-posed algebraic system is obtained. Its solution in the $\alpha\beta$ components of the duty cycles is:

$$\begin{cases} d_{\Delta\alpha} = \frac{i_{LV}^*}{p_{ac}} v_{\alpha}^* \\ d_{\Delta\beta} = \frac{i_{LV}^*}{p_{ac}} v_{\beta}^* \\ d_{B\alpha} = \frac{1}{V_{HV}} (v_{\alpha}^* + \Delta V \frac{i_{LV}^*}{p_{ac}} v_{\alpha}^*) \\ d_{B\beta} = \frac{1}{V_{HV}} (v_{\beta}^* + \Delta V \frac{i_{LV}^*}{p_{ac}} v_{\beta}^*) \end{cases} \quad (4.26)$$

The above equations constitute the core computation of the **MOV** routine and are graphically represented by the space vector diagram of Figure 4.13. Once the bottom and differential duty cycle vectors are obtained, the corresponding three-phase variables can be derived through the inverse $\alpha\beta \rightarrow 123$ transform:

$$\begin{bmatrix} \tilde{d}_{\Delta 1} & \tilde{d}_{\Delta 2} & \tilde{d}_{\Delta 3} \end{bmatrix}^T = [T_{\alpha\beta \rightarrow 123}] \begin{bmatrix} d_{\Delta\alpha} & d_{\Delta\beta} \end{bmatrix}^T \quad (4.27a)$$

$$\begin{bmatrix} \tilde{d}_{B1} & \tilde{d}_{B2} & \tilde{d}_{B3} \end{bmatrix}^T = [T_{\alpha\beta \rightarrow 123}] \begin{bmatrix} d_{B\alpha} & d_{B\beta} \end{bmatrix}^T \quad (4.27b)$$

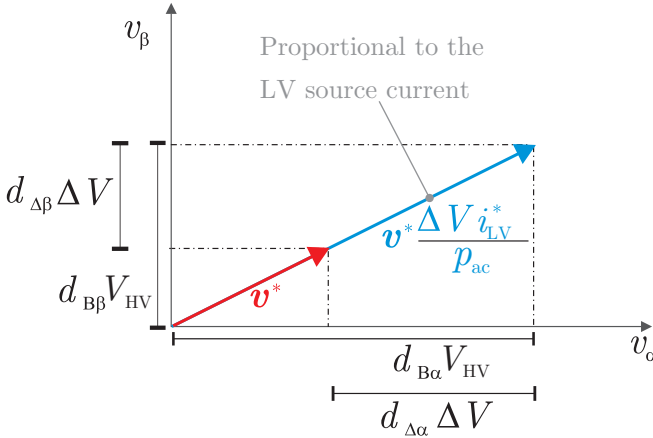


Figure 4.13. MOV space vector diagram.

where the transformation matrix is:

$$[T_{\alpha\beta\rightarrow 123}] = \begin{bmatrix} 1 & 0 \\ -1/2 & \sqrt{3}/2 \\ -1/2 & -\sqrt{3}/2 \end{bmatrix} \quad (4.28)$$

As known from the theory of $\alpha\beta$ transform [121], each of the three-phase sets sums up to zero, that is:

$$\sum_{k=1}^3 \tilde{d}_{Bk} = 0 \quad (4.29a)$$

$$\sum_{k=1}^3 \tilde{d}_{\Delta k} = 0 \quad (4.29b)$$

Therefore, at least one negative bottom duty cycle and differential duty cycle exist. Hence, the phase duty cycles obtained through (4.27a)-(4.27b) do not comply with the leftmost inequality in (4.20). Similarly, the rightmost inequality in (4.20) is not directly guaranteed by the inverse transform. For this reason, the duty cycles \tilde{d}_{Bk} and $\tilde{d}_{\Delta k}$ cannot be straightly employed to generate safe switching configurations of the MSI. The correct sets of bottom and differential duty cycles that comply with (4.20) are obtained by adding to the following zero-sequence terms:

$$d_{\Delta k} = \tilde{d}_{\Delta k} + z_{\Delta}, \quad k = 1, 2, 3 \quad (4.30a)$$

$$d_{Bk} = \tilde{d}_{Bk} + z_B, \quad k = 1, 2, 3 \quad (4.30b)$$

where

$$z_{\Delta} = -\min\{\tilde{d}_{\Delta 1}, \tilde{d}_{\Delta 2}, \tilde{d}_{\Delta 3}\} \quad (4.31a)$$

$$z_B = -\min\{\tilde{d}_{B1} - d_{\Delta 1}, \tilde{d}_{B2} - d_{\Delta 2}, \tilde{d}_{B3} - d_{\Delta 3}\} \quad (4.31b)$$

In fact, (4.30a) shifts the three differential duty cycles $d_{\Delta k}$ above the zero, ensuring the leftmost inequality in (4.20) and a safe operation of the converter. On the other hand, (4.30b) shifts each bottom duty cycle d_{Bk} above the differential duty cycle $d_{\Delta k}$ of the same phase, ensuring the middle inequality in (4.20). Ultimately, the proper duty cycles d_{Tk} for the

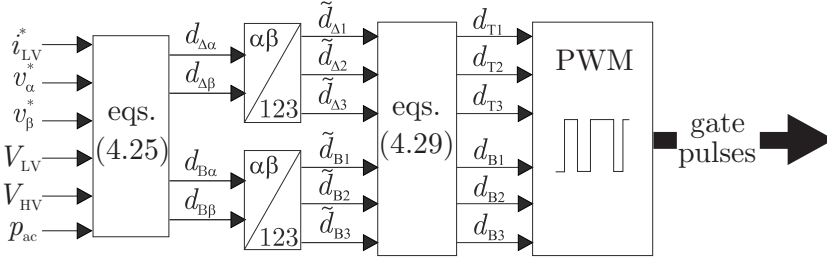


Figure 4.14. Block diagram of the multi-objective vector modulation.

top components can be obtained from (4.18). The overall processing from the input reference signals to the leg duty cycles can be summarized by the block diagram in Figure 4.14.

4.4.3 Operating domain

The rightmost inequality in (4.20) defines the boundary of linear modulation, whose limit occurs when the peak value of the bottom duty cycles d_{Bk} reaches the unit value. For standard PWM techniques of two-level inverters with zero-sequence signal injection, the linear modulation limit is reached when the fundamental line-to-line output voltage has a peak value \hat{V}_{LL} equal to V_{dc} [120]. For the MOVMM, the magnitudes of duty cycles depend simultaneously on the output voltage, output power, and low-voltage source current (see (4.26)), and the limit of linear modulation may be reached depending on the joint values of these quantities. In fact, the maximum differential duty cycle of each NPC leg depends on the dc input voltages as well as on the leg reference voltage [124]. Therefore, the maximum absolute value of current that can be imposed at the central point of the MSI will also depend on the system voltages. Specifically, the linear modulation limits can be formulated through the following constraint on the LV source power p_{LV} :

$$LT(\hat{V}_{LL}, V_{HV})p_{ac} \leq p_{LV} \leq UT(\hat{V}_{LL}, V_{HV}, V_{LV})p_{ac} \quad (4.32)$$

where the *per-unit* lower and upper power thresholds LT and UT have been introduced. As mentioned, these thresholds depend on the fundamental line-to-line peak output voltage and dc input voltages through the

relations

$$\text{LT} = \begin{cases} -\frac{V_{\text{LV}}}{\hat{V}_{\text{LL}}}, & \text{for } \hat{V}_{\text{LL}} \leq \Delta V \\ \frac{\hat{V}_{\text{LL}} - V_{\text{HV}}}{\hat{V}_{\text{LL}}}, & \text{for } \hat{V}_{\text{LL}} \geq \Delta V \end{cases} \quad (4.33a)$$

$$\text{UT} = \begin{cases} \frac{V_{\text{LV}}}{\hat{V}_{\text{LL}}}, & \text{for } \hat{V}_{\text{LL}} \leq V_{\text{LV}} \\ \frac{V_{\text{HV}} - \hat{V}_{\text{LL}}}{\hat{V}_{\text{LL}}} \cdot \frac{V_{\text{LV}}}{\Delta V}, & \text{for } \hat{V}_{\text{LL}} \geq V_{\text{LV}} \end{cases} \quad (4.33b)$$

It is worth noticing that the above thresholds do not depend on the output power, i.e., the *per-unit* MOV_M power limits are a sole function of the dc and ac voltage levels. For a positive output power, UT and LT determine the positive (i.e., discharge) and negative (i.e., recharge) power limit of the LV source, respectively. The opposite holds for a negative load power, i.e., when the ac motors operate as generators during braking.

Figure 4.15(a) shows the peak value of the bottom duty cycles d_{Bk} versus the line-to-line ac voltage and *per-unit* power of the LV source, while Figure 4.15(b) shows the corresponding 2-D linear contour, defining the MOV_M operating domain where three different regions can be identified. Together with the direction of load power flow, they result in the six feasible operating modes listed in Table 4.3. The MOV_M enables the MSI to control dc and ac power flows in every direction and allows for: load power sharing between sources (region A) and controlled charging of one source from another (regions B and C). Note that the stationary recharge of one source from the other is achievable if at standstill the motor is fluxed by dc currents and thus absorbs a small but non-null amount of power. Naturally, some of the modes may be unfeasible in a specific application due to the presence of unidirectional dc sources, but not due to the intrinsic limitations of this modulation technique. It can be noted that the upper threshold curve crosses the unity for $\hat{V}_{\text{LL}} = V_{\text{LV}}$, meaning that the LV source cannot process the entire load power when its voltage is lower than the line-to-line output voltage. If this source must potentially supply or recover the entire ac power (e.g. during braking, if V_{HV} is unidirectional), its voltage must be equal to the maximum load voltage. This also applies

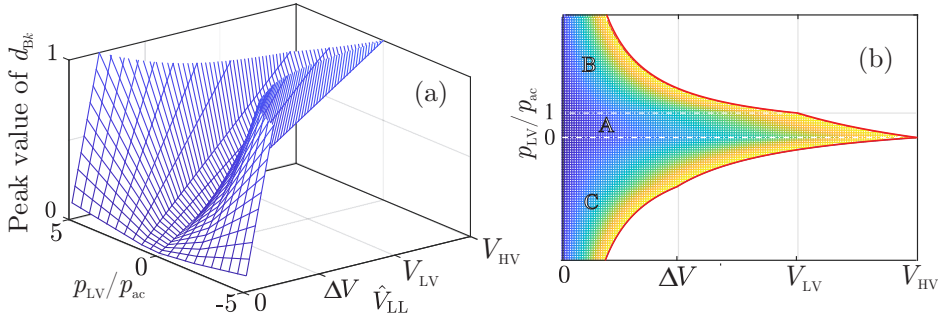


Figure 4.15. Modulation limits and operating domain of the MOVIM technique.

to the interleaving SVM strategy, but a fundamental difference exists. As seen above, in the case of interleaved SVM the peak value of \hat{V}_{LL} is bounded by V_{LV} to keep the MSI in full control of the input currents, irrespective of the actual share of load power supplied by the LV source. With the MOVIM, this limit is overcome: the ac output voltage level can be extended beyond that of the LV source without either compromising the control performance of the MSI drive or zeroing the power that can be processed by the LV source. Overall, from a comparison with Figure 4.7, it is evident how the MOVIM expands the operating area of the MSI in both voltage and power directions, also removing the quantization effect observed for the interleaved SVM.

Simulated switching waveforms for the same load voltage and current (corresponding to a positive load power) in the three different MOVIM regions are reported in Figures 4.16-4.18. In every condition, the constraint $d_{Bk} > d_{Tk}$ is always satisfied, proving the correctness of the zero-sequence components in (4.31b)-(4.30b). The MOVIM results in down-shifted modulating signals for the top switches [125], with each phase signal clamped at zero for one-third of the fundamental period T . On the other hand, the shape of the bottom-switch modulating signals varies with the operating condition. Specifically, when both sources supply the load (modulation region A), d_{Bk} and d_{Tk} have the same down-shifter shape and their amplitude discrepancy is directly proportional to the share of load power supplied by V_{LV} . In the two extreme cases of p_{LV} being either zero or equal to the full load power, either the duty cycles overlap (i.e., $d_{\Delta k} = 0$)

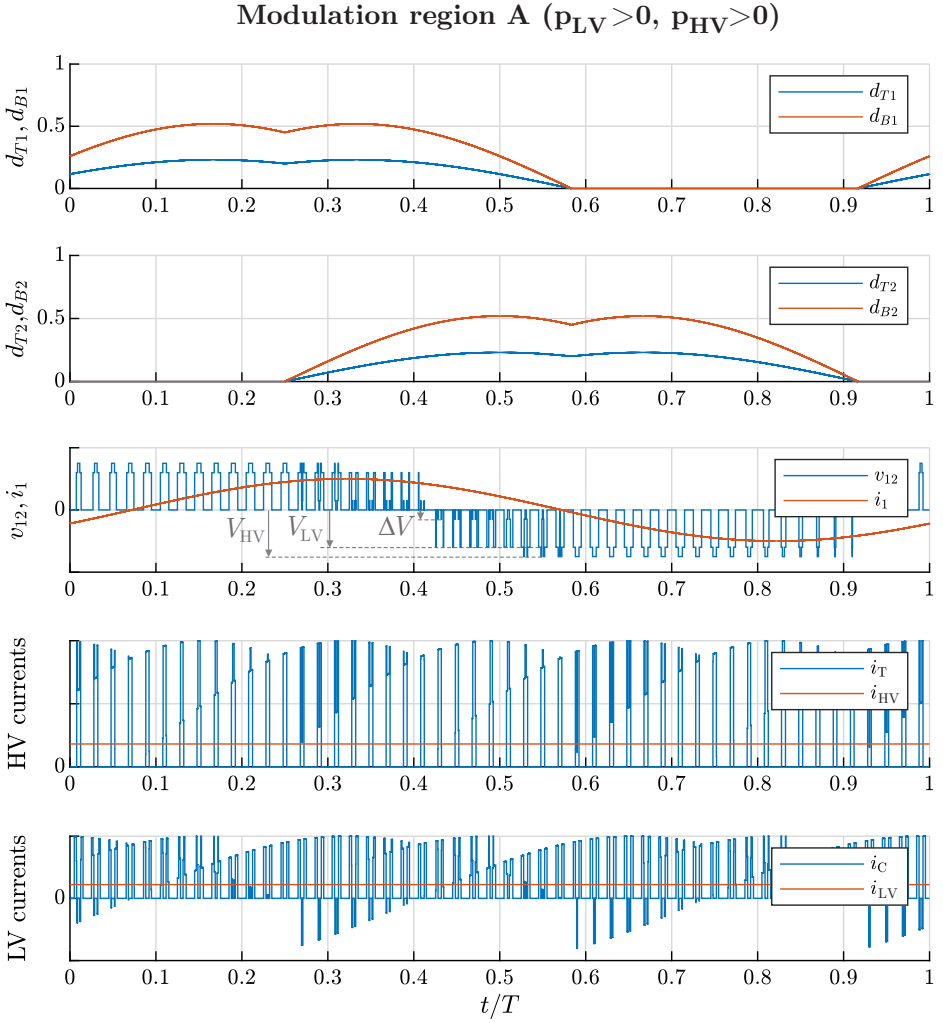


Figure 4.16. Switching waveforms of the MOVIM in modulation region A.

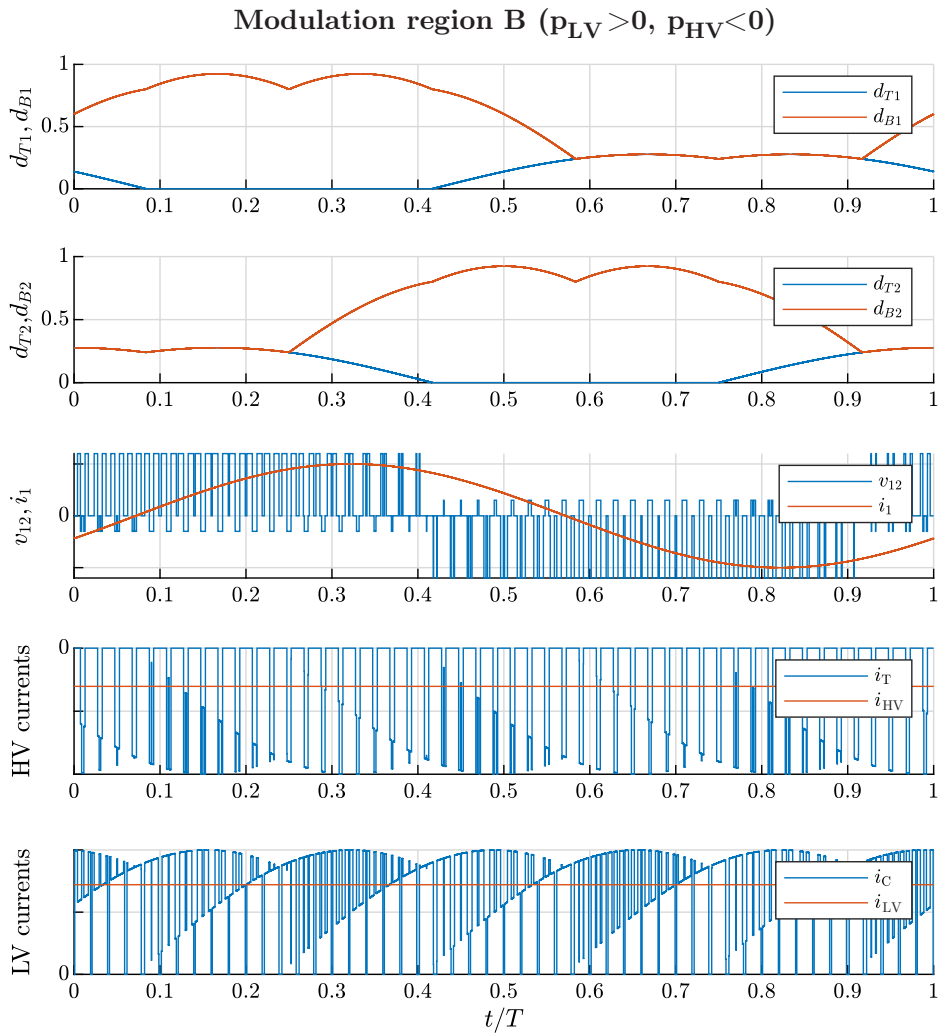


Figure 4.17. Switching waveforms of the MOV_M in modulation region B.

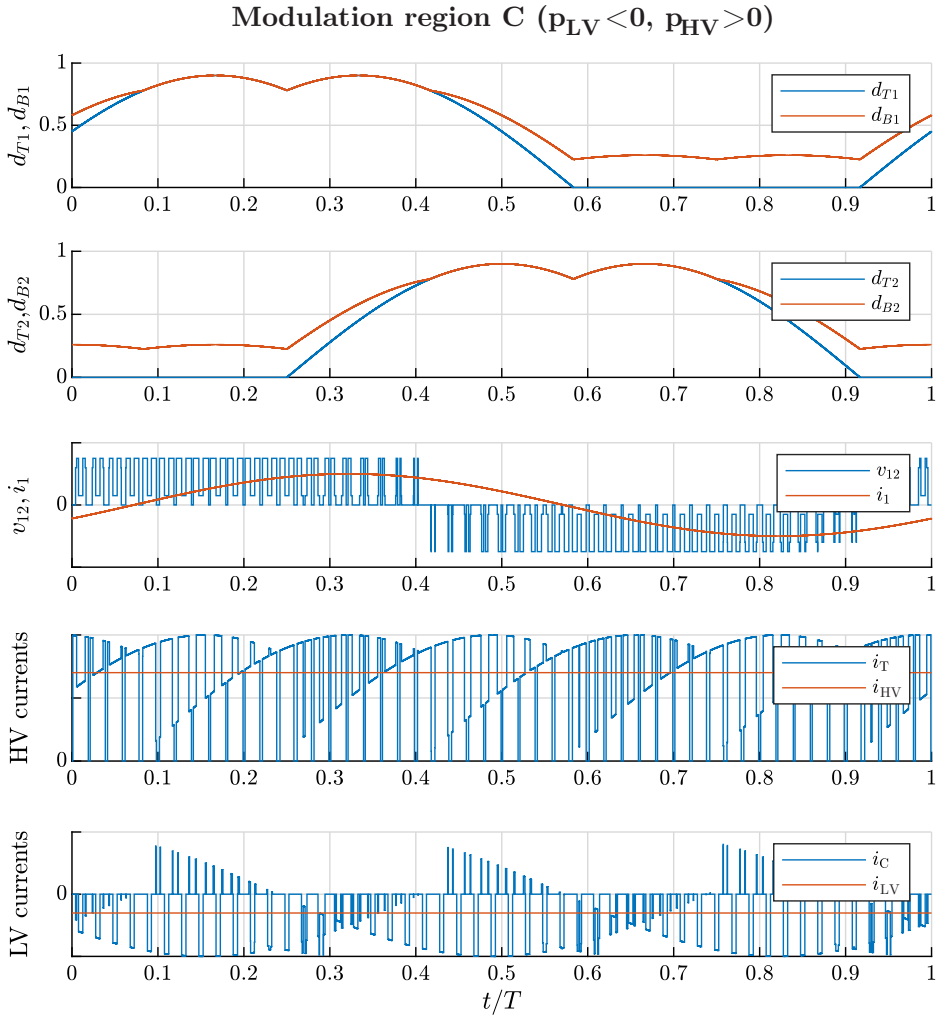


Figure 4.18. Switching waveforms of the MOV in modulation region C.

Table 4.3. MSI operating modes enabled by the MOVMM

Modulation region	Load operation	
	$p_{ac} \geq 0$	$p_{ac} < 0$
A	One or both sources supply the load with a controllable share	One or both sources recover the load power with a controllable share
B	V_{LV} supplies the load and charges V_{HV} with a controllable current	V_{LV} recovers all the load power and is also recharged by V_{HV} with a controllable current
C	V_{HV} supplies the load and charges V_{LV} with a controllable current	V_{HV} recovers all the load power and is also recharged by V_{LV} with a controllable current

or the top duty cycle is zero. When V_{HV} supplies the load and charges V_{LV} or vice-versa (regions B and C), the shapes of d_{Bk} differ from the previous conditions so that the desired positive or negative average current is imposed in the central terminal. In all conditions, the line-to-line voltage oscillates among multiple levels within a single switching period, consistently with the fact that the MOVMM is a multi-step technique.

4.4.4 Experimental results

The MOVMM is validated and compared to the interleaved SVM through experiments on the small-scale railway drive. The bench layout is the same used to test the interleaved SVM as depicted in Figure 4.8(a), with the rectifier as the HV source and the battery pack as the LV source. The deployed control diagram is shown in Figure 4.19. The $\alpha\beta$ voltages output by the FOC scheme are combined with the LV source current reference and processed by the MOVMM to generate the MSI gate pulses.

Steady-state operation

A first group of five tests is performed to evaluate the modulation technique in a steady-state condition. In the first four tests, the motor

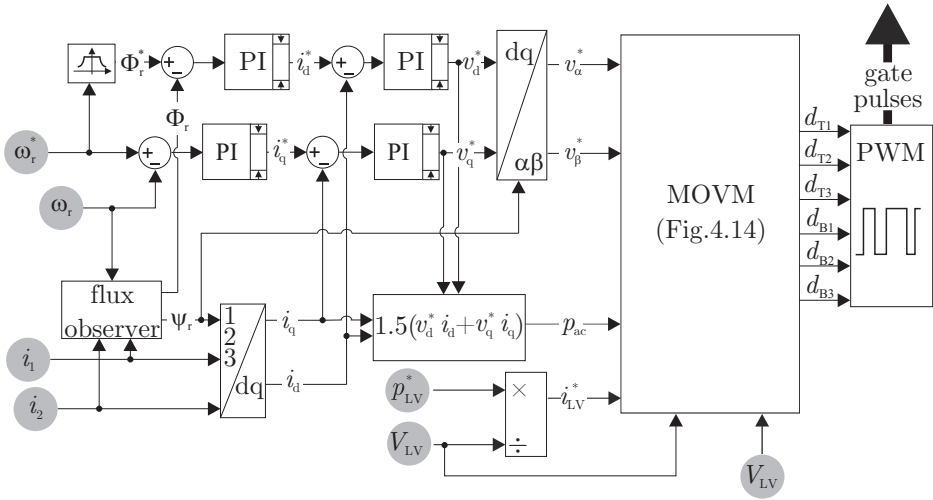


Figure 4.19. Control scheme for the experimental tests on the MOVIM.

is supplied with its rated currents at a constant frequency, and different levels and directions of power exchanged between the rectifier and the battery are imposed. In the last test, the motor is fluxed at zero speed and the recharge of the battery from the rectifier is requested. Two of the three motor currents and the two dc source currents for all five test conditions are shown on the next page.

In particular, Figures 4.20(a)-(b) show the MSI currents when the traction power is supplied only by the rectifier or by the battery, respectively. In both cases, the current of the inactive source is properly controlled to zero by the modulation algorithm. In Figure 4.20(c), both sources supply power to the motor and thus deliver a positive dc current. The in-motion recharge of the battery from the rectifier is shown in Figure 4.20(d). During the recharge, a negative current is injected into the battery pack, while the motor is still supplied with sinusoidal currents. In this condition, the rectifier provides charging power to the battery and traction power to the motor. From the waveforms obtained for these four tests with the motor in motoring operation, it can be noticed that any variation in the power processed by the dc sources does not impact the load operation. In fact, the ac currents magnitude and harmonic content

are not quantitatively affected by the different operating conditions of the sources. Low-frequency distortion in the motor currents can be associated with inherent motor nonlinearities and imbalances, while high-frequency ripple is due to switching operation.

Ultimately, the stationary recharge of the battery from the rectifier is shown in Figure 4.20(e). In this condition, the motor is fluxed with dc currents, and a negative current is injected into the battery. The rectifier provides charging power to the battery and also makes up for the small amount of Joule losses in the stator windings. Hence, a power transfer from one source to the other is also possible at zero speed if the motor is supplied with its rated magnetizing currents and absorbs a small but nonzero power.

In Figure 4.21, the dc currents drawn by the MSI when both sources supply the load are compared with those obtained for the same condition with the interleaved SVM. The Total Harmonic Distortion (THD) is here calculated as:

$$\text{THD} = \sqrt{\frac{i_{\text{RMS}}^2}{i_{\text{AVG}}^2} - 1} \quad (4.34)$$

where i_{AVG} and i_{RMS} are the mean and RMS value of the considered dc current over the acquisition window. The MOVm can reduce the harmonic distortion by a factor of three to five, due to the fact that the control of dc currents is integrated at the level of duty cycle generation. Hence, the control action is performed within a switching period and does not require any additional interleaving period of a longer duration, which is in turn responsible for the higher ripple in the dc currents observed with the interleaved SVM technique.

Full driving cycle

A complete driving cycle test is carried out to assess the performance of the MOVm technique in a dynamic operation of the traction drive. The motor windings are kept in the delta configuration so that the battery voltage is compatible with the load maximum voltage. In fact, this test only serves for further validation of the modulation, whereas other experiments in the more general setting of V_{LV} being lower than the peak motor voltage will be presented in Chapter 5.

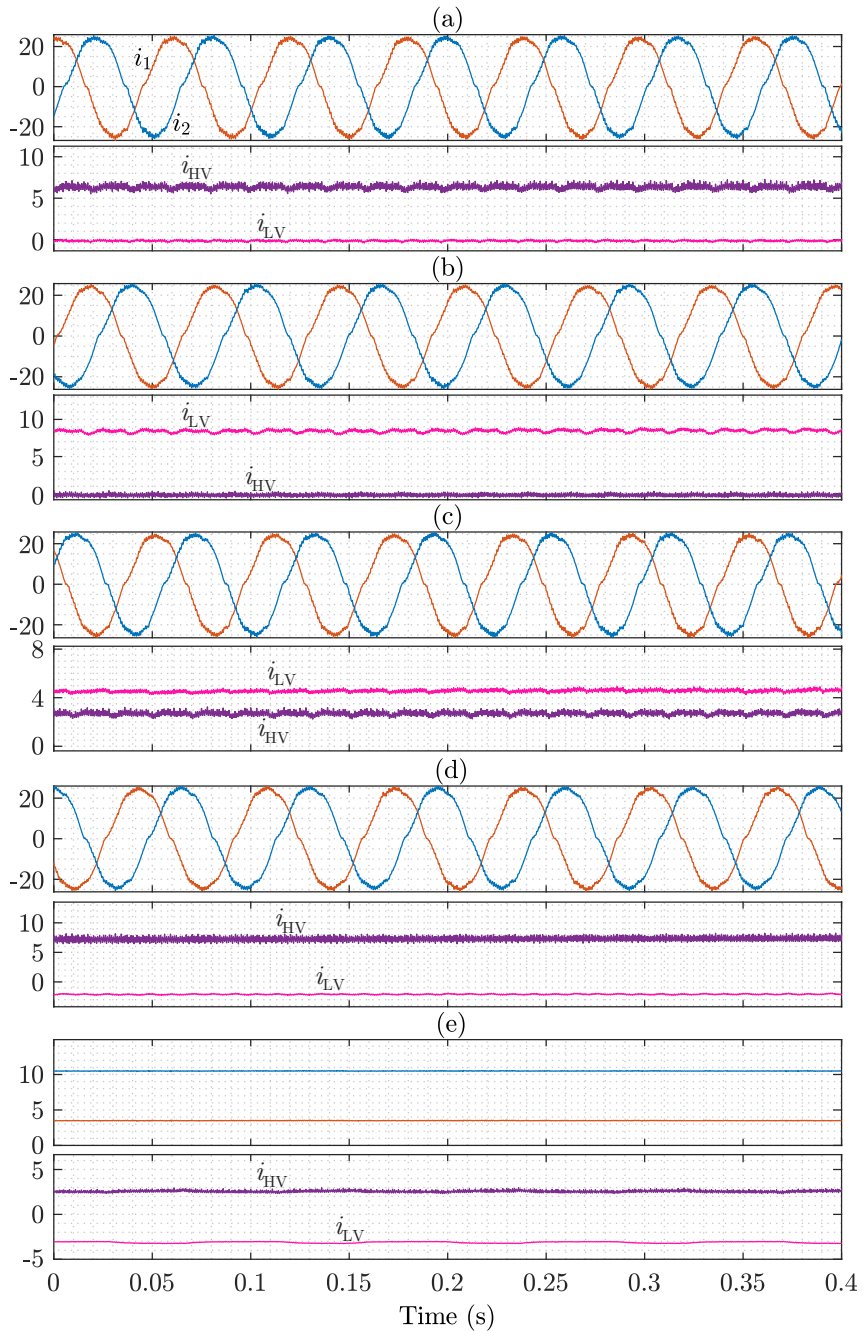


Figure 4.20. Steady-state ac and dc currents obtained with the MOVN.

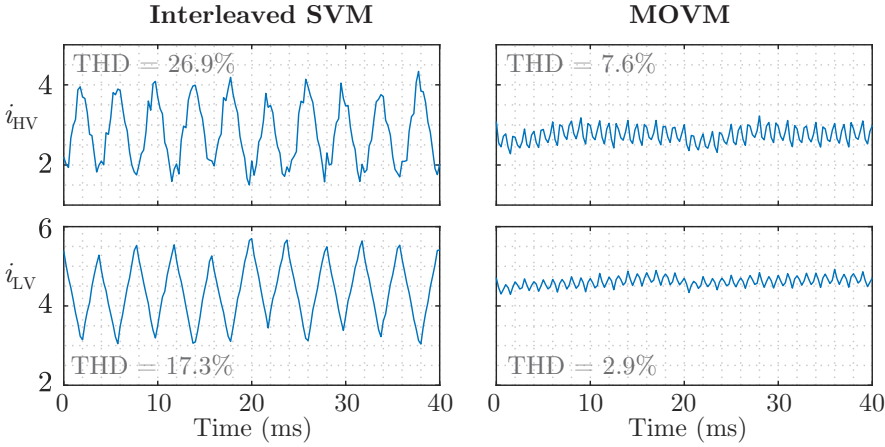


Figure 4.21. Steady-state dc currents drawn by the [MSI](#).

During the cycle, the following [EMS](#) is implemented to define at any instant the battery power reference:

1. peak shaving: during the acceleration, the battery pack assists the rectifier and limits its power output to 2.3 kW;
2. load leveling: during the cruising phase, the battery is recharged at a power level that brings the rectifier output power to 2.3 kW;
3. regenerative braking: during braking, the battery is controlled to recover the entire amount of braking energy, while the rectifier is inactive;
4. stationary battery charging: at standstill, the battery is recharged at 1.5 kW from the rectifier, while the motor is at standstill and develops no torque;

The results of the test are presented in [Figure 4.22](#). At the beginning of the acceleration, the dq-axis currents are at their rated values corresponding to the rated flux-linkage and torque of the machine. As long as the total traction power is lower than the peak-shaving threshold, the battery is kept inactive and the [MSI](#) draws power only from the rectifier. As the motor speed and power demand increase, a smooth clipping action of the rectifier

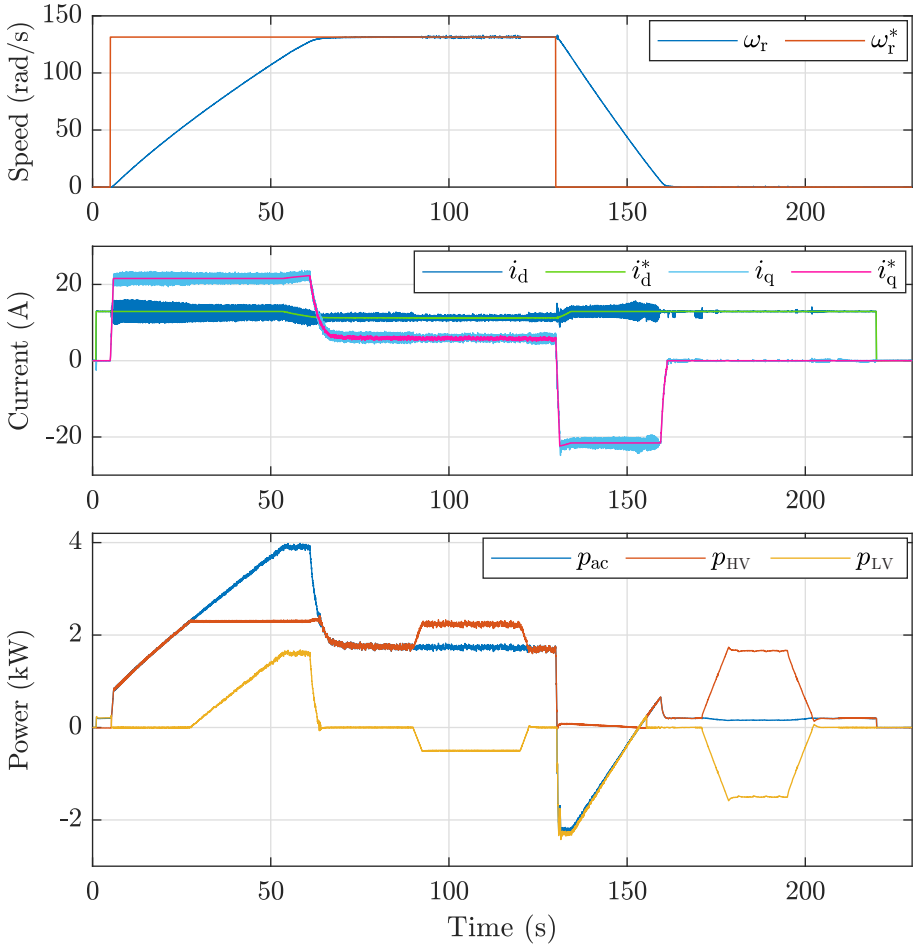


Figure 4.22. Results of the driving cycle test for the MOVIM modulation technique: (a) motor speed, (b) dq-axis current control, (c) system power flows.

power is achieved. During this phase, the battery power increases to follow the increase of traction power. Such increase is managed by the MOVIM with continuity, i.e., no quantization affects the power flows in the sources as with the interleaved SVM. As a result, the rectifier power output is stably kept at its reference level. During the last part of the acceleration,

the d-axis current is lowered to perform the flux weakening. In this phase, the ac output power remains constant and so does the battery power. When the target speed is reached and cruising begins, the q-axis current decreases to its steady-state value that balances drag and friction forces. The steady-state ac power decreases correspondingly at a level below the peak-shaving threshold. Thus, it gets entirely supplied by the rectifier, with the battery power falling rapidly to zero. After a few seconds, the controlled in-motion battery recharge from the rectifier through the MSI is operated. The rectifier power output increases again to its maximum value, and negative power is established at the battery terminals up to a few seconds before braking starts. During braking, the q-axis current is controlled to its peak negative value. After a very short operation in field weakening, the d-axis current and machine flux return to their rated values. In this phase, the rectifier is kept inactive and a full recovery of the braking power into the battery pack is obtained. Ultimately, the motor stops and remains at standstill. The direct-axis current is kept at its rated value to flux the motor, while the q-axis current is zero. Then, the stationary recharge of the battery from the primary supply is commanded. The rectifier power increases from the small amount of motor dc losses to the full power level injected into the battery.

Discussion

The experimental results confirm that the MOVMM can manage all the operating modes typically required from a traction system supplied by two independent sources, namely: power sharing between sources, power idle of one of the two sources, stationary and in-motion recharge of one source from the other, and power recovery during braking. Some of these modes are not feasible if the MSI is controlled through the interleaved SVM technique. Besides this prime and most important aspect, the MOVMM outperforms the interleaved SVM also with respect to the smoothness of the control action, the lower level of harmonic distortion in the dc currents, and the capability of injecting and extracting power into and from the LV source also for ac voltage levels greater than the LV voltage level.

Multi-source inverter: integration and control

5.1 Integration in semi-active architectures

In standard semi-active bimode traction circuits, a dc/dc converter interfaces and controls the power exchanged between the low-voltage source and the high-voltage systems. These architectures can be classified as two-stage (2S) topologies since the power flows from the LV source to the traction loads through the dc/dc converter and the traction inverter, which can be thus considered as connected in series. As a result, the power rating of the dc/dc converter has to match the peak power processed by the LV source during the vehicle mission profile. High-power dc/dc converters require bulky and heavy magnetics, which usually determine the highest share of weight and volume. Moreover, the power losses in inductors and power semiconductors scale with the power rating of the converter. Therefore, a reduction in the peak power to be processed by the converter can result in lower losses, weight, and volume.

It was shown in Chapter 4 that, if controlled through the MOVIM technique, the MSI can manage with flexibility the two dc sources connected at its inputs while supplying the traction loads as demanded by the vehicle speed profile. However, since the NPC circuit cannot boost the dc input voltages, the maximum power that can be drawn from the LV input is limited by its dc voltage level and by that of the ac load. Considering

that voltage boosting is often required in practical applications to compensate for the voltage drop across the terminals of the dc sources, a traction circuit based solely on the MSI would result in a severe limitation in the power processed by the LV source. This limitation may conflict with the expected operation of the bimode traction system, leading to an overall deficit in the performance and attractiveness of the suggested configuration. Therefore, using an MSI as the main traction converter does not completely exclude the need for a dc/dc converter.

Replacing the VSI of a semi-active traction circuit with an MSI results in what can be named a S2S semi-active system. Semi-active due to the presence of only one dc/dc converter that manages the two dc sources at different voltage levels. Semi-two-stage because, thanks to the direct connection provided by the MSI, part of the power of the LV source is processed in cascade by the dc/dc and MSI converters, while the remaining can flow directly through the MSI. The concept is displayed in figure 5.1, where the system power flows occurring in a standard 2S architecture are compared with those attainable with a S2S architecture. This inherent partial-power-processing capability of the S2S architecture can be exploited to reduce the current and power peaks in the dc/dc converter, with expected benefits in terms of power losses, weight, and volumes. The notion of S2S power conversion is not new and several concepts based on it can be found in the literature. For instance, in [126–128], a family of dual-input dc/ac converters that benefit from such a partial-power-processing operation is presented. These converters provide a direct path and a voltage-boosted indirect path between the dc input and the ac output. All the proposed converters are considered to be supplied by a single dc source. They are characterized by non-conventional circuit topologies and by switching cells that differ from standard two-level or three-level legs and thus need tailoring to some extent. Moreover, as the switching between the direct and indirect conduction path is controlled with a level-shifted PWM, the share of power that flows through each path is non-linearly linked to the output voltage magnitude and no degree of freedom for the control of the conduction configurations exists.

In a similar fashion, the work carried out in [111,112] concerns the integration of the MSI in a hybrid traction system for hybrid electric vehicles, with the ultimate goal of partially bypassing the dc/dc converter in some

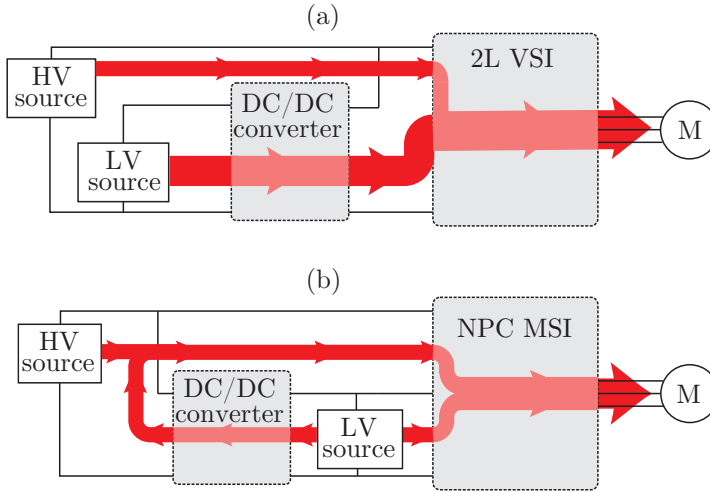


Figure 5.1. Conceptual system power flows in: (a) a conventional two-stage architecture based on the VSI, (b) semi-two-stage architecture based on the MSI.

driving conditions to reduce its power rating. Also in this case, the MSI inputs are connected to two buses at different voltage levels which, however, are derived from a unique battery pack either by direct connection or through a dc/dc boost converter. As a consequence, the MSI is controlled with the only goal of reducing the power flowing through the boost converter, and no additional requirement on the power-sharing between dc inputs is considered. Specifically, the LV and HV inputs are again selected according to the magnitude of the ac output voltage, meaning that the share of power drawn from either input is dictated by the voltage required by the ac motors. The uniqueness of the proposed topology and its control determines that the operating modes of a conventional hybrid powertrain have to be replaced with ones specific to the MSI-based circuit.

This chapter presents a control approach for MSI-based S2S architecture intended to cope with standard EMS policies used in bimode rail vehicles. In other terms, a coordinated control of the dc/dc and MSI converters is proposed that leads to a significant reduction in the dc/dc converter power rating without requiring peculiar EMS approaches differing from those typical of bimode rail vehicles discussed in Chapter 3.

5.2 Coordinated control of the power converters

In a **S2S** semi-active topology, a coordination rule must be conceived to split the overall **LV** source power between the **MSI** (direct path) and the dc/dc converter (indirect path). The optimal rule is such to minimize the power processed by the converter, while always meeting one of the following constraints:

- When both sources supply the vehicle (e.g., during acceleration), the share of power delivered by the **LV** source must follow its reference as dictated by the vehicle **EMS**.
- When the **LV** source alone supplies the vehicle (in case of an outage or temporary unavailability of the **HV** supply), the voltage of the **HV**-bus must be regulated at its rated level to ensure rated operation of the traction drives and auxiliary converters.

Hence, it can be stated that the objective of the control is to coordinate the **MSI** central point current reference $i_{\text{msi,LV}}^*$ and the dc/dc converter input current reference $i_{\text{dcdc,in}}^*$ according either to the **EMS** of the two sources or to the voltage control of the **HV** dc bus. Then the **MSI** reference current, together with the reference ac voltage, shall be processed by the **MOV**M, while the dc/dc converter reference current shall be tracked by a corresponding current control loop.

By recalling the operating plane and modulation limits of the **MOV**M algorithm, the reference currents that minimize the share of power flowing through the dc/dc converter can be obtained in either scenario as follows. When both sources are active, the **HV**-bus voltage is fixed by the **HV** source and the coordination of the converters must ensure the desired power distribution between sources. If the **LV** source power reference p_{LV}^* falls inside the **MOV**M plane it is processed entirely through the **MSI LV** terminal and the chopper is not used. In case the power reference exceeds the **MOV**M limits, the **MSI** draws from the **LV** terminal the maximum power (i.e., it operates at its modulation limit), and the dc/dc converter processes the extra amount. The two currents are then derived straightforwardly by dividing each power reference to the **LV** source voltage. The coordination strategy in the hybrid traction mode can be represented by the block diagram in Figure 5.2(a).

When the HV source is not present and the LV source is the only power supply, the HV-bus voltage must be actively regulated by the dc/dc converter. In fact, injecting or drawing current at the MSI LV input has no direct effect on the HV-bus voltage level. However, the voltage-regulating effort of the dc/dc converter can be still minimized by drawing as much traction power from the LV-bus as possible. This can be done again by comparing the reference traction power (not the reference LV source power, as in the hybrid traction mode) with the MOVIM limits. The extra amount of power exceeding the MOVIM thresholds, if any, is drawn through the HV input terminal from the dc/dc converter, which aims at keeping the HV-bus voltage at its reference level. The coordina-

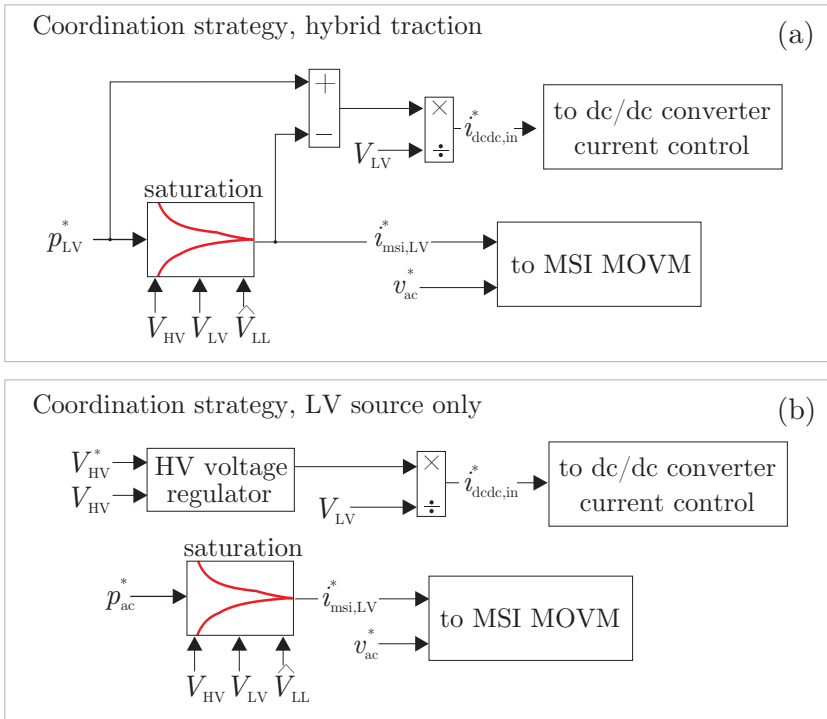


Figure 5.2. Coordination of the MSI and dc/dc converter reference currents when (a) the traction system is supplied by both sources and (b) by the LV source only.

tion strategy when the vehicle is supplied only by the **LV** source can be represented by the block diagram in Figure 5.2(b).

It must be noticed that a third possible scenario exists, in which the traction motors are supplied only by the **HV** source. However, this is not of practical interest for what concerns the coordination of the two converters. In fact, it corresponds to the case in which the **HV**-bus voltage is fixed, the dc/dc converter is off, and the **MSI** is modulated as a conventional **VSI** fed from the **HV** terminal (i.e., the current reference $i_{\text{msi,LV}}^*$ is zero).

It is also worth noticing that the **MOV** limits are not fixed but rather inversely proportional to the magnitude of the fundamental ac output voltage, as per equations (4.33a)-(4.33b). Recalling that the voltage required by the electric motors is roughly proportional to their speed, the amount of power that can be processed directly through the **MSI** is expected to vary significantly along the driving profile of the vehicle. The overall partial-power-processing performance of any **S2S** architecture shall be evaluated in the worst condition, i.e., in the operating point that corresponds to the lowest **MOV** power-processing capability.

5.3 Experimental results

Experimental tests are carried out to assess the performance of the proposed coordination of the **S2S** architecture over a complete driving cycle and under an **EMS** approach typical of bimode rail vehicles. The overall performance of the **S2S** traction system is evaluated in terms of motor speed and current control, dc power and voltage control, and reduction of the dc/dc converter peak power. Two possible arrangements for the dc sources will be considered, namely:

- A storage system is connected to the **HV** bus, while a non-receptive power supply is connected to the **LV** bus. This configuration is found in bimode vehicles with onboard fuel cells and batteries.
- A storage system is connected to the **LV** bus, while a non-receptive power supply is connected to the **HV** bus. This configuration is found in bimode vehicles with connection to the external line and onboard batteries or supercapacitors.

The tests are performed on the small-scale rail traction drive simulator described in Appendix A.

5.3.1 Non-receptive source on the high-voltage bus

For this group of tests, a diode-bridge rectifier is employed as the non-receptive high-voltage supply, whereas a battery pack represents the LV storage device. The battery is connected to the MSI LV terminal on one side and to the input of a half-bridge dc/dc converter on the other side. The output of the dc/dc converter and rectifier are connected to the MSI HV terminal. The motor windings are star-connected so that, at high speeds, the motor peak voltage is higher than the battery voltage and the dc/dc converter needs to handle a certain share of the LV source power. The main bench parameters are reported in Table 5.1, while the power circuit and overall control scheme are displayed in Figure 5.3. All the variables shown in the circuit diagram are measured, but only the ones in grey are actually employed by the control algorithm (the remaining ones are only for monitoring and visualization purposes). Correspondingly, variables highlighted by grey circles in the control diagram are either measurement or input signals. The motor speed is regulated by means of a standard FOC algorithm, which outputs the motor voltage references v_α^* and v_β^* and the instantaneous motor power p_{ac} . The management of the battery implemented for this test is representative of bimode vehicles with external power supply and onboard storage system, when running

Table 5.1. Test bench parameters

Component	Item	Value
Diode bridge rectifier	Output voltage	350 V
Battery pack	Output voltage	250 V
Power converters	Switching period	200 μ s
Motor	Connection	Wye
	Maximum power	3.2 kW
	Base speed	945 rpm
	Limit voltage	210 V _{rms}
	Maximum current	11.4 A _{rms}

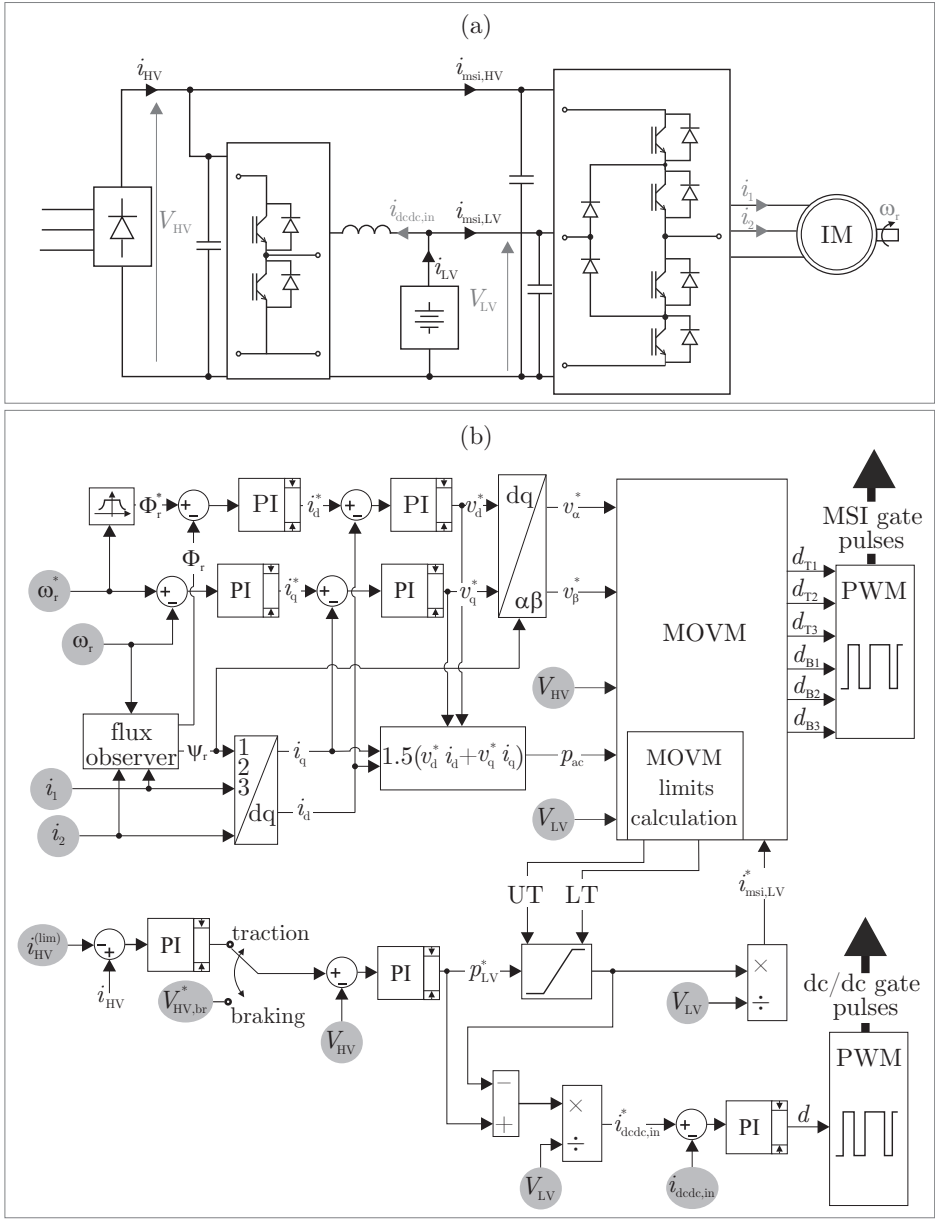


Figure 5.3. Power circuit configuration (a) and control scheme (b) for the tests on the S2S architecture with a non-receptive source on the HV-bus.

on electrified sections. Specifically, the battery power reference is set to limit the external supply current and to achieve maximum energy recovery. During motoring, the reference HV voltage V_{HV}^* is produced by the HV current regulator, whose output saturation levels are tuned to limit the HV current to the threshold value $i_{\text{HV}}^{(lim)}$. During braking, the diode rectifier cannot accept a negative current, and the HV voltage reference is set externally to the value of $V_{\text{HV,br}}^*$. In either case, the HV voltage error is processed by a voltage regulator which outputs the instantaneous battery power reference p_{LV}^* . The MSI LV current reference $i_{\text{msi,LV}}^*$ and dc/dc converter current reference $i_{\text{dcdc,in}}^*$ are then computed based on p_{LV}^* according to the coordination concept described in the previous section and based on the instantaneous power thresholds UT and LT. The MSI LV current reference, together with the FOC references voltages, is then processed by the MOVN to compute the MSI duty cycles and pulse signals. On the other hand, the dc/dc converter current reference $i_{\text{dcdc,in}}^*$ is processed by a closed-loop PI current regulator. The regulator outputs a duty cycle signal which is then used to generate the gate pulses of the half-bridge dc/dc converter. The HV current threshold $i_{\text{HV}}^{(lim)}$ and braking voltage reference $V_{\text{HV,br}}^*$ are set to 3 A and 355 V, respectively.

Figure 5.4 shows the overall system-level performance in terms of motor speed, d-q axis currents, and system power flows. In the first part of the acceleration, the motor is operated in its constant-torque region: the d-axis and q-axis currents are at their rated value. As soon as the rectifier power reaches the threshold of 1 kW, the battery starts supplying the extra power to achieve the required peak-shaving action. Hence, the battery power output increases together with the traction power. Up to a certain level of the motor speed, the power drawn from the battery is entirely processed by the MSI, and the dc/dc converter is not used. Then, the MSI reaches its LV power limit, and part of the battery power starts to flow through the dc/dc converter. During flux-weakening, the d-axis current is decreased and the motor continues to accelerate at constant power. Correspondingly, the battery power output becomes constant, and also the power delivered through the dc/dc converter is almost flat. When the traction drive reaches cruising speed, the q-axis current is controlled to compensate for the steady-state friction losses of the drive chain. The steady-state ac power falls correspondingly, but its level is higher than

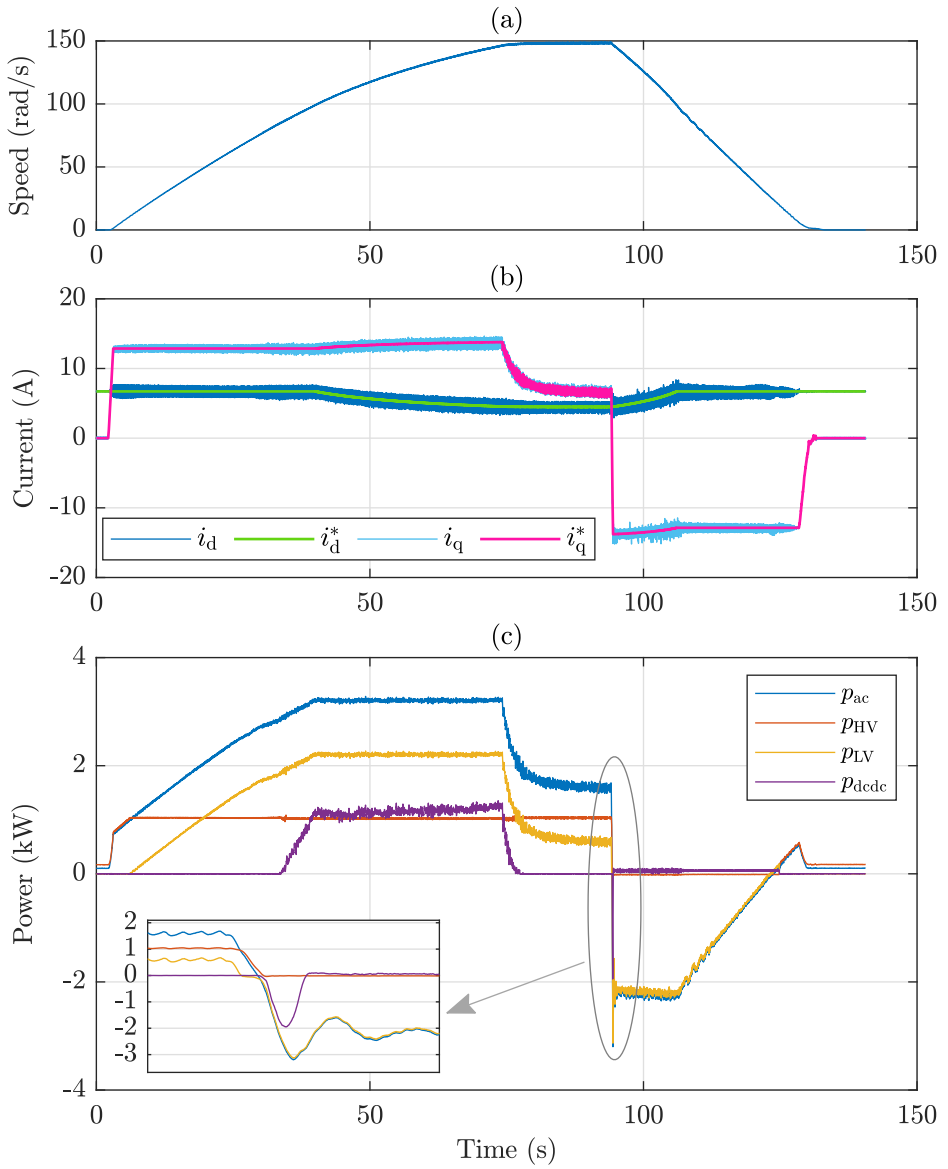


Figure 5.4. Experimental results for the S2S architecture with a non-receptive source on the HV-bus: (a) motor speed, (b) dq axis current control, (c) system power flows.

the peak-shaving threshold and a certain amount of power is still drawn from the battery through the **MSI LV** terminal, while the dc/dc converter returns to null power. At the beginning of braking, the q-axis current steps to its maximum negative value, and the motor develops a braking torque. The rectifier power is rapidly brought to zero, and all the power generated by the motor is managed by the battery. As the power flows invert with a steep dynamic, a zoomed view of this transient is reported. It can be appreciated that the battery power reaches a negative peak of 3.1 kW. However, the dc/dc converter is involved only at the very beginning of braking and processes a peak power of 1.9 kW, which corresponds to a 39% reduction compared to the entire battery power. Hence, a 39% reduction in the dc/dc converter peak power rating is achieved by the **S2S** architecture in the considered test conditions. Afterward, the chopper is not used and all the battery power flows through the **MSI LV** connection. Constant-power and constant-torque operations of the drive follow each other in reverse order with respect to the traction phase during the braking phase. At the end of the cycle, the motor stops and absorbs from the rectifier a few Joule losses produced by the dc magnetizing currents, while the battery is not used.

Further insight into the operation and coordination of the power converters can be gained by inspecting Figure 5.5, which shows the dc currents flowing in the **LV** and **HV** buses, the voltage of the dc sources together with the fundamental line-to-line peak ac voltage, and the duty cycles of the **MSI** first leg. In the early stage of the acceleration, the motor voltage \hat{V}_{LL} is below the battery voltage V_{LV} , and the entire traction power can be managed by the **MSI** without involving the dc/dc converter. In this condition, the rectifier current i_{HV} equals the **MSI HV** input current $i_{\text{msi},HV}$, the battery current i_{LV} equals the **MSI LV** input current $i_{\text{msi},LV}$, the input and output currents of the dc/dc converter are null, and the **MSI** bottom duty cycles are below unity. A few seconds after the crossing point between \hat{V}_{LL} and V_{LV} , the **MOV** limits are approached and the peak value of d_{B1} reaches unity. In this new condition, the current that can be injected into the **MSI LV**-bus is restricted by the **MOV** upper-threshold power to a level below the full battery current. As a result, a current starts to flow into the dc/dc converter to make up for the difference between i_{LV} and $i_{\text{msi},LV}$. On the **HV**-bus, the flow of current in the dc/dc converter

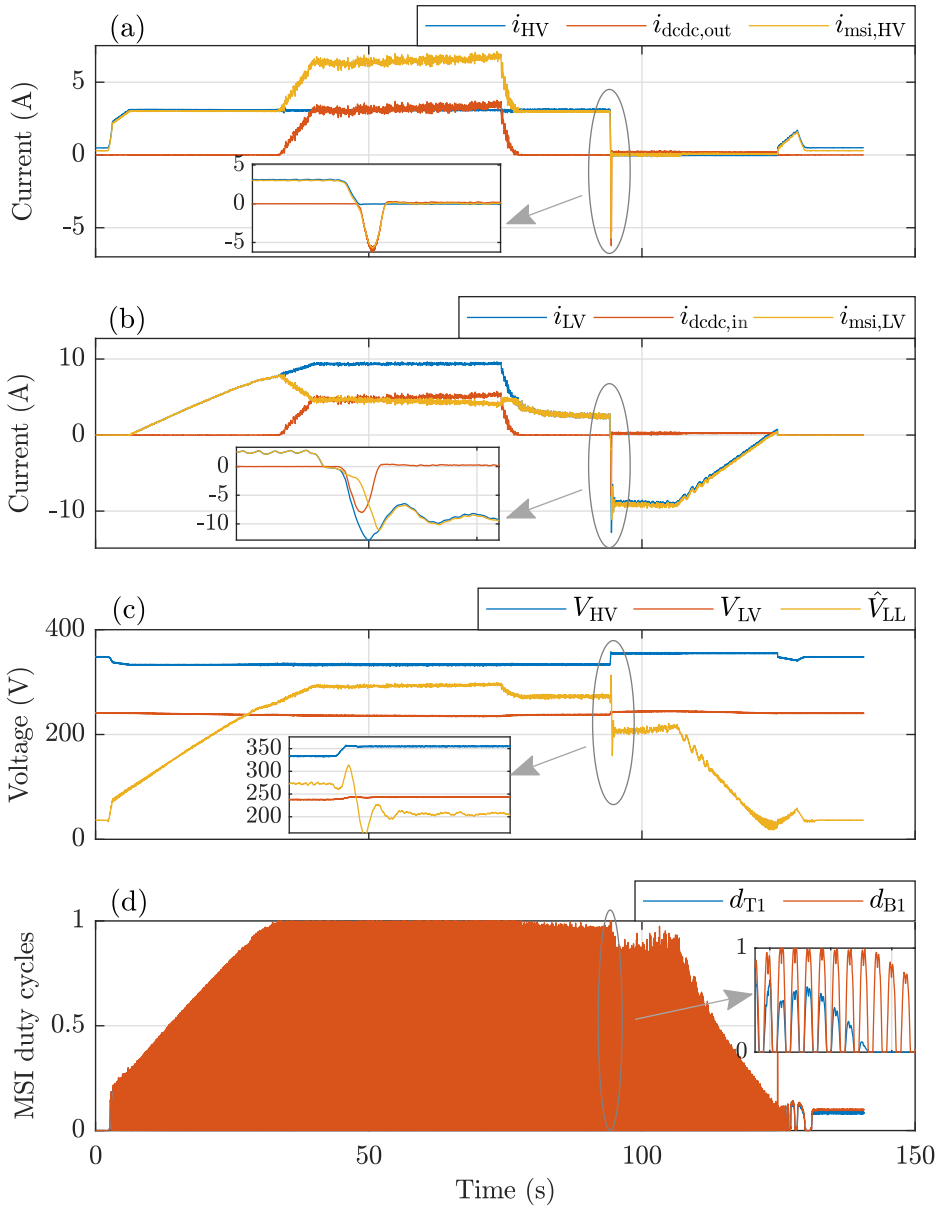


Figure 5.5. Experimental results, battery at 250 V: (a) HV-bus currents, (b) LV-bus currents, (c) motor and dc sources voltages, (d) MSI first-leg duty cycles.

reflects into a corresponding increase of the **MSI HV**-input current, while the rectifier current is not affected by the coordination between the two power converters and remains at its constant reference level. When the steady-state is approached, the battery current can fall to a lower level compared to the acceleration phase. Despite \hat{V}_{LL} being still higher than V_{LV} , this smaller amount of power falls inside the **MOV** power limits, so that the chopper current falls to zero. At the very beginning of braking (highlighted by the grey circles), the traction power rapidly decreases toward its negative peak and, according to the **EMS**, the battery power follows it (see also the zoomed view in Figure 5.4(c)). However, the level of p_{LV} falls outside the **MOV** power limits. The **MSI** is hence operated again at modulation limit, as testified by the unity peak value of the bottom duty cycles. While the current $i_{\text{msi,LV}}$ falls with the maximum possible steepness, the remaining amount of braking power reflects into a negative current $i_{\text{msi,HV}}$. As this current cannot flow into the diode bridge, it starts charging the **HV**-bus capacitor. As soon as V_{HV} reaches the braking voltage target of 355, the reference voltage selector switches to braking mode, and the **PI** regulator keeps V_{HV} at reference by forcing into the dc/dc converter output a current $i_{\text{dcdc,out}}$ that equals $i_{\text{msi,HV}}$. Of course, this current reflects into the dc/dc input as a negative current $i_{\text{dcdc,in}}$. This condition ends when the ac voltage \hat{V}_{LL} falls below the battery voltage V_{LV} . Indeed, as the crossing between these voltages occurs, the **MSI** can operate again within the **MOV** limits and regains full power-processing capability through its **LV** input terminal. The current $i_{\text{msi,LV}}$ equals the battery current i_{LV} , the top duty cycles become null and so does the current $i_{\text{msi,HV}}$, and the peak of the bottom duty cycles starts to decrease as well. Correspondingly, the input and output currents in the chopper drop to zero, and all the power generated by the motors up to the end of braking flows into the battery through the **MSI**, thus bypassing the dc/dc converter. Overall, over the entire driving cycle, the peak current at the chopper input is equal to 8.1 A, while the battery current has an absolute peak of 12.9 A. Their ratio determines the dc/dc converter current reduction achieved by the **S2S** architecture with respect to a standard **2S** architecture, in which all the battery current flows through the dc/dc conversion stage. For the implemented setup, this reduction amounts to 37%. Furthermore, the absolute total energy processed by the battery (i.e., the

time integral of $|p_{LV}(t)|$ during the tests amounts to 48.9 Wh, but only 12.9 Wh are observed to flow through the dc/dc converter. Therefore, a significant 73.6% drop in the energy that has to be processed by the chopper is achieved by the **S2S** topology.

It can be noticed from Figure 5.5(c) that the motor fundamental voltage is well above the battery voltage for a long portion of the traction phase. However, it is steadily below the battery voltage during braking, except for the very first instant. As already pointed out, this determines that the dc/dc converter is involved only during the first short portion of braking. Nevertheless, it can be interesting to discuss the **S2S** system performance also for a battery voltage level laying below the motor voltage for a significant duration of the braking phase. To this aim, the test is repeated with a lower battery voltage of 140 V. This is accomplished by simply excluding some of the cells inside the battery pack. The results are shown in Figure 5.6. The motor speed and current traces are not reported again as they are identical to the ones obtained in the previous test.

The results show how the lower battery voltage causes a reduced power-processing capability through the **MSI LV** terminal. This results in the **MSI** operating at modulation limit for a much longer portion of the driving cycle, as testified by the duty cycle plot. Compared to the results of the previous test, the dc/dc converter power rises at an earlier instant and settles to a higher level during the constant-power operation of the motor. During steady-state cruising, some of the battery power must still flow through the chopper due to the very low level of current that can be injected into the **MSI LV** input. This condition persists also for about half of the braking phase, with the dc/dc converter current and power traces well below the zero level up to the point of crossing between \hat{V}_{LL} and V_{LV} . Overall, the chopper is much more involved during all the phases of the traction diagram. In this case, the partial-power-processing performance of the **S2S** architecture is reduced. The peak current at the chopper input is equal to 17.7 A, while the current in the battery has an absolute peak of 21.0 A. The dc/dc converter current reduction achieved amounts to 15.7%. The absolute amount of energy flowing through the battery over the cycle equals 49.9 Wh but, in this case, the absolute energy processed by the dc/dc converter increases to 32.3 Wh (-35.3%).

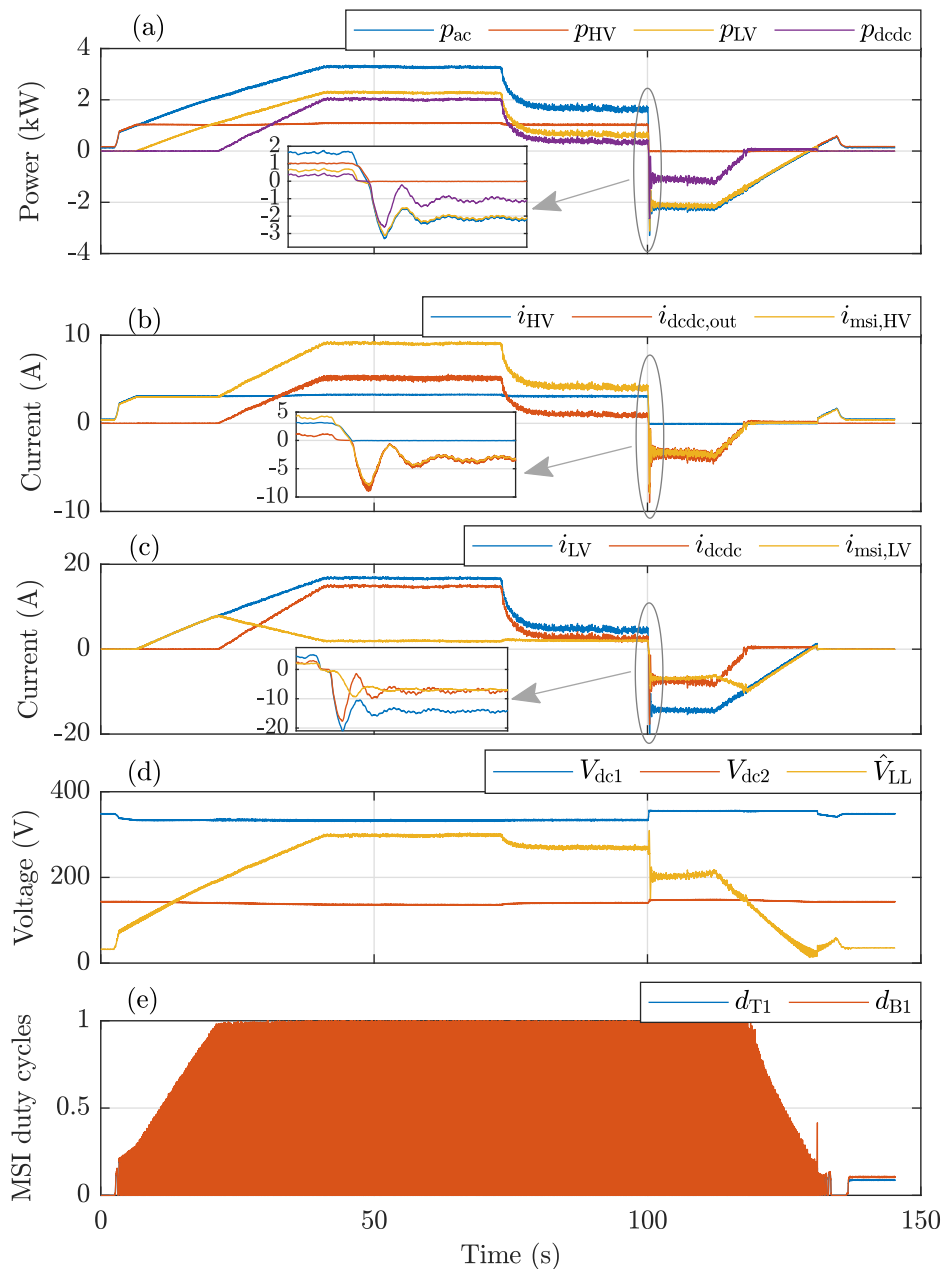


Figure 5.6. Experimental results, battery at 140 V: (a) system power flows, (b) LV-bus currents, (c) HV-bus currents, (d) motor and dc voltages, (e) duty cycles of the MSI first leg.

5.3.2 Non-receptive source on the low-voltage bus

A controllable dc power supply is employed to emulate a non-receptive low-voltage fuel cell system, while the battery pack is now employed as the HV bidirectional storage device. The dc power supply is connected to the MSI LV terminal on one side and to the input of a boost converter leg on the other side. The output terminals of the dc/dc converter and battery are connected to the MSI HV terminal. The motor winding connection is changed to delta so that the battery voltage is compatible with the motor maximum power. On the other hand, the dc power supply is set to a voltage well below the peak motor voltage, as in the previous tests, the dc/dc converter has to process a share of LV power at a certain stage of the driving cycle. The power circuit and overall control scheme are displayed in Figure 5.7, while the system and control parameters of this test are reported in Table 5.2. All the variables shown in the circuit diagram are measured, but only the ones in grey are actually employed by the control algorithm (the remaining ones are only for monitoring and visualization purposes). Correspondingly, variables highlighted by grey circles in the control diagram are either measurement or input signals.

The implemented management of the dc power supply is representative of bimode fuel cell vehicles. The system is always in power-control mode, since the battery pack is always connected to the HV bus and establishes its voltage level. Specifically, the LV power reference is set to follow the traction power and is bounded between two limits that simulate the idle

Table 5.2. Test bench parameters

Component	Item	Value
DC power supply	Output voltage	140 V
Battery pack	Output voltage	250 V
Power converters	Switching period	200 μ s
	Connection	Delta
	Maximum power	3.2 kW
Motor	Base speed	1100 rpm
	Limit voltage	150 V _{rms}
	Maximum current	21.5 A _{rms}

and maximum output power levels of the virtual fuel cell system. The **MSI LV** current reference $i_{\text{msi,LV}}^*$ and dc/dc converter current reference $i_{\text{dcdc,in}}^*$ are then computed from p_{LV}^* according to the coordination concept described above. The **MSI LV** current reference, together with the motor voltage references, is then processed by the **MOVIM** to compute the **MSI** duty cycles and pulse signals. On the other hand, the dc/dc converter current reference $i_{\text{dcdc,in}}^*$ is processed by a closed-loop **PI** current regulator. The regulator outputs a duty cycle signal which is then used to generate the gate pulses of the half-bridge dc/dc converter. The **LV** power limits are set to 0.3 kW and 1.3 kW, respectively.

Figure 5.8 shows the overall system-level performance in terms of motor speed, dq axis currents, and system power flows. In the initial part of the acceleration, the motor dq-axis currents are regulated at their rated value so that the motor operates at rated torque and flux linkage. The **LV** power increases from its minimum value following the ac load power, until it reaches the upper limit. At that point, the battery starts providing the remaining amount of traction power. Up to a certain speed, the constant power drawn from the dc power supply is entirely processed by the **MSI**, and the dc/dc converter is not used. Then, the **MSI** reaches its **LV** power limit, and part of the **LV** supply power starts flowing through the dc/dc converter. During flux-weakening, the d-axis current is decreased and the motor continues to accelerate at constant power. Correspondingly, the battery power output becomes constant, while the power delivered by the **LV** supply through the dc/dc converter is lightly decreasing. When the traction drive reaches the target speed, the q-axis current drops to the low steady-state value corresponding to the friction losses of the drive chain. Due to the ac power level reduction, the **MOVIM** power limits also decrease as per (4.33a)-(4.33b), and this results in a slight increase of the power that flows through the boost converter. When the motor starts to brake, the q-axis current reverses to its maximum negative value, and negative torque is developed. The steep transition from cruising to braking is properly controlled, with the dc power supply falling to its minimum level and the battery recovering the entire negative flow of energy. At this stage, the positive power to be drawn from the dc supply falls within the **MOVIM** limits and the boost converter is not used. Such condition persists for the entire braking phase, except for a short time interval when

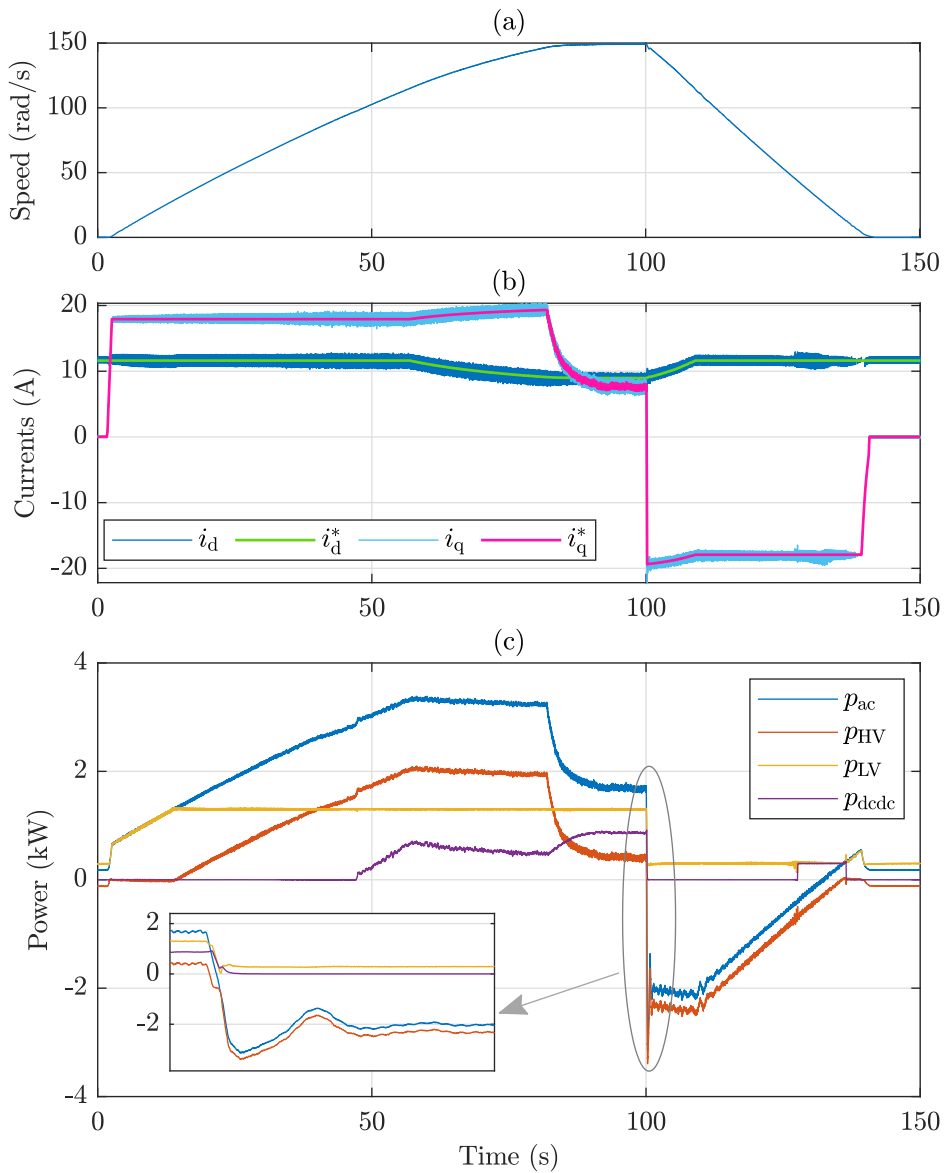


Figure 5.8. Experimental results for the S2S architecture with a non-receptive source on the LV-bus: (a) motor speed, (b) dq axis current control, (c) system power flows.

the traction power reverses its direction. As clear from (4.33a)-(4.33b), the zero-crossing of p_{ac} also determines the zero-crossing of the MSI LV power limits, so that the dc/dc converter has to be activated temporarily. At the end of the cycle, the LV power is still controlled at its minimum level which is however above the dc losses of the still motor. Consequently, the battery exerts a stationary load-leveling action through the MSI and absorbs the extra amount of power delivered by the dc supply.

Additional insight into the operation of the power converters can be gained by inspecting Figure 5.9, which shows the dc currents flowing in the LV and HV buses, the voltage of the dc sources together with the fundamental line-to-line peak ac voltage, and the duty cycles of the MSI first leg.

In the early stage of the acceleration, the motor voltage \hat{V}_{LL} is below the dc supply voltage V_{LV} , and the total power delivered by both sources is managed by the MSI without involving the dc/dc converter. In this condition, the battery current i_{HV} equals the MSI HV input current $i_{msi,HV}$, the battery current i_{LV} equals the MSI LV input current $i_{msi,LV}$, the input and output currents of the dc/dc converter are null, and the MSI bottom duty cycles are below unity. A few seconds after the crossing point between \hat{V}_{LL} and V_{LV} , the MOVm limits are approached and the peak value of d_{B1} reaches unity. In this new condition, the current that can be injected into the MSI LV terminal is bounded to the MOVm upper-threshold power and is lower than the total dc power supply current. Consequently, a current starts flowing into the dc/dc converter to compensate for this difference between i_{LV} and $i_{msi,LV}$. On the HV-bus, the flow of current in the dc/dc converter reflects into the MSI HV-input current becoming greater than the battery current. When the steady state is approached, the ac output power decreases. This, determines a reduction of the MOVm upper power limit, so that the MSI LV current and the boost converter current experience a further decline and increase, respectively, with the total LV current fixed at its maximum value as requested. At the very beginning of braking (highlighted by the grey circles), the traction power rapidly reverses and, according to the EMS, the minimum amount of power is drawn from the LV supply. This power level falls inside the MOVm power limits and can be thus processed entirely by the MSI. Indeed, the bottom duty cycles are well below unity, and the current in the chopper is zero. In this condition,

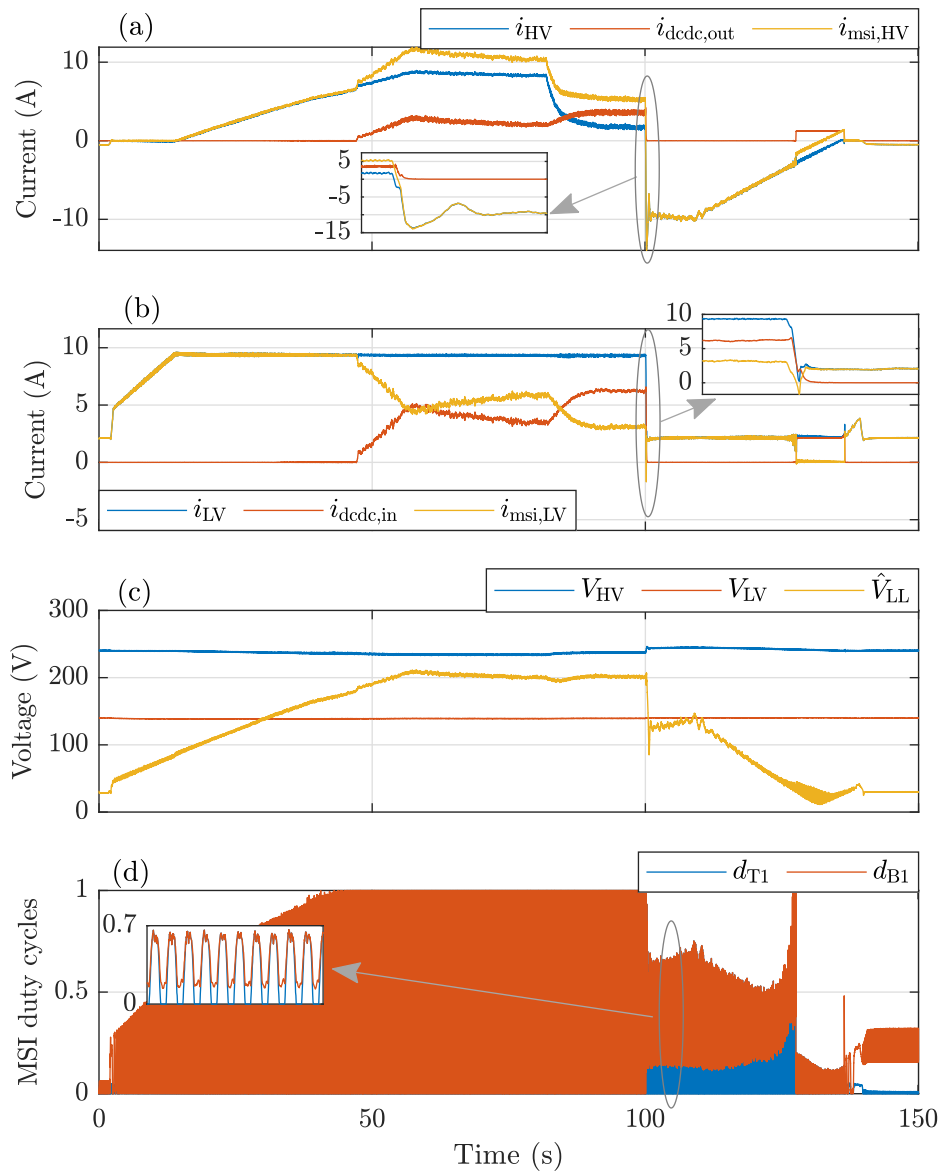


Figure 5.9. Experimental results for the S2S architecture with a non-receptive source on the LV-bus: (a) HV-bus currents, (b) LV-bus currents, (c) motor and dc sources voltages, (d) MSI first-leg duty cycles.

the MSI draws power from both the LV supply and braking motor and injects it into the battery, and the shape of the zoomed-in duty cycles can be seen to agree with the simulated waveforms reported in Figure 4.18. As the ac power approaches zero, the MOVm power limits narrow, and the duty cycles increase correspondingly. Around the zero-crossing of p_{ac} , all the LV current switches from the MSI LV input terminal to the boost converter input terminal. However, this fast transition does not affect i_{LV} , which remains flat at its target level. The opposite transition takes place after a few seconds when the MSI regains full control of the LV power and the dc/dc converter current drops again to zero. The peak input currents of the boost converter and LV supply equal 6.47 A and 9.51 A, respectively, with a 31.6% reduction in the converter peak current rating. Furthermore, the energy delivered by the dc supply amounts to 38.7 Wh, while only 9.7 Wh (i.e., a 25%) enter the dc/dc converter.

5.3.3 Discussion

An overview of the reductions in the dc/dc converter peak current and cycle energy achieved in every test condition is reported in Table 5.3. In either configuration of the power sources, the experimental results show that the MSI-based S2S topology fulfills the main tasks of controlling the ac motor and managing the power distribution between the dc sources. Thanks to the MOVm technique and the resulting coordination strategy of the two power converters, the MSI always processes the highest share

Table 5.3. Overview of the experimental results

		Non-receptive HV source		Non-receptive LV source
		$V_{LV} = 240V$	$V_{LV} = 140V$	$V_{LV} = 140V$
Peak current	LV source	12.9 A	21.0 A	9.5 A
	dc/dc converter	8.1 A	17.7 A	6.5 A
	difference	-37.2 %	-15.7 %	-31.6 %
Absolute cycle energy	LV source	48.9 Wh	49.9 Wh	38.7 Wh
	dc/dc converter	12.9 Wh	32.3 Wh	9.7 Wh
	difference	-73.6 %	-35.3 %	-74.9 %

of LV source power directly from its LV input terminal. Consequently, the dc/dc converter is either completely or partly bypassed, depending on the instantaneous level of the ac motor voltage. As expected, a higher level of the LV voltage results in lower amounts of power and energy that flow through the dc/dc converter during high-speed operation of the motor.

Chapter 6

Comparative numerical analysis

The proof-of-concept experimental validation of the [S2S](#) architecture has attested its potential of reducing the power rating of the dc/dc converter required to boost the voltage of the [LV](#) power source or storage device. However, the effective benefits of a [S2S](#) topology have to be evaluated in real-case applications taking into account the design and operating features of all the components in the traction system (i.e., dc/dc and traction converters, traction motors, filters, etc.). This chapter presents a comprehensive comparison between the [S2S](#) and [2S](#) architectures for two case studies based on the data of two real vehicles: a battery tram, and a fuel cell train. For each case study, a common driving cycle and [EMS](#) are considered, and the two topologies are compared with respect to the following quantities:

- VA rating of the power converters;
- Volume and weight of filters and heatsinks of the power converters;
- Power losses and efficiency in motors, power converters, and dc sources.

The electrical and thermal simulation models and the sizing procedures used for this analysis are detailed in [Appendix B](#) and [Appendix C](#), respectively.

6.1 Case study: battery tram

6.1.1 System architecture and control

The first case study considers a catenary/battery tram inspired by Bombardier's *Flexity 2* trams operated in the Chinese city of Nanjing. The vehicle, shown in Figure 6.1(a), is a five-segment low-floor tram with a rated loaded mass of 54 t. The maximum speed in catenary and catenary-free mode is equal to 70 km/h and 60 km/h, respectively. Four asynchronous motors with 120 kW of rated power produce the traction effort and traction power profiles shown in Figure 6.1(b). Each one of the two battery systems is made of two submodules of 24.5 kWh [129]. Each module is composed of 3.6 V/46 Ah NMC cells in a 148s2p configuration. This arrangement, according to the characterization done in [130] yields the OCV-SOC profile shown in Figure 6.1(c). The two traction architectures are shown in Figure 6.2. In the 2S topology, each traction unit is

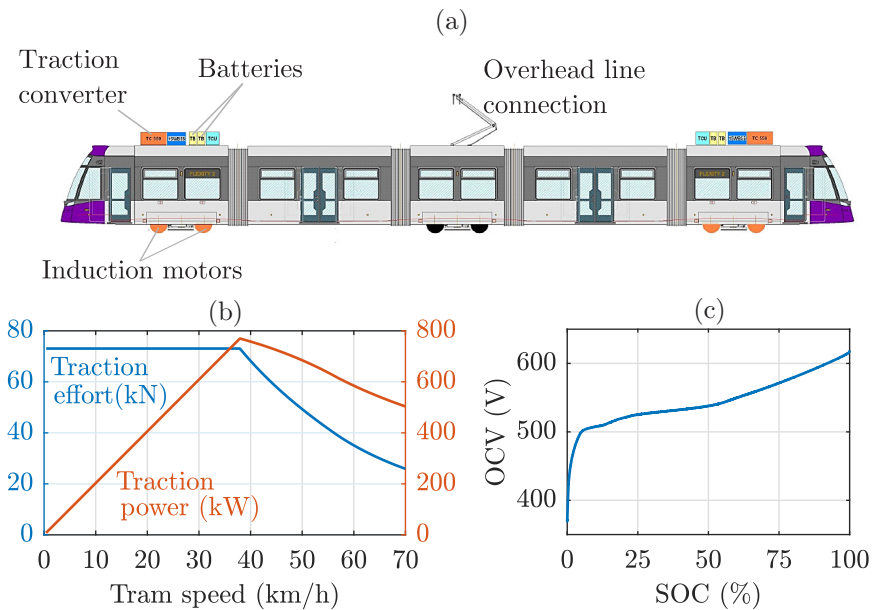


Figure 6.1. Battery tram: (a) vehicle layout, (b) traction effort/power curves, (c) OCV-SOC curve of the batteries.

connected to the pantograph and embeds a VSI traction converter driving two motors in parallel, a battery pack, an interleaved dc/dc converter, and HV LC filters. In the S2S system, each VSI is replaced by a T-NPC MSI, and an additional dc bus at battery voltage provides the direct connection between the MSI LV input and the battery through an additional LC filter. A total power consumption of 80 kW from the auxiliary converters is assumed in both topologies.

Since the EMS of the real tram is not known, the control discussed in [20] for a similar tram is taken as a reference and is implemented as shown by the control diagrams in Figure 6.3. When the overhead line supply is available, the batteries limit the pantograph current to 500 A during traction and the pantograph voltage to 850 V during braking. Hence, the external control loop switches between a line current control and a line voltage control. In the 2S system, the battery power reference p_{LV}^* is input to the dc/dc converter current control. In the S2S system, p_{LV}^* is split between the MSI and the dc/dc converter according to the envisioned coordination strategy. The SOC is controlled in a 45%-55% range so that the batteries can always process the maximum amount of power. To this aim, a double-hysteresis controller is implemented with two bands that, when crossed, engage a constant charging or discharging current reference. The hysteresis bands have a width of 5% of SOC, while the charge and discharge current references are set at ± 200 A (equal to 5C). In either topology, the reference $i_{SOC_ctrl}^*$ is input to the current control of the dc/dc converter only when the battery power reference p_{LV}^* falls to zero, which happens during low-load operations of the traction system.

In catenary-free operation, the dc/dc converters control the HV-bus voltage to the reference value $V_{HV,cf}$ to ensure the rated operation of traction and auxiliary converters. In the S2S system, the MSI is controlled to draw as much power as possible from the LV-bus, so as to minimize the voltage-regulating action of the dc/dc converter during all traction phases.

A standard vector control (not shown in the diagrams) is used to control the torque of the traction motors. At the low layer of power converter modulation, a conventional carrier-based PWM with third-harmonic injection is employed for the VSIs, while the MOVIM is employed for MSIs. The dc/dc converter is controlled with the usual phase-shift modulation adopted for interleaved topologies.

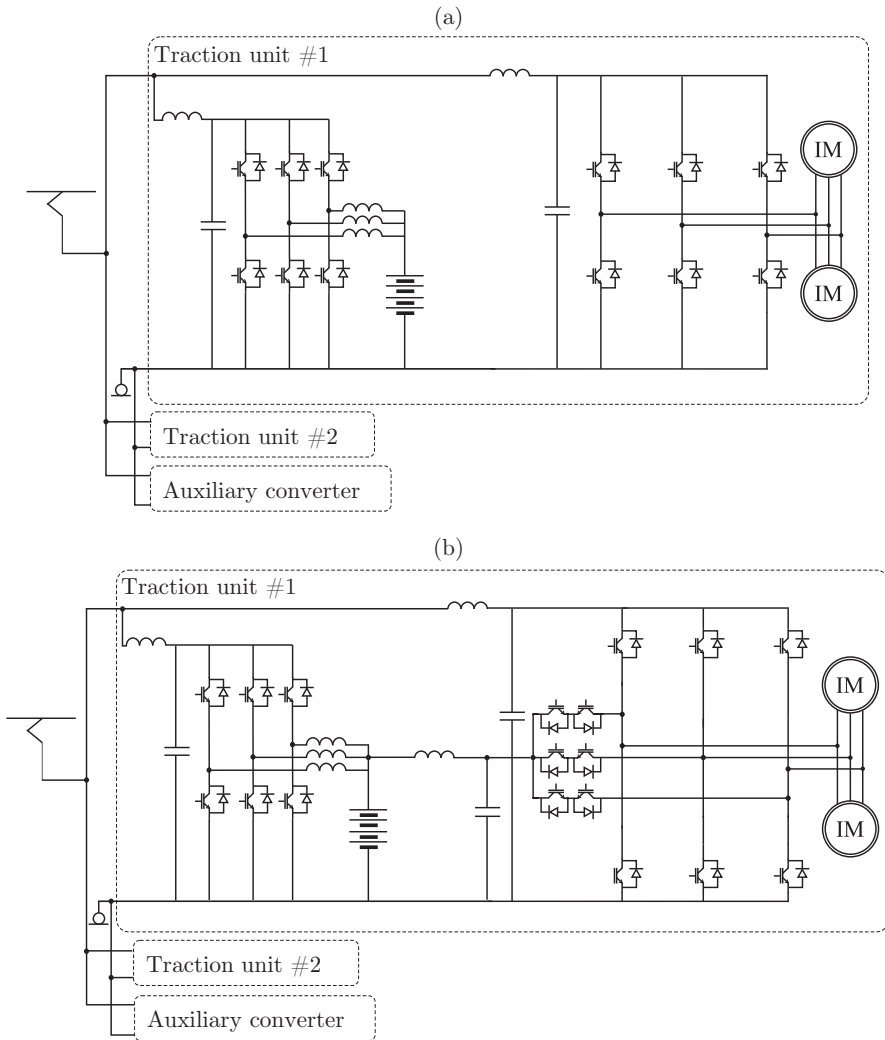


Figure 6.2. Traction circuits: (a) baseline semi-active architecture, (b) S2S semi-active architecture.

The considered driving cycle is shown in Figure 6.4. The tram runs through six steps for a total length of 2 km, with a two-stop non-electrified section of 700 m on which the tram is entirely powered by the batteries. A dwell time of twenty seconds is considered at each stop.

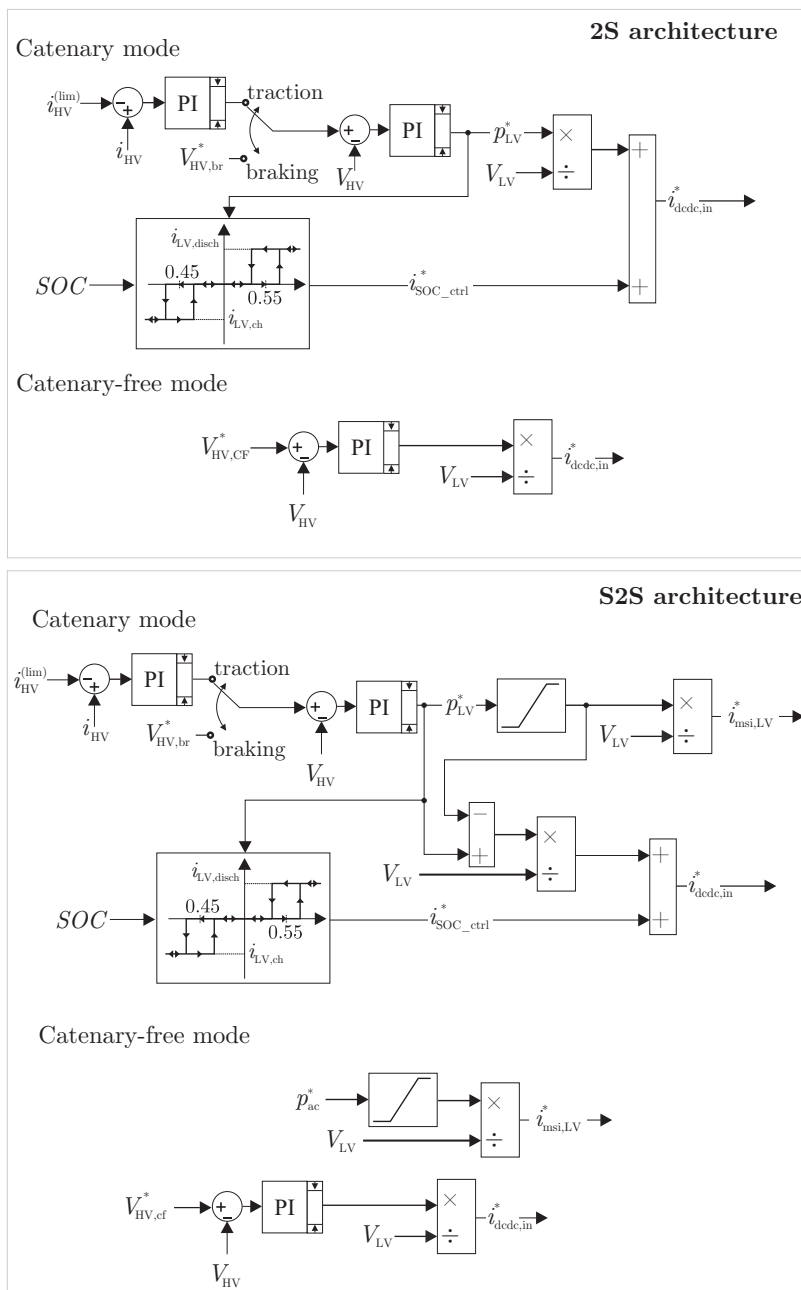


Figure 6.3. Control diagrams of the 2S and S2S traction circuits in catenary and catenary-free modes.

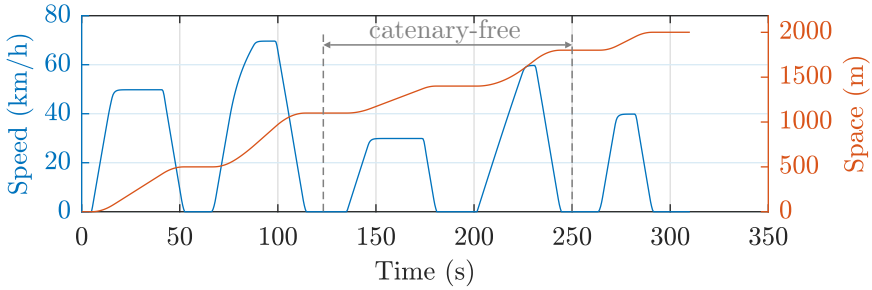


Figure 6.4. Driving cycle of the tram.

6.1.2 Sizing of power converters

Interleaved dc/dc converters

Bidirectional dc/dc converters are employed in both architectures. However, their peak current ratings will differ between the two architectures due to the partial-power-processing characteristic of the S2S topology. Indeed, preliminary calculation yield for the peak average currents at the input and output of each converter the following estimates:

$$\begin{aligned}\hat{i}_{\text{dcdc,in}}^{(\text{S2S})} &= 400\text{A}, \quad \hat{i}_{\text{dcdc,in}}^{(2\text{S})} = 710\text{A} \\ \hat{i}_{\text{dcdc,out}}^{(\text{S2S})} &= 245\text{A}, \quad \hat{i}_{\text{dcdc,out}}^{(2\text{S})} = 455\text{A}\end{aligned}$$

Considering these values and a peak-to-peak target ripple of 50 A in the input current [131], and selecting a switching frequency of 2 kHz, sizing equations (C.1)-(C.3) give for each leg inductor the specifications reported in Table 6.1. Based on these specifications, iron-core inductors are designed and the results are reported in Table 6.2. The geometry and the outcomes of magnetic and thermal Finite Element Analysis (FEA) simu-

Table 6.1. Leg inductors of the dc/dc converter: design specifications

	Inductance	Peak current
S2S	620 μH	220 A
2S	620 μH	320 A

lations of one leg inductor in the **S2S** topology are reported in Figure 6.5 for illustrative purposes.

The peak current in the leg inductors determines the current rating of the **IGBTs**, while the maximum permanent voltage of the catenary determines their blocking-voltage capability. Considering that a maximum permanent voltage of 900 V is allowed in 750 V railway systems, **IGBT**

Table 6.2. Leg inductors of the dc/dc converter: design results

	S2S	2S
Inductance	619 μH at 220 A	621 μH at 320 A
Cores	2xAMCC 630	4xAMCC 800A
Resistance	0.96 m Ω	0.86 m Ω
Volume	3.09 dm ³	5.56 dm ³
Weight	15.2 kg	31.9 kg

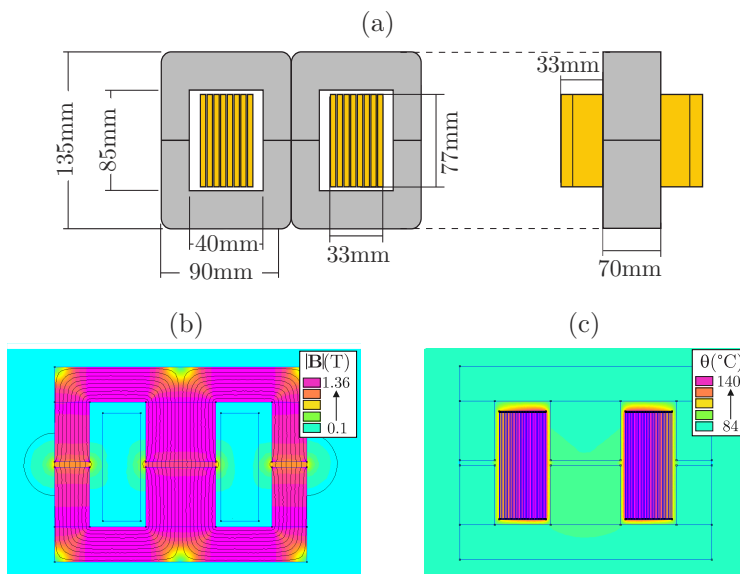


Figure 6.5. One leg inductor in the **S2S** architecture: (a) geometry, (b) flux-density distribution at peak current, (c) temperature distribution at peak **RMS** current.

Table 6.3. Dc/dc converter IGBTs VA rating

	VA rating	
	Blocking voltage	Rated current
S2S	1.7 kV	225 A
2S	1.7 kV	400 A

modules with the VA ratings reported in Table 6.3 are selected.

The LC filter prevents high-frequency harmonic currents injected by the converter from flowing into the catenary, filters the low-frequency voltage ripple engaged on the catenary by the main electric substation rectifier, and limits line voltage spikes or fluctuations. Its cut-off frequency is selected at 35 Hz, which is around a decade below the catenary voltage ripple (depending on the configuration of the substation rectifier) [52]. Considering an equal voltage ripple of 7.5 V (1% of the rated catenary voltage) and the above peak values of the average output current, sizing equations (C.4),(C.17)-(C.18) yield for the dc/dc converter LC filter the specifications reported in Table 6.4. The inductors are designed with an air core, which is a typical choice for line filters due to the intrinsic linearity at very high currents [52]. Film capacitors with sufficient RMS current rating and with a rated permanent voltage of 900 V are selected. The results of the inductor design and capacitor selection are reported in Table 6.5

In both topologies, the dc/dc converter process the highest power during the fourth section, i.e., when the tram runs without electrification up to the maximum speed of 60 km/h, and the batteries have to supply full traction and auxiliary power. With reference to this worst-case operating condition, the heatsinks reported in Table 6.6 are selected, which result in the temperature profiles shown in Figure 6.6.

Table 6.4. LC filter of the dc/dc converter: design specifications

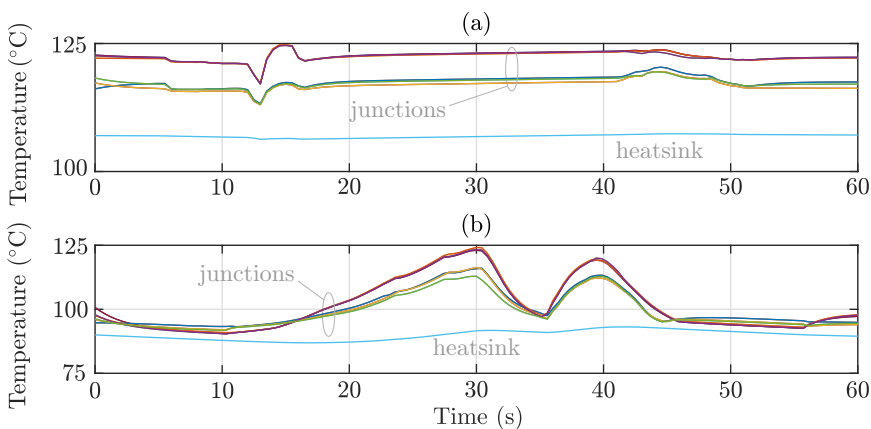
	Inductor		Capacitor	
	Inductance	Peak Current	Capacitance	Peak RMS Current
S2S	6.5 mH	245 A	3.2 mF	80 A
2S	3.6 mH	455 A	5.7 mF	110 A

Table 6.5. LC filter of the dc/dc converter: design results

		S2S	2S
Inductor	Inductance	6.55 mH	3.57 mH
	Resistance	23.9 m Ω	10.1 m Ω
	Volume	31.50 dm ³	44.47 dm ³
	Weight	166.24 kg	234.71 kg
Capacitors	Model	3xB25620B011	2xB25620B029
	Capacitance	3.3 mF	5.8 mF
	Resistance	0.5 m Ω	0.4 m Ω
	Rated current	240 A	200 A
	Volume	4.37 dm ³	7.42 dm ³
	Weight	4.65 kg	7.9 kg

Table 6.6. Heatsink of the dc/dc converter: design results

	S2S	2S
Thermal resistance	0.043 K/W	0.026 K/W
Thermal capacitance	3900 J/K	6200 J/K
Volume	4.78 dm ³	7.56 dm ³
Weight	4.4 kg	7.0 kg

**Figure 6.6.** Temperatures in the dc/dc converter for (a) S2S topology, (b) 2S topology.

Traction converters

The **VSI** and **T-NPC MSI** traction converters drive two motors in parallel which draw a peak current of 1000 A. The switches of the **VSI**s and the outer switches of the **MSI**s have to withstand the maximum catenary voltage of 900 V. On the other hand, the **MSI** inner switches have to withstand the maximum battery voltage of 600 V at full **SOC**. Based on these requirements, **IGBT**s with the VA ratings reported in Table 6.7 are selected.

Table 6.7. Inverter **IGBT**s VA rating

		VA rating	
		Blocking voltage	Rated current
MSI	Outer switches	1.7 kV	1200 A
	Inner switches	1.2 kV	
VSI		1.7 kV	1200 A

The traction inverters are operated at variable switching frequency following a hybrid PWM approach [132]: at low speed, asynchronous PWM at 1.5 kHz constant frequency is employed; at medium and high speeds, synchronous PWM with a triple and odd carrier frequency ratio is used. As for the dc/dc converter, LC input filters with a cutoff frequency of 35 Hz are connected at the **HV** input of **VSI**s and **MSI**s to filter the voltage and current harmonics generated by the inverter and substation rectifier. In the **S2S** architecture, an LC filter is also present at the **LV** input of the **MSI** to filter the high-frequency harmonic currents drawn by the **MSI** at the **LV** terminal. Indeed, the battery current must not be altered by the **S2S** configuration, i.e., its harmonic content must be equal to that in the **2S** standard architecture. As the **MSI LV** input is fed by the stiff voltage level provided by the battery, the cut-off frequency of the **LV** LC filter is tuned based on the **MSI** switching frequency [133], and a cutoff frequency of 75 Hz is selected. The maximum currents drawn by the traction converters from their terminals are estimated to be:

$$\hat{i}_{\text{vsi}} = 580\text{A}$$

$$\hat{i}_{\text{msi,HV}} = 410\text{A}, \hat{i}_{\text{msi,LV}} = 480\text{A}$$

Considering the above maximum currents and imposing a voltage ripple of 7.5 V on the VSI and MSI HV buses and of 5 V on the MSI LV bus (i.e., 1% of either rated voltage), sizing equations (C.4),(C.20)-(C.21) yield for filter inductors and capacitors the specifications reported in Table 6.8. Film capacitors with a rated permanent voltage of 900 V and 700 V are

Table 6.8. LC filter of the traction inverter: design specifications

		Inductor		Capacitor	
		Inductance	Peak Current	Capacitance	Peak RMS Current
MSI	HV side	3.7 mH	410 A	5.5 mF	400 A
	LV side	450 μ H	480 A	9.9 mF	400 A
VSI		3.1 mH	580 A	6.6 mF	400 A

selected for the HV and LV connections, respectively. Air-core inductors are again designed for the inductors in the HV-side filters. The results of the inductor design and capacitor selection are given in Table 6.9, while the FEA magnetic and thermal simulations of the VSI line inductor are shown in Figure 6.7 as an illustrative example.

Table 6.9. LC filter of the traction inverter: design results

			MSI	VSI
		HV-side	LV-side	
Inductor	Inductance	3.74 mH	448 μ H at 480 A	3.07 mH
	Resistance	11.3 m Ω	0.42 m Ω	7.6 m Ω
	Core	Air	4xAMCC 1000	Air
	Volume	51.6 dm ³	8.4 dm ³	64.0 dm ³
	Weight	272.65 kg	48.10 kg	337.80 kg
Capacitors	Model	7x B25690A0787	4x B25690A0258	6x B25620B011
	Capacitance	5.5 mF	10.0 mF	6.6 mF
	Resistance	0.3 m Ω	0.2 m Ω	0.2 m Ω
	Rated current	490 A	400 A	420 A
	Volume	7.75 dm ³	10.0 dm ³	8.78 dm ³
	Weight	9.8 kg	10.0 kg	9.6 kg

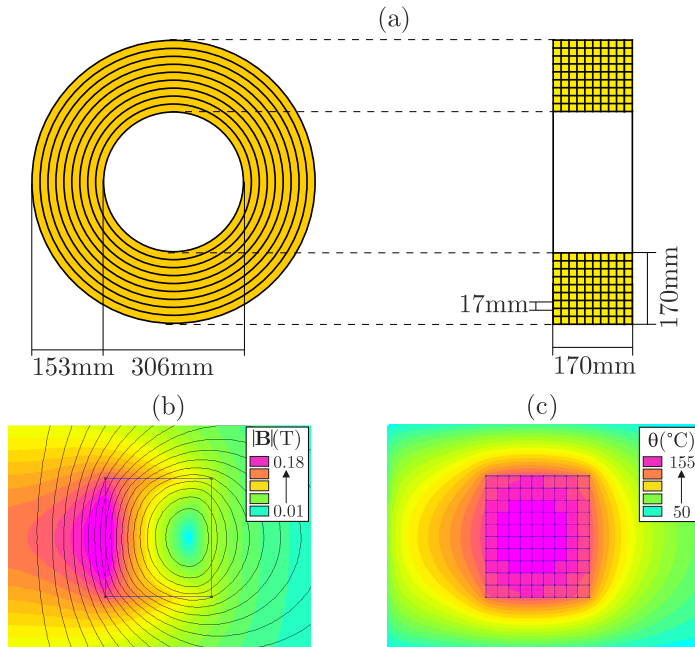


Figure 6.7. VSI line inductor: (a) geometry, (b) flux-density distribution at peak current, (c) temperature distribution at peak current.

The converter's most demanding operation is in the first driving section, in which the vehicle is propelled by both sources and reaches its maximum speed of 70 km/h. Considering a repeated operation of the converter over this worst-case section, the thermal design procedure yields the heatsink parameters given in Table 6.10 and the corresponding heatsink and junction temperature profiles shown in Figure 6.8.

Table 6.10. Heatsink of the traction inverter: design results

	MSI	VSI
Thermal resistance	0.0083 K/W	0.0075 K/W
Thermal capacitance	24900 J/K	26400 J/K
Volume	30.24 dm ³	32.30 dm ³
Weight	28.0 kg	29.9 kg

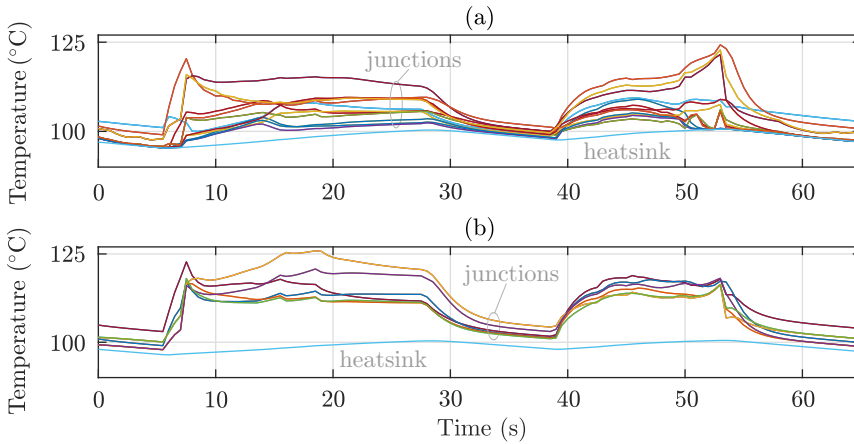


Figure 6.8. Temperatures in the traction converters: (a) MSI, (b) VSI.

6.1.3 VA rating, weight, and volume comparison

The VA rating of one converter is here calculated as the sum of the ratings of all power semiconductors employed in the converter. In Figure 6.9, the VA ratings of the power converters in one traction unit are displayed. The VA rating of the dc/dc converter is reduced by 43.9% in the S2S thanks to the lower current stress on the IGBTs. Due to the doubled part count, the equal switch current rating, and the lower blocking voltage of the inner switches, the rating of the MSI increases by 70.6% with respect to the VSI. Overall, the VA rating of power semiconductors increases by 42% in the S2S topology, and a similar increase in their cost is expected.

The breakdown of volumes and weights required by passive filters and heatsinks in the power converters of both configurations is shown in Figure 6.10. The dc/dc converter volume and weight reductions achieved by the S2S topology are apparent and are mainly due to the reduced size of input and output inductors, which have a lower current rating and can be made smaller (-33.4%) and lighter (-35.9%). Capacitors and heatsinks also contribute to the general improvement, although to a smaller extent, with relative reductions of 41% and 37% in volume, and 41% and 37% in weight, respectively. Overall, the S2S topology allows saving 26.21 liters

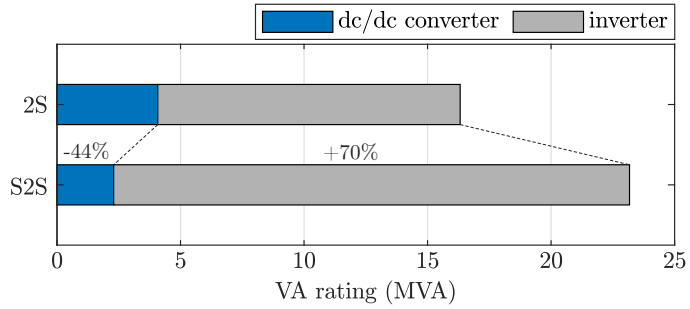


Figure 6.9. VA ratings of the power converters in the 2S and S2S topologies.

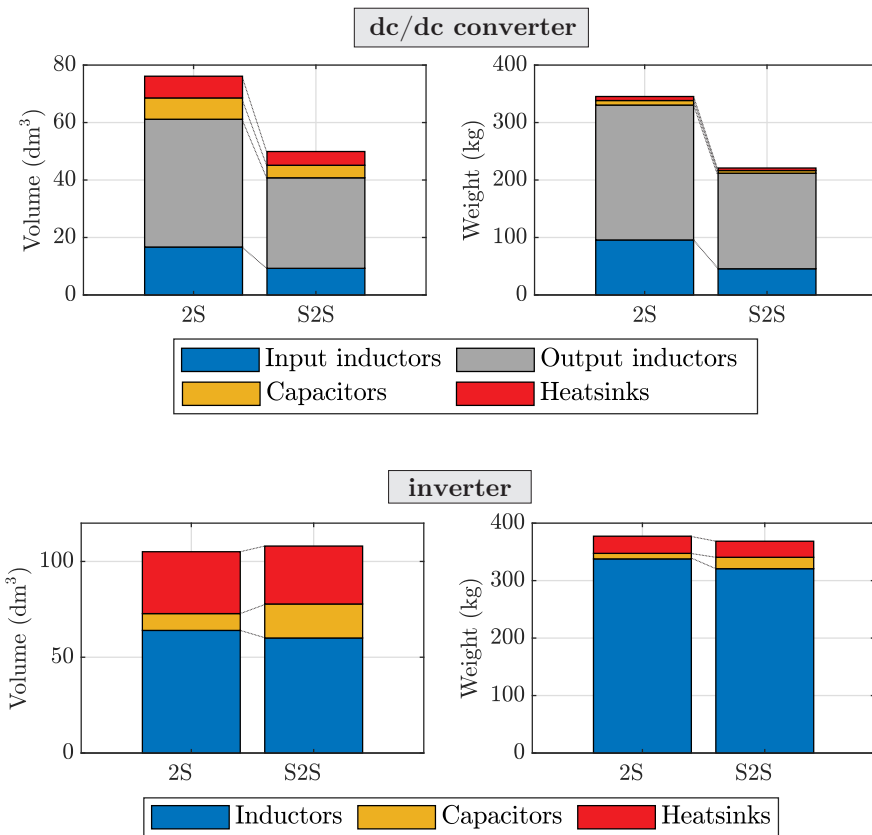


Figure 6.10. Breakdown of volume and weight of power converters in the S2S and 2S architectures.

(-34%) and 124.42 kg (-36%) in the dc/dc converter. The volume required by filters and heatsinks in the traction converters is almost the same, 105.1 liters for the **VSI** and 108.0 liters for the **MSI** (+2.8%). In this case, the volume saving yielded by a smaller line inductor is compensated by the extra volume required by the additional LC filter on the **LV** dc bus. However, the extra iron-core magnetics and capacitors do not significantly affect the weight, and the **MSI** benefits from a moderate 2.3% weight reduction (368.6 kg, against 377.3 kg required by the **VSI**). When looking at the two converters of each motored car as a whole power electronics system, volume and weight savings of 22.7 liters (-13%) and 133.2 kg (-19%) are achieved by the **S2S** traction architecture. According to the system-level specifications provided by the battery manufacturer [129], this could allow adding 2.9 kWh (+6%) for the same system volume, or 11.7 kWh (+24%) for the same system weight.

6.1.4 Dynamic performance and power losses

The complete models of the **2S** and **S2S** traction system are simulated over the given driving cycle for two initial **SOC** levels of 35% and 50%. In Figure 6.11(a-e), the traction effort, ac current, dc power flows, and **SOC** of one traction unit are reported for each driving condition and circuit configuration. The traction motors operate equally in the two topologies, as required by the common vehicle speed profile. The two motors develop a maximum traction effort of 36 kN and absorb from the traction converter a peak **RMS** current of 675 A. The power absorbed from the catenary entering the unit is limited to 172 kW A (corresponding to 250 A of current) and drops to zero during every braking as well as on the non-electrified driving section. The **SOC** decreases most notably during the catenary-free driving section but remains above the lower control threshold of 45% when starting from 50% so that the battery-charging functionality is not activated. In this condition, the battery delivers an absolute maximum power of 344 kW which is compatible with the maximum non-continuative current of 736 A (8C). This is also the absolute peak of the power processed by the dc/dc converter in the **2S** system. This peak rating reduces to 183 kW (-47 %) in the **S2S** system. On the other hand, a net battery charging of +1.5% is achieved along the driving cycle for a starting **SOC** is 35%, meaning that repeated driving in this condition would bring the **SOC** in

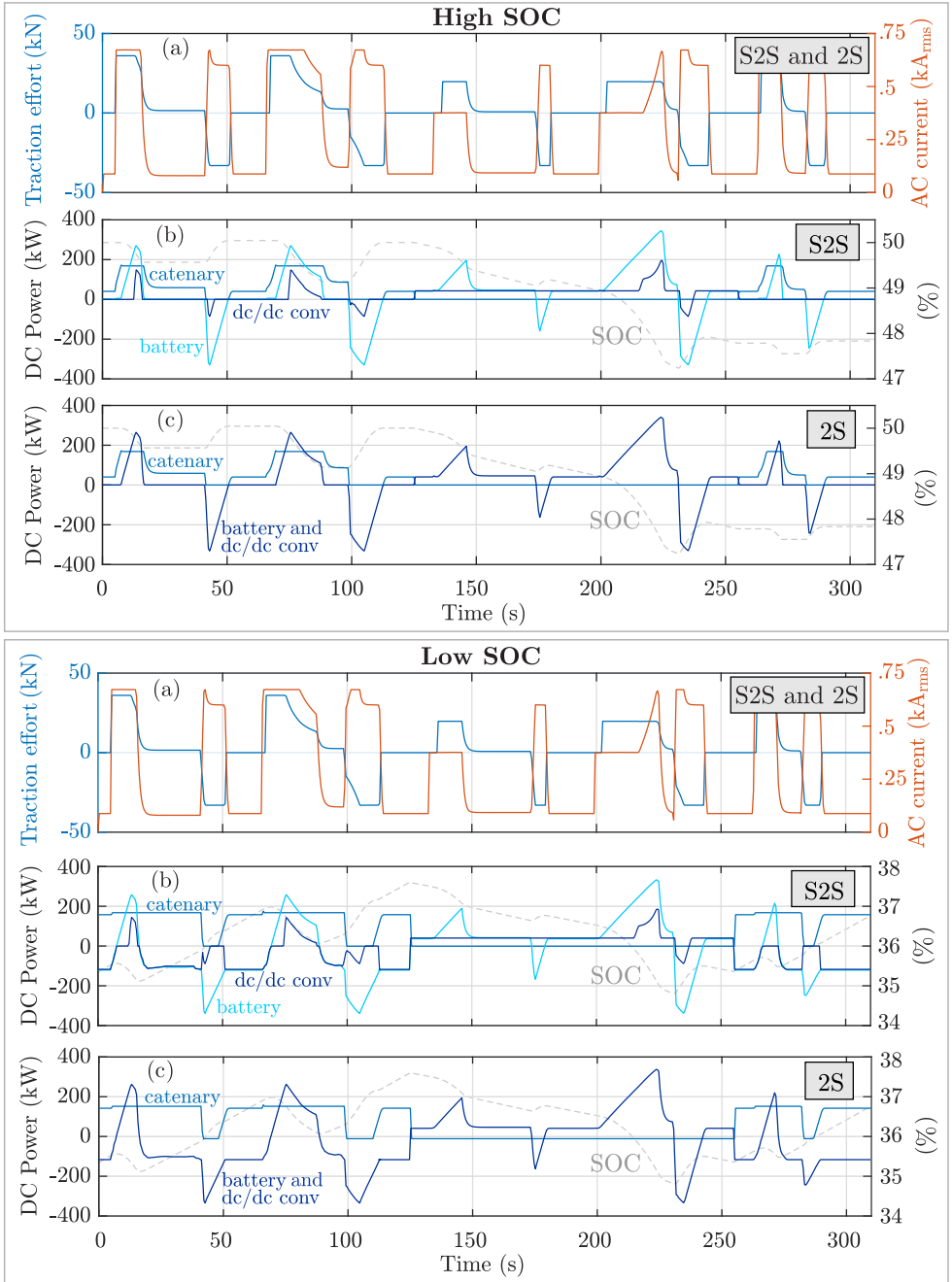


Figure 6.11. Simulation results with high and low SOC: (a) traction effort and motor RMS current, (b-c) dc power levels and battery SOC.

the desired range (without even considering a deeper recharge during terminal stops). The peak power levels in the catenary, battery, and dc/dc converter are equal to the previous case since recharging is commanded during standstill and low-load constant-speed intervals and does not affect the operation during high-power transients.

In Figure 6.12, the operating points at time instants $t_1 = 30$ s (steady-state speed, power drawn only from catenary), $t_2 = 76$ s (maximum traction power in catenary traction mode), $t_3 = 224$ s (maximum traction power in catenary-free mode), and $t_4 = 235$ s (maximum braking power in catenary-free mode) of the driving cycles starting from 50% SOC are highlighted by a view of the main system variables. The traction drive voltages and currents reflect typical PWM waveforms with variable switching frequency. A peak current of 1030 A is drawn from the traction converters. The ac current distortion is the highest at time instant t_1 , which corresponds to a high-speed low-torque operation of the drive, and greater for the MSI. This is expected because the SVM technique generally yields a lower ac THD with respect to down-shifted modulations like the MOVIM [134], especially at low loads and low carrier frequency ratios. In either configuration, the line current entering the traction unit i_{HV} (which is half of the total pantograph current) has almost no ripple thanks to the HV LC filters of the two converters. In the 2S architecture, the battery current i_{LV} is equal to the current entering the dc/dc converter and benefits from its three-phase interleaved topology, which produces a total current ripple much lower than that of the individual leg currents and with a triple equivalent switching frequency. Thanks to the LV LC filter in the S2S topology, the high-frequency harmonic ripple produced by the MSI is almost absent in the battery current, whose harmonic distortion is mostly affected by the dc/dc converter switching operation. The currents drawn by one leg inductor have a similar shape but very different peak values in the two topologies, most notably at time stamps t_3 and t_4 when all the traction power is supplied by the battery and the partial-power-processing feature of the S2S system gives the greatest benefit in terms of dc/dc converter peak current reduction. The absolute current peak in each leg inductor is 190 A and 305 A for the S2S and 2S topologies, while that of each MSI LV inductor is 160 A. These limits are compliant with the design specifications derived above. From these time-domain plots, it

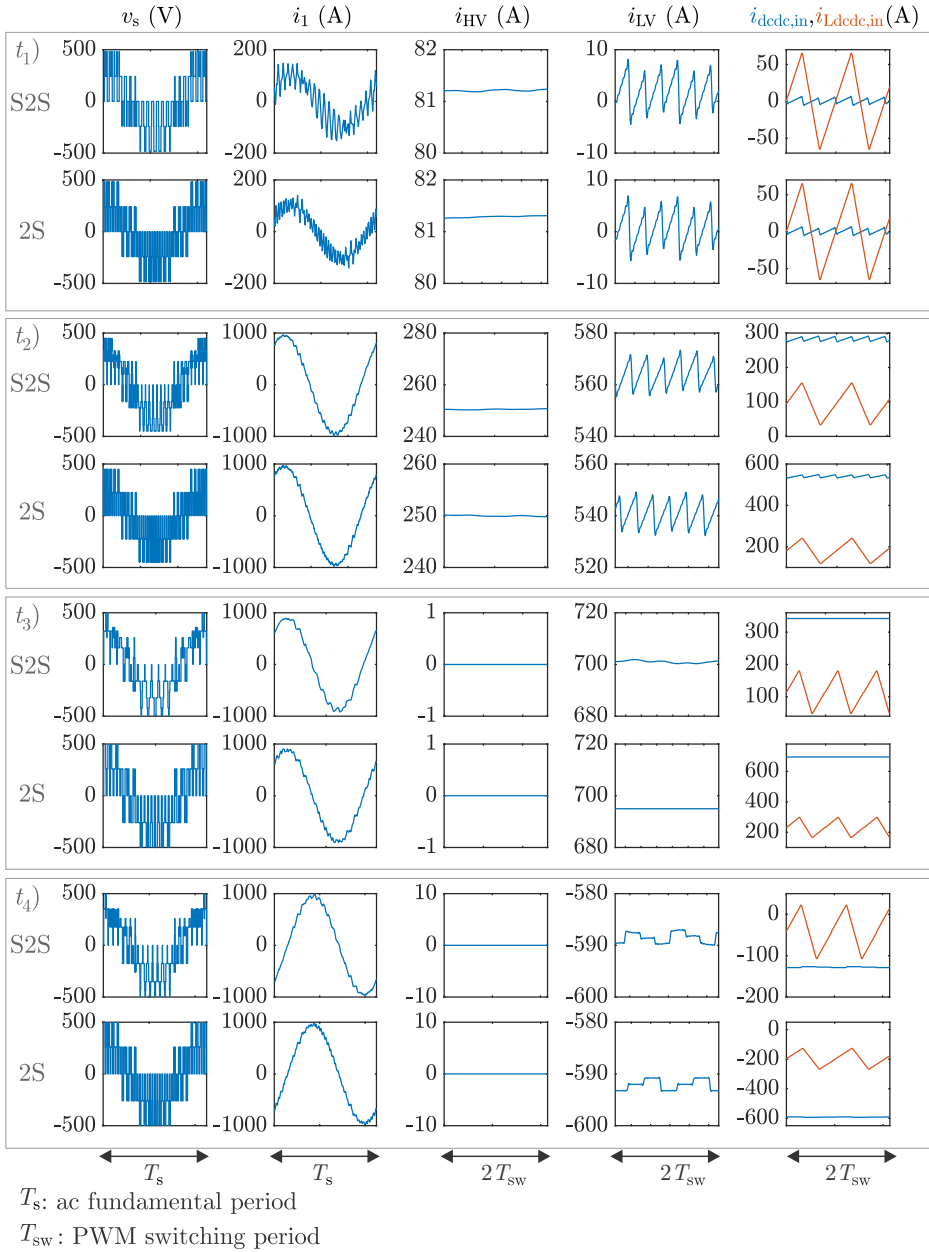


Figure 6.12. Waveforms of the main dc and ac variables at different time stamps of the driving cycle at high SOC.

can be said that the **S2S** topology proposed in Figure 6.2(b) is equivalent to the standard **2S** semi-active topology as regards the operation of the traction drive, catenary, and battery systems.

Although the **S2S** configuration is primarily envisioned to reduce the weight and volume of the onboard dc/dc converter, the analysis of power losses is mandatory to ensure that the **S2S** system efficiency is not impacted. Power losses in the components of one traction unit are evaluated with reference to the driving cycle starting from 50% of **SOC**. Figure 6.13 shows the power losses of one traction motor and a scatter plot of its efficiency values collected along the driving cycle. The power loss curves mostly coincide, with some minor displacement at very light loads due to the aforementioned better **THD** characteristic of the **SVM** modulation. Overall, 624.7 Wh and 625.29 Wh are dissipated in the motor windings in the **2S** and **S2S** topologies, respectively. Similarly, the efficiency calculation yields very similar results, with the two scatter plots almost over-

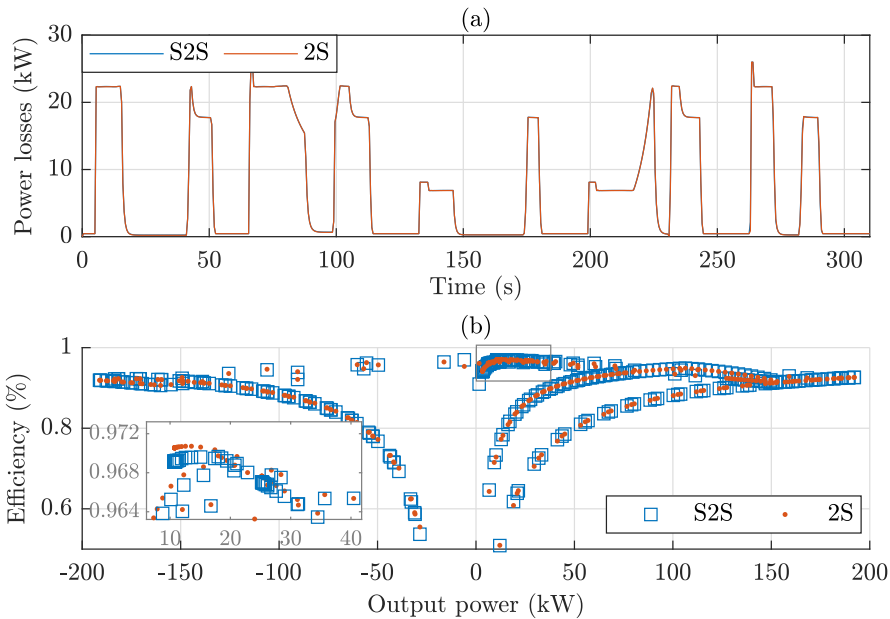


Figure 6.13. Motor power losses (a) and efficiency (b) over the driving cycle in the **2S** and **S2S** topologies.

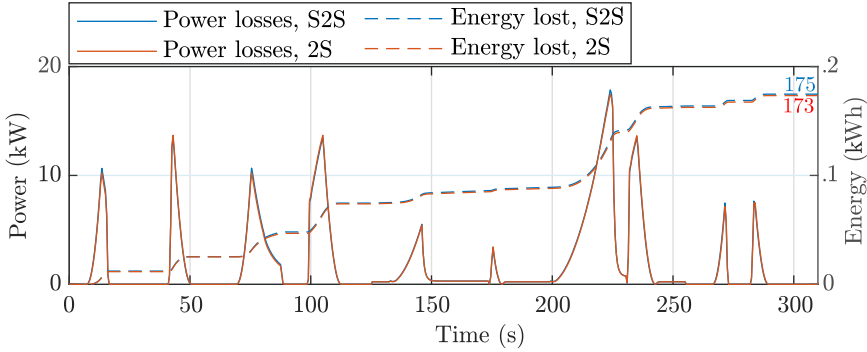


Figure 6.14. Battery internal losses in the **S2S** and **2S** topologies.

lapping over the output power range of the motor. It can be thus inferred that the adoption of the **MSI** as traction inverter does not alter the electrical and thermal performance of the motor.

The battery internal losses are also evaluated, as they might differ between the two architectures due to possible differences in the **RMS** current profile. As shown in Figure 6.14, there is no evidence of any degradation of the battery efficiency in the **S2S** architecture. The final amounts of energy dissipated inside the storage device are 173.3 Wh and 174.8 Wh (+0.76%) in the **2S** and **S2S**, respectively.

Energy is dissipated in electronic converters mainly due to conduction and switching losses in the semiconductors, and Joule losses in inductors and capacitors. Figures 6.15(a)-(b) present a detailed breakdown of instantaneous power losses and cycle energy losses in the **MSI** and **VSI** traction converters (all energy losses in the pie diagrams are normalized with respect to the **VSI** total losses). Conduction losses are always larger in the **MSI**, especially during high-current operation, due to the doubled switch count and on-state voltage drop of the conduction paths involving the inner switches. Globally, conduction losses in the **MSI** increase by 17% (from 41% to 48%). On the other hand, switching losses are much lower in the **MSI**. In fact, for most of the time the **MOV** works as a down-shifted **PWM** (see also Figure 4.16) and only two legs are switched at the same time, whereas in the **SVM** all three legs are switched simultaneously. Overall, the energy lost due to switching in the **MSI** reduces by one-third (from 46% to 30%). As expected, power losses in the filters are mainly located

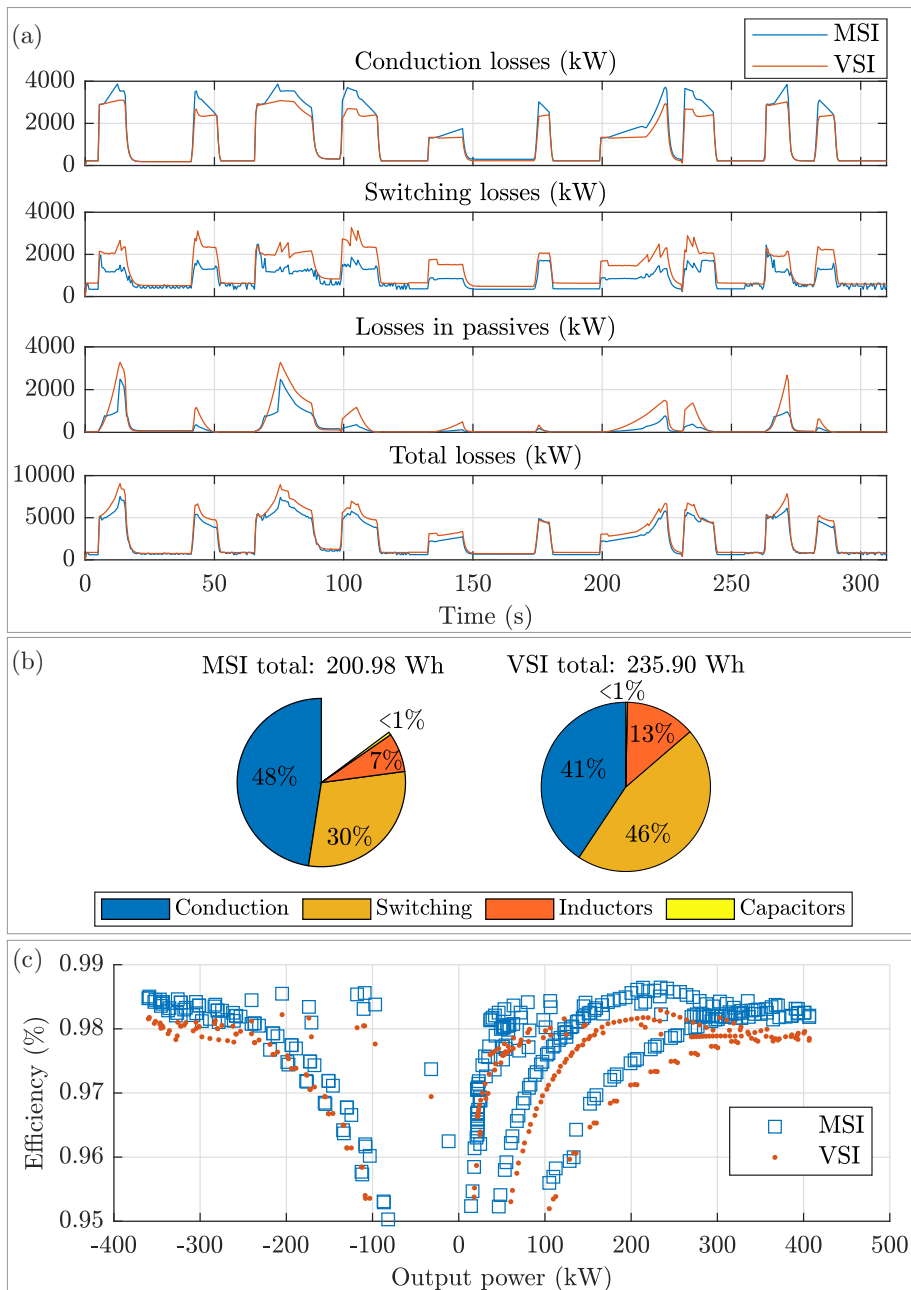


Figure 6.15. Breakdown of power losses (a) and cycle energy losses (b), and efficiency (c) of the MSI and VSI traction converters.

in the inductors. Despite having one input inductor more, the **MSI** also displays lower filter losses. Thanks to the iron-core design (which yields few turns) and parallel arrangement, the additional **LV** inductors in the **MSI** give a minor contribution to the total losses, which are mostly caused by the resistance of the **HV** line filter. However, the **MSI** line inductor has a lower resistance, due to its smaller inductance and fewer turns, and processes a lower dc current, due to the partial-power-processing operation of the **S2S** topology. Over the entire cycle, the inductor losses are reduced by 46% in the **MSI** (from 13% to 7%). Overall, the total energy lost in the traction converters over the driving cycle is 15% lower in the **MSI**, and the scatter plot of Figure 6.15(c) confirms that the **MSI** reaches slightly higher efficiencies for either positive and negative ac power levels.

The same analysis is done for the dc/dc converter and yields the results shown in Figure 6.16. In this case, the impact of the **S2S** partial-power-processing on the converter losses is apparent, with every share of power loss being lower in the **S2S** topology. As a matter of fact, conduction losses are almost halved (from 28% to 15%), switching losses are reduced by one-fourth (from 41% to 31%), and copper losses in the inductors are significantly reduced by a factor of 75% (from 31% to 8%). Overall, the energy lost in the power converter along the driving cycle reduces by 46%. It is however worth noticing that this result derives only from the fact that the converter processes a reduced amount of power, both as peak values and on average, and therefore dissipates a reduced amount of energy. These cycle energy savings do not reflect an inherent higher efficiency of the dc/dc converter in the **S2S** configuration. On the contrary, the efficiency is higher in the **2S** topology, probably because semiconductors with a higher current rating are used in the converter.

When looking at the cycle energy losses of the whole system, the traction motors, dc/dc and dc/ac power converters, and battery packs in one traction unit of the **S2S** and **2S** circuits dissipate 1.041 kWh and 1.109 kWh, respectively. Although not impressive, this 6.1% reduction in the total cycle energy losses suggests that the **S2S** architecture does not affect the energy efficiency of the traction system but, conversely, can improve it to a moderate extent through a different routing of the system power flows.

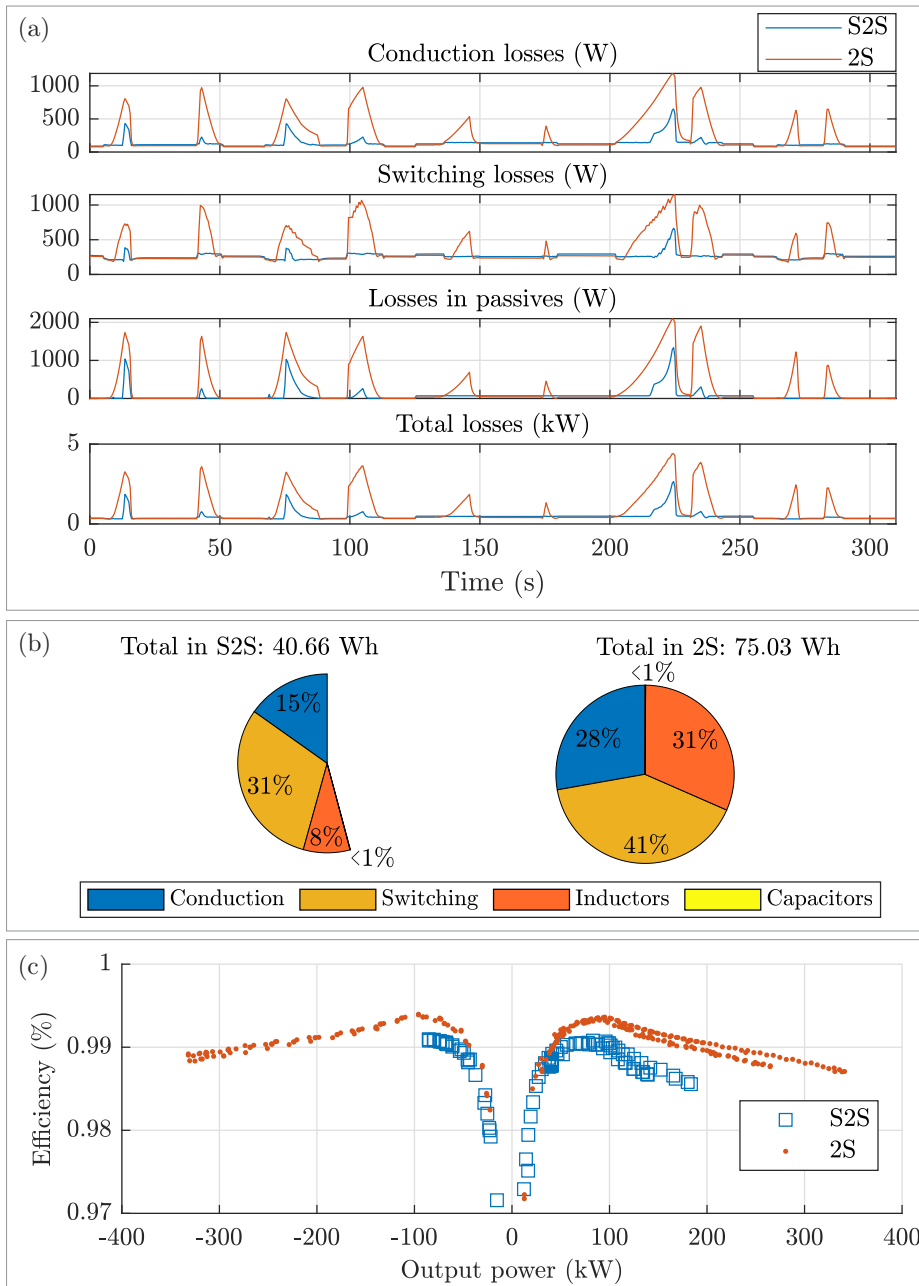


Figure 6.16. Breakdown of power losses (a) and cycle energy losses (b), and efficiency (c) of the dc/dc converter in the S2S and 2S topologies.

6.2 Case study: fuel cell train

6.2.1 System architecture and control

The second case study focuses on the FV-E991 fuel cell/battery train developed by JR East, Hitachi, and Toyota [70]. The vehicle, shown in Figure 6.17(a), has one motored and one trailer car, a rated loaded mass of 78 t, and can reach a maximum speed of 100 km/h with a startup acceleration of 0.64 m/s^2 . Each of the two bogies under the motored car is equipped with two 95 kW asynchronous motors, which yield the total traction effort and traction power curves of Figure 6.17(b). The onboard battery system has a rated voltage of 750 V and a rated energy of 240 kWh. It is assumed that 3.6V/85 Ah NMC cells in a 200s4p arrangement are employed to assemble the battery pack, resulting in the voltage-SOC profile of Figure 6.17(c). The fuel cell system is made from the parallel connection of four 60 kW PEMFC stacks with a voltage of 450 V at rated load, for a total nominal output power of 240 kW. The polarization and efficiency curves of one FC stack, obtained by parametrizing the model developed in [135] based on these power and voltage ratings, are shown in Figure 6.17(d)-(e).

The 2S and S2S traction architectures of the vehicle under comparison are depicted in Figure 6.18. In the 2S architecture, the centralized fuel cell system is interfaced through an interleaved boost converter to the HV bus, to which the battery is directly attached. The HV dc-link feeds two traction drives in parallel, each one constituted by a VSI supplying two induction motors. The boost converter and VSIs are equipped with LC input filters to prevent switching harmonicst flow through the HV bus into the battery. In the S2S system, the additional LV bus at FC voltage level is present which connects the power source directly to the LV inputs of the traction MSIs through an additional LC filter. The filter reduces the harmonics generated by the MSIs, which would otherwise flow into the FC. In both cases, a constant power consumption of 50 kW from the auxiliary converter is assumed.

The EMS of this specific hydrogen train is not known, so the state-machine control presented in [93] for an equal traction architecture is here considered. To operate the FC system at an efficiency always above 35%, its output power is constrained between a lower threshold $P_{\text{FC},\text{min}}$ of 40

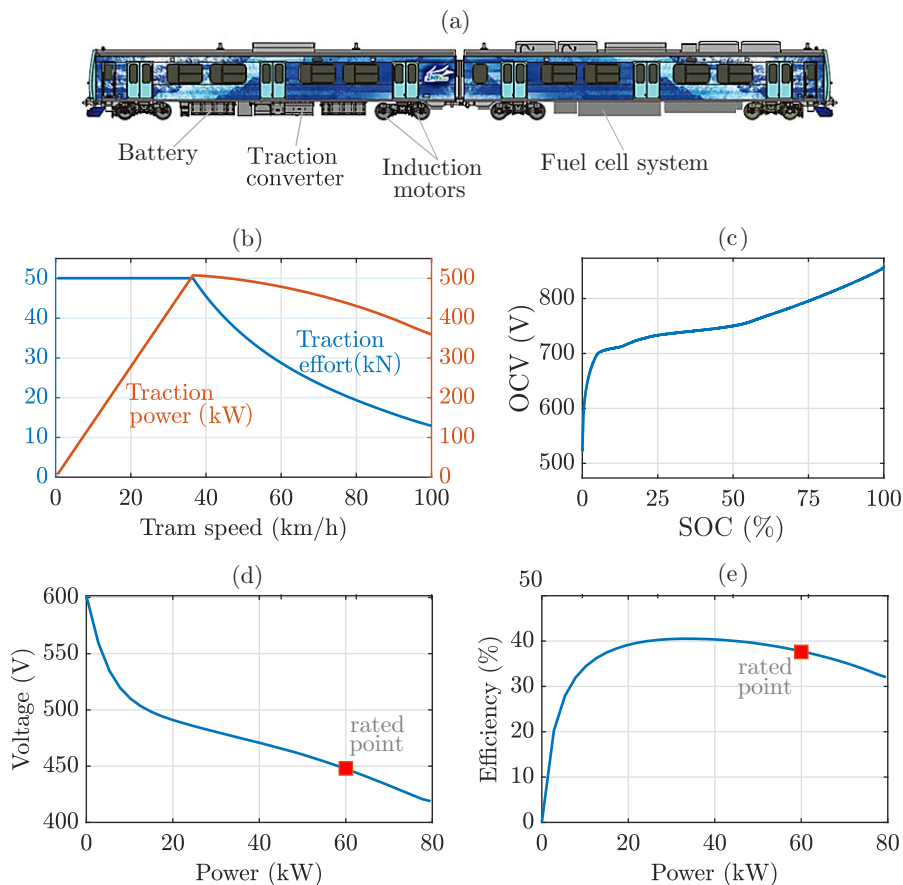


Figure 6.17. Fuel cell train: (a) vehicle layout, (b) traction effort/power curves, (c) OCV-SOC curve of the battery, (d) polarization curve and (e) efficiency curve of one FC stack.

kW and an upper threshold $P_{FC,max}$ of 280 kW. The rated power $P_{FC,r}$ is 240 kW, while the peak efficiency of 40% is obtained at the optimum power level $P_{FC,opt}$ of 120 kW. Regarding the battery SOC, three ranges are defined: high ($SOC > 60\%$), medium ($40\% < SOC < 60\%$), and low ($SOC < 40\%$). Based on these definitions and on the instantaneous traction power demand P_t , the FC power reference (labeled P_{LV}^* for consistency with the symbols used so far) is assigned by the following state-machine:

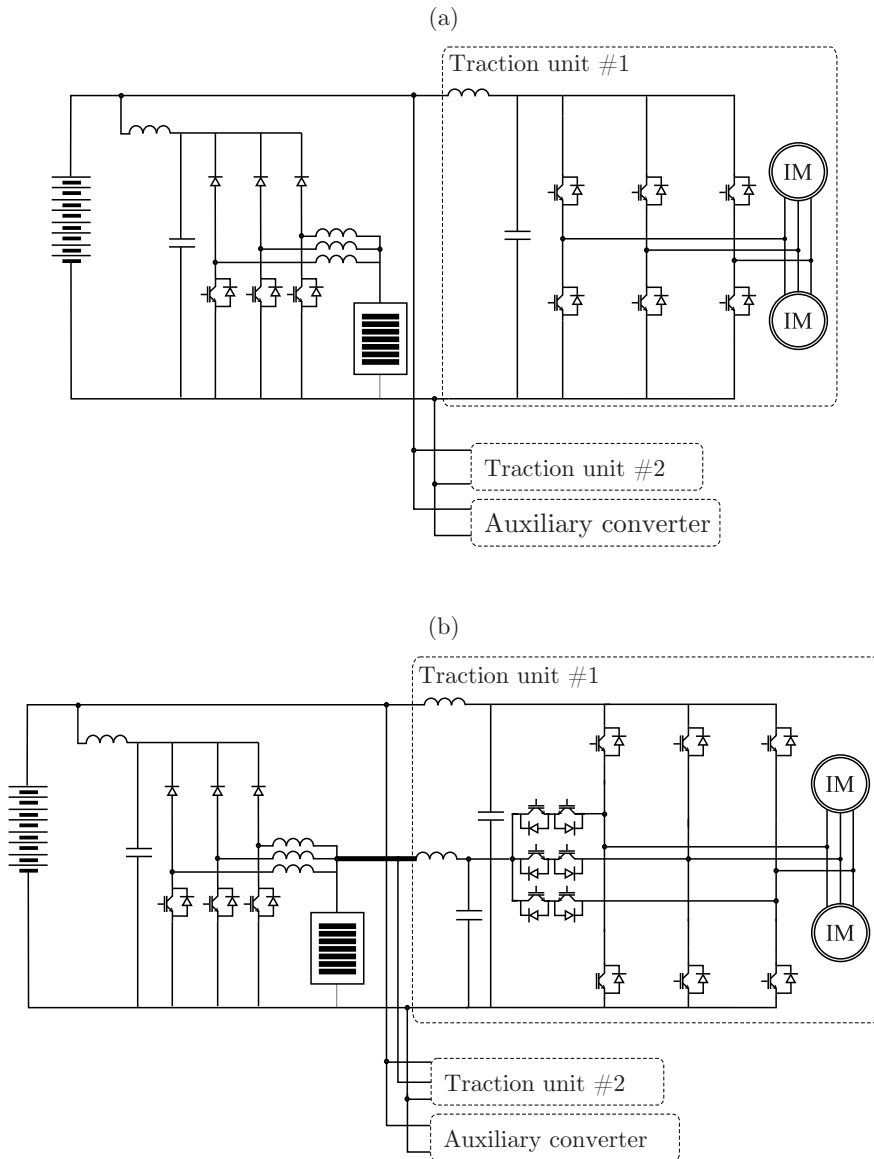


Figure 6.18. Traction circuits: (a) baseline semi-active architecture, (b) S2S semi-active architecture.

Train stopped ($P_t = 0$)

State 1 SOC is low, and the FC recharges the battery at rated power:

$$P_{LV}^* = P_{FC,r}.$$

State 2 SOC is medium, and the FC recharges the battery at optimum power: $P_{LV}^* = P_{FC,opt}$.

State 3 SOC is high, and the FC is operated at minimum power:

$$P_{LV}^* = P_{FC,min}.$$

Traction ($P_t > 0$)

State 4 SOC is high and $P_t < P_{FC,opt}$: $P_{LV}^* = P_t$, i.e., the FC delivers the entire traction power.

State 5 SOC is high and $P_t > P_{FC,opt}$: $P_{LV}^* = P_{FC,opt}$, i.e., the FC is at optimum power and the battery supplies the surplus traction power.

State 6 SOC is medium and $P_t < P_{FC,r}$: $P_{LV}^* = P_{FC,r}$, i.e., the FC is at rated power and recharges the battery.

State 7 SOC is medium and $P_t \in [P_{FC,r}, P_{FC,max}]$: $P_{LV}^* = P_{FC,max}$, i.e., the FC delivers maximum power and recharges the battery.

State 8 SOC is medium and $P_t > P_{FC,max}$: $P_{LV}^* = P_{FC,max}$, i.e., the FC delivers maximum power and the battery makes up for the surplus of traction power.

State 9 SOC is low: $P_{LV}^* = P_{FC,max}$, i.e., the FC is operated at full power, while the battery is recharged or discharged depending on the instantaneous level of traction power required by the train.

Braking ($P_t < 0$)

State 10 $P_{LV}^* = P_{FC,min}$, i.e., the FC is always operated at minimum power, and the battery recovers the braking power.

The torque of the traction motors is controlled through a standard field-oriented control scheme. Conventional carrier-based PWM with third-harmonic injection and the MOVIM are employed for the modulation of

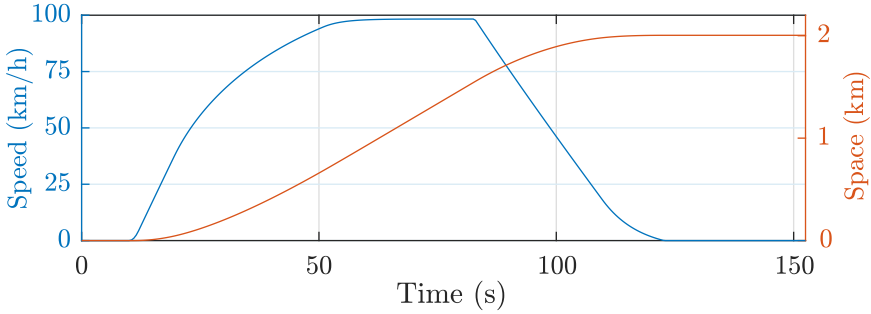


Figure 6.19. Driving cycle of the fuel cell train.

the VSIs and MSIs, respectively, while a phase-shift modulation is used for the three-phase interleaved dc/dc converter.

The two traction systems are compared with reference to the driving cycle in Figure 6.19. The train runs for a distance of 2 km and reaches its maximum speed of 100 km/h. Ten and thirty seconds of dwell time at the beginning and end of the cycle are considered, respectively.

6.2.2 Sizing of power converters

Interleaved boost converter

In each topology, the converter peak current depends on the EMS state and hence on the battery SOC. Preliminary calculations with a low SOC yield the following worst-case average-current peaks at the converter input and output:

$$\begin{aligned} \hat{i}_{\text{dcdc,in}}^{(\text{S2S})} &= 405\text{A}, \quad \hat{i}_{\text{dcdc,in}}^{(2\text{S})} = 670\text{A} \\ \hat{i}_{\text{dcdc,out}}^{(\text{S2S})} &= 245\text{A}, \quad \hat{i}_{\text{dcdc,out}}^{(2\text{S})} = 400\text{A} \end{aligned}$$

Considering a worst-case peak-to-peak ripple of 50 A in the input currents and a switching frequency of 2 kHz, sizing equations (C.1)-(C.3) give for each leg inductor the specifications in Table 6.11. Iron-core inductors are designed to meet these specifications, and the results of the design are reported in Table 6.12.

Based on the peak current in each leg inductor, and considering that

Table 6.11. Leg inductors of the dc/dc converter: design specifications

	Inductance	Peak current
S2S	480 μH	230 A
2S	480 μH	315 A

Table 6.12. Leg inductors of the dc/dc converter: design results

	S2S	2S
Inductance	486 μH at 230 A	490 μH at 315 A
Cores	2xAMCC 500	4xAMCC 400A
Resistance	0.77 m Ω	1.03 m Ω
Volume	2.81 dm ³	3.66 dm ³
Weight	13.26 kg	20.14 kg

the maximum battery voltage is below 900 V, IGBTs with the VA rating reported in Table 6.13 selected for the dc/dc converter.

In this case, the train has no connection to an overhead supply connected to a station rectifier. Hence, no low-frequency line voltage ripple mitigation is required, and the LC filter at the converter output has to function to reduce the switching current harmonics flowing into the HV bus and battery. The cutoff frequency is selected to 300 Hz, which is 1/20 of the equivalent switching frequency of 6 kHz yielded by three-phase interleaving. Imposing an output voltage ripple of 7.5 V (1% of the rated battery voltage) and considering the absolute peak current output by the converter in the two architectures, sizing equations (C.4),(C.17)-(C.18) yield for filter inductor and capacitor the specifications reported in Table 6.14. Iron-core inductors and film capacitors with a rated permanent volt-

Table 6.13. Dc/dc converter IGBTs VA rating

	VA rating	
	Blocking voltage	Rated current
S2S	1.7 kV	225 A
2S	1.7 kV	400 A

age of 900 V are designed and selected, respectively, with the outcomes reported in Table 6.15.

The heatsinks of the converters are sized considering again a driving cycle under a condition of low SOC, as this case corresponds to the maximum power and energy transferred through the dc/dc converter. With reference to this worst-case driving condition, the heatsink design procedure returns the results given in Table 6.16 with the corresponding temperature profiles shown in Figure 6.20.

Traction converters

The VSI and T-NPC MSI traction converters supply two motors in parallel, which draw an absolute peak current of 570 A. The switches of the VSIs and the outer switches of the MSIs have to withstand the maximum battery voltage of 850 V. On the other hand, the MSI inner

Table 6.14. LC filter of the dc/dc converter: design specifications

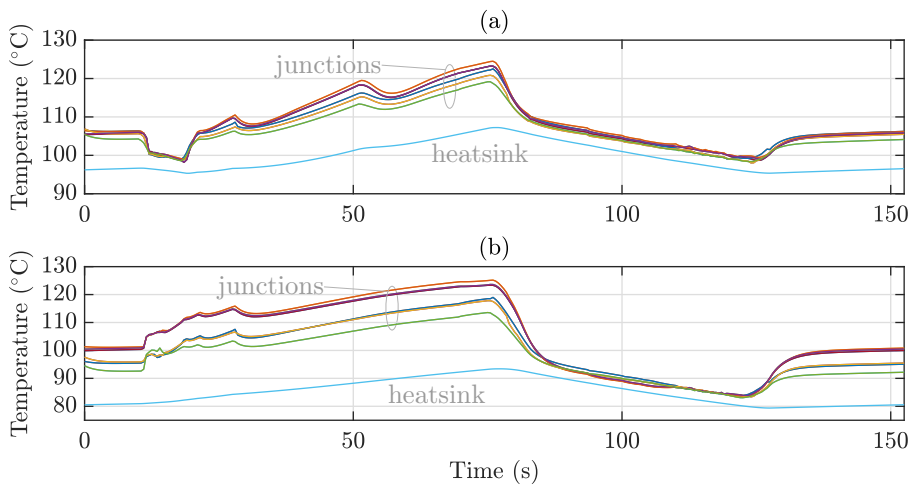
	Inductor		Capacitor	
	Inductance	Peak Current	Capacitance	Peak RMS Current
S2S	135 μH	245 A	2.2 mF	75 A
2S	65 μH	400 A	4.4 mF	105 A

Table 6.15. LC filter of the dc/dc converter: design results

		S2S	2S
Inductor	Inductance	136 μH at 245 A	63 μH at 400 A
	Cores	2xAMCC 250	2xAMCC 320
	Resistance	0.20 m Ω	0.08 m Ω
	Volume	1.54 dm ³	1.96 dm ³
	Weight	8.50 kg	9.65 kg
Capacitors	Model	1xB25620B02	2xB25620B02
	Capacitance	2.2 mF	4.4 mF
	Resistance	1.3 m Ω	0.65 m Ω
	Rated RMS current	80 A	160 A
	Volume	2.68 dm ³	5.36 dm ³
	Weight	2.85 kg	5.70 kg

Table 6.16. Heatsink of the dc/dc converter: design results

	S2S	2S
Thermal resistance	0.039 K/W	0.016 K/W
Thermal capacitance	4560 J/K	12450 J/K
Volume	5.54 dm ³	15.12 dm ³
Weight	5.13 kg	14.0 kg

**Figure 6.20.** Temperatures in the dc/dc converter in: (a) S2S topology, (b) 2S topology

switches have to withstand the maximum fuel cell voltage of 600 V at no-load. Based on these requirements, IGBTs with the VA ratings reported in Table 6.17 are selected.

Table 6.17. Inverter IGBTs VA rating

		VA rating	
		Blocking voltage	Rated current
MSI	Outer switches	1.7 kV	600 A
	Inner switches	1.2 kV	
VSI		1.7 kV	600 A

The traction inverters operate at variable switching frequency [132]: at low speed, asynchronous PWM at 1.5 kHz constant frequency is employed; as the fundamental frequency increases, synchronous PWM with a triple and odd carrier frequency ratio is used. The LC filters at the input of VSIs and MSIs are tuned to filter the switching-frequency current harmonics injected by the inverters. Their cutoff frequency is chosen with resonant-frequency considerations based on the inverter switching frequency [133] and is set to 75 Hz. The maximum current drawn by one traction converter in the different configurations is estimated to be:

$$\begin{aligned}\hat{i}_{\text{vsi}} &= 365\text{A} \\ \hat{i}_{\text{msi,HV}} &= 365\text{A}, \hat{i}_{\text{msi,LV}} = 165\text{A}\end{aligned}$$

It is worth noticing at this point that, the maximum current flowing through the HV input inductor is equal for the MSI and VSI. The current peak occurs during braking when all the power generated by the motors is sent back to the battery. Since the storage device is connected directly to the HV-bus, the current flowing towards the battery through the HV inductor is the same irrespective of the topology. Considering these peak-current ratings and imposing a voltage ripple of 7.5 V on the VSI and MSI HV buses and of 4.5 V on the MSI LV bus (i.e., 1% of either rated voltage), sizing equations (C.4),(C.20)-(C.21) yield for filter inductors and capacitors the specifications reported in Table 6.18. Film capacitors with a rated permanent voltage of 900 V and 700 V are selected for the HV and LV connections, respectively. All the inductors are designed with an iron core. The results of the inductor design and capacitor selection are given in Table 6.19.

Table 6.18. LC filter of the traction inverter: design specifications

		Inductor		Capacitor	
		Inductance	Peak Current	Capacitance	Peak RMS Current
MSI	HV side	1.3 mH	365 A	3.5 mF	240 A
	LV side	750 μ H	165 A	6.0 mF	240 A
VSI		1.3 mH	365 A	3.5 mF	240 A

Table 6.19. LC filter of the traction inverter: design results

		MSI		VSI
		HV-side	LV-side	
Inductor	Inductance	1.29 mH at 365 A	758 μ H at 165 A	1.29 mH at 365 A
	Core	8xAMCC 1000	4xAMCC 800B	8xAMCC 1000
	Resistance	1.26 m Ω	0.93 m Ω	1.26 m Ω
	Volume	14.39 dm ³	2.78 dm ³	14.39 dm ³
	Weight	87.12 kg	13.23 kg	87.12 kg
Capacitors	Model	3x B25620B0128	4x B25690A0158	3x B25620B0128
	Capacitance	3.6 mF	6.0 mF	3.6 mF
	Resistance	0.4 m Ω	0.3 m Ω	0.4 m Ω
	Rated current	240 A	320 A	240 A
	Volume	5.10 dm ³	6.21 dm ³	5.10 dm ³
	Weight	5.55 kg	6.40 kg	5.55 kg

The heatsinks of the traction converters are dimensioned considering a repeated low-SOC driving condition. The sizing procedure yields the outcomes reported in Table 6.20, with the corresponding junction and heatsink temperature profiles shown in Figure 6.21.

6.2.3 VA rating, weight, and volume comparison

The VA rating of the dc/dc converter is reduced by 44% in the S2S topology thanks to a lower current rating of the switches. On the other hand, the increase in the VA rating of the MSI is only partly mitigated by the choice of a lower blocking voltage for the inner switches and amounts to a + 70%. Overall, the S2S architecture requires semiconductors with a VA rating increased by 24.8% compared to the conventional architecture,

Table 6.20. Heatsink of the traction inverter: design results

	MSI	VSI
Thermal resistance	0.0165 K/W	0.0210 K/W
Thermal capacitance	11620 J/K	8300 J/K
Volume	14.11 dm ³	12.6 dm ³
Weight	13.06 kg	11.32 kg

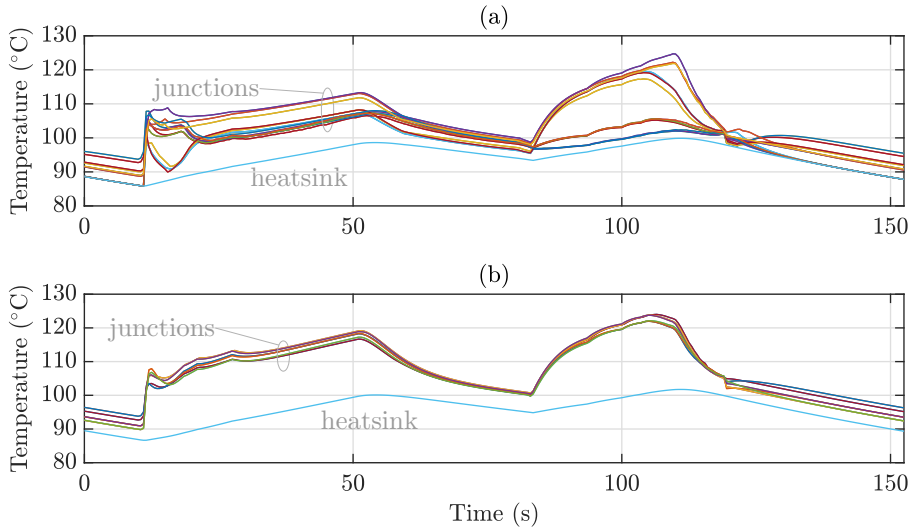


Figure 6.21. Temperatures in the traction converters: (a) **MSI**, (b) **VSI**.

suggesting a comparable increase in the semiconductor supply costs.

The breakdown of volumes and weights in the dc/dc converter and one traction inverter is shown in Figure 6.22. A volume saving of 15.2 liters (-46%) in the dc/dc converter is mainly achieved due to more compact heatsinks and output capacitors, while iron-core input and output magnetics have in this case a minor impact. On the other hand, inductors and heatsinks have the most impact on the total weight, which reduces by 33.51 kg (-37%). Nevertheless, these significant reductions are undermined by the weight and volume increase in the **MSI**s. As previously pointed out, since the extra **LV** connection between the **MSI** and the **FC** does not determine a reduced current rating of the **HV** inductor, all the volume and weight required by the **LV** LC filter simply adds to the total count. As a result, each traction **MSI** requires 10.5 liters (+33%) and 21.37 kg (+21%) more than the **VSI**. Overall, the **S2S** topology adds 6.9 liters (+7%) and 9.2 kilograms (+3%) to the power electronics. It is hence apparent that the volume and weight savings in the dc/dc converter alone are significant but, when looking at the whole traction circuit, the **S2S** topology fails in yielding a smaller and lighter system.

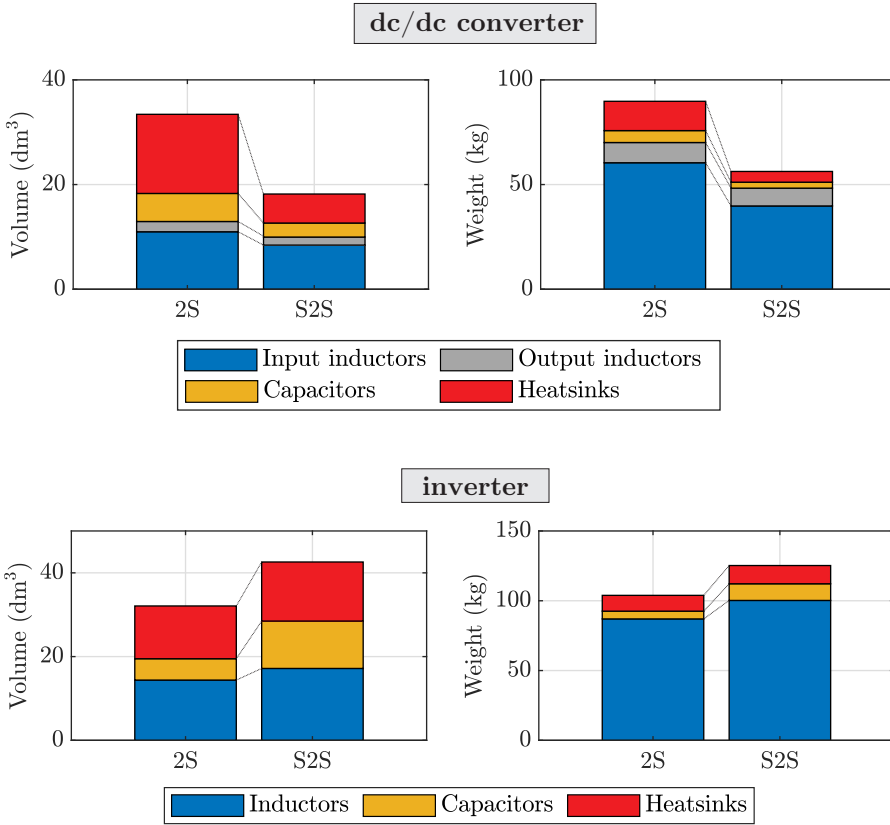


Figure 6.22. Breakdown of volume and weight of power converters in the S2S and 2S architectures.

6.2.4 Dynamic performance and power losses

The two traction architectures are simulated over the given driving cycle for two initial SOC levels of 50% and 38%. In Figures 6.23(a-e), the traction effort and ac current of one traction drive, the dc power levels, and the battery SOC in each condition are depicted. In a medium-SOC state, the battery is lightly recharged during cruising and stops at the optimal FC power level of 120 kW. As required, the FC is at the minimum power of 40 kW during the entire braking, and the battery recovers all the power generated by the motors. Over the entire driving cycle, a slight

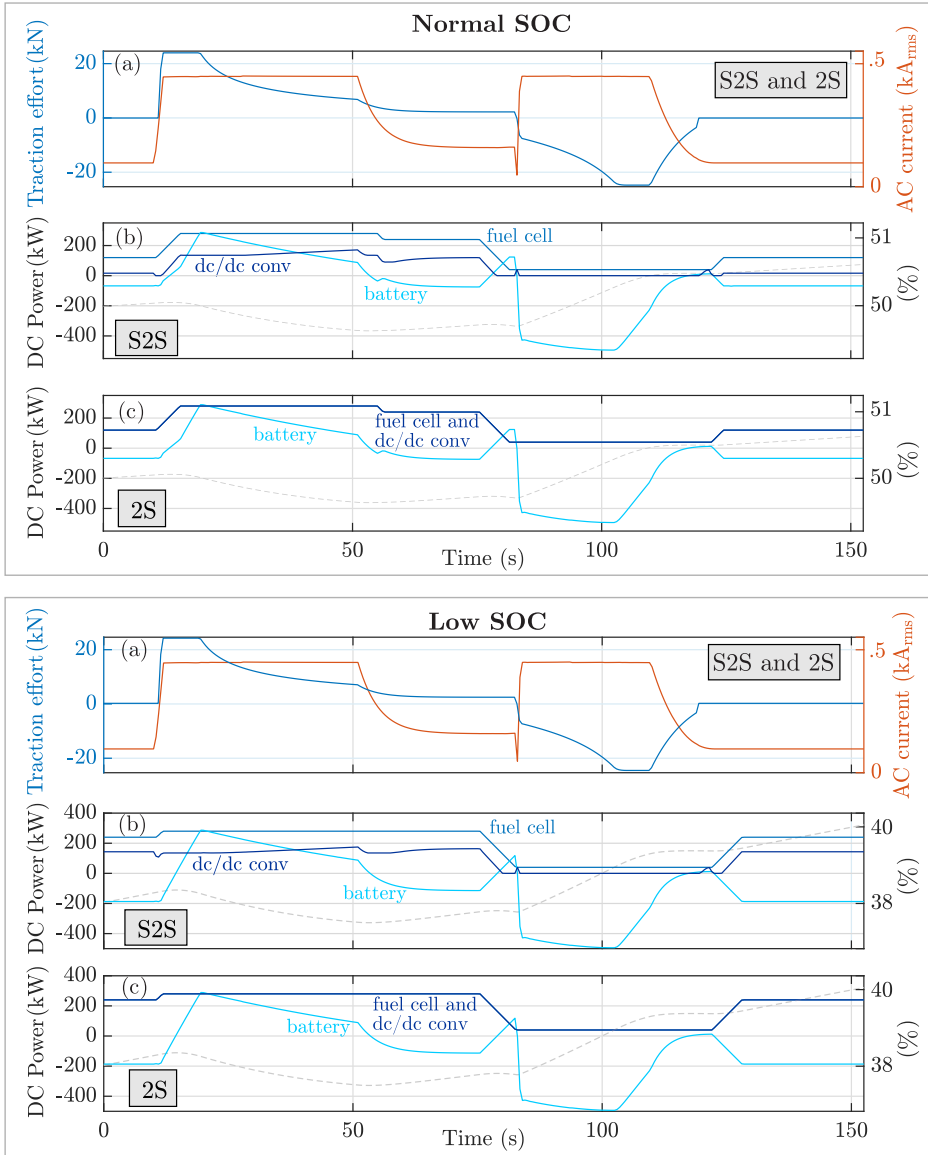
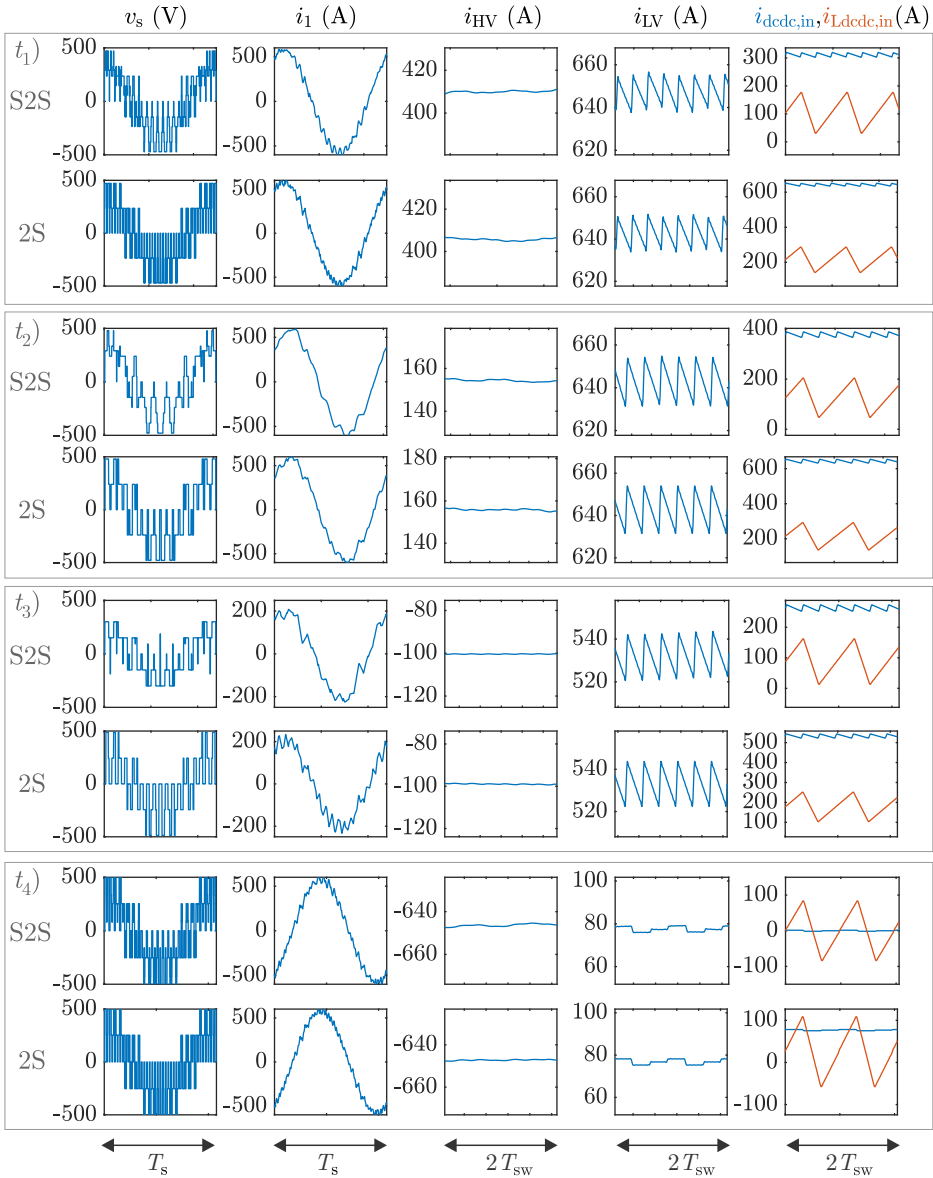


Figure 6.23. Simulation results with medium and low SOC: (a) traction effort and motor RMS current of one traction drive, (b-c) dc power levels and battery SOC.

increase of 0.5% in the SOC is observed, which corresponds to a SOC-sustaining action with no significant recharging effect, in compliance with a medium-charge condition. In the low-SOC condition, the FC output power is increased during acceleration, cruising, and dwell times, so that a net battery recharge of 2% can be accomplished over the considered top-speed driving cycle. During acceleration and cruising, the partial-power-processing operation of the S2S is most evident and yields a 37% reduction in the peak power rating of the dc/dc converter.

The operation of the 2S and S2S topologies at time stamps $t_1 = 20$ s (peak power-assist from the battery during acceleration), $t_2 = 47$ s (end of the acceleration), $t_3 = 70$ s (light battery recharge during cruising), and $t_4 = 101$ s (peak power recovery from the battery during braking) of the medium-SOC cycle is highlighted by a view of the main system variables in Figure 6.24. At the ac side of one traction drive, the VSI and MSI voltage and current waveforms differ because of the different modulation techniques employed. However, the fundamental current is the same and corresponds to an equal average torque produced by the motors at each time instant. The shape and level of the battery currents in the two architectures coincide since an equal LC filter is used between the storage device and the traction inverter. Similarly, the current delivered by the FC is not affected by the S2S configuration, thanks to the LV LC filter that prevents current harmonics from flowing into the FC through the LV bus. The only ripple in the FC current is caused by the dc/dc converter and is much lower than the current ripple in each leg of the converter, thanks to the interleaved topology. On the other hand, it is apparent how the leg inductors carry only a reduced share of the overall FC current in the S2S topology and the whole FC current in the 2S topology.

The power losses and efficiencies of the traction equipment are evaluated with reference to a medium-SOC driving cycle. As in the previous case study, Joule losses in the motor are practically the same in the two configurations, confirming that the MOVIM does not introduce relevant distortion in the motor current compared to the standard SVM. Indeed, the cycle energy losses in two traction motors amount to 177.1 Wh in the S2S architecture and 177.4 Wh in the 2S architecture. The same is true for the battery and FC internal losses, which vary less than 0.5% between the two topologies due to the equal harmonic content of their currents.



T_s : ac fundamental period
 T_{sw} : PWM switching period

Figure 6.24. Waveforms of the main dc and ac variables at different time stamps of the driving cycle at medium SOC.

The breakdown of power losses and efficiencies of one **MSI** and **VSI** are displayed in Figure 6.25. Conduction and switching losses follow the same pattern observed in the former case study. In particular, conduction losses are always higher in the **MSI**. This difference is higher during acceleration and cruising, when a significant power enters the **LV** terminal of the **MSI** and flows through the inner switches, while reduces during braking when only the minimum **FC** power is drawn from the **MSI LV** terminal. On the entire cycle, an 18% increase in energy lost due to conduction is observed for the **MSI**. On the other hand, switching losses experience a more significant reduction of 37% in the **MSI**, going from 41% to 26% over the complete cycle. Differently from the previous case, power losses in the passives are doubled in the **MSI**, due to the additional losses in the **LV** LC filter that are not compensated by those in the **HV** inductor, which has the same inductance and current rating of the **VSI** inductor. However, all inductors are designed with an iron core and have few turns, and their Joule losses amount to only a few percent of the total converter losses. Switching losses have the highest impact on the total losses, so that, overall, the **MSI** is still more efficient than the **VSI** and saves a 5% of energy over the driving cycle. This finds confirmation in the efficiency scatter plot of the two converters, in which the efficiency points of the **MSI** are positioned slightly above those of the **VSI** in the whole range of output power.

Finally, Figure 6.26 shows the energy losses breakdown and efficiency of the dc/dc converter. As expected, every type of power loss in the dc/dc converter is lower in the **S2S** architecture: conduction and switching losses are almost halved (-47% and -39%, respectively) while winding losses in the input and output inductors decrease by a factor of six. On the entire cycle, an energy saving of 44% is observed. However, these energy savings come only from a reduced power rating, whereas the efficiency of the converter in the **2S** architecture is slightly higher, since semiconductors with a higher current rating are employed.

Overall, a total energy of 1.51 kWh and 1.54 kWh is dissipated by the components of the **S2S** and **2S** architectures. This 1.9 % reduction is in line with the results of the previous case study and confirms that, despite the higher device count and circuit complexity, the **S2S** topology does not suffer from a worse efficiency but rather improves it to a moderate extent.

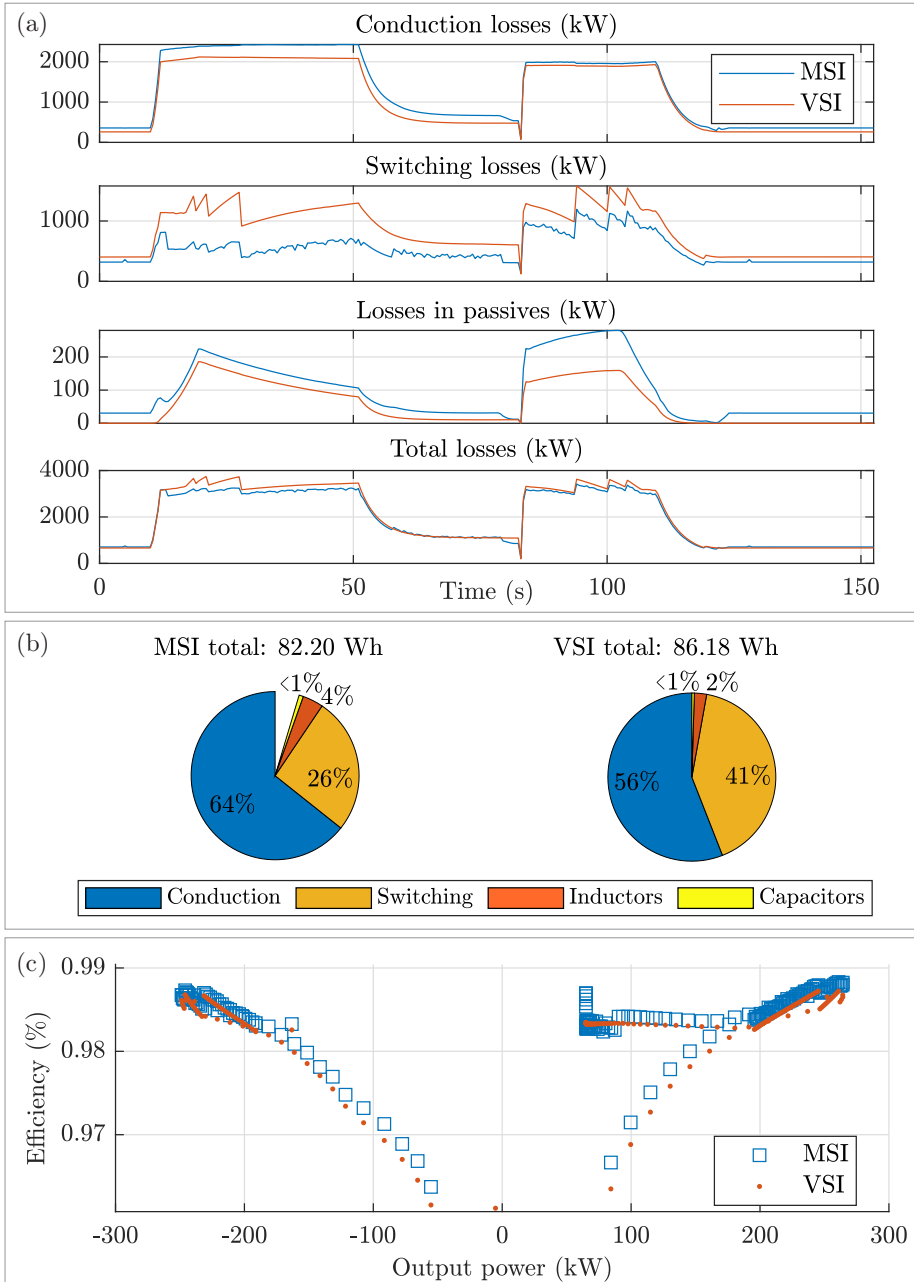


Figure 6.25. Breakdown of power losses (a) and cycle energy losses (b), and efficiency (c) of the VSI and MSI traction converters.

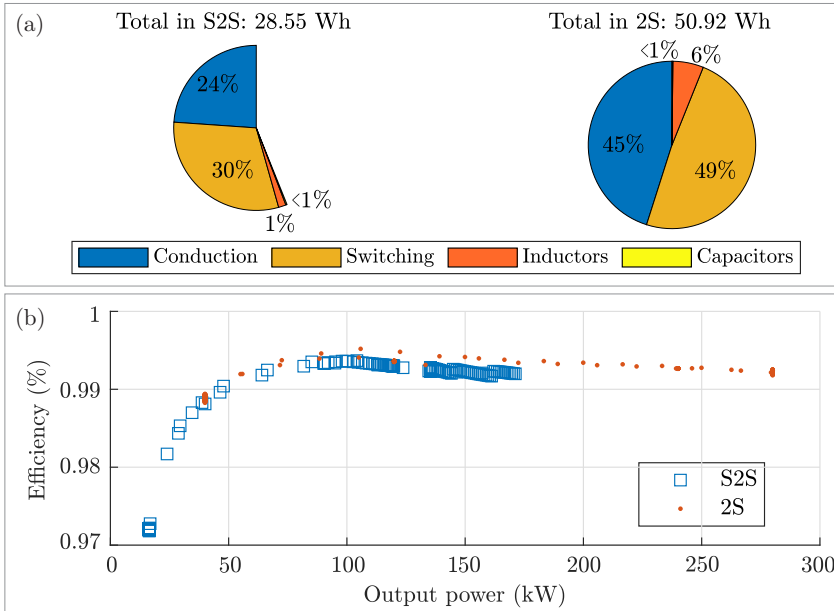


Figure 6.26. Breakdown of energy losses (a) and efficiency (b) of the dc/dc converter in the S2S and 2S topologies.

6.3 Discussion

The outcomes of the two case studies reveal some common features and some discrepancies. In either application, the analysis further confirms that the S2S MSI-based architecture is able to operate the traction system as required by the vehicle mission profile and EMS, with no difference with respect to the standard 2S configuration as concerns the functionality and dynamic behavior of the circuit. From an efficiency point of view, a slight improvement is observed for the power converters of the S2S topology. In the MSI, this is mainly due to the MOVIM technique that reduces the switching losses by a significant amount and compensates for the increase in conduction losses caused by a higher switch count and voltage drop on the MSI conduction paths. In the dc/dc converter, it is the direct result of a lower power rating. On the other hand, no relevant discrepancy is observed between the two systems concerning the RMS current and

losses in the onboard storage devices and fuel cell systems, thanks to the integration of the additional LC filter on the LV bus that prevents any increase in the harmonic distortion of the LV source current. However, the overall VA rating of the power electronic converters is always higher in the S2S architecture and indicates a likely increase in the system capital cost, at least for what concerns the supply of semiconductors.

Concerning the ability of the S2S topology to reduce weight and volumes not only in the dc/dc converters but rather in the entire traction circuit, two different results have been obtained. In the tram with onboard batteries, the receptive storage device is on the LV dc bus, meaning that the power can flow through the additional LV bus of the S2S circuit during both traction and braking. This permits for the line-frequency LC filters on the HV bus an effective downsizing, which is not undermined by the limited size of the switching-frequency LV LC filter. Therefore, for this bimode vehicle, the S2S architecture can achieve relevant savings in the volume (-34%) and weight (-36%) required by passives and heatsinks of the high-power choppers, while leaving the volume and weight of traction converters practically unaltered. In the fuel cell/battery train, the LV bus of the S2S architecture is connected to the unidirectional fuel cell. This determines that the current in the HV inductor of the MSI is reduced only during traction, while it is equal to that of the VSI inductor during braking when all the power is redirected to the battery. Hence, HV inductors of equal current rating are required by the two traction converters, and the additional LC filters in the MSIs bring a net weight and space increase that outweigh the savings yielded by the smaller and lighter FC boost converter. In this case, the S2S topology is unable to improve the power density of a standard semi-active configuration, but rather determines a bulkier (+7%) and heavier (+3%) traction system.

Conclusions

This work explored the integration of the [MSI](#) as main traction inverter in multimode rail vehicles for urban and regional rail services.

A comprehensive review of the traction systems found in numerous multimode vehicles in recent or present operation was first presented. The high number of applications found shows the increasing attractiveness that multimode architectures are gaining thanks to their several advantages. When running on urban railways with high electrification rates, multimode vehicles employ batteries, supercapacitors, or a combination of both to reduce the peak power absorption from the line, maximize the braking energy recovery, and allow partial catenary-free operation. On medium and long-range regional routes with low electrification, hydrogen fuel cell plants in combination with larger battery systems become attractive for diesel-free operation with zero local emissions. The review showed that many multimode trains belong to the category of bimode vehicles, i.e., they employ one storage device (batteries or supercapacitors) and one primary energy source (external line or fuel cell plant). All the reviewed bimode traction systems employ two-level [VSIs](#) to drive the traction motors and one or two dc/dc converters to interface the onboard sources and storage devices to the common dc link. The semi-active configuration, which employs only one dc/dc converter, is often preferred due to its reduced cost and complexity, as high-power choppers feature bulky and heavy magnetics and add considerable weight and volume to the traction system.

The concept of the MSI was reviewed and its state-of-literature interleaved SVM modulation technique was thoroughly discussed and evaluated. The main objective of the MSI is to provide a single-stage conversion between two dc sources and one ac load without intermediate dc/dc converters. Its established modulation technique, the interleaved SVM, operates the converter as two interleaved VSIs in parallel to accomplish the desired sharing of load power between the HV and LV sources. The technique was examined theoretically and assessed experimentally and, despite its simplicity, showed many important limitations in terms of system controllability, feasible operating modes, and input current distortion. For this reason, a different modulation technique was developed and proposed. The MOVIM exploits the space-vector model of the NPC circuit and achieves a smoother and more versatile control of the MSI input currents. Experimental tests confirmed that the envisioned MOVIM remarkably overcomes the limitations of the literature modulation.

Since the NPC circuit lacks any voltage-boosting capability, the maximum power that the MSI can draw from its LV input is limited by the ratio between the LV voltage level and the ac fundamental voltage magnitude. Therefore, a dc/dc converter is still required in a MSI-based traction architecture. For this reason, the integration and control of the MSI in a semi-active architecture employing a dc/dc converter were investigated. In this non-conventional semi-two-stage architecture, the direct connection between the LV source and the load results in a partial bypass of the dc/dc converter. To effectively minimize the peak power and energy processed by the chopper for any operation of the traction system, a strategy for the coordination of the two power converters was proposed. Extensive experimental tests for different configurations and representative EMS controls of the input sources validated the S2S architecture and control. The results showed that the S2S system ensures the proper operation of the motor drive and power sources while achieving reductions in the peak current and cycle energy processed by the chopper of up to 37.2% and 73.6% in the tested conditions.

Extensive numerical investigations were performed to assess the effective potential of an MSI-based S2S architecture for two different real-case applications: a battery tram, and a fuel cell train. For each vehicle, the study compared the VA rating, power losses and efficiencies, and weight

and volume requirements of the **S2S** topology against a conventional semi-active topology with **VSI**s. The comparison focused not only on the dc/dc converter alone but rather on the entire traction system. To this aim, specific modeling and sizing procedures making use of electrical, thermal, and magnetic models in circuit and **FEA** domains were adopted. The outcomes of the two case studies showed many common features but also important differences. As expected, the VA ratings of **S2S** topologies are always higher than that of the **2S** topologies due to the doubled switch count in the **MSI**. However, thanks to a lower current rating of the dc/dc converter and a lower voltage rating of the T-NPC **MSI** inner switches, the total VA rating does not double. Indeed, its increase was quantified in 42% and 25% for the battery tram and hydrogen train, respectively. Regarding the time-domain behavior of dc and ac currents and voltages, the **S2S** architecture proved to be equivalent to the standard one thanks to the presence of an additional low-pass filter at the **MSI LV** input, which prevents an increase in the distortion of the **LV** source current caused by switching in the **MSI**. As a consequence of this time-domain equivalent behavior, power losses and efficiencies in the traction motors and input sources were found almost unchanged in either case study, meaning that the size and thermal management of motors, fuel cells, and storage devices is not altered by the **S2S** configuration. On the other hand, the efficiency and power losses of the onboard converters improved in the **MSI**-based architecture. This result is intuitive for the dc/dc converter, which in the **S2S** topology processes a reduced amount of energy and power and is thus affected by up to 46% fewer losses. However, the efficiency of the **MSI** was also found to be always higher than that of the **VSI**, with reductions in the cycle energy losses of the **MSI** between 6% and 15%. Despite a higher switch count and increased conduction losses, switching losses are much lower in the **MSI** because the **MOV**M mostly operates as a down-shifted modulation and switches only two legs at a time, keeping the third off for one-third of the modulation period. When looking at the energy efficiency of the complete traction circuits, a decrease of 6% and 2% in the energy dissipated by the traction equipment was obtained from the **S2S** topology. Despite not being indicative of an actual energy saving, this result testifies that the **S2S** architecture does not degrade the efficiency of the traction system but can rather improve it to a modest extent. The weight and

volume analysis of the two configurations yielded very different results for the two case studies. In the battery tram, each storage device is involved both during traction and braking, and the additional path of power flow provided by the MSI is exploited in either of these traction phases. As a result, not only the passives of the dc/dc converters but also the HV input inductors of the traction converters can be sized for a lower current rating. This downsizing more than compensates for the extra volume and weight added by LV input filters of the MSIs. Overall, the dc/dc converters require 34% less volume and 36% less weight respectively, while the volume and weight of the traction converters remain practically unaltered. In the hydrogen train, the fuel cell is mainly involved during positive traction efforts, whereas all the power flows through the HV dc bus towards the battery when the train brakes. For this reason, neither the current rating nor the size and weight of the MSI HV inductor can be reduced, and the additional input filter of the MSI adds net poundage and bulkiness to the traction converter. Despite a significant reduction in the volume (-46%) and weight (-37%) of the boost converter, the overall balance penalizes the S2S traction system, which requires 7% more volume and weighs 3% more than the 2S system. It can be therefore concluded that the envisioned S2S topology shows attractiveness for semi-active propulsion systems in which high-power LV battery packs are employed as onboard storage devices.

Many possible directions can be conceived for future work on the MSI for multimode traction systems. The MSI has been here considered only in its three-level NPC variant for application to bimode rail vehicles. The five-level NPC topology with three independent voltage inputs could be explored for application to multimode trains powered by a combination of three different sources and storage elements. To this aim, an extension of the MOVIM algorithm to the three-input case should be developed and tested, and its operating domain and modulation limits derived correspondingly. On the other hand, the comparative analysis could be refined by considering a wider selection of core materials and geometries and implementing an optimized design of magnetics. More broadly, the application of the MSI could be explored in many other sectors including air and marine transport, in which ever-increasing research efforts towards electrification are being profused.

Small-scale rail traction drive simulator

The small-scale traction drive simulator used for the experimental tests is composed of a mechanical part and an electrical part. The mechanical subsystem reproduces the coupling between the traction motor and the inertial load constituted by the rotating and translating masses of the train. The subsystem is shown in Figure A.1 and consists of a three-phase squirrel cage induction motor (1), connected through a toothed coupling (2) to a gearbox unit with three gears (3,4,5) driving two coaxial hollow shafts (7,8) connected to the shaft of the driving wheels (10) through two sets of rods (6,9). The driving wheels are then coupled through two wheel sets to the shaft of two flywheels, which determine the most part of the total inertia and represent the translating masses of the real train. The main parameters of the traction motor and drivetrain are reported in Table A.1. As regards the motor, the reported data refer to the machine nameplate. However, the base frequency and limit voltage have been adjusted from test to test depending on the specific conditions and purposes.

The electrical subsystem comprises power electronic converters, a battery storage device, and unidirectional dc sources. The power converters employed for the experimental tests are the MSI and the dc/dc converter, pictured in Figure A.2(a)-(b). The MSI is realized by an NPC circuit with 1200 V/75 A Semikron IGBTs modules and an 800 V/9.4 μ F capacitor bank. The dc/dc converter is derived from a standard three-phase IGBT

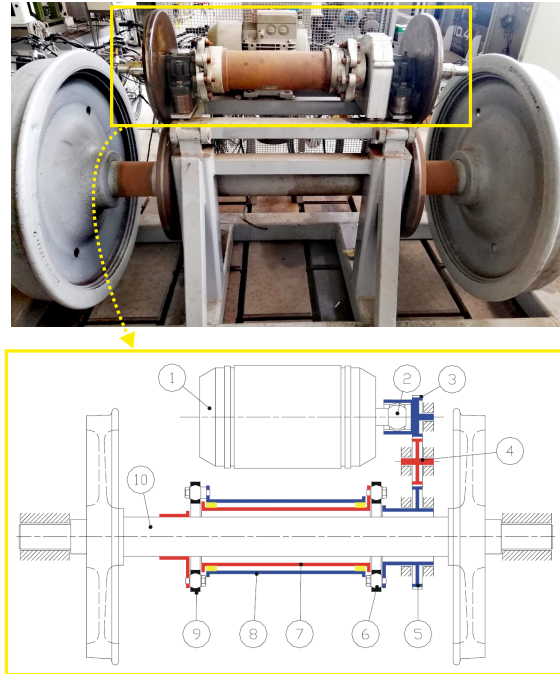


Figure A.1. Mechanical subsystem of the rail traction drive simulator: traction motor, gearbox, wheel sets, and driven flywheels.

Table A.1. Main parameters of traction motor and driveline

Induction motor	
Rated power	5.5 kW
Rated speed	1455 rpm
Rated voltage (wye/delta)	400/230 V
Rated current (wye/delta)	11.4/19.7 A
Gearbox and wheel set	
Flywheel diameter	0.9 m
Total transmission ratio	3.26:1
Equivalent inertia (referred to motor axle)	3.7 kgm ²

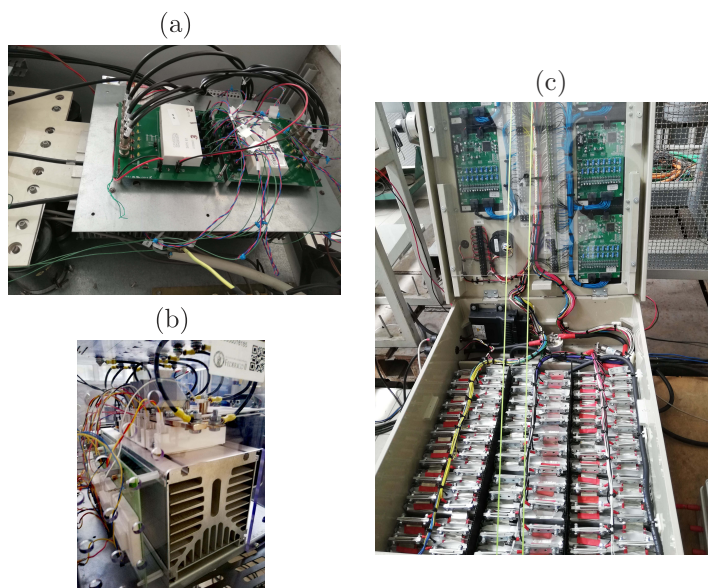


Figure A.2. (a) MSI converter, (b) dc/dc converter, (c) battery pack.

bridge with 1200 V/50 A Semikron components and an 800 V/1.1 μ F capacitor bank. In either converter, the semiconductors are switched on and off by stand-alone Semikron gate drivers interfaced with the control system via BNC connectors. The control and modulation of the converters is deployed on a dSpace 1103 real-time controller platform. As regards the sources of the traction drive, a diode bridge rectifier fed by an auto-transformer simulates a catenary voltage, while a unidirectional dc power supply with a maximum voltage and power of 360 V and 1.5 kW is used to simulate a fuel cell stack. All tests make use of a 250 V battery composed by 75 3.3 V/40 Ah LFP pouch cells connected in series, pictured in Figure A.2(c). The battery is monitored by a Battery Management System (BMS) composed of five slave boards connected in daisy chain with a master controller. The master controller collects the voltage, temperature, and SOC of all the cells in the pack and communicates this data to a host PC via serial communication.

Appendix **B**

Traction circuit simulation models

B.1 Complete model

The precise time-domain dynamic behavior of the traction system and its power losses are assessed by means of a blended Simulink/PLECS simulation routine. At each time step, the traction effort target is evaluated by the driver's model based on the actual speed, space, and section length. At the same time, the high-level [EMS](#) logic defines the target power levels of the onboard sources and [ESSs](#). These targets are processed by the high-level coordinated control and lower-level modulation layers of the power converters to produce adequate switching signals. The switching signals can be then used to solve the switched model of the traction circuit and determine the current and voltage waveforms of interest. At the same time, the torque produced by the traction motors is input to a one-dimensional dynamic model of the vehicle to update the speed and proceed toward the subsequent time step.

As the overall system-level model is obtained through the aggregation of subcomponent models, the individual modeling equations of motors, power converters, filters, auxiliary power supplies, dc sources, and storage devices are detailed in the following.

B.1.1 Vehicle dynamics

The vehicle motion is simulated by means of its one-dimensional dynamics:

$$\frac{dv_t}{dt} = \frac{1}{m_v} (F_t - F_r) \quad (\text{B.1})$$

where m_v is vehicle loaded mass, F_t and F_r are traction effort and motion resistance, respectively. The traction effort is linked to the torque T_m developed by each of the N_{mot} traction motors through the drive-chain transmission ratio τ and efficiency η , and wheel diameter D_w :

$$F_t = \frac{2\tau}{D_w} N_{\text{mot}} T_m \eta^{\text{sign}(T_m)} \quad (\text{B.2})$$

The motion resistance is evaluated according to the well-known Davis equation.

B.1.2 Traction motors

The dynamic model of the asynchronous motor in the stationary reference frame is used to determine the shaft torque and stator currents produced by the switched voltages fed by the traction inverter. By selecting the stator flux and current space vectors Φ_s and i_s as state variables, i.e., $\mathbf{x} = [i_s, \Phi_s]^T$, the state evolves as as:

$$\dot{\mathbf{x}} = A(\omega_r)\mathbf{x} + B\mathbf{v}_s \quad (\text{B.3})$$

with

$$A(\omega_r) = \begin{bmatrix} -\left(\frac{R_s}{\sigma L_s} + \frac{f_r}{\sigma} - ip\omega_r\right) & \frac{1}{\sigma L_s}(f_r - ip\omega_r) \\ -R_s & 0 \end{bmatrix} \quad (\text{B.4})$$

$$B = \begin{bmatrix} \frac{1}{\sigma L_s} \\ 1 \end{bmatrix} \quad (\text{B.5})$$

$$\sigma = 1 - L_m/L_s L_r, \quad f_r = R_r/L_r$$

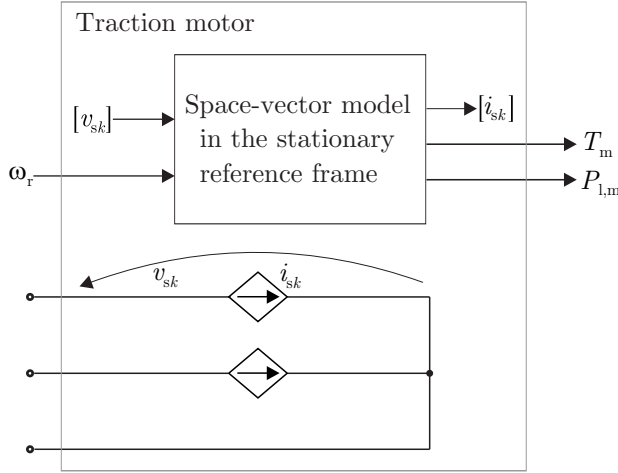


Figure B.1. Modeling of the asynchronous traction motors.

with the obvious meaning of symbols. The torque is:

$$T_m = -\frac{3}{2}p\Im m \{ \Phi_s \check{i}_s \} \quad (\text{B.6})$$

while the Joule losses $P_{l,m}$ can be easily calculated as:

$$P_{l,m} = \frac{3}{2}(R_s i_s^2 + R_r i_r^2) \quad (\text{B.7})$$

where $i_r = (\Phi_s - L_s i_s)/L_m$. The electrical model can be easily merged into a circuit simulation by integrating (B.3) for a given angular speed and set input phase voltages v_{sk} and forcing the corresponding stator currents i_{sk} via controlled current sources, as shown in Figure B.1. On the other hand, the output torque is used as input of the vehicle motion dynamics, whose solution updates the linear and angular speeds in the model.

B.1.3 Traction inverters

In the **VSI**, the leg output voltages v_k are calculated based on the dc input voltage V_{HV} and the switching signals s_k as:

$$v_k = s_k V_{\text{HV}} \quad (\text{B.8})$$

The dc input current depends on the ac phase currents i_k and the converter losses. The output currents are calculated from the motor model and the number of motors fed by one single inverter. On the other hand, switching and conduction losses $P_{1,\text{vsi}}$ in the converter are evaluated by means of PLECS thermal modeling, using the semiconductor thermal models provided by manufacturer Infineon [136]. Overall, the current entering the **VSI** is:

$$i_{\text{T,vsi}} = \sum_k s_k i_{sk} + \frac{P_{1,\text{vsi}}}{V_{\text{HV}}} \quad (\text{B.9})$$

The PLECS thermal model also outputs the junction temperatures Θ_j and heatsink temperature Θ_{hs} by solving the thermal network of the power converter, given a specific heatsink design.

In the **MSI**, the leg output voltages are calculated based on the dc input voltages V_{HV} and V_{LV} and the gate signals of the top and bottom switches:

$$v_k = s_{\text{B}k} V_{\text{LV}} + s_{\text{T}k} (V_{\text{HV}} - V_{\text{LV}}) \quad (\text{B.10})$$

The central-terminal input current shall be controlled by the **MSI** modulation algorithm, hence it is computed based only on the switching signals and ac output currents. On the other hand, the top-terminal input current is also affected by the converter losses $P_{1,\text{msi}}$ calculated by PLECS. Overall, the dc currents entering the **MSI** are:

$$i_{\text{C,msi}} = \sum_k (s_{\text{B}k} - s_{\text{T}k}) i_{sk} \quad (\text{B.11})$$

$$i_{\text{T,msi}} = \sum_k s_{\text{T}k} i_{sk} + \frac{P_{1,\text{msi}}}{V_{\text{HV}}} \quad (\text{B.12})$$

Since the dissipated thermal power simulated in PLECS does not correspond to the electrical power consumed by the converter (i.e., switching

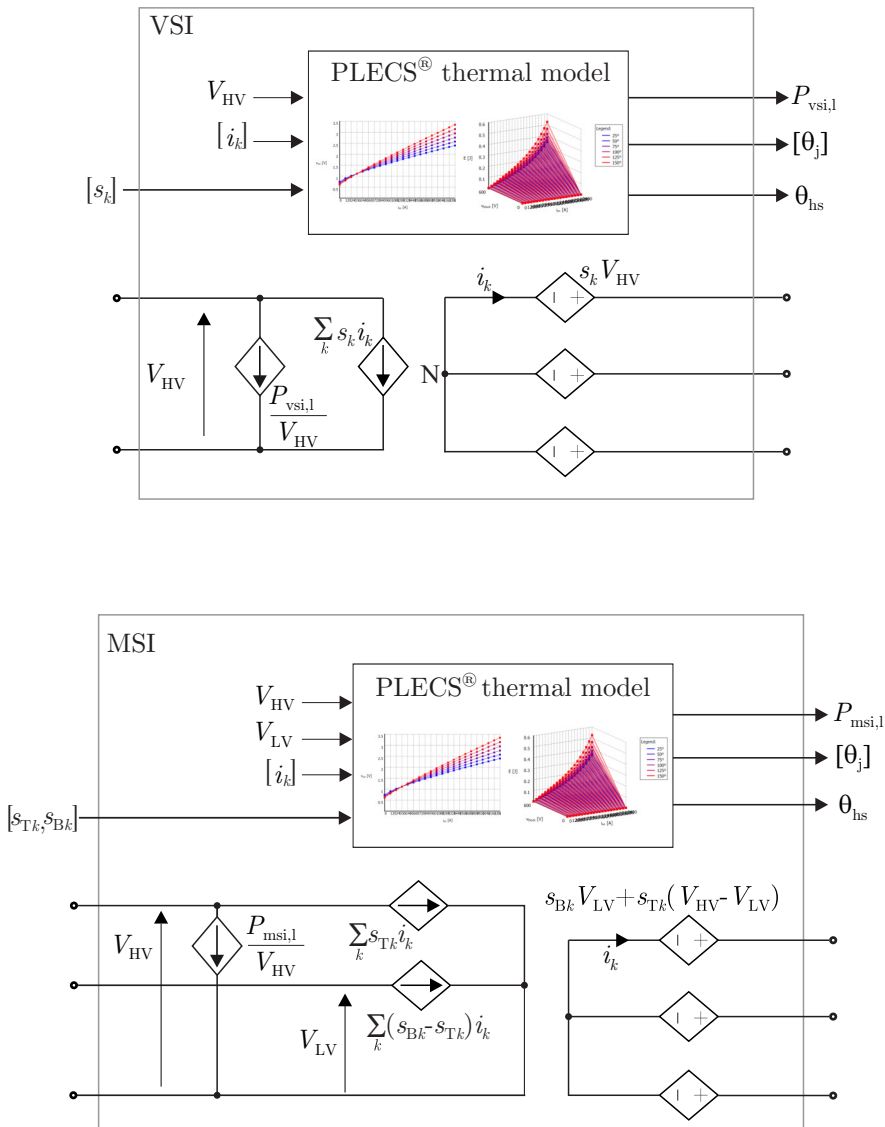


Figure B.2. Modeling of the traction converters: (a) VSI, (b) MSI.

and conduction losses do not affect current and voltage waveforms in a PLECS circuit), the output of the thermal model is integrated into a circuit-level simulation via two-port elements with controlled voltage and current sources, as in Figure B.2.

B.1.4 Interleaved dc/dc converters

Similarly to the traction converters, the dc/dc converter is represented by means of a two-port element with controlled voltage and current sources, shown in Figure B.3. For a generic interleaved topology with N_l legs, the voltage of the k -th input terminal is calculated according to the HV-bus voltage level and k -th switching signal as:

$$v_{LV,k} = s_k V_{HV} \quad (\text{B.13})$$

The current output by the convert at its HV terminal is given by the currents entering the LV input terminals as well as by the converter power losses $P_{\text{dcdc},l}$ calculated in PLECS as:

$$i_{\text{dcdc,out}} = \sum_k i_{\text{dcdc,in},k} - \frac{P_{\text{dcdc},l}}{V_{HV}} \quad (\text{B.14})$$

The junction and heatsinks temperatures are also retrieved from the thermal model.

B.1.5 Passive filters

Inductors and capacitors are modeled by ideal inductances and capacitances in series with an equivalent resistance accounting for parasitic losses.

B.1.6 Power sources and energy storage devices

The external supply found in electrified railway systems is modeled with the simple zero-order circuit shown in in Figure B.5(a), where the voltage source E_{cat} is representative of the no-load system voltage level and the resistance R_{cat} accounts for the ohmic losses in the feeding wire and return rails.

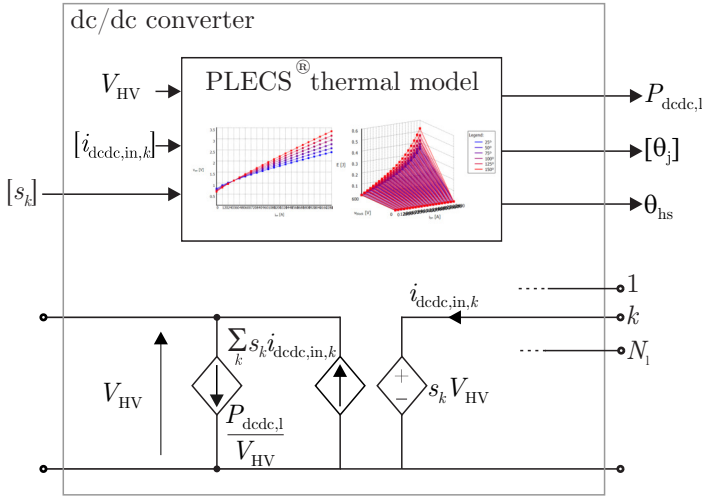


Figure B.3. Interleaved dc/dc converter modeling.

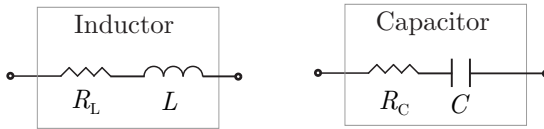


Figure B.4. Modeling of inductors and capacitors.

Battery cells are modeled by means of the well-known first-order equivalent circuit shown in Figure B.5(b). A SOC-dependent voltage source is connected to a series resistance, accounting for ac losses, and an RC network with the double-layer capacitance C_{dl} and charge-transfer resistance R_{ct} . The SOC is updated via Coulomb counting, i.e., by integrating the current delivered by the battery:

$$\text{SOC}(t_f) = \text{SOC}(t_i) - \frac{1}{C_n} \int_{t_i}^{t_f} i_{\text{bat}}(t) dt \quad (\text{B.15})$$

where C_n is the nominal capacity in Ah. The relationship between SOC and the open-circuit voltage is retrieved by means of a look-up table. A battery pack model is simply obtained by cascading and paralleling multiple cell models.

The voltage generated by a single fuel cell is calculated as the sum of the open-circuit Nernst's voltage E_{FC} , the activation overvoltage v_{act} , the concentration overvoltage v_{conc} , and the ohmic voltage drop v_{Ω} [135]:

$$v_{\text{FC}} = E_{\text{FC}} - v_{\text{act}} - v_{\text{conc}} - v_{\Omega} \quad (\text{B.16})$$

$$v_{\text{act}} = v_{\text{act},0} + v_{\text{act},a} \left(1 - e^{(-c_1 i_{\text{FC}})} \right) \quad (\text{B.17})$$

$$v_{\text{conc}} = \left(c_2 \frac{i}{i_{\text{FC,max}}} \right)^{c_3} \quad (\text{B.18})$$

$$v_{\Omega} = R_{\Omega} i_{\text{FC}} \quad (\text{B.19})$$

Nonlinear resistances R_{act} and R_{conc} corresponding to the activation and concentration overvoltages are defined straightforwardly. All the above terms present complex nonlinear relationships with several system variables (e.g., cathode and anode partial pressures, temperatures, mass flows, humidities, oxygen excess ratio, etc.). For the present purposes, the complex model detailed in [135] is tuned and simulated offline to evaluate the reversible voltage and internal voltage drops of the whole stack for different output currents at rated oxygen excess ratio. The auxiliary power self-consumption of the FC plant is also included. The curve is then loaded into a look-up table and used for the circuit-level simulations. To account for the dynamic charge double-layer phenomenon occurring at the stack terminals, a capacitor C_{dl} is added in parallel to the activation and concentration resistances [137]. Overall, the FC stack circuit model is shown in Figure B.5(c).

B.1.7 Auxiliaries

The auxiliary power consumption is modeled as a constant-power load supplied by the HV dc link of the traction circuit.

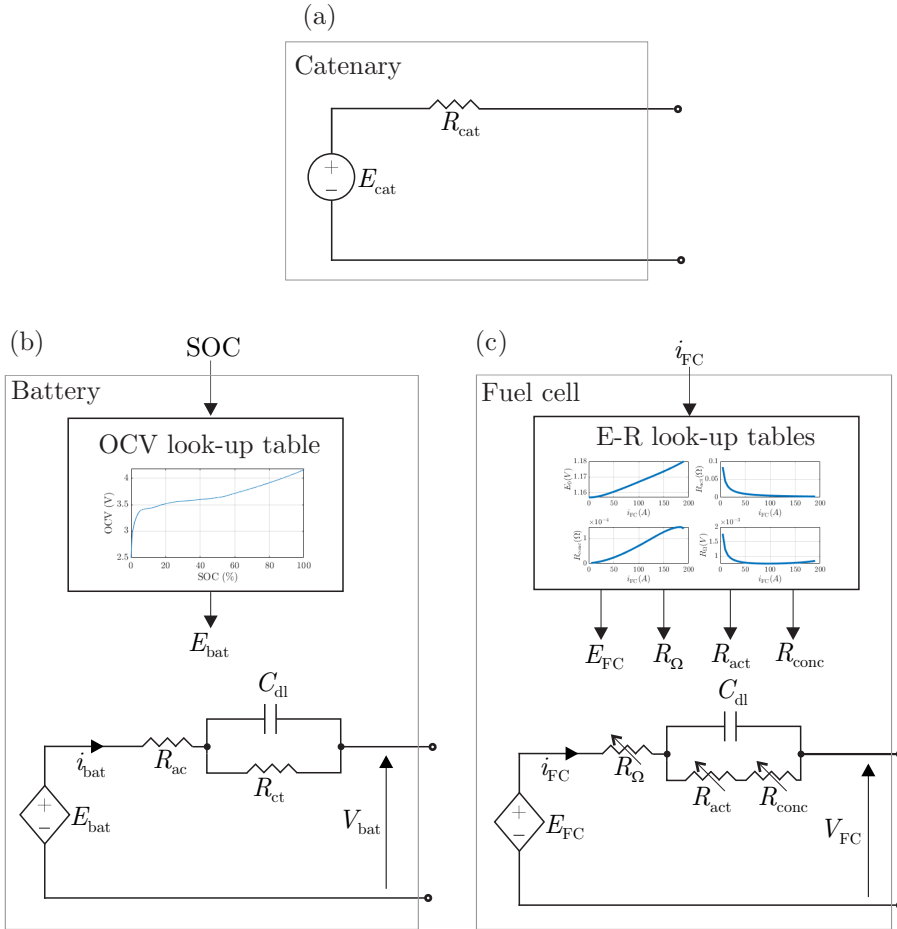


Figure B.5. Modeling of power sources and ESSs: (a) external line, (b) battery, (c), fuel cell.

B.2 Simplified model

A simplified averaged model can be implemented when the switching operation and losses of the power electronic converters are not of interest, and only the main dynamics have to be evaluated (e.g., for tuning the controllers or in a preliminary system design). In this setting, the models of traction motors and vehicle dynamics presented above can be still

adopted, whereas major simplifications are made for power converters and power sources. First, the dc/dc and dc/ac converter models presented in Figures B.3-B.2 are simplified by removing the thermal calculation, and the corresponding controlled current sources in the circuit. Second, average duty cycles are fed to the model instead of switched signals, so that ripple-free continuous voltage and current waveforms are produced at the input and output terminals. The parasitic resistances of inductors and capacitors are neglected. The models of the power sources are simplified and made static and time-invariant by removing the capacitors and fixing the variable resistances to a value corresponding to the rated current output of the source.

Filters and heatsink design in power converters

The main share of volume and weight of a power electronic converter is determined by inductors, capacitors, and heatsinks [138, 139]. To make a reasonable comparison between the volume and weight of power electronics, common criteria for the dimensioning and design or selection of these components are here defined. The peak electrical and thermal stresses that these components must withstand over a reference driving cycle depend not only on the tram speed profile but also on how the power converters are controlled. Therefore, in each considered configuration, the driving cycle profile is preliminary simulated with the simple averaged model of the traction system detailed in B to estimate the peak average currents (i.e., without switching ripples) in the circuit. These estimates are then input to design routines detailed here.

Inductors

Iron and air-core inductors are employed for the input stage of the boost dc/dc converters and as part of input/output LC filters. For a generic interleaved dc/dc converter with N_1 legs switching at a frequency f_{sw} , the phase inductance $L_{dc,dc,in}$ is dimensioned by maximizing the fol-

lowing equation over the converter mission profile [131]:

$$L_{\text{dcdc,in}} = \frac{V_{\text{HV}}}{\Delta i_{\text{dcdc,in}}^* f_{\text{sw}} N_1} (\lfloor d' N_1 \rfloor + 1 - d' N_1) (d' N_1 - \lfloor d' N_1 \rfloor) \quad (\text{C.1})$$

where $d' = (1 - d)$ is complementary to the top-switches duty cycle (which is the same for each converter leg in interleaved topologies), and $\Delta i_{\text{dcdc,in}}^*$ is the peak-to-peak target ripple of the total current entering the converter LV input. On the other hand, the peak-to-peak current ripple in each phase inductor is given by:

$$\Delta i_{L_{\text{dcdc,in}}} = \frac{V_{\text{HV}} d d'}{f_{\text{sw}} L_{\text{dcdc,in}}} \quad (\text{C.2})$$

Hence, if the maximum averaged input current $\hat{i}_{\text{dcdc,in}}$ over the converter mission profile is known, the maximum current for which the phase inductors have to be designed is equal to:

$$\hat{i}_{L_{\text{dcdc,in}}} = \frac{\hat{i}_{\text{dcdc,in}}}{N_1} + \frac{V_{\text{HV}} d d'}{2 f_{\text{sw}} L_{\text{dcdc,in,k}}} \quad (\text{C.3})$$

When part of an LC filter with cutoff frequency f_{cut} , the filter inductance is simply calculated as:

$$L_{\text{LC}} = \frac{1}{4\pi^2 f_{\text{cut}}^2 C_{\text{LC}}} \quad (\text{C.4})$$

where C_{LC} is the filter capacitance (see below for its dimensioning equation). By assuming that all the ripple current flows into the filter capacitor, the absolute peak current for which the inductor must be designed is derived from the HV-bus voltage level and maximum active power processed by the converter to which the filter is connected over the considered mission profile. The power inductors are designed through a FEA-assisted analytic design procedure to yield the required inductance at the peak current rating. In the case of iron-core inductors, Metglas 2605SA1 C-shaped amorphous cores are used due to their very high saturation flux density B_{sat} of 1.56 T required by high-current applications [131], with foil windings. They are paired as shown in Figure C.1(a) to obtain an

EE equivalent core. Multiple EE cores can be then stacked according to the design needs. The preliminary analytic design is based on the area-product approach [140,141] and goes through the following steps:

1. Define the target inductance L , maximum peak current \hat{i}_L , winding current density J_0 , maximum core flux density $\hat{B}_c \leq B_{\text{sat}}$, window utilization factor k_u , and current waveform factor k_i (i.e., the ration between the RMS and peak values of the current).
2. Calculate the required area product A_p as:

$$A_p^* = \frac{k_i L \hat{i}_L^2}{\hat{B}_c k_u J_0} \quad (\text{C.5})$$

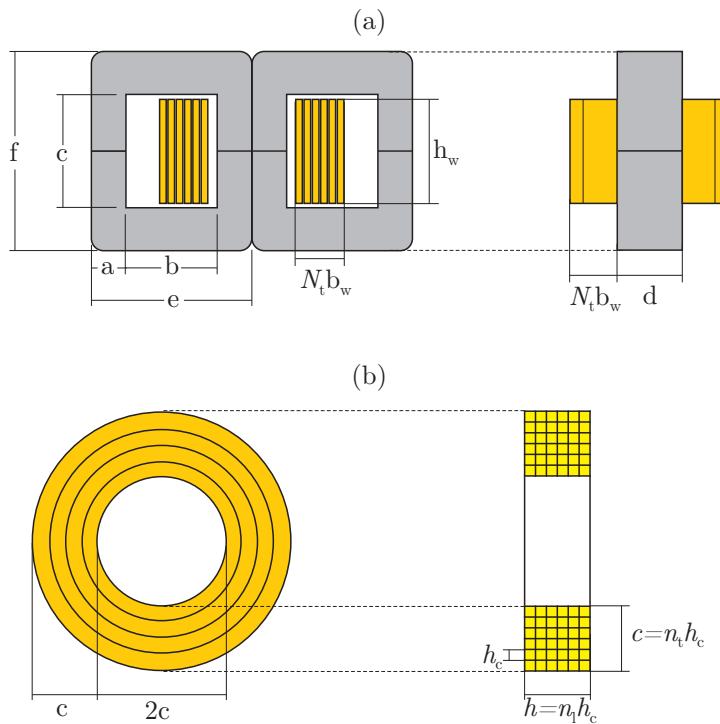


Figure C.1. Geometries of the iron-core (a) and air-core (b) inductors.

3. Select and arrange the minimum even number of cores N_c with an effective core area A_c , window area of A_w , and mean magnetic length l_m that yield an area product A_p equal or greater than A_p^* ,
4. Calculate the required number of turns as:

$$N_t = \text{round} \left(\frac{L \hat{i}_L}{A_c \hat{B}_c} \right) \quad (\text{C.6})$$

5. Calculate the required airgap length as:

$$l_g = \frac{\mu_0 N_t \hat{i}_L}{\hat{B}_c} - \frac{l_m}{\mu_r} \quad (\text{C.7})$$

where μ_r is the relative permeability of the core considering the dc-flux bias.

A current density of 200 A/cm² is always selected. The preliminary design is then fine-tuned and validated through **FEA** magnetic simulations using FEMM4.2 software. The specific winding losses are then evaluated as

$$p_w = \rho J_0^2. \quad (\text{C.8})$$

On the other hand, the specific core losses are calculated by means of the modified Steinmetz equation [140]:

$$p_c = K_c f_{sw}^\alpha \left(\frac{\Delta B}{2} \right)^\beta \quad (\text{C.9})$$

where ΔB is the peak-to-peak magnitude of the ac flux density, and K_c, α, β are parameters provided by the manufacturer. The specific losses p_w and p_c are then input to a **FEA** steady-state thermal simulation with an ambient temperature of 45 °C, forced-air cooling with a heat transfer coefficient of 50 W/m²K intensity, and class-H resin insulation [52]. If the insulation and core temperature limits of 180°C and 150°C respectively are not reached, the inductor design procedure terminates and yields as output the inductor inductance L and resistance R_L . The mass and vol-

ume are calculated as:

$$m_L = 2N_t b_w h_w \left(\frac{N_c}{2} d + 2N_t b_w + 2a \right) \delta_{cu} + N_c (ef - bc) d \delta_{fe} \quad (C.10)$$

$$V_L = 2e \left(\frac{N_c}{2} d + 2N_t b_w \right) \left(f + \frac{l_g}{3} \right) \quad (C.11)$$

where δ_{cu} and δ_{fe} are the densities of copper and core material.

For air-core inductors, multilayer windings of width c and height h shown in Figure C.1(b) are considered. The inductor has n_l layers, n_t turns per layer, and is realized with square cross-section conductors. To obtain the desired inductance with the minimum length of wire, Brooks coil geometry is chosen, a circular coil inductor of square cross-section with an inner diameter twice the width of the winding. The inductance value of a Brook coil is given by:

$$L = k_L c N_t^2 \quad (C.12)$$

where $k_L = 2.029\mu_0$. The design procedure goes through the following steps:

1. Define the target inductance L , maximum peak current \hat{i}_L , winding current density J_0 , conductor height h_c , and cross-section utilization factor k_u .
2. Calculate the height c as:

$$c = \sqrt[5]{\frac{L \hat{i}_L^2}{k_L J_0^2 k_u^2}} \quad (C.13)$$

3. Estimate the number of turns as:

$$N_t = \text{round} \left(\frac{J_0 c^2 k_u}{\hat{i}_L} \right) \quad (C.14)$$

4. If N_t is an exact root, pick $n_l = n_t = \sqrt{N_t}$. Otherwise, pick $n_t = \lfloor \sqrt{N_t} \rfloor$ and $n_l = n_t + 1$. Recalculate the winding width c and height h based on n_l , n_t , and h_c .

5. Refine the turns number based on the inductance equation for air-core axis-symmetric inductors [115].

The preliminary design is then validated through **FEA** magnetic and thermal simulations, and the precise inductance and resistance values are recorded. The volume and mass of the inductor are simply calculated as:

$$m_L = 3\pi hc^2 \delta_{\text{cu}} \quad (\text{C.15})$$

$$V_L = h(4c)^2 = 16hc^2 \quad (\text{C.16})$$

Capacitors

Capacitors are used together with inductors in the LC filters on the **LV** and **HV**-bus. When part of the output LC filter of an interleaved dc/dc converter with N_1 legs, the capacitance is selected by maximizing the following equation over the converter mission profile:

$$C_{\text{dcdc,out}} = \frac{\hat{i}_{\text{dcdc,out}} \hat{d}}{N_1 f_{\text{sw}} \Delta V^*} \quad (\text{C.17})$$

where $\hat{i}_{\text{dcdc,out}}$ is the peak value of the converter averaged output current, \hat{d} is the duty cycle corresponding to the maximum boost ratio between **LV** and **HV** voltage levels, and ΔV^* is the desired voltage ripple at the **HV** terminals. The peak capacitor **RMS** current is calculated based on [142]:

$$\begin{aligned} \hat{I}_{C,\text{RMS}} = & \frac{\hat{i}_{\text{dcdc,in}}}{N_1} \left[(dN_1 - \lfloor dN_1 \rfloor)(\lfloor dN_1 \rfloor + 1 - dN_1) + \right. \\ & + \frac{1}{12d^2} \left(\frac{\Delta i_{L\text{dcdc,in}}}{\hat{i}_{\text{dcdc,out}}} \right)^2 \left[(\lfloor dN_1 \rfloor + 1)(dN_1 - \lfloor dN_1 \rfloor)^3 + \right. \\ & \left. \left. + \lfloor dN_1 \rfloor^2 (\lfloor dN_1 \rfloor + 1 - dN_1)^3 \right] \right]^{\frac{1}{2}} \quad (\text{C.18}) \end{aligned}$$

On the other hand, it is well known that the current drawn by a VSI is equal to:

$$i_{\text{vsi}} = \sum_{k=1}^3 s_k i_k \quad (\text{C.19})$$

where s_k represents the top-switch gate signal on the k -th leg. By specializing the above equation to the case of sinusoidal and symmetric load voltages and currents, and by assuming that the whole ripple component in i_{vsi} is filtered by the capacitor, the following sizing equation can be derived [143, 144]:

$$C = \frac{\hat{i}_{\text{ac}}}{16\Delta V^* f_{\text{sw}}} \sqrt{\hat{m}^2 \left[6 - \frac{96\sqrt{3}}{5\pi} \hat{m} + 4\hat{m}^2 \right] \cos^2 \varphi + \frac{8\sqrt{3}\hat{m}^3}{5\pi}} \quad (\text{C.20})$$

where \hat{i}_{ac} is the maximum value of the ac output current magnitude, and $\hat{m} = 2\hat{d}/\sqrt{3}$ with \hat{d} the maximum peak value of the VSI duty cycles. The peak RMS current in the capacitor is then given by:

$$\hat{I}_{\text{C,RMS}} = \hat{i}_{\text{ac}} \sqrt{\hat{m} \left[\frac{\sqrt{3}}{2\pi} + \left(\frac{2\sqrt{3}}{\pi} - \frac{9}{8} \hat{m} \right) \right]} \quad (\text{C.21})$$

Recalling (4.16b)-(4.16c) in Chapter 4, it can be noted that the currents drawn at the MSI HV and LV terminals are given by expressions identical to (C.20), the only difference lying in the switching functions used in each equation. Therefore, the capacitors can be still sized according to (C.20) with the distinction:

$$\hat{m} = \begin{cases} \frac{2}{\sqrt{3}} \hat{d}_{\text{T}}, & \text{for the HV capacitor} \\ \frac{2}{\sqrt{3}} \hat{d}_{\Delta}, & \text{for the LV capacitor} \end{cases} \quad (\text{C.22})$$

where \hat{d}_{T} and \hat{d}_{Δ} are the maximum peak values of the MSI top and differential duty cycles. The expression of the RMS current in either capacitor can be derived in a similar fashion.

Once the capacitance and peak RMS current are derived, a number N_{cap} of dc film capacitors with adequate voltage and current rating to be

connected in parallel are chosen from the catalog of manufacturer TDK. Clearly, the volume and mass of the entire capacitor bank are calculated based on N_{cap} and on the size and weight data of each capacitor reported by the manufacturer.

Heatsinks

Heatsinks in the dc/dc and traction converters are sized to avoid overtemperatures in the semiconductor junctions. This is generally done by considering a steady-state operation of the power converter and the corresponding steady-state thermal network, in which only thermal resistances appear [102, 139]. However, the power converters of a traction system operate in highly-variable load conditions, and a steady-state approach for the thermal design would be too conservative and lead to unneeded oversizing. Indeed, high-power heatsinks are characterized by thermal time constants of hundreds of seconds, comparable with the load cycling times, so that the condition of constant steady state is seldom reached. Therefore, each heatsink is sized through the nested iterative procedure shown in Figure C.2, which goes through the following steps:

1. An initial candidate is chosen based on the converter peak power and the semiconductor thermal resistances. Furthermore, considering the actual mission profile of the vehicle, the worst-case mission profile of the converter is identified.
2. The converter thermal model (see Figures B.2-B.3) accounting for the thermal resistance and capacitance of the heatsink is simulated iteratively. The iterations stop when a periodic steady-state condition is reached, i.e., when the initial and final values of every temperature in the model are equal.
3. If the maximum junction temperature over the simulated mission profile is above/below the limit value of 125 °C, a different heatsink with lower/higher thermal resistance is selected and the thermal model iterations start again. Otherwise, the procedure stops, and the mass and volume of the selected heatsink are recorded.

The thermal simulations are run with an ambient temperature of 45 °C and air-forced cooling of the heatsink at 5 m/s. The catalog of aluminum

heatsinks producer ABL [145] is employed as the database for the iterative design procedure.

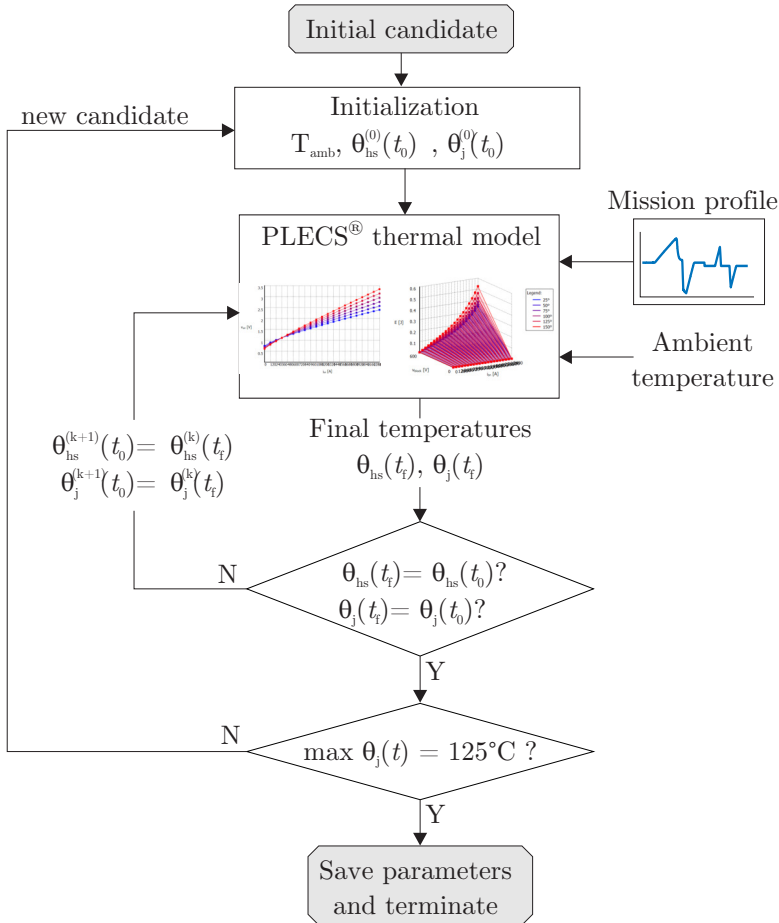


Figure C.2. Flowchart of the heatsink sizing procedure.

Bibliography

- [1] International Energy Agency (IEA), “The role of CCUS in low-carbon power systems,” Tech. Rep., 2020. [Online]. Available: https://iea.blob.core.windows.net/assets/ccdcb6b3-f6dd-4f9a-98c3-8366f4671427/The_role_of_CCUS_in_low-carbon_power_systems.pdf
- [2] European Commission, “2050 long-term strategy | Climate Action,” 2018. [Online]. Available: https://ec.europa.eu/clima/policies/strategies/2050_en
- [3] International Energy Agency (IEA), “Rail,” Paris, 2021. [Online]. Available: <https://www.iea.org/reports/rail>
- [4] International Energy Agency (IEA) and International Union of Railways (UIC), “Railway Handbook 2017. Energy Consumption and CO2 Emissions. Focus on Passenger Rail Services,” 2017. [Online]. Available: https://uic.org/IMG/pdf/handbook_iea-uic_2017_web3.pdf
- [5] International Energy Agency (IEA), “The Future of Rail Opportunities for energy and the environment,” 2019. [Online]. Available: www.iea.org/t&c/
- [6] E. Fedele, D. Iannuzzi, and A. Del Pizzo, “Onboard energy storage in rail transport: Review of real applications and techno-economic assessments,” *IET Electrical Systems in Transportation*, vol. 11, no. 4, pp. 279–309, 12 2021.
- [7] N. Ghaviha, J. Campillo, M. Bohlin, and E. Dahlquist, “Review of Application of Energy Storage Devices in Railway Transportation,” *Energy Procedia*, vol. 105, pp. 4561–4568, 2017.
- [8] A. González-Gil, R. Palacin, and P. Batty, “Sustainable urban rail systems: Strategies and technologies for optimal management of regenerative braking energy,” *Energy Conversion and Management*, vol. 75, pp. 374–388, 2013.

-
- [9] “Reducing Fuel Consumption and Greenhouse Gas Emissions of Medium- and Heavy-Duty Vehicles, Phase Two: Final Report,” National Academies of Sciences, Engineering, and Medicine, Tech. Rep., 10 2019.
- [10] A. Rufer, *Energy storage: Systems and components*. Taylor & Francis, 2017.
- [11] A. G. Olabi, C. Onumaegbu, T. Wilberforce, M. Ramadan, M. A. Abdelkareem, and A. H. Al – Alami, “Critical review of energy storage systems,” *Energy*, vol. 214, p. 118987, 1 2021.
- [12] F. Ciccarelli, “Energy management and control strategies for the use of supercapacitors storage technologies in urban railway traction systems,” Ph.D. dissertation, University of Naples Federico II, Naples, Italy, 2014. [Online]. Available: <http://www.fedoa.unina.it/9633/>
- [13] Y. Wang, D. F. Ruiz Diaz, K. S. Chen, Z. Wang, and X. C. Adroher, “Materials, technological status, and fundamentals of PEM fuel cells – A review,” pp. 178–203, 1 2020.
- [14] E. Rivard, M. Trudeau, and K. Zaghib, “Hydrogen Storage for Mobility: A Review,” *Materials*, vol. 12, no. 12, p. 1973, 6 2019.
- [15] J. Adams, C. Houchins, and R. Ahluwalia, “Onboard Type IV Compressed Hydrogen Storage System - Cost and Performance Status,” US Department of Energy, Tech. Rep., 11 2019.
- [16] X. Liu and K. Li, “Energy storage devices in electrified railway systems: A review,” *Transportation Safety and Environment*, vol. 2, no. 3, pp. 183–201, 10 2020.
- [17] A. M. Abdalla, S. Hossain, O. B. Nisfindy, A. T. Azad, M. Dawood, and A. K. Azad, “Hydrogen production, storage, transportation and key challenges with applications: A review,” *Energy Conversion and Management*, vol. 165, no. March, pp. 602–627, 2018.
- [18] P. Ralon, M. Taylor, A. Ilas, H. Diaz-Bone, and K.-P. Kairies, “Electricity storage and renewables: Costs and markets to 2030,” International Renewable Energy Agency (IRENA), Abu Dhabi, UAE, Tech. Rep. October, 10 2017. [Online]. Available: https://www.irena.org/-/media/Files/IRENA/Agency/Publication/2017/Oct/IRENA_Electricity_Storage_Costs_2017.pdf
- [19] M. Ogasa, “Onboard storage in Japanese electrified lines,” in *Proceedings of EPE-PEMC 2010 - 14th International Power Electronics and Motion Control Conference*. [Piscataway, N.J.]: IEEE, 2010.
-

-
- [20] M. Ogasa and Y. Taguchi, "Power electronics technologies for a lithium ion battery tram," in *2007 Power Conversion Conference - Nagoya*. Piscataway N.J.: IEEE, 4 2007, pp. 1369–1375.
- [21] H. Ozawa and T. Ogihara, "Running test of contactwire-less tramcar using lithium ion battery," *IEEE Transactions on Electrical and Electronic Engineering*, vol. 3, no. 3, pp. 360–362, 2008.
- [22] K. Tokuyama, M. Shimada, K. Terasawa, and T. Kaneko, "Practical application of a hybrid drive system for reducing environmental load," *Hitachi Review*, vol. 57, no. 1, pp. 23–27, 2008.
- [23] R. Furuta, J. Kawasaki, and K. Kondo, "Hybrid traction technologies with energy storage devices for nonelectrified railway lines," *IEEE Transactions on Electrical and Electronic Engineering*, vol. 5, no. 3, pp. 291–297, 2010.
- [24] H. Kakinuma and H. Ihara, "Development of Motor-Assisted Hybrid Traction System," *The Journal of the Institute of Electrical Installation Engineers of Japan*, vol. 28, no. 11, pp. 826–829, 2008. [Online]. Available: <http://www.railway-research.org/IMG/pdf/r.2.2.3.4.pdf>
- [25] M. Ogasa, "Application of energy storage technologies for electric railway vehicles-examples with hybrid electric railway vehicles," *IEEE Transactions on Electrical and Electronic Engineering*, vol. 5, no. 3, pp. 304–311, 2010.
- [26] S. Akiyama, "Low Floor Battery-driven LRV (SWIMO)," *Journal of the Society of Mechanical Engineers*, vol. 111, no. 1075, pp. 468–469, 2008.
- [27] M. Ogasa and Y. Taguchi, "Development of contact-wire/battery hybrid LRV hybrid technology with lithium ion rechargeable battery for LRV," in *2010 IEEE Vehicle Power and Propulsion Conference, VPPC 2010*. Piscataway, NJ: IEEE, 2010, pp. 1–6.
- [28] Y. Taguchi, S. Kadowaki, T. Nakamura, G. Yoshikawa, K. Hatakeda, H. Hatanaka, and T. Kaneko, "Development and Evaluation of the Traction Circuit for Battery-Powered and AC-Fed Hybrid Train," *Quarterly Report of RTRI*, vol. 32, no. 1, pp. 41–47, 2018.
- [29] Y. Kono, N. Shiraki, H. Yokoyama, and R. Furuta, "Catenary and storage battery hybrid system for electric railcar series EV-E301," in *2014 International Power Electronics Conference, IPEC-Hiroshima - ECCE Asia 2014*. IEEE, 2014, pp. 2120–2125.
- [30] H. Takiguchi, "Overview of series EV-E301 catenary and battery-powered hybrid railcar," pp. 19–21, 2015. [Online]. Available: https://www.jreast.co.jp/e/development/tech/pdf_31/tec-31-27-32eng.pdf
-

-
- [31] S. Tritschler and K. Ji, “Studie zum Einsatz von Hybrid-Fahrzeugen im SPNV Endfassung,” Stuttgart, Germany, 2016. [Online]. Available: https://www.nvbw.de/fileadmin/nvbw/mediathek/downloads/Einsatz_von_Hybrid-Fahrzeugen_im_SPNV_Endfassung.pdf
- [32] “MITRAC Energy Saver (brochure), Bombardier Inc.,” [Online]. Available: <http://www.bombardier.com/content/dam/Websites/bombardiercom/supporting-documents/BT/Bombardier-Transportation-ECO4-EnerGstor-EN.pdf>
- [33] D. Murray-smith, “A Review of Developments in Electrical Battery, Fuel Cell and Energy Recovery Systems for Railway Applications,” Scottish Association for Public Transport, Glasgow, Scotland, Tech. Rep. November, 2019. [Online]. Available: <http://eprints.gla.ac.uk/204435/1/204435.pdf>
- [34] “Toshiba Successfully Test Drives SCiB Powered Energy Storage System for Trams,” 2015. [Online]. Available: <https://www.toshiba.co.jp/sis/en/topics/2015/20150423.htm>
- [35] J. Swanson and J. Smatlak, “State of the Art in Light Rail Alternative Power Supplies,” in *13th National Light Rail and Streetcar Conference: Transforming Urban Areas*. Washington, D.C.: Transportation Research Board, 2015, pp. 47–64.
- [36] C. King, G. Vecia, I. Thompson, H. Electric, R. A. Systems, C. King, G. Vecia, and I. Thompson, “Innovative Technologies for Light Rail and Tram : A European reference resource,” *Sintropher*, vol. 17, no. September, pp. 1–17, 2015. [Online]. Available: <https://www.polisnetwork.eu/wp-content/uploads/2019/06/nimh-and-primove-systems-2-finalpolis.pdf>
- [37] “TramLink Low-floor Lightrail Vehicle: EMTU Santos, Brazil.” [Online]. Available: <https://www.stadlerrail.com/media/pdf/tlemtu0816e.pdf>
- [38] J. F. Reynaud, M. Garmendia, and T. Nieva, “Comprehensive integration of Onboard Energy Storage systems in tramways: Birmingham tram case study,” in *2018 IEEE International Conference on Electrical Systems for Aircraft, Railway, Ship Propulsion and Road Vehicles & International Transportation Electrification Conference (ESARS-ITEC)*. [Place of publication not identified]: IEEE, 11 2018, pp. 1–6.
- [39] “Birmingham city centre tram extension opens to passengers ahead of schedule,” 2019. [Online]. Available: <https://westmidlandsmetro.com/2019/12/11/birmingham-city-centre-tram-extension-opens-to-passengers-ahead-of-schedule/>
-

-
- [40] “Technical Specification: Bozankaya Tram,” 2018. [Online]. Available: <https://www.bozankaya.com.tr/wp-content/uploads/2018/08/BOZANKAYA-TRAM-EN.pdf>
- [41] Y. Laperrière, “Realize your vision with Bombardier TALENT 3 BEMU,” in *APTA 2019 Rail Conference*, ser. APTA 2019 Rail Conference, 2019. [Online]. Available: https://www.apta.com/wp-content/uploads/Realize-your-vision-with-Bombardier-TALENT-3-BEMU_Yves_Lappierre.pdf
- [42] Stadler Rail Group, “Flirt trimodal multiple unit,” 2019. [Online]. Available: <https://www.stadlerrail.com/media/pdf/fwbbmu0519e.pdf>
- [43] “Vivarail launches fast charge system for the Class 230 battery trains – the UK’s only battery train with a range of 60 miles between charges - Vivarail,” 2019. [Online]. Available: <http://vivarail.co.uk/vivarail-launches-fast-charge-system-for-the-class-230-battery-trains-the-uks-only-battery-train-with-a-range-of-60-miles-between-charges/>
- [44] N. Devereux, “Vivarail battery hybrid trials underway,” 2019. [Online]. Available: <https://www.therailwayhub.co.uk/8495/vivarail-battery-hybrid-trials-underway/>
- [45] “ÖBB Cityjet eco battery train to enter services,” 2019. [Online]. Available: <https://www.railwaypro.com/wp/obb-cityjet-eco-battery-train-to-enter-services/>
- [46] Siemens AG, “Desiro ML ÖBB cityjet,” 2016. [Online]. Available: <https://www.mobility.siemens.com/mobility/global/SiteCollectionDocuments/de/rail-solutions/commuter-and-regional-trains/desiro-platform/datasheet-desiro-oebb-de.pdf>
- [47] M. Steiner and J. Scholten, “Energy storage on board of DC fed railway vehicles,” in *PESC Record - IEEE Annual Power Electronics Specialists Conference*, vol. 1. IEEE, 2004, pp. 666–671.
- [48] M. Steiner, M. Klohr, and S. Pagiela, “Energy storage system with Ultracaps on board of railway vehicles,” in *2007 European Conference on Power Electronics and Applications, EPE*. IEEE, 2007, pp. 1–10.
- [49] Y. Sekijima, M. Inui, Y. Monden, and I. Aoyama, “Development of an energy storage system for DC electric rolling stock by applying electric double layer capacitors,” in *Japanese Railway Engineering*, 2006, no. 156, p. 35. [Online]. Available: <http://www.railway-research.org/IMG/pdf/307-2.pdf>
-

-
- [50] J. P. Moskowitz and J. L. Cohuau, "STEEM: ALSTOM and RATP experience of supercapacitors in tramway operation," in *2010 IEEE Vehicle Power and Propulsion Conference, VPPC 2010*. IEEE, 2010, pp. 1–5.
- [51] CAF Power & Automation, "EVODRIVE: energy efficiency." [Online]. Available: <https://www.cafpower.com/en/systems/energy-storage-system-greentech/evodrive-energy-efficiency>
- [52] G. Abad, *Power Electronics and Electric Drives for Traction Applications*, G. Abad, Ed. Chichester West Sussex United Kingdom: Wiley, 2016.
- [53] Y. Ruf, T. Zorn, P. A. De Neve, P. Andrae, S. Erofeeva, F. Garrison, and A. Schwilling, "Study on the use of fuel cells and hydrogen in the railway environment - Final Study," p. 50, 2019. [Online]. Available: https://www.fch.europa.eu/sites/default/files/Studyontheuseoffuelcellsandhydrogenintherailwayenvironment_final.pdf
- [54] East Japan Railway company, "Development of the World's First Fuel Cell Hybrid Railcar." p. 1, 2006. [Online]. Available: <https://www.jreast.co.jp/e/press/20060401/>
- [55] K. Ogawa, T. Yamamoto, H. Hasegawa, and T. Furuya, "Development of the fuel-cell/battery hybrid railway vehicle," in *5th IEEE Vehicle Power and Propulsion Conference, VPPC '09*. IEEE, 2009, pp. 1730–1735.
- [56] S. Johnston, "Fuel cell tram evolution," 2017. [Online]. Available: <http://www.tautonline.com/fuel-cell-tram-evolution/>
- [57] "Qingdao opens fuel cell tram route," 2016. [Online]. Available: <https://www.railwaygazette.com/qingdao-opens-fuel-cell-tram-route/42177.article>
- [58] A. v. d. S. Taake Manning, "Overview of hydrogen and fuel cell developments in China," 2019. [Online]. Available: <https://www.nederlandwereldwijd.nl/binaries/nederlandwereldwijd/documenten/publicaties/2019/03/01/waterstof-in-china/Holland+Innovation+Network+in+China+-+Hydrogen+developments.+January+2019.pdf>
- [59] "CSR Sifang to deploy eight fuel cell powered trams in Foshan, China using Ballard modules," *Fuel Cells Bulletin*, vol. 2017, no. 3, p. 1, 2017.
- [60] "Foshan welcomes hydrogen fuel cell tram,," 2019. [Online]. Available: <https://www.railwaygazette.com/modes/foshan-welcomes-hydrogen-fuel-cell-tram/55268.article,retrieved2020.6>
-

-
- [61] S. Johnston, "Hydrogen trams enter service and begin testing," 2019. [Online]. Available: <http://www.tautonline.com/hydrogen-trams-enter-service-begin-testing/>
- [62] W. Klebsch, N. Guckes, and P. Heining, "Bewertung klimaneutraler Alternativen zu Dieseltriebzügen - Wirtschaftlichkeitsbetrachtungen am Praxis-Beispiel ›Netz Düren‹," p. 99, 2020. [Online]. Available: <https://www.railwaygazette.com/traction-and-rolling-stock/batteries-beat-hydrogen-on-cost-and-efficiency-vde-study-shows/57041.article%0A>
- [63] Elena Hof, "Germany Strategy for Sustainable Rail Transport: Projects and Political Initiatives," Rome, Italy, 2018. [Online]. Available: https://hydrail.appstate.edu/sites/hydrail.appstate.edu/files/13_hoff.pdf
- [64] "Whistle blows in Germany for world's first hydrogen train fleet." [Online]. Available: <https://www.france24.com/en/live-news/20220824-whistle-blows-in-germany-for-world-s-first-hydrogen-train-fleet>
- [65] IRJ, "Zillertalbahn hydrogen train design revealed," 2019. [Online]. Available: <https://www.railjournal.com/fleet/zillertalbahn-hydrogen-train-design-revealed/>
- [66] ALSTOM, "Alstom's hydrogen train Coradia iLint completes successful tests in the Netherlands | Alstom," 2020. [Online]. Available: <https://www.alstom.com/press-releases-news/2020/3/alstoms-hydrogen-train-coradia-ilint-completes-successful-tests>
- [67] "Mireo Plus," 2019. [Online]. Available: <https://www.fch.europa.eu/sites/default/files/05-Siemens-Katrin-Seeger.pdf>
- [68] R. Thorne, A. H. Amundsen, and I. Sundvor, "Battery electric and fuel cell trains: Maturity of technology and market," Oslo, Norway, p. 28, 2019. [Online]. Available: <https://www.toi.no/getfile.php?mmfileid=52027>
- [69] "Development of a Fuel Cell Hybrid Test Train." [Online]. Available: <https://www.jreast.co.jp/e/development/theme/energy/energy04.html>
- [70] "JR East, Hitachi and Toyota to Develop Hybrid Fuel Cell Railway Vehicles Powered by Hydrogen." [Online]. Available: <https://global.toyota/en/newsroom/corporate/33954855.html>
- [71] D. Ronanki, S. A. Singh, and S. S. Williamson, "Comprehensive Topological Overview of Rolling Stock Architectures and Recent Trends in Electric Railway Traction Systems," *IEEE Transactions on Transportation Electrification*, vol. 3, no. 3, pp. 724–738, 9 2017.
-

-
- [72] S. Sone, "Improvement of traction power feeding/regeneration system by means of energy storage devices," in *International Conference on Electrical Systems for Aircraft, Railway and Ship Propulsion, ESARS 2010*, 2010.
- [73] Siemens AG, "Mass transit solutions for operation without overhead contact line." 2012. [Online]. Available: <https://assets.new.siemens.com/siemens/assets/api/uuid:8d5d713e-2046-4972-bf20-7a7dca321dba/brochure-mass-transit-solutions-e.pdf>
- [74] M. Popescu and A. Bitoleanu, "A review of the energy efficiency improvement in DC railway systems," *Energies*, vol. 12, no. 6, p. 1092, 3 2019.
- [75] A. F. Obando, V. I. Herrera, H. Gaztanaga, B. Gallardo, T. Nieva, and M. Varela, "Optimization methodology of infrastructure and onboard energy storage system for cost-reduction in tramway lines design," in *2017 IEEE Vehicle Power and Propulsion Conference, VPPC 2017 - Proceedings*, vol. 2018-January, 2018.
- [76] C. Wu, S. Lu, F. Xue, L. Jiang, and M. Chen, "Optimal Sizing of Onboard Energy Storage Devices for Electrified Railway Systems," *IEEE Transactions on Transportation Electrification*, vol. 6, no. 3, pp. 1301–1311, 9 2020.
- [77] V. I. Herrera, H. Gaztanaga, A. Milo, A. Saez-de Ibarra, I. Etxeberria-Otadui, and T. Nieva, "Optimal Energy Management and Sizing of a Battery-Supercapacitor-Based Light Rail Vehicle With a Multiobjective Approach," *IEEE Transactions on Industry Applications*, vol. 52, no. 4, pp. 3367–3377, 7 2016.
- [78] D. Cornic, "Efficient recovery of braking energy through a reversible dc substation," in *International Conference on Electrical Systems for Aircraft, Railway and Ship Propulsion, ESARS 2010*. IEEE, 10 2010, pp. 1–9.
- [79] J. Varney, "Coradia iLint – Hydrogen Fuel Cell Train," 2019. [Online]. Available: https://www.apta.com/wp-content/uploads/Coradia-iLint-\T1\textendash-Hydrogen-Fuel-Cell-Train_James_Varney-1.pdf
- [80] A. Hoffrichter, S. Hillmansen, and C. Roberts, "Conceptual propulsion system design for a hydrogen-powered regional train," *IET Electrical Systems in Transportation*, vol. 6, no. 2, pp. 56–66, 2016.
- [81] S. Kent, "FCEMU Project - Phase 1 Report - Issue 1," University of Birmingham, Hitachi Rail, Fuel Cell Limited System, Tech. Rep. 1, 2016. [Online]. Available: <https://www.birmingham.ac.uk/Documents/college-eps/railway/1-Class-156-Fuel-Cell-Electric-Multiple-Unit-Feasibility-Study-Issue-1.pdf>
-

-
- [82] W. Schwab and A. Frixen, "Utilization of Fuel Cells for Trains Coradia iLINT Alstom Transport Coradia iLINT," 2018. [Online]. Available: https://www.jttri.or.jp/docs/180221_presentation-03.pdf
- [83] V. I. Herrera, E. Martinez-Laserna, H. Camblong, A. Milo, and H. Gaztanaga, "Techno-economic assessment of lithium-ion battery lifetime estimation methods for sizing and operation conditions definition in railway applications," in *2017 IEEE Vehicle Power and Propulsion Conference, VPPC 2017 - Proceedings*, vol. 2018-Janua, 2018.
- [84] T. Fletcher, R. Thring, and M. Watkinson, "An Energy Management Strategy to concurrently optimise fuel consumption & PEM fuel cell lifetime in a hybrid vehicle," *International Journal of Hydrogen Energy*, vol. 41, no. 46, pp. 21 503–21 515, 12 2016.
- [85] Z. Song, H. Hofmann, J. Li, X. Han, X. Zhang, and M. Ouyang, "A comparison study of different semi-active hybrid energy storage system topologies for electric vehicles," *Journal of Power Sources*, vol. 274, pp. 400–411, 1 2015.
- [86] F. Becker and A. Dammig, "Catenary free operation of light rail vehicles - Topology and operational concept," in *2016 18th European Conference on Power Electronics and Applications, EPE 2016 ECCE Europe*. IEEE, 2016, pp. 1–10.
- [87] M. Meinert, "New mobile energy storage system for rolling stock," in *2009 13th European Conference on Power Electronics and Applications, EPE '09*. Piscataway, NJ: IEEE, 2009, pp. 1–10.
- [88] M. Meinert, E. Peter, and K. Rechenberg, "Energy efficient and overhead contact line free operation of trams," in *9th UITP Light Rail Conference*, 2008, p. 10. [Online]. Available: <https://www.dcstreetcar.com/wp-content/uploads/2014/08/Section-D-Part-1-1-280-pagesred.pdf>
- [89] F. Peng, Y. Zhao, X. Li, Z. Liu, W. Chen, Y. Liu, and D. Zhou, "Development of master-slave energy management strategy based on fuzzy logic hysteresis state machine and differential power processing compensation for a PEMFC-LIB-SC hybrid tramway," *Applied Energy*, vol. 206, pp. 346–363, 11 2017.
- [90] Z. X. Liu, Q. Y. Bu, W. R. Chen, Q. Li, M. Li, and B. C. Sun, "Fuel cell based hybrid power system design for a passenger tram," *WHEC 2016 - 21st World Hydrogen Energy Conference 2016, Proceedings*, vol. 51, no. 3, pp. 1119–1121, 2016. [Online]. Available: https://hydrail.appstate.edu/sites/hydrail.appstate.edu/files/11_zhang.pdf<http://www.jsju.org/index.php/journal/article/view/119>
-

-
- [91] A. Allègre, A. Bouscayrol, and R. Trigui, "Flexible real-time control of a hybrid energy storage system for electric vehicles," *IET Electrical Systems in Transportation*, vol. 3, no. 3, pp. 79–85, 9 2013.
- [92] J. P. Trovão, P. G. Pereirinha, H. M. Jorge, and C. H. Antunes, "A multi-level energy management system for multi-source electric vehicles - An integrated rule-based meta-heuristic approach," *Applied Energy*, vol. 105, pp. 304–318, 5 2013.
- [93] P. Garcia, L. M. Fernandez, C. A. Garcia, and F. Jurado, "Energy management system of fuel-cell-battery hybrid tramway," *IEEE Transactions on Industrial Electronics*, vol. 57, no. 12, 2010.
- [94] L. Cheng, W. Wang, S. Wei, H. Lin, and Z. Jia, "An Improved Energy Management Strategy for Hybrid Energy Storage System in Light Rail Vehicles," *Energies*, vol. 11, no. 2, p. 423, 2 2018. [Online]. Available: <http://www.mdpi.com/1996-1073/11/2/423>
- [95] M. E. Choi, J. S. Lee, and S. W. Seo, "Real-time optimization for power management systems of a battery/supercapacitor hybrid energy storage system in electric vehicles," *IEEE Transactions on Vehicular Technology*, vol. 63, no. 8, 2014.
- [96] Z. Song, H. Hofmann, J. Li, J. Hou, X. Han, and M. Ouyang, "Energy management strategies comparison for electric vehicles with hybrid energy storage system," *Applied Energy*, vol. 134, pp. 321–331, 12 2014.
- [97] L. Cheng, P. Acuna, R. P. Aguilera, J. Jiang, J. Flether, and C. Baier, "Model predictive control for Energy Management of a hybrid energy storage system in Light Rail Vehicles," in *2017 11th IEEE International Conference on Compatibility, Power Electronics and Power Engineering, CPE-POWERENG 2017*, 2017.
- [98] V. I. Herrera, H. Gaztanaga, A. Milo, A. Saez-De-Ibarra, I. Etxeberria-Otadui, and T. Nieva, "Optimal energy management of a battery-supercapacitor based light rail vehicle using genetic algorithms," in *2015 IEEE Energy Conversion Congress and Exposition, ECCE 2015*, 2015.
- [99] D. Ronanki and S. S. Williamson, "Modular Multilevel Converters for Transportation Electrification: Challenges and Opportunities," *IEEE Transactions on Transportation Electrification*, vol. 4, no. 2, pp. 399–407, 6 2018.
- [100] M. Glinka and R. Marquardt, "A new AC/AC multilevel converter family," *IEEE Transactions on Industrial Electronics*, vol. 52, no. 3, 2005.
-

-
- [101] D. Ronanki and S. S. Williamson, "Evolution of Power Converter Topologies and Technical Considerations of Power Electronic Transformer-Based Rolling Stock Architectures," *IEEE Transactions on Transportation Electrification*, vol. 4, no. 1, pp. 211–219, 3 2018.
- [102] M. Hagiwara, K. Nishimura, and H. Akagi, "A medium-voltage motor drive with a modular multilevel PWM inverter," *IEEE Transactions on Power Electronics*, vol. 25, no. 7, pp. 1786–1799, 2010.
- [103] N. Mukherjee and P. Tricoli, "A new state of charge control of modular multilevel converters with supercapacitors for traction drives," in *2015 IEEE Energy Conversion Congress and Exposition, ECCE 2015*, 2015.
- [104] M. Coppola, A. Del Pizzo, and D. Iannuzzi, "A power traction converter based on Modular Multilevel architecture integrated with energy storage devices," in *Electrical Systems for Aircraft, Railway and Ship Propulsion, ESARS*, 2012.
- [105] C. Gan, Q. Sun, J. Wu, W. Kong, C. Shi, and Y. Hu, "MMC-Based SRM Drives with Decentralized Battery Energy Storage System for Hybrid Electric Vehicles," *IEEE Transactions on Power Electronics*, vol. 34, no. 3, 2019.
- [106] I. Krastev and P. Tricoli, "Boost Multilevel Cascade Inverter for Hydrogen Fuel Cell Light Railway Vehicles," *IEEE Transactions on Industrial Electronics*, vol. 69, no. 8, 2022.
- [107] K. A. Corzine, S. D. Sudhoff, and C. A. Whitcomb, "Performance characteristics of a cascaded two-level converter," *IEEE Transactions on Energy Conversion*, vol. 14, no. 3, pp. 433–439, 1999.
- [108] V. Oleschuk, R. Bojoi, G. Griva, and F. Profumo, "Dual inverter-fed traction drive with DC sources power balancing based on synchronized PWM," in *Proceedings of IEEE International Electric Machines and Drives Conference, IEMDC 2007*, vol. 1, 2007.
- [109] C. Attaianesi, M. Di Monaco, and G. Tomasso, "Power Control for Fuel-Cell-Supercapacitor Traction Drive," *IEEE Transactions on Vehicular Technology*, vol. 61, no. 5, pp. 1961–1971, 2012.
- [110] M. Chymera, A. C. Renfrew, M. Barnes, and J. Holden, "Simplified power converter for integrated traction energy storage," *IEEE Transactions on Vehicular Technology*, vol. 60, no. 4, pp. 1374–1383, 5 2011.
- [111] L. Dorn-Gomba, P. Magne, B. Danen, and A. Emadi, "On the Concept of the Multi-Source Inverter for Hybrid Electric Vehicle Powertrains," *IEEE Transactions on Power Electronics*, vol. 33, no. 9, pp. 7376–7386, 9 2018.
-

-
- [112] L. Dorn-Gomba, J. Guo, and A. Emadi, "Multi-Source Inverter for Power-Split Hybrid Electric Powertrains," *IEEE Transactions on Vehicular Technology*, vol. 68, no. 7, pp. 6481–6494, 7 2019.
- [113] L. Dorn-Gomba, E. Chemali, and A. Emadi, "A novel hybrid energy storage system using the multi-source inverter," in *Conference Proceedings - IEEE Applied Power Electronics Conference and Exposition - APEC*, vol. 2018-March. Institute of Electrical and Electronics Engineers Inc., 4 2018, pp. 684–691.
- [114] T. Mizobuchi, K. Kondo, Y. Dairaku, T. Shinomiya, and K. Ishikawa, "Energy-Management Method to Reduce the Capacity of Lithium-Ion Batteries in Hybrid-Voltage-Source Three-Level Inverter for DC-Electrified Railway Vehicles," *IEEE Open Journal of Industry Applications*, vol. 3, pp. 41–55, 2022.
- [115] H. Ahmad and M. Hagiwara, "A Compact High-Power Noninverting Bidirectional Buck-Boost Chopper for Onboard Battery Energy Storage Systems," *IEEE Transactions on Power Electronics*, vol. 37, no. 2, pp. 1722–1735, 2 2022.
- [116] K. Takao, Y. Tanaka, K. Sung, K. Wada, T. Shinohe, T. Kanai, and H. Ohashi, "High-power converters with high switching frequency operation using SiC-PiN diodes and Si-IEGTs," in *2011 1st International Conference on Electric Power Equipment - Switching Technology, ICEPE2011 - Proceedings*, 2011.
- [117] N. Soltan, E. Wiesner, E. Stumpf, S. Idaka, and K. Hatori, "Electric-Energy Savings using 3.3 kV Full-SiC Power-Modules in Traction Applications," in *2020 15th International Conference on Ecological Vehicles and Renewable Energies, EVER 2020*, 2020.
- [118] J. San-Sebastian, A. Rujas, L. Mir, A. Berasategi, and T. Nieva, "Performance improvements using silicon carbide hybrid IGBT modules in traction application," in *2016 International Conference on Electrical Systems for Aircraft, Railway, Ship Propulsion and Road Vehicles and International Transportation Electrification Conference, ESARS-ITEC 2016*, 2016.
- [119] N. Celanovic and D. Boroyevich, "A comprehensive study of neutral-point voltage balancing problem in three-level neutral-point-clamped voltage source PWM inverters," *IEEE Transactions on Power Electronics*, vol. 15, no. 2, 2000.
- [120] K. Zhou and D. Wang, "Relationship between space-vector modulation and three-phase carrier-based PWM: A comprehensive analysis," *IEEE Transactions on Industrial Electronics*, vol. 49, no. 1, pp. 186–196, 2 2002.
-

-
- [121] S. Chattopadhyay, M. Mitra, and S. Sengupta, “Clarke and Park Transform,” in *Electric Power Quality*. Springer, 2011, pp. 89–96.
- [122] I. Lopez, S. Ceballos, J. Pou, J. Zaragoza, J. Andreu, I. Kortabarria, and V. G. Agelidis, “Modulation Strategy for Multiphase Neutral-Point-Clamped Converters,” *IEEE Transactions on Power Electronics*, vol. 31, no. 2, pp. 928–941, 2 2016.
- [123] J. Zaragoza, J. Pou, S. Ceballos, E. Robles, C. Jaen, and M. Corbalan, “Voltage-Balance Compensator for a Carrier-Based Modulation in the Neutral-Point-Clamped Converter,” *IEEE Transactions on Industrial Electronics*, vol. 56, no. 2, pp. 305–314, 2 2009.
- [124] A. Cervone, G. Brando, and O. Dordevic, “Hybrid Modulation Technique With DC-Bus Voltage Control for Multiphase NPC Converters,” *IEEE Transactions on Power Electronics*, vol. 35, no. 12, pp. 13 528–13 539, 12 2020.
- [125] Y. Huang, J. Walden, A. Foote, H. Bai, D. Lu, F. Jin, and B. Cheng, “Analytical Characterization of CM and DM Performance of Three-Phase Voltage-Source Inverters under Various PWM Patterns,” *IEEE Transactions on Power Electronics*, vol. 36, no. 4, pp. 4091–4104, 4 2021.
- [126] F. Yang, H. Ge, J. Yang, R. Dang, and H. Wu, “A Family of Dual-Buck Inverters with an Extended Low-Voltage DC-Input Port for Efficiency Improvement Based on Dual-Input Pulsating Voltage-Source Cells,” *IEEE Transactions on Power Electronics*, vol. 33, no. 4, pp. 3115–3128, 4 2018.
- [127] H. Wu, L. Zhu, and F. Yang, “Three-Port-Converter-Based Single-Phase Bidirectional AC–DC Converter With Reduced Power Processing Stages and Improved Overall Efficiency,” *IEEE Transactions on Power Electronics*, vol. 33, no. 12, pp. 10 021–10 026, 12 2018.
- [128] F. Yang, H. Ge, Z. Yu, Y. Li, and H. Wu, “Topology and Control of Four-Quadrant Dual-DC-Port Dual-Buck Inverters for Semi-Two-Stage DC-AC Power Conversion,” *IEEE Transactions on Industrial Electronics*, vol. 68, no. 11, pp. 10 718–10 729, 11 2021.
- [129] Akasol, “Rail battery systems brochure.” [Online]. Available: https://www.akasol.com/library/Downloads/Brosch%C3%BCren/AKASOL_rail_applications_brochure_18.pdf.pdf
- [130] J. Klink, J. Grabow, N. Orazov, R. Benger, A. Börger, A. Ahlberg Tidblad, H. Wenzl, and H.-P. Beck, “Thermal fault detection by changes in electrical behaviour in lithium-ion cells,” *Journal of Power Sources*, vol. 490, p. 229572, 4 2021.
-

-
- [131] A. Rujas, V. M. López, A. García-Bediaga, A. Berasategi, and T. Nieva, “Influence of SiC technology in a railway traction DC-DC converter design evolution,” in *2017 IEEE Energy Conversion Congress and Exposition, ECCE 2017*, vol. 2017-Janua. Institute of Electrical and Electronics Engineers Inc., 11 2017, pp. 931–938.
- [132] L. Diao, J. Tang, P. C. Loh, S. Yin, L. Wang, and Z. Liu, “An Efficient DSP–FPGA-Based Implementation of Hybrid PWM for Electric Rail Traction Induction Motor Control,” *IEEE Transactions on Power Electronics*, vol. 33, no. 4, pp. 3276–3288, 4 2018.
- [133] K. S. Rajashekara, V. Rajagopalan, A. Sevigny, and J. Vithayathil, “DC Link Filter Design Considerations in Three-Phase Voltage Source Inverter-Fed Induction Motor Drive System,” *IEEE Transactions on Industry Applications*, vol. IA-23, no. 4, pp. 673–680, 7 1987.
- [134] B. Shihab, H. Che, and W. Hew, “Symmetrical six-phase PWM methods using similar and dissimilar zero-sequence signals injection,” in *4th IET Clean Energy and Technology Conference (CEAT 2016)*. Institution of Engineering and Technology, 2016, pp. 78 (6 .)–78 (6 .).
- [135] J. T. Pukrushpan, A. G. Stefanopoulou, and H. Peng, *Control of Fuel Cell Power Systems: Principles, Modeling, Analysis and Feedback Design*, 2006.
- [136] “Simulation Model - Infineon Technologies.” [Online]. Available: <https://www.infineon.com/cms/en/design-support/finder-selection-tools/product-finder/simulation-model/?redirId=156404>
- [137] J. Larminie and A. Dicks, *Fuel cell systems explained*, 2013.
- [138] J. Loncarski, V. G. Monopoli, R. Leuzzi, P. Zanchetta, and F. Cupertino, “Efficiency, Cost and Volume Comparison of Si-IGBT Based T-NPC and 2-Level SiC-MOSFET Based Topology with dv/dt Filter for High Speed Drives,” in *ECCE 2020 - IEEE Energy Conversion Congress and Exposition*, 2020.
- [139] E. Gurpinar and A. Castellazzi, “Single-Phase T-Type Inverter Performance Benchmark Using Si IGBTs, SiC MOSFETs and GaN HEMTs,” *IEEE Transactions on Power Electronics*, pp. 1–1, 2015.
- [140] W. G. Hurley and W. H. Wölflé, *Transformers and Inductors for Power Electronics: Theory, Design and Applications*, 2013.
- [141] T. McLyman, *Transformer and Inductor Design Handbook, Fourth Edition*, 2017.
-

-
- [142] “Benefits of multiphasing buck converters - Part 1 - EE Times.” [Online]. Available: <https://www.eetimes.com/benefits-of-multiphasing-buck-converters-part-1/>
- [143] P. Argo Dahono, Y. Sato, and T. Kataoka, “Analysis and Minimization of Ripple Components of Input Current and Voltage of PWM Inverters,” *IEEE Transactions on Industry Applications*, vol. 32, no. 4, pp. 945–950, 1996.
- [144] J. Kolar, “Analytical calculation of the RMS current stress on the DC link capacitor of voltage DC link PWM converter systems,” in *9th International Conference on Electrical Machines and Drives*. IEE, 1999, pp. 81–89.
- [145] “ABL Heatsinks.” [Online]. Available: <http://www.abl-heatsinks.co.uk/index.php?page=extrudedresults>
-

Author's Publications

A. Del Pizzo, L. P. Di Noia and **E. Fedele**, "An analytical evaluation of rotor eccentricity effects on synchronous drives with surface mounted permanent magnet brushless motors," *2020 IEEE 20th Mediterranean Electrotechnical Conference (MELECON)*, 2020, pp. 35-40.

A. Dannier, **E. Fedele** and M. Coppola, "Sizing approach of high torque density motors for aircraft application," *2020 International Symposium on Power Electronics, Electrical Drives, Automation and Motion (SPEEDAM)*, 2020, pp. 497-501.

A. Del Pizzo, L. P. Di Noia, and **E. Fedele**, "A Simple Analytical Model of Static Eccentricity for PM Brushless Motors and Validation through FEM Analysis," *Energies*, vol. 13, no. 13, p. 3420, Jul. 2020.

E. Fedele, D. Iannuzzi, and A. Del Pizzo, "Onboard energy storage in rail transport: Review of real applications and techno-economic assessments," *IET Electr. Syst. Transp.*, vol. 11, no. 4, pp. 279–309, Dec. 2021.

E. Fedele, D. Iannuzzi, P. Tricoli and A. Del Pizzo, "NPC-based Multi-Source Inverters for Multimode DC Rail Traction Systems," in *IEEE Transactions on Transportation Electrification* (early access).

A. Di Pasquale, **E. Fedele**, D. Iannuzzi and M. Pagano, "Contribution of Wayside Energy Storage Systems to Short Circuit Currents in DC Railway Traction Power Systems," *2022 International Power Electronics Conference (IPEC-Himeji 2022- ECCE Asia)*, 2022, pp. 1101-1106.

E. Fedele, A. Di Pasquale, D. Iannuzzi and M. Pagano, "Integration of Onboard Batteries and Supercapacitors Based on the Multi-Source Inverter for Light Rail Vehicles," *2022 International Power Electronics Conference (IPEC-Himeji 2022-ECCE Asia)*, 2022, pp. 698-704.

E. Fedele, A. Cervone, I. Spina, D. Iannuzzi and A. D. Pizzo, "Multi-Objective Vector Modulation for Improved Control of NPC-based Multi-Source Inverters in Hybrid Traction Systems," in *IEEE Journal of Emerging and Selected Topics in Power Electronics* (early access).

E. Fedele, D. Iannuzzi and I. Spina, "Semi-Two-Stage Traction System based on the NPC Multisource Inverter for Tram Vehicles with Onboard Supercapacitors," *2022 International Symposium on Power Electronics, Electrical Drives, Automation and Motion (SPEEDAM)*, 2022, pp. 277-282.

I. Spina, **E. Fedele** and A. Cervone, "Simplified low-cost experimental setup for battery loss evaluation in MMC converters," *2022 International Symposium on Power Electronics, Electrical Drives, Automation and Motion (SPEEDAM)*, 2022, pp. 534-540.

A. Dannier, **E. Fedele**, I. Spina, and G. Brando, "Doubly-Fed Induction Generator (DFIG) in Connected or Weak Grids for Turbine-Based Wind Energy Conversion System," *Energies*, vol. 15, no. 17, p. 6402, Sep. 2022.

A. Dannier, F. Di Bruno, F. Fiume, **E. Fedele**, G. Brando, "Hairpin Winding Technology for Electric Traction Motors: Design, Prototyping, and Connection Rules," *2022 International Conference on Electrical Machines (ICEM)*, 2022, pp. 1170-1175.

C. Attaianese, A. Di Pasquale, **E. Fedele**, D. Iannuzzi, M. Pagano, and M. Ribera, "Energy Efficiency Assessment for an Ultra-Fast Charging Station," *2022 IEEE Vehicle Power and Propulsion Conference (VPPC)*, 2022.

La borsa di dottorato è stata cofinanziata con risorse del
Programma Operativo Nazionale Ricerca e Innovazione 2014-2020 (CCI 2014IT16M2OP005)
Fondo Sociale Europeo, Azione 1.1 "Dottorati Innovativi con caratterizzazione Industriale"



UNIONE EUROPEA
Fondo Sociale Europeo



*Ministero dell'Università
e della Ricerca*



PON
RICERCA
E INNOVAZIONE
2014 - 2020